

**LOW TEMPERATURE GAS DESULPHURISATION  
USING MIXED COBALT-ZINC OXIDES**

By

---

**Robert William Hoyle**

**A Thesis Submitted for the Degree of Doctor of Philosophy of  
University of Glasgow, January 1995**

---

ProQuest Number: 11007853

All rights reserved

INFORMATION TO ALL USERS

The quality of this reproduction is dependent upon the quality of the copy submitted.

In the unlikely event that the author did not send a complete manuscript and there are missing pages, these will be noted. Also, if material had to be removed, a note will indicate the deletion.



ProQuest 11007853

Published by ProQuest LLC (2018). Copyright of the Dissertation is held by the Author.

All rights reserved.

This work is protected against unauthorized copying under Title 17, United States Code  
Microform Edition © ProQuest LLC.

ProQuest LLC.  
789 East Eisenhower Parkway  
P.O. Box 1346  
Ann Arbor, MI 48106 – 1346

Thesis  
10052  
Copy 1



**To Marian**

---

---

## ACKNOWLEDGEMENTS

I wish to thank Dr. Diane Stirling for her invaluable assistance and encouragement throughout this project and for the many times she has had to read this thesis.

I also wish to thank Dr. Peter Williams for his interest in the project and for the opportunity to do the XPS work at ICI Katalco. In connection with this work I would also like to thank Dr. Mick Morris for his time and assistance.

I am grateful to Dr. Tom Baird for the TEM micrographs and to Dr. Max Huxam for the EELS analysis. I owe thanks to Dr. Peter Holliman for his practical assistance and helpful discussions throughout the project and for the time he took in helping with the preparation of this thesis. For their continued interest throughout the project and handy hints I wish to thank Drs. Pat Denny and K.C. Campbell.

I am indebted to all the technical staff at the University of Glasgow, especially Mr Murdo McDonald and Dougie McLeod in the Department of Geology; Ms. Vicky Yates for printing my micrographs and to the all singing and dancing Ms. Rose Millar for all her help and good cheer.

I am grateful to Stewart Riddell for processing my samples at ICI, to Nick Pope for translating a paper used in the introduction, to Dr. Alan Kennedy for the hydrozincite picture, to Ann Massinon from Belgium for her contribution to my work in relation to the precursor aging studies and to Gerry Montgomery for scanning some pictures.

A huge massive thanks goes to all the people, past and present, in 105, The Stanleys, The Centre of Excellence, 281 and the Fluorine labs; they made the last three years such a joy!

Finally I acknowledge The Science and Engineering Council for the grant award.

## ABSTRACT

The hydrogen sulphide absorption capacity of a range of mixed cobalt-zinc oxides was determined using a continuous flow microreactor. The mixed oxides were prepared by the thermal decomposition of hydroxycarbonate precursors. The precursors were synthesized by the coprecipitation method using the mixed metal nitrates and ammonium or sodium carbonate.

X-Ray diffraction studies of the precursors synthesized from ammonium carbonate revealed that at low cobalt loadings hydrozincite,  $\text{Zn}_5(\text{CO}_3)_2(\text{OH})_6$ , was present as the predominant phase and spherocobaltite,  $\text{CoCO}_3$ , as the minor phase. At cobalt loadings  $\geq 50\%$  spherocobaltite was observed as the major phase. However, the Co/Zn 100/0 precursor revealed only the presence of a metastable phase,  $\text{Co}(\text{CO}_3)_{0.5}(\text{OH})_{1.0} \cdot 0.1\text{H}_2\text{O}$  which had been previously identified by Porta *et al.*<sup>45</sup> UV-VIS-NIR diffuse reflectance spectroscopy revealed that the cobalt was present in the 2+ oxidation state in an octahedral environment in all the precursors. When sodium hydrogen carbonate was used as the precipitating agent sodium zinc carbonate,  $\text{Na}_2\text{Zn}_3(\text{CO}_3)_4 \cdot 13\text{H}_2\text{O}$ , was formed. This was believed to be an intermediate in the formation of hydrozincite. For the Co/Zn 30/70 loading the pH used during the coprecipitation altered the predominant phase structure found in the final precursor.

The major phase obtained on calcination of the precursors with a Co/Zn ratio  $\leq 30/70$  was ZnO with the a 'cobalt oxide type' phase (taken to be  $\text{Co}_3\text{O}_4$ ) present as a minor phase. As the cobalt loading was increased this situation was reversed and  $\text{Co}_3\text{O}_4$  became the major phase. Varying the temperature at which the precursor was calcined to the oxide revealed that the highest surface area was achieved when the precursor was calcined at *ca.* 200°C. An X-Ray photoelectron study of the oxides calcined at 350°C revealed that only  $\text{Co}^{3+}$  and  $\text{Zn}^{2+}$  ions were present at the surface suggesting the presence of a 'surface spinel',  $\text{ZnCo}_2\text{O}_4$ . Segregation of cobalt to the surface was observed. This segregation was believed to be determined during the synthesis of the precursor and was carried through to the oxide.

The reaction of the mixed oxides with  $\text{H}_2\text{S}$  was restricted to *ca.* 3 monolayers on average, based on calculations from surface areas, and is therefore largely confined to the surface of the oxides. For the oxides calcined at  $\geq 350^\circ\text{C}$  the linear relationship observed between the surface area and the sulphur uptake suggested that lattice diffusion played a major role in the rate determining step, the main role of the cobalt being to increase the surface area. The oxides calcined  $\leq 250^\circ\text{C}$  showed no correlation between surface area and sulphur uptake. It is likely that both pore and lattice diffusion contributed to the rate of sulphur uptake in these oxides. The oxides with a Co/Zn ratio of 100/0 were found to be the best sulphur absorbents. Calculations indicated that a bulk reaction had taken place in these oxides. Transmission electron micrographs of the mixed oxides before and after sulphidation revealed the presence of a sheet-like material which became more prevalent the more the mixed oxide was sulphided. Electron energy loss spectroscopy indicated that these sheet-like regions were predominantly zinc in composition.

## CONTENTS

<b>ACKNOWLEDGEMENTS</b>	i
<b>ABSTRACT</b>	iii
<b>CHAPTER 1. INTRODUCTION</b>	
<b>1.1 Introduction</b>	1
<b>1.2 Methods Used in Industry for the Removal of Hydrogen Sulphide</b>	3
1.2.1 Absorption into Liquid	
1.2.2 Adsorption onto and Absorption into a Solid	
<b>1.3 Reaction of Hydrogen Sulphide and Zinc Oxide</b>	6
1.3.1 Techniques used to Investigate the H <sub>2</sub> S/ZnO Reaction	
1.3.2 Literature Survey of H <sub>2</sub> S/ZnO Reaction	
1.3.2a High Temperature (350-450°C)	
1.3.2b Ambient Temperature	
<b>1.4 Comparison of Zinc Oxide and Transition Metal Oxides</b>	22
1.4.1 Doping Zinc Oxide with a 1st Row Transition Metal	
<b>1.5 Preparation of a Multicomponent Oxide</b>	27
1.5.1 Precipitation at Low Supersaturation (LSS)	
1.5.2 Precipitation at High Supersaturation (HSS)	
1.5.3 Titration Method (TM)	
<b>1.6 Mixed Metal Hydroxycarbonates and their Products of Decomposition</b>	30
<b>1.7 Structures of the Hydroxycarbonate Precursors</b>	33
1.7.1 Hydrozincite	
1.7.2 Spherocobaltite	
<b>CHAPTER 2. THEORY OF TECHNIQUES</b>	
<b>2.1 Powder X-ray Diffraction (XRD)</b>	35
2.1.1 Introduction	
2.1.2 Bragg's Law	
2.1.3 Instrument	
2.1.4 Phase Determination	
2.1.5 Quantitative Analysis	
2.1.6 Particle Size Measurement	

<b>2.2 UV-VIS-NIR Diffuse Reflectance Spectroscopy (DRS)</b>	<b>39</b>
2.2.1 Introduction	
2.2.2 Types of Reflection Associated With DRS	
2.2.3 Kubelka-Munk Theory of DRS	
2.2.4 Instrumental Considerations	
2.2.5 Spectra Arising From d-d Transitions	
<b>2.3 X-ray Photoelectron Spectroscopy (XPS)</b>	<b>45</b>
2.3.1 Theory of XPS	
2.3.2 Experimental Instrumentation	
2.3.2a X-ray Source	
2.3.2b Ultra-high Vacuum	
2.3.2c Photoelectron Detection Analyzer	
2.3.2d Preparation/Analysis	
2.3.3 Primary Structure	
2.3.3a Core Levels	
2.3.3b Relative Intensities	
2.3.3c Peak Widths	
2.3.3d Chemical Shifts	
2.3.3e Auger Emissions	
2.3.4 Secondary Structure	
2.3.4a Relaxation	
2.3.4b Multiplet Splitting	
2.3.4c Shake-up Satellites	
2.3.4d Plasmons	
2.3.5 Charging and Referencing	
2.3.6 Data Analysis	
2.3.6a Background Removal	
2.3.6b Spectral Smoothing	
2.3.6c Peak Fitting	
2.3.6d Integration	
2.3.6e Quantitative Analysis	
<b>CHAPTER 3. OBJECTIVES</b>	<b>62</b>
<b>CHAPTER 4. EXPERIMENTAL</b>	
<b>4.1 Absorbent Preparation and Analysis</b>	<b>64</b>
<b>4.2 Absorbent Characterisation</b>	<b>65</b>
4.2.1 Powder X-ray Diffraction	
4.2.2 Transmission Electron Microscopy	
4.2.3 UV-VIS-NIR Diffuse Reflectance Spectroscopy	
4.2.4 Fourier-Transform Infra-red Spectroscopy	
4.2.5 Thermal Analysis	
4.2.6 Surface Area Determination	
4.2.7 Microanalysis	
4.2.8 X-ray Photoelectron Spectroscopy - Qualitative Analysis	

<b>4.3 Absorbent Testing</b>	68
<b>4.4 Cobalt-Zinc 1st Series</b>	70
<b>4.5 XPS Study of Cobalt-Zinc 1st Series</b>	70
<b>4.6 Optimisation of Calcination Parameters</b>	71
<b>4.7 Cobalt-Zinc 2nd Series</b>	72
<b>4.8 Aging Study of Co/Zn 30/70 Loading</b>	73
<b>4.9 Different Methods of Precursor Preparation</b>	73
4.9.1 Precipitation at Low Supersaturation	
4.9.2 Precipitation at High Supersaturation	
4.9.3 Titration Method	
 <b>CHAPTER 5. TREATMENT OF RESULTS</b>	
<b>5.1 'Breakthrough' Rig Data</b>	76
<b>5.2 XRD d-spacings</b>	77
<b>5.3 Micrographs - Particle Size</b>	77
<b>5.4 Atomic Absorption</b>	77
<b>5.5 XPS Analysis</b>	78
5.5.1 Qualitative Analysis	
5.5.2 Quantitative Analysis	
 <b>CHAPTER 6. RESULTS</b>	
<b>6.1 Cobalt-Zinc 1st Series</b>	81
6.1.1 Characterisation of the Precursors	
6.1.2 Characterisation of the Oxides	
6.1.3 Sulphided Oxides	
<b>6.2 XPS Study of Cobalt-Zinc 1st Series</b>	99
6.2.1 Precursors	
6.2.2 Oxides (Cal.350°C, 16 hrs.)	
6.2.3 Oxides (Cal. Var. Temps., 8hrs.)	
6.2.4 Sulphided Oxides	
<b>6.3 Optimisation of Calcination Parameters</b>	114

<b>6.4 Cobalt-Zinc 2nd Series</b>	117
6.4.1 Characterisation of the Precursors	
6.4.2 Characterisation of the Oxides	
6.4.3 Absorbent Testing	
<b>6.5 Aging Study of Co/Zn 30/70</b>	132
6.5.1 Characterisation of the Precursors	
6.5.2 Characterisation of the Oxides	
6.5.3 Sulphided Oxides	
<b>6.6 Different Methods of Precursor Preparation</b>	139
6.6.1 Characterisation of the Precursors	
6.6.2 Characterisation of the Oxides	
6.6.3 Sulphided Oxides	
 <b>CHAPTER 7. DISCUSSION</b>	
<b>7.1 Introduction</b>	151
<b>7.2 Precursors</b>	151
7.2.1 Ammonium Carbonate Precursors - Standard Method	
7.2.1a Nucleation	
7.2.1b Crystal Growth	
7.2.1c Thermogravimetric Analysis	
7.2.1d Structure of Cobalt Doped Hydrozincite	
7.2.2 Ammonium Carbonate Precursors - Variations	
7.2.3 Sodium Carbonate Precursors	
<b>7.3 Oxides</b>	161
7.3.1 Decomposition of Precursors	
7.3.2 Nature of Solid-Solutions	
7.3.3 Surface Effects	
7.3.3a Ionic Charge at Surface	
<b>7.4 Sulphide Oxides</b>	168
7.4.1 Sulphidation of Oxides Calcined $\geq 300^{\circ}\text{C}$	
7.4.2 Sulphidation of Oxides Calcined $\leq 250^{\circ}\text{C}$	
7.4.3 Effect of Sodium	
7.4.4 Segregation of Phases	
<b>7.5 Conclusion</b>	174
<b>APPENDIX A - Abbreviations</b>	177
<b>APPENDIX B - Solubility Constant Calculations</b>	181
<b>APPENDIX C - XRD Computer Program</b>	183
<b>REFERENCES</b>	184

**CHAPTER 1**  
**INTRODUCTION**

---

---

## 1.1 INTRODUCTION

The transition metal catalysts used in the modern ammonia and methanol plants are extremely active and highly selective. However they are also very sensitive to poisoning by sulphur compounds which can be present in the feedstock gas.

The feedstocks used in these processes can originate from various sources. Natural gas is the most commonly used feedstock for the production of synthesis gas ( $\text{CO-CO}_2\text{-H}_2$ ) by steam reforming. In oil rich regions associated gas (gas released in oil-production) is often used as the feedstock for ammonia plants. In countries which have access to cheap coal, methanol can be manufactured from the synthesis gas obtained from coal gasification. All these feedstocks originate from fossil fuels. Sulphur-generating bacteria may have been present during the formation of these hydrocarbon fuels, or during their removal from the ground. These bacteria generate hydrogen sulphide which in turn can form COS and various organo-sulphur compounds.<sup>1</sup> These sulphur impurities can be present from ppm to percentage levels.

The feedstocks must be free of sulphur contaminants to ensure the efficient and long term running of these industrial plants. This is because the transition-metal catalysts used in the processes cited are prone to deactivation by Lewis type bases, such as  $\text{H}_2\text{S}$ , capable of donating electrons into the unfilled d-orbitals of the metals.<sup>2</sup> These sulphur compounds are thought to chemisorb on to the transition metals by forming bonds in which previously unshared lone pair electrons on the sulphur atom are donated into the d-orbitals of the metal.<sup>2</sup> Sulphur bonds so strongly to metal surfaces that a marked reduction in activity can occur even at extremely low gas-phase concentrations,

where the sulphur can only just be detected.<sup>3</sup> It has been recognised that sulphur adsorbed on metal surfaces interferes with catalytic processes at concentrations of gaseous sulphur compounds well below the levels necessary to form bulk metal sulphides. For example, transition metal catalysts used for catalytic reforming are often presulphided with very small quantities of H<sub>2</sub>S in order to change the selectivity of the products.<sup>4</sup> Therefore small quantities of sulphide poisoning could have a very serious effect. This, coupled with the cumulative effect of large quantities of feedstock gas passing over the catalyst, can mean that the commercial lifetime of the catalyst could be reduced to only a few months or weeks. This catalyst poisoning is essentially irreversible as regeneration is usually impossible or impractical.<sup>5</sup>

Hydrogen sulphide is also extremely odorous and highly poisonous. Its long-term exposure limit is 10 ppm. Sulphur-containing compounds are known to contribute significantly to acid rain and hence have a detrimental effect on the environment. With the increasing need for cleaner automotive exhaust emissions, processes have been developed to prevent H<sub>2</sub>S emissions during their catalytic purification.<sup>6</sup>

Sulphur compounds are very highly corrosive and the corrosion of pipelines, resulting in the reduction in the lifetime of a plant, is a major problem. These requirements demand that the sulphur contaminants in feedstocks should be less than 0.1 ppm. Most modern gas purification processes will reduce the sulphur content of the feedstock to less than 0.02 ppm.

## 1.2 METHODS USED IN INDUSTRY FOR THE REMOVAL OF HYDROGEN SULPHIDE

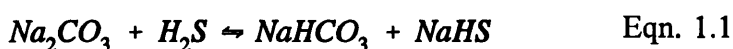
There are many methods which have been or are being used to remove hydrogen sulphide from natural, refinery or synthesis gas streams. Each method has its own advantages and disadvantages which may or may not suit the conditions under which the process must operate.

The primary operation of the gas purification process generally falls into one of the following categories,

- (i) Absorption into a liquid
- (ii) Adsorption onto and absorption into a solid.

### 1.2.1 Absorption into a Liquid

The advantages of the liquid processes are that the absorbent can be regenerated and that elemental sulphur is produced. One such process, typical of many, was the Seaboard Process, developed *circa* 1920.<sup>7</sup> This process was used commercially for H<sub>2</sub>S removal at ambient temperatures. It was based upon the absorption of H<sub>2</sub>S by dilute sodium carbonate, see Eqn. 1.1,



The sodium carbonate was then regenerated using air. This was an extremely simple operation and very economical. However the major disadvantage was the disposal of the foul air containing H<sub>2</sub>S.

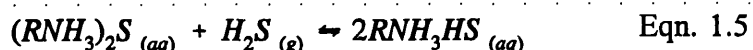
Another method employed was the Fisher process which used iron complexes. Alkaline ferricyanide solution was used to oxidise H<sub>2</sub>S to sulphur

according to Eqn. 1.2, with regeneration being achieved electrolytically, Eqn. 1.3,



There are many other liquid phase oxidation processes on which extensive research has been carried out.<sup>8</sup>

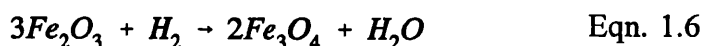
Solutions of alkanolamines such as monoethanolamine, MEA and diethanolamine, DEA can be used to selectively remove H<sub>2</sub>S and/or CO<sub>2</sub>. The principal reactions occurring when solutions of these amines are contacted with H<sub>2</sub>S are represented in Eqn 1.4 and 1.5 below,



Selective absorption of H<sub>2</sub>S or CO<sub>2</sub> is seen depending on the substitution of the amine used and the alkalinity of the solutions. For example it is claimed that absorption of H<sub>2</sub>S is favoured using sterically hindered amines.<sup>9</sup> It has been suggested that gas desulphurisation offshore should be a combination of 'roughing' with selective alkanolamines, i.e. reducing the H<sub>2</sub>S content from percentage to ppm levels, and then 'polishing' with a zinc oxide absorbent.<sup>10</sup> This has each system working within its own limits.

### 1.2.2 Adsorption onto and Absorption into a Solid

For many years hydrogen sulphide was removed from natural gas feedstocks by absorption in beds of iron oxide.<sup>11</sup> The beds were loaded as Fe<sub>2</sub>O<sub>3</sub> and then converted with H<sub>2</sub> at 175°C to Fe<sub>3</sub>O<sub>4</sub>, Eqn. 1.6,



Absorption of H<sub>2</sub>S was carried out at 350-400°C according to the reaction shown in Eqn. 1.7,

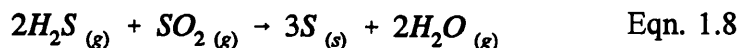


On exposure to air regeneration of the iron oxide was obtained with the formation of sulphur. The iron oxide has a very high capacity for removal of H<sub>2</sub>S and is inexpensive. However the H<sub>2</sub>S is easily stripped from the iron oxide by hydrogen and steam and these gases are frequently found during start-up and shut-down of a steam reformer. Furthermore, iron sulphides are pyrophoric and working with them can be potentially hazardous.

In North America sulphur is removed from natural gas at ambient temperatures by adsorption onto activated charcoal or molecular sieves.<sup>12</sup> Impregnation of the active charcoal with a first row transition metal can improve sulphur uptake. However, regeneration involves the use of steam and this results in an environmentally hazardous effluent which is difficult to handle.

The Claus process can be used when very high percentages of H<sub>2</sub>S are present, but it is not really a gas purification process as it will only reduce H<sub>2</sub>S to ppm levels. It is most commonly used at the tail-end of coal gasification

procedures. The process involves H<sub>2</sub>S being dissolved in a solvent and reacted with SO<sub>2</sub> to form sulphur and water. The reaction is as shown in, Eqn. 1.8, and is carried out over promoted alumina,

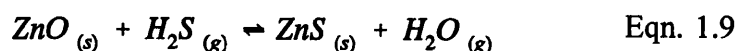


If hydrogen sulphide is present in concentrations, <10%, zinc oxide can effectively be used as an absorbent to reduce it to below 0.02 ppm levels.<sup>12</sup> Regeneration of the spent absorbent is usually performed off site by a metal reclamation firm to produce ZnO and sulphuric acid.

Modern synthesis plants generally use a cobalt-molybdate on alumina, (CoO/MoO<sub>3</sub>/Al<sub>2</sub>O<sub>3</sub>), catalyst sandwiched between two zinc oxide absorption beds. The first zinc oxide bed acts as an absorbent for H<sub>2</sub>S and low boiling mercaptans. It can also behave as an hydrogenation catalyst for the more reactive organo-sulphur compounds. The next stage involves hydrodesulphurisation over the presulphided Co/MoO<sub>3</sub>/Al<sub>2</sub>O<sub>3</sub> catalyst at 370°C. This breaks down the organic sulphur-containing molecules to H<sub>2</sub>S. This H<sub>2</sub>S is subsequently absorbed by ZnO in the final bed.<sup>9</sup>

### 1.3 REACTION OF HYDROGEN SULPHIDE AND ZINC OXIDE

Zinc sulphide and water are produced in the reaction between zinc oxide and hydrogen sulphide. Firstly the hydrogen sulphide must adsorb onto the surface of the zinc oxide. The water must then desorb away. The sulphide ion must diffuse into the bulk of the solid, whilst oxide ions diffuse to the surface for further reaction to occur. The overall stoichiometric equation is shown below in Eqn. 1.9,



The sulphide ion is *ca.* 32% larger than the oxide ion and its incorporation into the bulk results in a marked loss of porosity.<sup>13</sup> The equilibrium is strongly in favour of sulphide formation, i.e.  $\Delta H_r^\circ = -59.5 \text{ kJmol}^{-1}$  and  $\Delta G_r^\circ = -76.0 \text{ kJmol}^{-1}$ . However, due to the reasons discussed above, the overall rate of reaction is controlled by pore and lattice diffusion.

A typical diagram of moles of  $\text{H}_2\text{S}$  consumed versus time of reaction is shown in Fig. 1.1. Initially the rate of reaction is very high but as the reaction proceeds it begins to decrease. Eventually the difference in the rate of adsorption and the rate of desorption of  $\text{H}_2\text{S}$  on the surface becomes very small. There is still a net consumption of  $\text{H}_2\text{S}$  but it is negligible. This situation is called the pseudo-steady state rate, (pss).

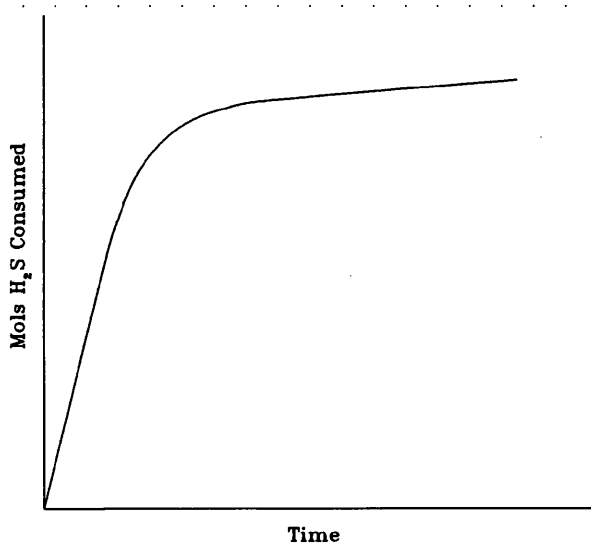


**Fig. 1.1** Diagram of change in the rate of reaction of the  $\text{H}_2\text{S}/\text{ZnO}$  reaction as it proceeds with time.

Zinc oxide is a hexagonal close packed structure (hcp) with the zinc atoms occupying the interstitial  $T_+$  sites. It is believed that the hcp structure is

retained initially on sulphidation, i.e. the wurtzite ( $\alpha$ -ZnS) is formed on replacing  $O^{2-}$  with  $S^{2-}$ . This then slowly converts to the cubic close packed (ccp), sphalerite ( $\beta$ -ZnS).<sup>13</sup> This is not unlikely as even though the  $\Delta G_r$  for the formation of  $\beta$ -ZnS is more thermodynamically favourable<sup>†</sup> the formation of  $\alpha$ -ZnS initially does not involve such severe structural changes.

### 1.3.1 Techniques used to Investigate the $H_2S/ZnO$ Reaction

There are several methods available for determining the  $H_2S$  absorption capacity of ZnO. The most commonly used method is the continuous flow ‘breakthrough’ test. The concentration of  $H_2S$  in the balance gas can be varied from 200 ppm to 100% so that much higher levels of  $H_2S$  can be used than might be encountered in an industrial situation. This allows tests to be completed over a shorter timescale. The mixed gas is passed through the absorbent bed, during which reaction conditions (temperature and space velocity) are kept constant until  $H_2S$  can be detected in the outlet stream. This  $H_2S$  can be detected in the exit stream in a number of ways: a) by bubbling the gas through an alkaline lead acetate and observing the formation of lead sulphide, (detection limit *ca.* 2-3 ppm); b) by using a thermal conductivity detector (TCD) fitted to a G.C., (limit of detection *ca.* 0.5%); or c) by using a flame photometric detector (FPD) fitted to a G.C. An FPD is very sensitive to sulphur compounds and can measure their concentration down to ppm levels. The time taken for the  $H_2S$  to be initially detected is known as the ‘breakthrough’ time, and occurs when the pseudo-steady state is reached. An

---

<sup>†</sup> $\Delta G_r(298) = -59.5 \text{ kJmol}^{-1}$   $\alpha$ -ZnS;  $-72.8 \text{ kJmol}^{-1}$   $\beta$ -ZnS. The data was obtained from Ref. 14 and Appendix 20 in Ref. 12.

absolute value for sulphur removal to 'breakthrough' can be determined by this method, but a more satisfactory use of the test data is to compare a range of absorbents which have all been tested on the same rig. The balance gas is typically nitrogen, methane or naphtha.

Lawrie<sup>15</sup> used a differential analysis technique. The partial pressure of H<sub>2</sub>S in the exit stream was continuously monitored using an FPD detector. This was used to calculate overall absorbent capacities and initial reaction rates for a variety of H<sub>2</sub>S/H<sub>2</sub>O/N<sub>2</sub> feed streams.

Another method which has been used to investigate the sulphur capacity of an absorbent is a pulse reactor connected to a gas vacuum line.<sup>16</sup> Known volumes of H<sub>2</sub>S were added to the N<sub>2</sub> stream which was continuously flowing over the absorbent bed. Again 'breakthrough' was determined when H<sub>2</sub>S was detected in the exit stream. Other experiments have been carried out to measure the initial rates of reaction using a microbalance<sup>17</sup>, and DRIFTS in combination with a pulse reactor has been used to investigate the ZnO/H<sub>2</sub>S reaction.<sup>18</sup> Hydrogen sulphide labelled with the radioactive isotope <sup>35</sup>S has been used in conjunction with the continuous flow microreactors.<sup>13,19</sup> Autoradiography was used in these experiments to obtain an image of the distribution of the radioactive material over a pellet section. In this technique the pellets were split in half and exposed for a period of time to a photoemulsion which was sensitive to β<sup>-</sup> emissions. The position of the sulphide could then be determined in the pellets from different sections of the reactor bed.

### 1.3.2 Literature Survey of H<sub>2</sub>S/ZnO Reaction

#### 1.3.2a High Temperature (350-450°C)

Furmer *et al.*<sup>19-21</sup> investigated the H<sub>2</sub>S/ZnO reaction at 350°C using various concentrations of H<sub>2</sub>S (4, 8, 15 or 100%) with N<sub>2</sub> as the balance gas. They found that when powdered zinc oxide<sup>†</sup> was made into pellets, using a laboratory press, and then tested until 'breakthrough' there was a reduction in the total pore volume and an increase in the size of the predominant pore radii (see Table 1.1).

**Table 1.1** Data obtained by Furmer *et al.*<sup>20,21</sup>

Moulding Pressure	Before Sulphidation		After Sulphidation
	Average Pore Size (Å),	Total Pore Volume (cm <sup>3</sup> /g)	Average Pore Size (Å),
Starting Material	1250	0.397	
15.6MPa	250	0.203	800
25.2MPa	160	0.140	310

The change in these parameters was greatest for the pellets produced at the higher moulding pressure. The rate of sulphidation of the absorbents prepared using the higher moulding pressure was significantly less than that for the absorbents moulded at 15.6MPa. If the concentration of H<sub>2</sub>S was changed from 15 to 4 vol% the sulphur capacity of the sample after exposure to the H<sub>2</sub>S/N<sub>2</sub> gas changed from 16.6 to 15% for the 15.6MPa granules and from 10 to 2% for the 25.2MPa granules. The fact that the reduction of the sulphur capacity

---

<sup>†</sup>The zinc oxide was obtained by the calcination in air of ZnCO<sub>3</sub>.

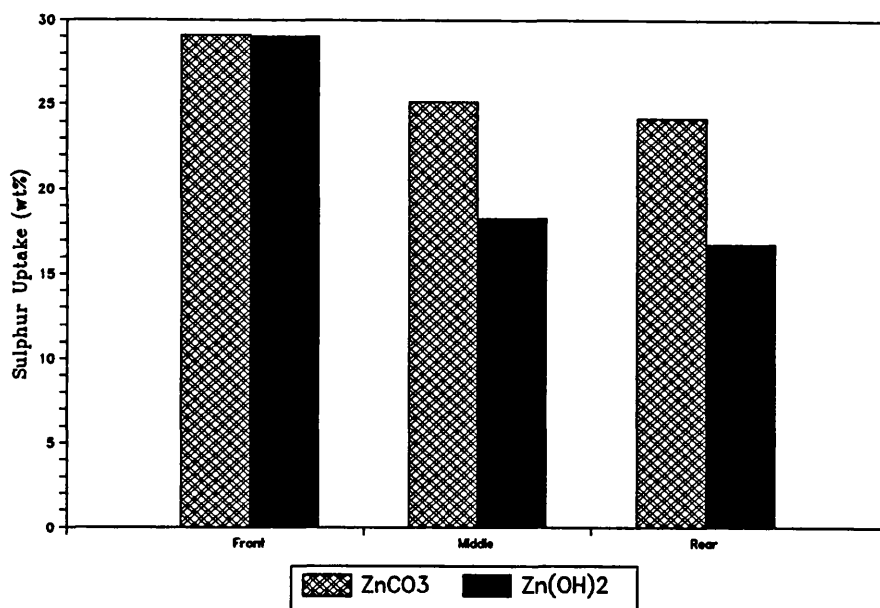


**Fig. 1.2** Absorption profile at various bed depths for ZnCO<sub>3</sub> and Zn(OH)<sub>2</sub> derived ZnO.

was significantly larger for the 25.2MPa granules than it was for the 15.6MPa suggests that at lower concentrations of H<sub>2</sub>S the larger initial pore volume and predominant pore radii are very important. This is especially important in an industrial situation where *ca.* 0.1% H<sub>2</sub>S level is encountered.

When zinc oxide was prepared under identical conditions from either Zn(OH)<sub>2</sub> or ZnCO<sub>3</sub> there were significant differences in the sulphur absorption capacity of the respective oxides. The absorption profiles of the ZnCO<sub>3</sub>-ZnO and Zn(OH)<sub>2</sub>-ZnO absorbents are shown in Fig. 1.2. The sulphur uptake was much higher for the zinc oxide formed from the carbonate compared to the oxide formed from the hydroxide. The pore volumes of the carbonate and hydroxide absorbents, expressed as percentages, were 60.0 and 50.0% respectively. It can be seen from Table 1.2 that there was a decrease in the

pore volume of both the ex-carbonate zinc oxide and ex-hydroxide zinc oxide after sulphiding.

**Table 1.2** Comparison of ZnO originating from Zn(OH)<sub>2</sub> and ZnCO<sub>3</sub> precursors.

Sulphur Saturation at 'breakthrough' (wt%)		Zn(OH) <sub>2</sub>	ZnCO <sub>3</sub>
Front layer		29.0	29.1
middle layer		18.3	25.1
bottom layer		16.8	24.2
Pore Volume of Absorbent, %			
Fresh		50.0	60.0
Spent	Front	24.2	36.7
	Middle	26.0	40.0
	Bottom	39.0	40.0

However the decrease was larger for the Zn(OH)<sub>2</sub> based absorbent which had the smaller sulphur capacity. This indicated that the higher the initial pore volume and the smaller the loss in pore volume on sulphiding, the longer before 'breakthrough' occurs. Furmer *et al.*<sup>20</sup> suggested that the reason for this was that the reaction of H<sub>2</sub>S with pelletized ZnO was limited by the rate of diffusion of the gas through the chemically inert region of zinc sulphide. Therefore the overall reaction rate would decrease as the reaction proceeded and the spent layer increased.

A number of commercially available ZnO absorbents were tested by Carnell & Denny.<sup>13</sup> These absorbent pellets were made either by granulation or extrudation. The absorbents were tested at a temperature of 350°C, a

pressure of 30 bar and a space velocity of 1000 h<sup>-1</sup>. A 2% H<sub>2</sub>S in natural gas feed was used.

Autoradiographic examination of the spent pellets showed that the ZnO pellets were surrounded by a sulphide shell. As the degree of sulphidation increased the ZnO centre became smaller whilst the sulphide shell increased. The growth of this sulphide shell was isotropic and decreased with increasing bed depth. There was no evidence of sulphur penetration to the centre at low levels of sulphidation.

The Relative Sulphur Uptake (RSU) and the surface areas of the absorbents obtained by Carnell & Denny have been plotted in Fig 1.3. They reported that there was no correlation between the (RSU) and the surface areas. However if the absorbents are separated by their physical forms; granular or extrudite, it can be seen that a linear relationship does exist for the extrudite samples. Unfortunately there are only two points available for the granular absorbents. Carnell & Denny felt the best correlation was between the total pore volume and the RSU (see Fig. 1.4). It shows that there is a critical porosity of about 0.67 ml/ml. Good absorbents were those with porosities greater than this value. This critical pore volume relates to the work of Furmer *et al.* where they observed that the higher the initial pore volume the greater the degree of sulphidation achieved before 'breakthrough' occurred. This indicated that the overall rate determining step was controlled by the ability of the H<sub>2</sub>S to penetrate the inert sulphide shell. The rate at which this penetration of the inert shell decreased was dependent on the initial total pore volume. After sulphidation they also noted that there was an appreciable decrease in

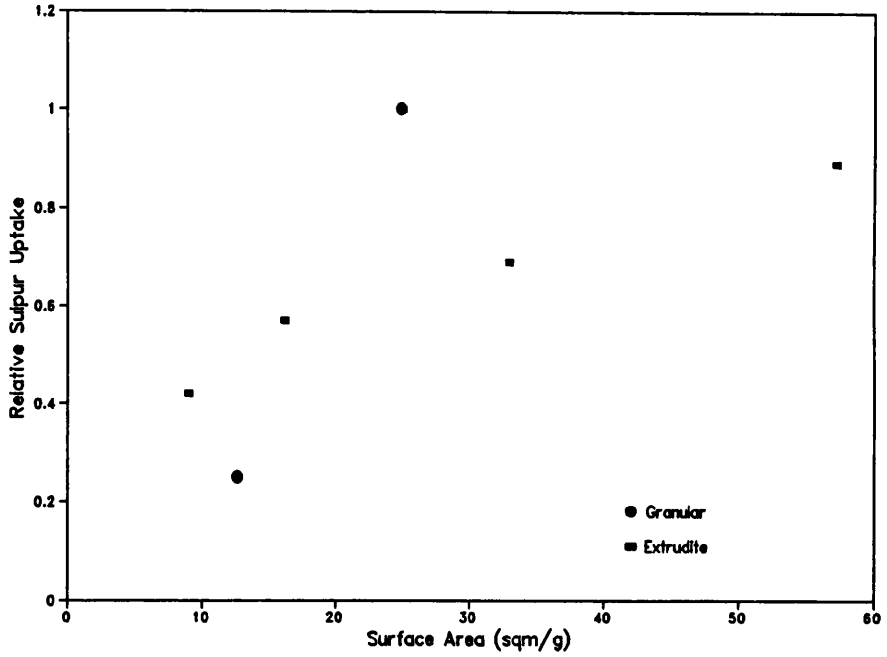


**Fig. 1.3** Plot of Relative Sulphur Uptake Vs. Surface Area.

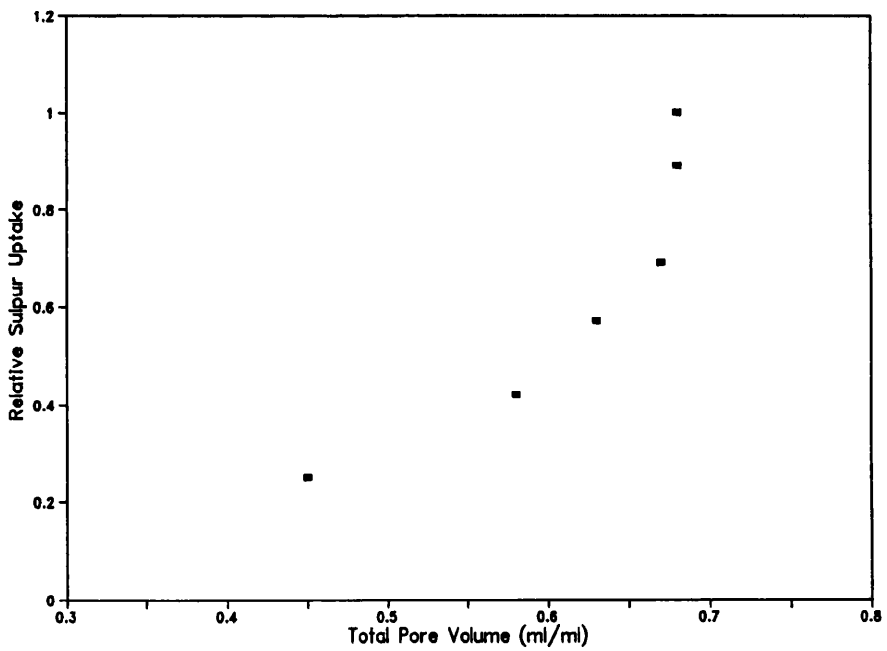


**Fig. 1.4** Plot of Relative Sulphur Uptake Vs. Total Pore Volume.

both surface area and the total pore volume. An explanation of this observation was that when ZnO was converted to ZnS there was a volume increase of about 32% ( $S^{2-}$  larger than  $O^{2-}$ ). However there was no corresponding increase in the volume of the whole particle, which meant that the porosity of the sulphided regions must have decreased. The model shown in Fig. 1.5 showed that the creation of larger pore radii on sulphiding was related to the reduction in surface area. It is this decrease in the pore volume which could have caused the destruction of the smaller pore radii. This, coupled with the autoradiographic studies, suggests that the sulphided outer regions had tended to block access to the cores and this could account for the observation that when a discharged particle is split in two, the redetermined surface area and porosity increased. Carnell & Denny suggested that pore diffusion was the overall limiting factor, with the initial pore volume also being very important. However lattice diffusion, as indicated by the relationship between the surface area and the RSU, cannot be fully discounted as having no effect, even if it is very small.

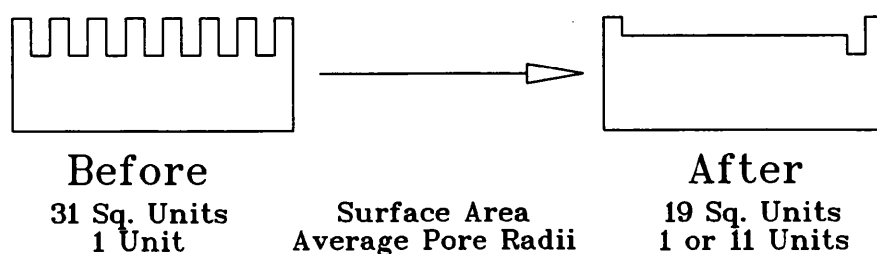


**Fig. 1.5** Model of the change in surface area and pore volume after sulphidation.

The absorbents were tested again, this time using naphtha as the balance gas. The RSU for the results were identical within experimental error with the exception of one absorbent which had a much larger mean pore radius and lower surface area compared to the other samples. It was believed that the pores in this type of formulation were easily blocked by the large hydrocarbon molecules.

The previous papers have not stated how the precursors, i.e.  $\text{Zn(OH)}_2$ ,  $\text{ZnCO}_3$ , basic zinc carbonate (BZC) used for the formation of zinc oxide were obtained. These precursors can be obtained by precipitation from a zinc nitrate solution and a precipitating agent. Gour *et al.*<sup>22</sup> investigated the effect of using different precipitating agents to synthesize several zinc oxysalt precursors and their subsequent zinc oxide products of decomposition. The precipitating agents used were: sodium carbonate, ammonium oxalate, ammonia solution, ammonium carbonate and ammonium bicarbonate. The hydrogen sulphide absorption capacity of the oxides was tested at 400°C using a naphtha feed stream containing 33.2% hydrogen and 10.5ppm hydrogen sulphide by volume. A figure for the sulphur capacity of each absorbent was calculated from the 'breakthrough' time, indicated by a lead acetate indicator, and the flow rate of the  $\text{H}_2\text{S}$ . Measurements of specific surface area, porosity and pore distribution were made before and after sulphiding. Attempts were made to relate these physical characteristics to the sulphur capacity of the absorbents. The non-stoichiometry of the ZnO samples was also examined with respect to sulphur uptake. The data obtained has been tabulated in Table 1.3 and selected

plots of excess zinc, surface area and total pore volume versus sulphur uptake (wt/wt) are shown in Figs 1.6a, 1.6b, 1.6c respectively.

**Table 1.3** Data obtained by Gour *et al.*<sup>22</sup>

Sample No.	Precipitating Agent	Surface Area (m <sup>2</sup> g <sup>-1</sup> )	Total Pore Volume (ml/g)	Excess Zinc (ppm)	Sulphur Capacity (wt/wt)
1	sodium carbonate	31.6	0.384	5.49	28.53
2	ammonium oxalate	24.7	0.536	5.83	28.99
3	ammonia solution	2.9	0.257	0.45	20.61
4	ammonium carbonate	21.7	0.648	6.58	32.75
5	ammonium bicarbonate	11.7	0.504	4.62	28.44

It can be seen from Table 1.3 that the highest surface areas were obtained using oxalates or carbonates as precipitating agents. After sulphidation the surface area of each sulphided absorbent was 50-75% lower whilst the total pore volume decreased by 10-30%.

Gour *et al.* concluded, from the data presented in Fig. 1.6a, that the level of excess, non-stoichiometric zinc was the most important factor in determining sulphur uptake. They interpreted this in terms of the role of interstitial zinc in facilitating the transport of ions in the lattice. They further proposed that the reducing environment resulted in the diffusion of hydrogen into the lattice which led to the creation of further interstitial zinc atoms and oxygen vacancies. The excess zinc metal would be easily excited and would readily lose an electron on heating and in this singly ionised form it could move readily towards the surface where it would interact with hydrogen sulphide. The ZnS<sup>-</sup> species thus formed would not be stable but might retain

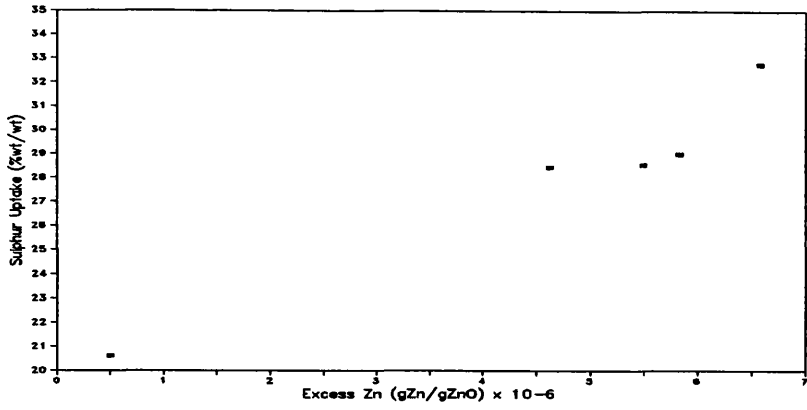


**Fig. 1.6a**

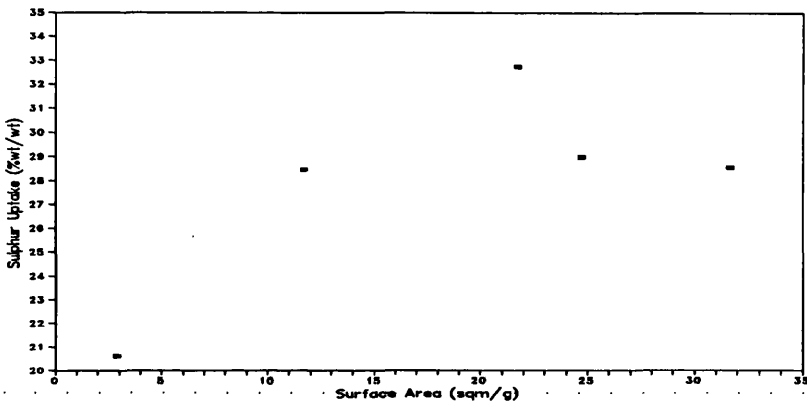


**Fig. 1.6b**

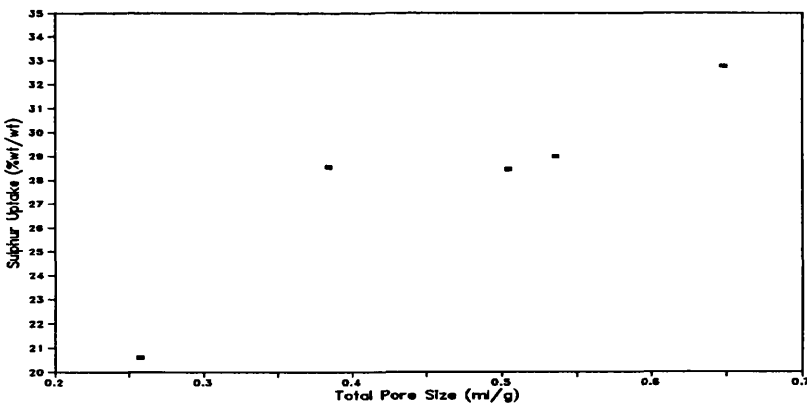


**Fig. 1.6c**

**Fig. 1.6** Plot of Sulphur Uptake Vs. a) Excess Zinc, b) Surface Area of oxides and c) Total Pore Volume, (after Gour *et al.*<sup>22</sup>).

the mobility of interstitial zinc. Also the oxygen vacancies created by the reducing atmosphere could facilitate transfer of sulphur from ZnS. It can clearly be seen in Fig. 1.6b that there was no relationship between the surface area and the sulphur uptake above a surface area of ca.  $20 \text{ m}^2\text{g}^{-1}$  in accordance with the conclusions of Gour *et al.* However Fig. 1.6c shows the plot of total pore volume versus sulphur uptake. It has the same shape as the excess zinc plot and suggests that there was some correlation between the total pore volume and an absorbent's capacity to remove sulphur. There was a conversion plateau reached at ca. 28% wt/wt but the sulphur uptake rapidly increased when the total pore volume increased past ca. 0.6 ml/g. This adds substance to the claim of Carnell & Denny that a critical pore volume exists. However, as discussed by Lawrie<sup>15</sup> it is "...difficult to place unambiguous interpretation on the data.." due to the fact that no mention of contamination by cations is made which might have occurred during the precipitation or pelletizing processes. Also the sulphur uptake of samples 1, 2 and 5 are all very similar. As has been seen suggested earlier, pore diffusion seems to be the limiting factor rather than lattice diffusion at elevated temperatures ( $>300^\circ\text{C}$ ).

In conclusion, it seems that pore diffusion is the limiting factor in determining the extent of reaction of  $\text{H}_2\text{S}$  with ZnO at high temperatures. However, the initial pore volume of the absorbent is also important and must be above a critical volume of ca. 0.7 ml/ml for a good absorbent. The reaction proceeds by initially covering the available surface of the ZnO. Lattice diffusion may play a small part at this point in the regeneration of the surface for further reaction. Hence the sign of a possible relationship between

absorbents of low sulphur capacity and surface area. The H<sub>2</sub>S gas will also be diffusing down the pores of the absorbent and reacting with the first available ZnO it encounters. As this reaction proceeds an inert sulphide shell will push deeper into the centre of the pellet. This shell prevents fresh ZnO diffusing to the surface for reaction with the H<sub>2</sub>S. However the H<sub>2</sub>S will be able to travel through this inert shell via pore diffusion although these pores are blocked by the increased size of the S<sup>2-</sup> ions. At the ZnO/H<sub>2</sub>S interface within the pores, lattice diffusion will play a part in the regeneration of the ZnO to the gas/solid interface. However the extent of this diffusion will again be curtailed by the formation of an inert sulphide layer. The lattice diffusion both here and at the surface may be assisted by the presence of excess interstitial zinc. As the micropores become blocked they collapse to form macropores and reduce the overall surface area of the pellet. The zinc oxide at the centre of the pellet will not be affected.

### ***1.3.2b Ambient Temperature***

The results discussed so far have been for the reaction of ZnO with H<sub>2</sub>S at temperatures in the region 300-400°C. However, several studies have been conducted at lower temperatures and these will be discussed here.

Lawrie and co-workers<sup>15,23</sup> passed H<sub>2</sub>S (0.06-0.7% v/v) and H<sub>2</sub>O (up to 0.5%) in a N<sub>2</sub> carrier gas over a high surface area (110 m<sup>2</sup>g<sup>-1</sup>) commercially available zinc oxide absorbent. The temperature of the absorbent was held at between 0°C-25°C. In this study it was seen that the initial rate of reaction

decayed with time and the subsequent pseudo-steady state reaction rate for each run was determined.

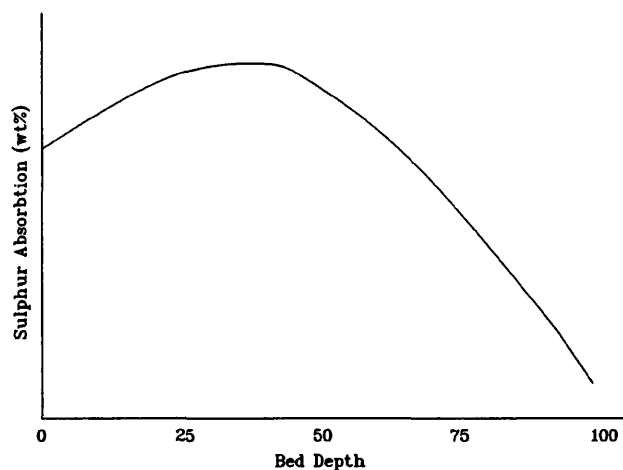
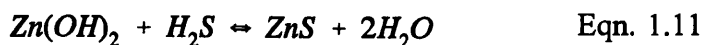
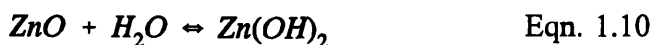


**Fig. 1.7** Diagram of typical absorption profile of ZnO.

It had been noted previously that sulphur absorption profiles (see Fig. 1.7) of zinc oxide using a 'dry' feedstock went through a small maximum before tailing off at a bed depth of 100%.<sup>24</sup> The rise in the absorption profile of ZnO was due to the creation of water at the front of the bed. Lawrie *et al.* showed that the water had an autocatalytic effect on the reaction of hydrogen sulphide with zinc oxide. This increase in absorption just after the front of the bed has been explained by the creation of water from the front of the bed due to Eqn. 1.9. Lawrie observed that the partial pressure of H<sub>2</sub>S in the exit stream rose most rapidly when no water was present in the feed gas. As the partial pressure of water in the feed increased, the rate at which the reaction rate decayed with time decreased. Lawrie proposed the simple reaction scheme shown in Eqns. 1.10 and 1.11 to explain this.



It was suggested that the presence of the water assisted solid state rearrangement by diffusion, bringing fresh absorbent to the surface of the crystallites. In the mechanism water initially absorbed via the consumption of an oxygen vacancy. This adsorption of water on the surface was reversible and involved only the breaking of an O-H bond and formation of Zn-O and OH surface bonds. The presence of surface -OH groups sterically assisted the formation of a surface -Zn-S-H species and the loss of water with the subsequent formation of an oxygen vacancy. Rearrangement of the surface zinc species and this vacancy led to the formation of surface zinc and -SH groups. Migration of oxygen vacancies into the bulk allowed diffusion of the sulphur atom into the lattice and replenishment of oxygen in the form of -OH at the surface.

Lawrie<sup>15</sup> also found that increasing the temperature from 0°C to 25°C had an inverse effect on the rate of reaction. This was attributed to the loss of surface water as the temperature was increased. The effect upon the kinetic rate constant, diffusivities and defect concentrations was far outweighed by the deleterious effect of the loss of water on the surface of the absorbent. At higher temperatures no water would be present and the mechanism by which the overall rate is determined would be quite different (see *Section 1.3.2a*).

In the range of feedstock conditions used it was found that, unlike the marked dependence of the reaction rate upon the partial pressure of water, the

pseudo-steady state rate, (pss), showed no great trend with partial pressure of H<sub>2</sub>S in the inlet feed gas.

Lawrie also showed that if the run was interrupted and left overnight the partially sulphided absorbent underwent some physical change. Her evidence for this was the observation of a higher, though short lived, reaction rate, similar to that observed for the unsulphided sample. The pss rate of the second run was only 20% of the pss rate of the first and corresponded to an increase in the absorbent conversion from 31.7% to 38.6% wt/wt.

Furmer *et al.*<sup>20</sup> also noted that a reduction in temperature of the reactor bed from 350°C to 150°C caused a significant reduction in the sulphur capacity of the zinc oxide absorbents. They concluded that the influence of the pore structure was still significant at this temperature. They suggested that with a reduction in temperature the overall 'breakthrough' time/reaction rate was limited to a greater extent by the rate of the chemical reaction.

It can be concluded therefore that whereas at high temperatures the rate determining step for the ZnO/H<sub>2</sub>S reaction is pore diffusion, at ambient temperatures it is lattice diffusion, i.e. diffusion of the oxide ions to the surface and the sulphide ions into the lattice. Water plays a dominant role in the H<sub>2</sub>S/ZnO reaction at ambient temperatures by assisting the mechanism by which regeneration of the surface takes place.

## 1.4 COMPARISON OF ZINC OXIDE AND TRANSITION-METAL OXIDES

Previously Westmoreland & Harrison<sup>25</sup> identified the oxides of Fe, Zn, Mn, Mo, V, Ca, Sr, Ba, Co, Cu and W as showing thermodynamic feasibility for the removal of H<sub>2</sub>S from low-Btu gas streams. However, these calculations were for high temperature desulphurisation (above 300°C). A more limited study of the ambient temperature thermodynamics of H<sub>2</sub>S uptake by various metal oxides is reported in Table 1.4. The results of this work show that for the reaction where the data is available, the  $\Delta G_r^\circ$  is negative and so the

**Table 1.4** Thermodynamics for the Reaction of Selected Transition-metal Oxides with H<sub>2</sub>S at 25°C.

Oxide	Products of Reaction	$\Delta H_r^\circ$ (kJmol <sup>-1</sup> )	$\Delta G_r^\circ$ (kJmol <sup>-1</sup> )
ZnO+H <sub>2</sub> S	→ ZnS+H <sub>2</sub> O	-59.5	-76.0
CuO+H <sub>2</sub> S	→ CuS+H <sub>2</sub> O	-117.0	-119.1
Fe <sub>2</sub> O <sub>3</sub> +3H <sub>2</sub> S	→ FeS+FeS <sub>2</sub> +3H <sub>2</sub> O	-117.6	-110.7
Co <sub>3</sub> O <sub>4</sub> +4H <sub>2</sub> S	→ CoS+Co <sub>2</sub> S <sub>3</sub> +4H <sub>2</sub> O	-225.9	-251.0

reactions are favourable. In addition, all the reactions shown in the table are exothermic and should not therefore require an external energy input. In order to confirm the suitability of the oxides in the table it would be necessary to carry out kinetic experiments involving H<sub>2</sub>S uptake at the temperatures required.

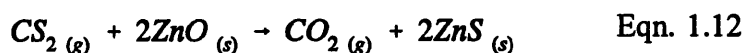
A further study by Westmoreland *et al.*<sup>26</sup> into the kinetics of the reaction of H<sub>2</sub>S with MnO, CuO, ZnO and V<sub>2</sub>O<sub>3</sub> between 300 and 800°C

showed that all the reactions were first order and obeyed the Arrhenius equation.

There are many factors influencing the choice of oxide for desulphurisation. In Europe zinc oxide is the predominantly used absorbent.<sup>27,28</sup> This is because it is cheap, readily available and is easier to handle safely and environmentally than hydrated iron oxide which has previously been used. Absorption of H<sub>2</sub>S by ZnO is stoichiometric at 350°C but falls off rapidly as the temperature is reduced. There is an increasing need to purify gases at low temperatures (<200°C) to improve energy efficiency and although this requirement has been partially met by the recent development of a high-surface area ZnO<sup>10</sup> there is still considerable scope for improvement.

#### 1.4.1 Doping Zinc Oxide with a 1st Row Transition Metal

Doping the zinc oxide with a transition metal is believed to improve the sulphur capacity of the absorbent. The influence of copper doped in zinc oxide on H<sub>2</sub>S absorption, over the temperature range 200-370°C, was investigated by Cognion.<sup>29</sup> It was believed that the presence of the copper served a triple role; (i) it promoted ZnO, increasing its activity in exchange reactions such as Eqn. 1.12,



(ii) it absorbed sulphur and (iii) in the presence of hydrogen it hydrogenated certain sulphur compounds. It is likely that pore diffusion limited the rate of reaction of H<sub>2</sub>S with the copper doped ZnO over this temperature range, as suggested previously (see *Section 1.3.2a*).

Zinc titanate,  $Zn_2TiO_4$ , and zinc ferrite,  $ZnFe_2O_4$ , have been widely used as high temperature desulphurisation absorbents for coal gasification. Many papers and patents can be found relevant to these commercial processes within the literature.<sup>30</sup> However they are outwith the scope of this thesis and will not be dealt with here.

Stirling *et al.*<sup>16</sup> investigated the effect of doping zinc oxide with the 1st-row transition metals listed in Table 1.4, i.e. Cu, Co and Fe. The doped zinc oxide absorbents contained *ca.* 5% wt/wt dopant and were prepared by either the impregnation (IMP) of ZnO with metal nitrates or by the coprecipitation (COP), of metal/zinc nitrates and ammonium/sodium carbonate. The resulting precursors were calcined in air to give the oxide. The resulting absorbents were then tested as powders for their ability to remove sulphur using a pulse testing rig at ambient temperatures.

It was found that oxides prepared by the coprecipitation route had higher surface areas and a greater capacity for  $H_2S$  removal than their impregnated counterparts. Furthermore, doping zinc oxide with copper or cobalt was found to greatly enhance the sulphur capacity of zinc oxide.

The plot of 'moles of  $H_2S$  absorbed' versus surface area is shown in Fig. 1.8. The  $H_2S$  uptake was found to increase linearly with surface area for the COP samples. This suggests that lattice diffusion was the rate limiting step. The function of the metal dopant was to increase the surface area by lowering the ZnO particle size. The metal dopant may also have increased the rate of diffusion of ions to and from the oxide lattice. The copper and cobalt doped zinc samples were all present as a single phase for both the precursors and

oxides. The transition-metal ions were envisaged as being retained within the hydrozincite-like precursor structure,  $Zn_{5-x}M_x(CO_3)_2(OH)_6$  where  $M=Cu$  or  $Co$ . Such species have been observed previously for copper doped hydrozincite.<sup>31</sup> Examination by transmission electron microscopy, (TEM), of the absorbents prepared by impregnation showed that the zinc oxide particles were much larger than for the COP samples and that the transition metal oxide was present as a separate phase in the form of an interconnected network over the ZnO particles.

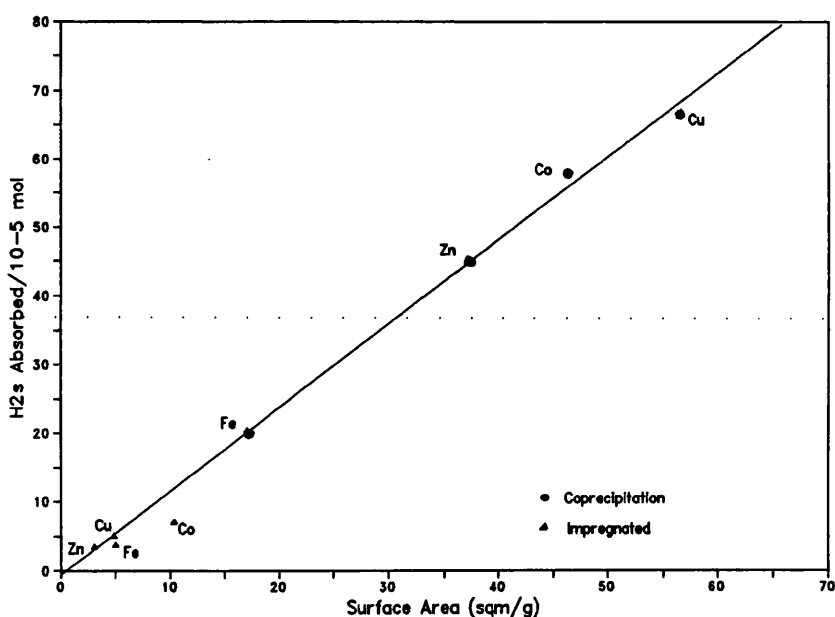


**Fig. 1.8** Plot of mols. of H<sub>2</sub>S absorbed Vs. surface area of 5% doped ZnO, (after Stirling *et al.*<sup>16</sup>).

The IMP samples showed a deviation from the linear plot of H<sub>2</sub>S absorbed versus surface area observed for the COP samples. This deviation was greatest for the IMP-Co sample (see Fig. 1.8). This could indicate that lattice diffusion was not the limiting step. The increase in surface area made available by doping with 1st-row transition-metal ions was not contributing to the

reaction. It is thought that  $H_2S$  uptake in the IMP samples may have occurred by (i) dissociation of  $H_2S$  on the  $ZnO$ ; (ii) preferential dissociation of  $H_2S$  on the transition-metal oxides followed by spillover of a high concentration of  $SH^-$  at the  $ZnO$  particle surface enhancing the sulphidation of the doped  $ZnO$  above that of  $ZnO$  itself; (iii) sulphidation of the transition-metal oxides. Calculations showed that the  $H_2S$  uptake in all the samples was restricted to *ca.* 0.6 monolayers. However microcrystallites of  $ZnS$  were detected by electron

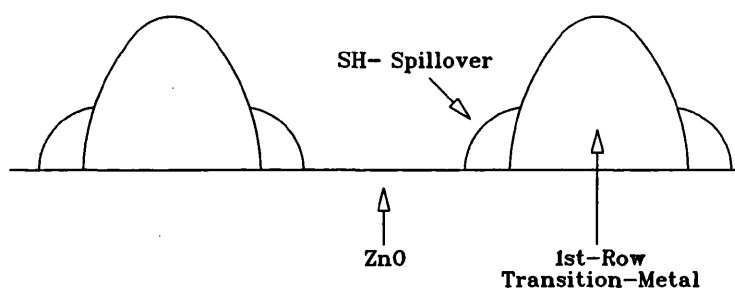


**Fig. 1.9** Diagram of the sulphidation of the impregnated samples.

diffraction. This suggests that some migration of sulphide ions must have taken place as a monolayer coverage is not sufficient to give a diffraction pattern. From this evidence it could be hypothesized that processes (ii) and (iii) were the main mechanisms by which sulphidation occurred. However the spillover would occur only to regions surrounding the transition-metal network where mechanism (i) could also occur due the close association of the transition-metal and zinc causing a synergic effect with respect to reaction with  $H_2S$ . The preferential adsorption of  $H_2S$  onto the transition-metal rather than  $ZnO$  would account for the deviation from the surface area plot (see Fig. 1.9). The linear relationship seen for the COP samples suggests that there was a high interdispersion of the two metals.

## 1.5 PREPARATION OF A MULTICOMPONENT OXIDE

The coprecipitation route via oxysalt precursors, such as hydroxycarbonates, oxalates or acetates has been extensively used by various authors.<sup>32-34</sup> It has the advantage that there is a high dispersion of metal ions in the precursor which is likely to be maintained in the oxides after calcination. Also this high dispersion makes it possible to obtain a single phase oxide which contains a solid-solution of the doped transition-metal. The precursors are safe and easy to handle and there are no harmful gaseous products formed on decomposition to the oxide. These precursors can be calcined at relatively low temperatures (250-450°C) to give high surface area oxide without sintering.

The coprecipitation method, which is outlined in Fig. 1.10, goes through five stages before the oxide is obtained: precipitation, aging, washing, drying and calcination. As the chemical and physical properties of mixed oxides depends on the mode of preparation of their precursors, and their mode of decomposition to the oxides, the coprecipitation route allows for the conditions such as metal nitrate ratios, precipitating agent, pH, temperature, aging time in the mother liquor and calcination temperature/time to be easily altered. A change in any of these conditions can drastically alter the resulting oxide stoichiometry, component interdispersion and morphology and this will affect the sulphur absorption capacity of the oxide.

A disadvantage of the precipitation route is that the stoichiometry and the homogeneity of phases and the degree of atomic mixing of the metal ions is dependant on the solubility products of the compounds involved.<sup>35</sup> This determines whether precipitation of the ion will occur under the conditions of

Mixed Metal Nitrates/Carbonate soln.

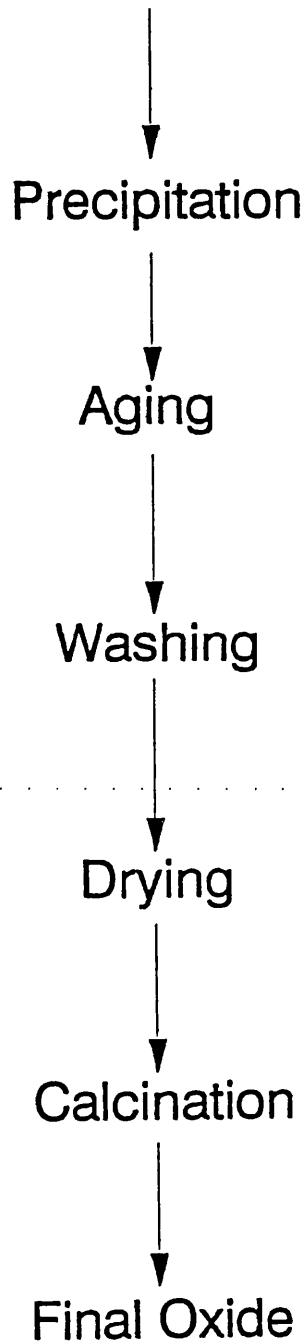


**Fig. 1.10** Diagram to route of preparation of oxides via oxysalt precursors.

temperature, concentration and pH being used. The equilibrium for the precipitation of metal hydroxides can be written,

$$K_{sp} = [metal][OH^-] \quad \text{Eqn. 1.13}$$

In Fig. 1.11 it can be seen that the conditions of supersaturation which must be satisfied for precipitation to occur can be met by increasing the pH so that the solubility curve effectively moves to the right, i.e. the equilibrium, Eqn. 1.13 is pushed to the left. Supersaturation can also be satisfied by decreasing the temperature, A→B, or by increasing the concentration of the cation, A→C.<sup>36</sup> The condition where the requirements of supersaturation are only just satisfied is known as the metastable region. In Table 1.5 values of precipitation pH for the hydroxides of a few metals are listed, (see Appendix B for calculations). It is therefore necessary, in order to obtain the required stoichiometry, dispersion and homogeneity of the ‘target’ precursors, to precipitate at a pH higher than or equal to the one at which the more soluble hydroxide precipitates.<sup>37</sup> However if too high a pH is used some metals will redissolve, for example Al<sup>3+</sup> redissolves at pH 9-12.

**Table 1.5** pH of precipitation of some M<sup>2+</sup> hydroxides.

	pH at [10 <sup>1</sup> ]M	pH at [10 <sup>-2</sup> ]M
Cu <sup>2+</sup>	4	5
Zn <sup>2+</sup>	5.5	6.5
Ni <sup>2+</sup>	6	7
Fe <sup>2+</sup>	6.5	7.5
Co <sup>2+</sup>	6.5	7.5

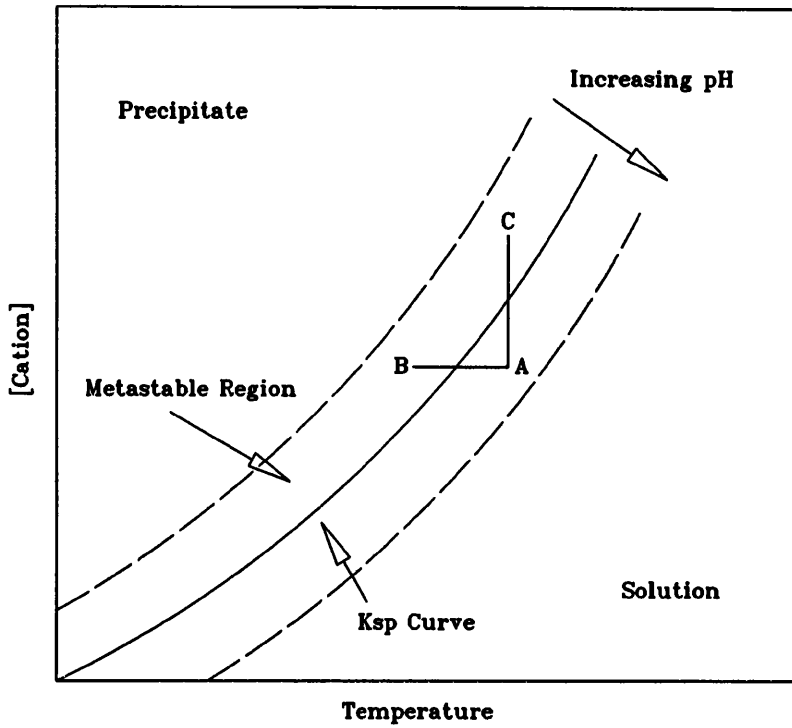


**Fig. 1.11** Diagram of conditions required for precipitation at supersaturation to occur.

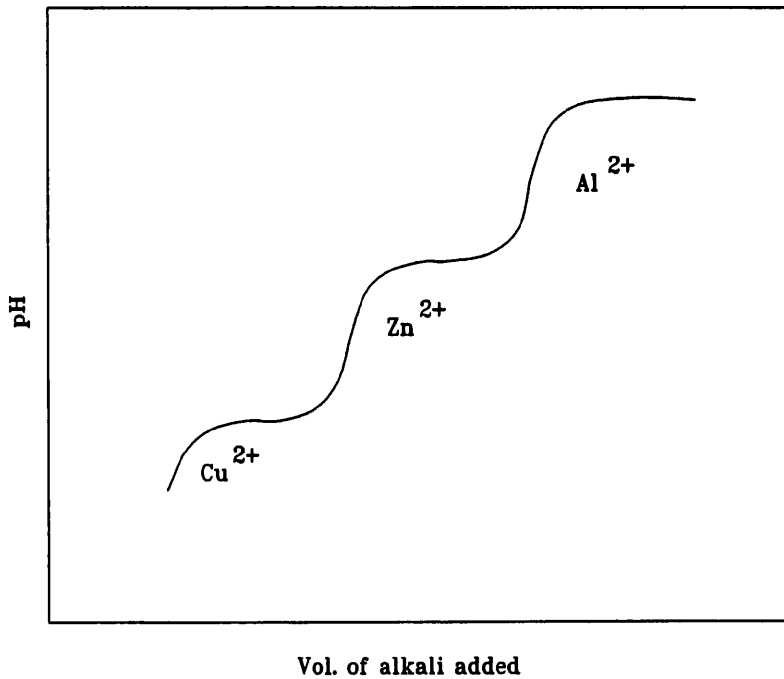


**Fig. 1.12** Diagram of the rise in pH during coprecipitation by the titration method (see Section 1.5.3).

The type and number of phases present and the particle size of the precursor are dependant upon the order of mixing of the precipitating agents and the metal salt solutions.

Three methods have been used

- (i) Precipitation Low Supersaturation (LSS)
- (ii) Precipitation High Supersaturation (HSS)
- (iii) Titration Method (TM)

### **1.5.1 Precipitation at Low Supersaturation (LSS)**

Coprecipitation at LSS, at constant pH, is the method most frequently used for the preparation of single phase hydroxycarbonates. The solutions and precipitating agent are mixed by pumping the solutions simultaneously at low flow rate into a precipitation vessel. Precipitation is generally carried out over the pH range 7-10, at a temperature between 60 and 80°C. Some aging is usually done under the conditions of precipitation, followed by washing and drying (<120°C). LSS generally gives rise to precipitates which are crystalline.

### **1.5.2 Precipitation at High Supersaturation (HSS)**

Typically, precipitation is carried out by very rapidly adding a metal nitrate mixture to the carbonate solution. The temperature is maintained at 60-80°C whilst the pH is raised to 7-10. This is again followed by aging, washing and drying. This method of preparation generally gives rise to less crystalline material than that obtained by the LSS method. This is because the rate of nucleation is higher than the rate of crystal growth.

### 1.5.3 Titration Method (TM)

The titration method involves adding carbonate solution dropwise to the nitrate solution at a given temperature, followed by aging in the mother liquor. As is demonstrated in Fig. 1.12, the precipitation of an hydroxycarbonate is not just a simple multi-step sequential precipitation but also one where coprecipitation occurs.<sup>38</sup> This is suggested by the lowering of the pH of precipitation of hydroxides when the metals are mixed together as compared to the titration of a solution containing only one cation. A problem with this method is that hydroxynitrates are often formed along side the desired hydroxycarbonates.<sup>39</sup>

## 1.6 MIXED METAL HYDROXYCARBONATES AND THEIR OXIDE PRODUCTS OF DECOMPOSITION

Mixed metal oxides are of great catalytic importance in industry. Much literature work exists on the bulk and surface characterisation of the coprecipitated precursors and their oxide products of decomposition. A wide and continually growing series of mixed metal precursors and their oxides have been investigated: Cu/Zn mixed oxides, which are of industrial interest for the low temperature and pressure methanol synthesis<sup>31,32</sup>; mixed Co/Cu oxides, which are active catalysts for the oxidation of CO with O<sub>2</sub><sup>34</sup>; Co/Cu (containing Al or Cr, Zn and an alkali metal), which are used for the conversion of synthesis gas (Co-CO<sub>2</sub>-H<sub>2</sub>) to higher alcohols<sup>40</sup>; mixed Cu-Co-Zn-Cr oxides, which have been tested for the synthesis of hydrocarbons<sup>41</sup>; and Co/Zn oxides, which are active catalysts for methane oxidation.<sup>42</sup>

Porta and his co-workers have studied extensively the preparation of hydroxycarbonate precursors and their oxide products of decomposition. They studied Co/Cu carbonate and their oxides, synthesizing the precursors by the low supersaturation procedure from Co/Cu nitrate solutions and  $\text{NaHCO}_3$  at pH 8.<sup>43-45</sup> Cobalt-containing malachite  $\text{Cu}_{2-x}\text{Co}_x\text{CO}_3(\text{OH})_2$  precursors were formed for Co/Cu atomic ratios from 0/100 to 33/77 whereas  $\text{CoCO}_3$ , spherocobaltite and Cu-containing spherocobaltite,  $\text{Co}_{0.85}\text{Cu}_{0.15}\text{CO}_3$  were formed for Co/Cu ratios equal to 100/0 and 85/15 respectively. They also observed that there was a decrease in the cell volume of the cobalt doped malachite structure with increasing cobalt content. Even though  $\text{Co}^{2+}$  is larger than  $\text{Cu}^{2+}$ , incorporation of  $\text{Co}^{2+}$  resulted in a decrease in local octahedral distortion and hence a decrease in the cell volume. The authors believed this to be a consequence of the different electron configurations of Cu  $d^9$  and Co  $d^7$  ions, the former having a greater tendency to give elongation of the oxygen octahedra. Their study also demonstrated that a monophasic solid solution with a malachite structure could be formed with up to 33% cobalt content. A further study showed that at higher cobalt loadings a metastable phase was formed alongside the the copper doped spherocobaltite. The XRD patterns of of the precursors with Co/Cu ratios of 50/50 and 70/30 suggested that poorly crystalline materials were formed which could be indexed to hydroxycarbonate structures of chemical formulae  $\text{Co}_{0.49}\text{Cu}_{0.51}(\text{CO}_3)_{0.43}(\text{OH})_{1.14}$  and  $\text{Co}_{0.67}\text{Cu}_{0.33}(\text{CO}_3)_{0.4}(\text{OH})_{1.2}$  respectively. The Co/Cu ratio of 100/0 resulted in the formation of the basic cobalt carbonate,  $\text{Co}(\text{CO}_3)_{0.5}(\text{OH})_{1.0} \cdot 0.1\text{H}_2\text{O}$ .

Oxides were prepared by calcination of the precursors in a N<sub>2</sub> or air atmosphere. Bulk characterisation of the N<sub>2</sub> derived oxides showed that the reduced cobalt oxide, CoO was formed. Dissolution of copper in the oxide phase at higher loadings was deduced by noticing that the X-ray lines corresponding to the CoO and Co<sub>3</sub>O<sub>4</sub> phases were systematically displaced towards higher 2θ values than those expected for pure CoO and Co<sub>3</sub>O<sub>4</sub>. The Co<sub>3</sub>O<sub>4</sub> oxide was the predominant phase obtained when calcination was carried out in air rather than nitrogen.

**Table 1.6** Summary phase obtained for selected oxides.<sup>43</sup>

Co/Cu	N <sub>2</sub>	Air
100/0	CoO	Co <sub>3</sub> O <sub>4</sub>
70/30	Cu <sub>x</sub> Co <sub>1-x</sub> O+CuCoO <sub>2</sub> +Cu <sub>x</sub> Co <sub>3-x</sub> O <sub>4</sub>	Co <sub>3</sub> O <sub>4</sub> +CuO
50/50	CuCoO <sub>2</sub> +Cu <sub>x</sub> Co <sub>1-x</sub> O+Cu <sub>x</sub> Co <sub>3-x</sub> O <sub>4</sub>	Cu <sub>x</sub> Co <sub>3-x</sub> O <sub>4</sub> +CuO
0/100	---	CuO

A study by X-ray photoelectron spectroscopy (XPS) of the hydroxycarbonate precursors revealed only the presence of Co<sup>2+</sup> and Cu<sup>2+</sup> ions at the surface. Quantitative analysis suggested evidence of cobalt enrichment at the surface of the mixed precursors. This segregation was interpreted in terms of a strain-energy effect. The Co<sup>2+</sup> ions are bigger than Cu<sup>2+</sup> and prefer less distorted octahedral symmetry (highly distorted MetalO<sub>6</sub> polyhedra are present in pure malachite). As a consequence of this, Co<sup>2+</sup> ions tend to segregate at the surface, the driving force being the strain-energy term of the segregation enthalpy. However, the cobalt enrichment could also be ascribed to the higher reactivity (chemical driving force) of the Co<sup>2+</sup> ions with oxygen-

containing media such as the mother liquor during the coprecipitation or the air and/or moisture during drying.

Examination of the  $\text{Co}2p_{3/2}$  transition binding energies of the oxides showed evidence of  $\text{Co}^{2+}$ ,  $\text{Co}^{3+}$ ,  $\text{Cu}^{2+}$  and  $\text{Cu}^+$  ions being present at the surface of the oxides calcined in  $\text{N}_2$ . However oxides obtained from the air calcination showed that only  $\text{Co}^{2+}$ ,  $\text{Co}^{3+}$  and  $\text{Cu}^{2+}$  ions were present. Quantitative analysis revealed that the samples calcined in  $\text{N}_2$  were characterised by a homogeneous distribution of cobalt and copper between the bulk and the surface. However, the original cobalt enrichment of the precursors was preserved for the corresponding samples calcined in air.

This study illustrates the range of surface and bulk compositions that can be obtained in mixed metal hydroxycarbonate precursors and the oxides. Thus, it is possible to have multiphase solid solutions, systematic changes in the cell volume or surface enrichment of one metal in the precursor which may or may not be carried through to the oxide.

## **1.7 STRUCTURES OF THE HYDROXYCARBONATE PRECURSORS**

The predominant precursor phases encountered in this work are discussed in this section.

### **1.7.1 Hydrozincite**

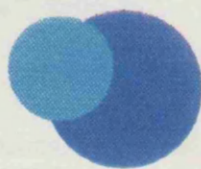
Hydrozincite,  $\text{Zn}_5(\text{CO}_3)_2(\text{OH})_6$ , is the most commonly obtained structure formed from the precipitation of zinc nitrate. The molecular structure is shown in Fig. 1.13. The structure was determined by Ghose<sup>46</sup> and was shown to be

CERIUS

alan

Date: 21 Jun 94

Time: 14:44:29



Molecular  
Simulations

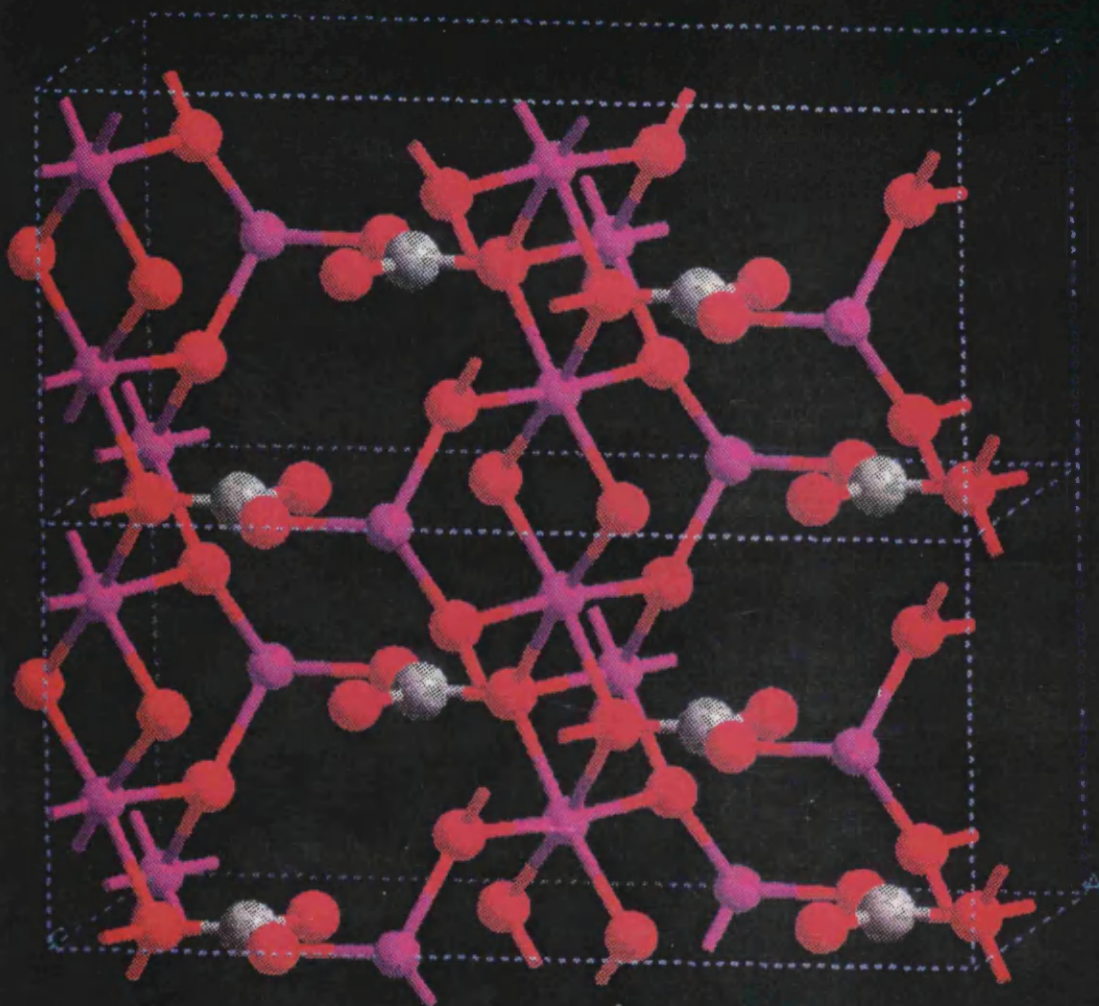


Fig. 1.13 Model of the molecular structure of hydrozincite.

monoclinic with  $a_0 = 13.62$ ,  $b_0 = 6.30$ ,  $c_0 = 5.42\text{\AA}$ ,  $\alpha = 95^\circ.50'$ , space group  $C2/m$ , and two formula units per cell. The zinc atoms are present in both octahedral and tetrahedral positions, in the ratio 3:2. The molecule consists of complex sheet structures which are connected by carbonate groups. These carbonate groups lie normal to the zinc sheets. The complex sheet could be described as chains composed of one  $\text{Zn(1)(OH)}_4\text{O}_2$  octahedron and two  $\text{Zn(2)(OH)}_4\text{O}_2$  octahedra sharing four and three edges alternately. These chains are joined together by sharing an octahedral edge to form a sheet with holes in it. Two  $\text{Zn(3)(OH)}_3\text{O}$  tetrahedra then occur above and below these holes such that they share two common corners with the two types of octahedral zinc. The  $\text{OH}:\text{CO}_3$  ratio is variable in natural and synthetic samples. The  $\text{CO}_3^{2-}$  deficient phases are believed to be highly stacking disordered because they facilitate mistakes in the layer sequence.

### 1.7.2 Spherochalcite

Spherochalcite,  $\text{CoCO}_3$ , is isomorphous with  $\text{NaNO}_3$ . It adopts a  $\text{NaCl}$ -like arrangement of  $\text{Co}^{2+}$  and  $\text{CO}_3^{2-}$  ions, though distorted due to the spatial requirements of the complex anions. The symmetry is rhombohedral, with a bimolecular unit which has the dimensions  $a_0 = 5.6650\text{\AA}$  and  $\alpha = 48^\circ 33'$ .<sup>47</sup>

**CHAPTER 2**  
**THEORY OF TECHNIQUES**

---

---

## **2.1 POWDER X-RAY DIFFRACTION**

### **2.1.1 Introduction**

Powder X-ray diffraction is a simple and extensively used technique for determining the phase(s) present in a crystalline powder. It can be used qualitatively to determine whether impurities or solid-solutions are present or, if more than one phase is present, quantitatively to determine the ratio of one phase to the other. Just as light is diffracted at a pair of slits and the resulting interference pattern depends on the wavelength of the light and the distance between the slits, so X-rays are diffracted by a pair of atoms and the interference pattern which is produced depends on the wavelength of the X-rays and the distance between the atoms. As the X-rays used are monochromatic and the wavelength is known, a direct measurement of distances between atoms can be made. This calculation is based on Bragg's Law.

### **2.1.2 Bragg's Law**

The Bragg approach to the diffraction of X-rays is to regard crystals as being built up in layers or planes such that each acts as a semi-transparent mirror. Thus each plane will partly reflect the impinging X-rays with a certain angle of incidence. The X-rays which strike the planes at other angles will be transmitted to be subsequently reflected by succeeding planes. The Bragg angle,  $\theta$ , represents the condition under which each plane in a crystal diffracts exactly one wavelength later than the preceding plane and all diffracted beams therefore are in phase and constructive interference occurs. The perpendicular

distance between pairs of adjacent planes, the d-spacing,  $d$ , is related to Bragg's angle by Bragg's law, Eqn. 2.1,

$$2d\sin\theta = n\lambda \quad \text{Eqn. 2.1}$$

where  $\lambda$  is the wavelength of the radiation used/ $\text{\AA}$  and  $n$  is the order of diffraction - usually taken as 1. The conditions required to satisfy Bragg's law are shown diagrammatically in Fig. 2.1. When Bragg's law is satisfied the reflected beams are in phase and interfere constructively. At angles of incidence other than the Bragg angle the reflected beams are out of phase and therefore destructive interference occurs.

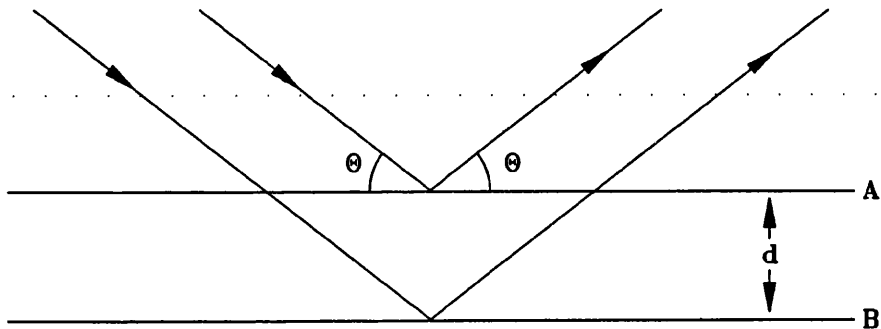


**Fig. 2.1** Diagram of conditions required to satisfy Bragg's Law.

### 2.1.3 Instrument

There are three main parts to a powder X-ray diffractometer,

- a) radiation
- b) sample
- c) detector

A schematic diagram of an X-ray diffractometer is shown in Fig. 2.2. A

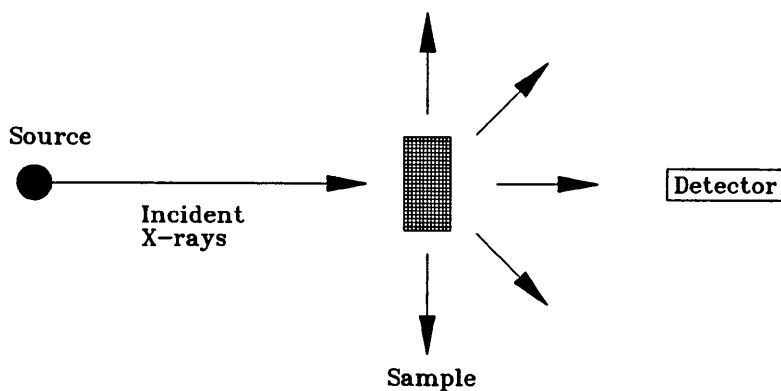


**Fig 2.2** Diagram of a typical X-ray diffractometer

monochromatic beam of X-rays, either  $\text{CuK}_\alpha$  ( $\lambda=1.5404\text{\AA}$ ) or  $\text{CoK}_\alpha$  ( $\lambda=1.7902\text{\AA}$ ), strike a finely powdered sample which has crystallites randomly arranged in every possible crystallographic orientation. As the sample is scanned across a range of  $\theta$  values and each crystal can diffract in the normal way at least some of the crystals must be orientated at a Bragg angle to the incident beam. Therefore the whole assembly will give cones of refraction. These can be observed as circles on photographic plates. More usually, however, the powder diffractometer has a scintillation counter as the detector. This is connected to a chart recorder or some sort of digital output.

To aid equipment design the X-ray source and detector are fixed and the sample is rotated at a constant angular velocity over a range of  $2\theta$ , typically over the range  $2\theta = 10^\circ - 80^\circ$  at a scanning speed of  $2^\circ \text{ min}^{-1}$ .

#### **2.1.4 Phase Structure Determination**

A paper trace, diffractogram, is obtained (see Fig. 2.3). The trace represents intensity,  $I$ , versus  $2\theta$ . The d-spacings of the peaks can be calculated from the value of  $2\theta$  using Bragg's Law. The intensities of the peaks are calculated

from the measured peak heights, with the most intense given the value of 100 and the rest scaled accordingly.

As the pattern of lines arising from the powder depends on the cell dimensions and symmetry, and line intensities depend on atom positions and their atomic weights, powder diffractograms provide excellent 'fingerprints' for crystalline substances.<sup>48</sup> Files for patterns for thousands of elements and compounds exist have been collected by the JCPDS Powder Diffraction File Joint Committee on Powder Diffraction Standards<sup>49</sup> so unknowns can be identified rapidly by comparison with known standards.

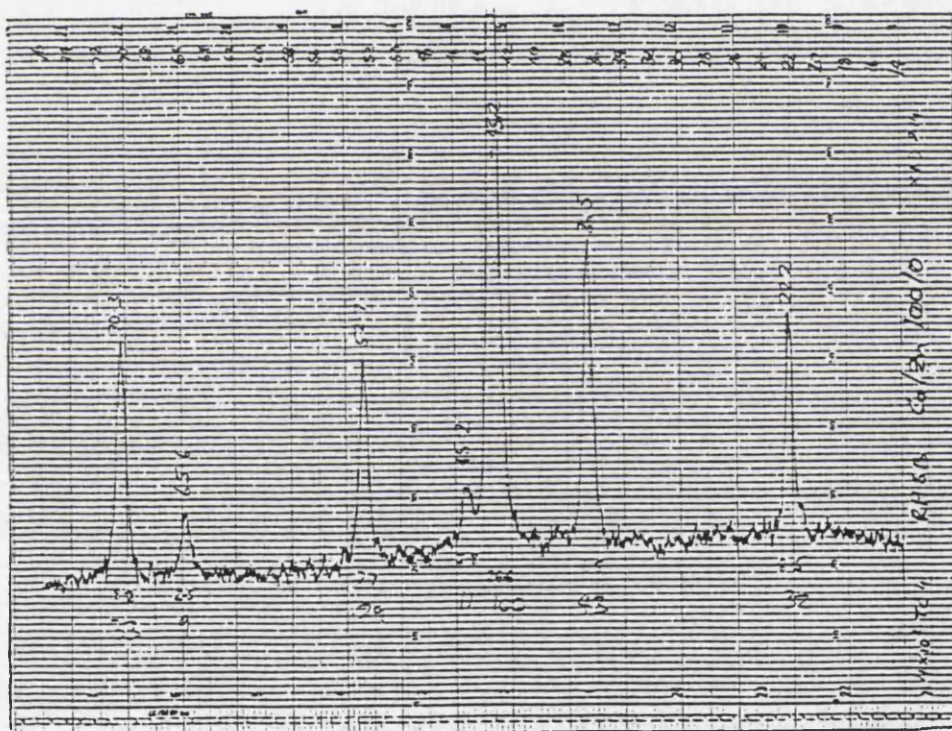


**Fig. 2.3** Typical example of paper trace obtained from the diffractometer. The example shown is cobalt oxide,  $\text{Co}_3\text{O}_4$ .

## 2.2 UV-VIS-NIR DIFFUSE REFLECTANCE SPECTROSCOPY

### 2.2.1 Introduction

To measure the absorption/transmission spectra of a solid in the range 200-2000 nm the solid can be dissolved in a suitable solvent and then studied. However, if that solid does not dissolve readily into a suitable solvent and/or its structure is destroyed on dissolution then the material must be studied as a solid. Such compounds include transition metal oxides and sulphides. UV spectroscopy differs from infra-red in that it is not possible to dilute the oxide with KBr and press thin, translucent discs for investigation. This is because UV spectroscopy uses a much shorter wavelength of radiation and this causes too much scattering.

However it is possible to measure the absorption of a solid indirectly by measuring the diffusely reflected light from that solid. The immediate problem which has to be faced is that scattered light is also reflected and measured. A theory known as Kubelka-Munk(KM) theory has been developed to alleviate this problem. The Kubelka-Munk theory will be discussed after first outlining the types of reflection associated with this technique.

### 2.2.2 Types of Reflection Associated with DRS

When light strikes a powdered sample there are two types of reflections which can occur. The first type of reflection is when the reflected beam follows the path of the incident beam but in the reverse direction, i.e. mirror-like, (see Fig. 2.4). This is known as *specular reflection*. However, when reflection is not mirror-like, such that its angular distribution is independent of the angle of

incidence, i.e. like the reflection of sunlight from a sunlit whitewashed wall, then *diffuse reflection* occurs. Reflection under conditions where reflection is predominantly diffuse is termed *reflectance*. The reflectance spectra run for the powdered oxide samples detailed in this thesis were obtained in diffuse reflectance mode with a specular trap inserted to remove specular reflectance, (see *Section 2.2.4*).

### 2.2.3 Kubelka-Munk Theory of DRS

The theory builds upon a concept first introduced by Schuster<sup>50</sup> that the radiation flux in a plane parallel layer can be regarded as the balance between the fluxes in two opposite directions across a layer. The theory has been discussed in greater depth by Kortüm<sup>51</sup>, Wendlandt and Hecht<sup>52</sup> and Stone<sup>53</sup>.

Monochromatic light, intensity  $I_0$ , per unit area, can strike a plane, parallel to the surface, composed of solid particles which are randomly distributed (see Fig. 2.5). The positive direction can be regarded as downward and denoted by  $x$ , the illuminated surface being at  $x=0$  and the layer having a thickness of  $d$ . The light will be partly absorbed and partly scattered. At an infinitesimally thin layer  $dx$  within the solid the incident intensity will be reduced to  $I_{dx}$ . In addition, the layer  $dx$  will receive radiation from layers of atoms above  $dx$ . Here the mean free path,  $d\xi_I$ , is given by,

$$d\xi_I = \mu dx \quad \text{Eqn. 2.5}$$

where  $\mu$  is the integral that takes into account the fact that the rays strike at all angles. The layer  $dx$  will also receive radiation from the opposite direction on

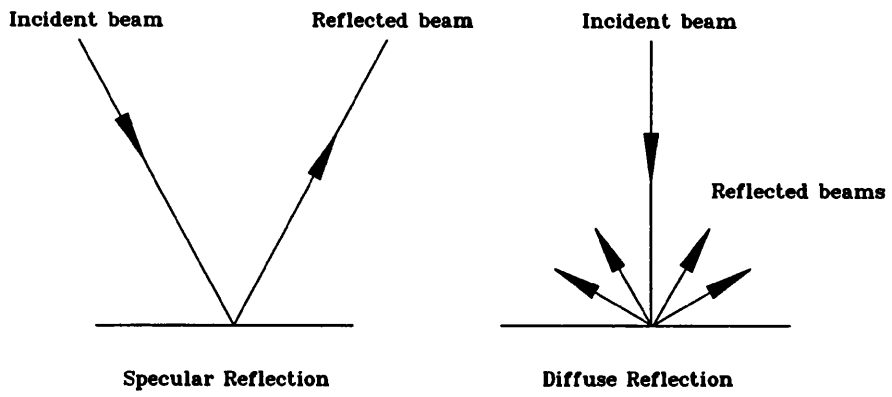


Fig. 2.4 Diagram of specular and diffuse reflection.

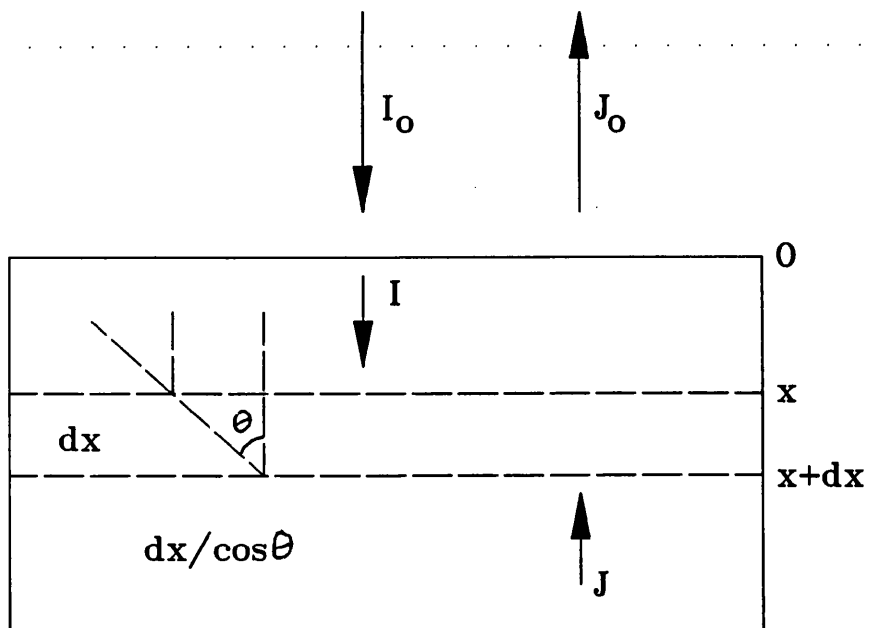


Fig. 2.5 Diagram of the Kubelka-Munk theory.

account of atoms below it scattering light. Here the mean free path,  $d\xi_J$  is given by,

$$d\xi_J = v dx \quad \text{Eqn. 2.6}$$

Some of the radiation arriving at the layer  $dx$  either from above or below the layer, will be absorbed and some radiation will be scattered. Therefore the reduction in  $I$  at  $dx$  will consist of two components,

$$\kappa d\xi_I \text{ absorbed} + \sigma d\xi_I \text{ scattered} \quad \text{Eqn. 2.7}$$

where  $\kappa$  is the fraction absorbed and  $\sigma$  the fraction scattered per unit path length. However the scattered fraction of intensity (which decreases  $I_{dx}$ ) will be offset by the scattered fraction of  $J$ , i.e. scattering from lower layer, (which increases  $I_{dx}$ ). Therefore the overall change in the flux of  $I_{dx}$  on passing through layer  $dx$  is,

$$-dI = \kappa I d\xi_{I \text{ absorbed}} + \sigma I d\xi_{I \text{ scattered}} - \sigma J d\xi_{J \text{ scattered}} \quad \text{Eqn. 2.8}$$

Given that  $dJ$  is obtained by the same reasoning and that  $d\xi_I = d\xi_J = 2dx$  the equations which describe the absorption and scattering are obtained,

$$-\frac{dI}{dx} = (k+s)I - sJ \quad \text{Eqn. 2.9}$$

$$\frac{dJ}{dx} = (k+s)J - sI \quad \text{Eqn. 2.10}$$

where  $k = 2\kappa$  and  $s = 2\sigma$ . Solutions of the above integrals give two general solutions which, when integrated over the whole thickness of the layer, i.e.  $x=0$  to  $x=d$ , shows that the reflectance,  $R$ , of the sample is given by Eqn. 2.11 and the transmittance,  $T$ , by Eqn. 2.12.

$$R = \frac{J_o}{I_o} \quad \text{Eqn. 2.11}$$

$$T = \frac{I_d}{I_o} \quad \text{Eqn. 2.12}$$

When the layer is of infinite thickness,  $d=\infty$ , then from Eqn. 2.12  $T_\infty=0$  and from Eqn. 2.11, via expansion and rearrangement of the equation, the following is obtained,

$$\frac{k}{s} = \frac{(1-R_\infty)^2}{2R_\infty} \equiv F(R_\infty) \quad 2.13$$

where  $F(R_\infty)$  is the Kubelka-Munk function,  $k$  equals the absorption constant and  $s$  the scattering constant. This equation can be rearranged to give,

$$\log F(R_\infty) = \log k - \log s \quad \text{Eqn. 2.14}$$

## 2.2.4 Instrumental Considerations

Diffuse reflectance spectroscopy is usually carried out by comparing the sample's reflectance to that of a standard. The ideal standard should have 100% reflectance over the whole 200-2000 nm range. However such a material is not yet known. The standard for work within this thesis is barium sulphate,  $\text{BaSO}_4$ , which possesses nearly 100% reflectance over large portions of this range.

A diagram of a typical set-up for diffuse reflectance UV spectroscopy is shown in Fig. 2.6. Light from a source,  $L$ , is passed through a monochromator and on to an oscillating mirror,  $M$ . The beam either travels to



the sample, S or to the standard, S'. The reflected beams from both sample and standard are collected by an integrating sphere which carries on its inner surface a highly reflecting coating, C (usually BaSO<sub>4</sub>). The beams are then registered by the detector, D. The detector unit is usually a combination of an end-on photomultiplier tube for the UV/VIS region and a PbS solid state detector for the VIS/NIR region. The detector is connected to an online computer for data acquisition and manipulation.

For the Kubelka-Munk function to apply the sample must be of infinite thickness. This condition is satisfied when the sample is *ca.* 3mm thick. The particle size of the sample is also very important with the optimum size being between 0.1 and 1  $\mu\text{m}$ .

### **2.2.5 Spectra Arising From d-d Transitions**

UV-VIS-NIR diffuse reflectance spectroscopy has, like solution UV, been extensively used to examine the d-d transitions of 3d transition metal ions. The transitions involved have been well established by ligand field theory.<sup>54</sup> The transitions result from the lifting of the degeneracy of the d-orbitals as a result of the departure from spherical symmetry in the d<sup>n</sup> cation (where n = the number of d electrons) when it is surrounded by anions with a particular geometry and field strength. The transitions between energy levels of an ion in an octahedral environment are strictly speaking, Laporte-forbidden. However transitions do occur due to orbital mixing or vibronic coupling. There are four main factors which affect the position and number of bands in the spectra

- i) the number of d electrons on the transition metal,

- ii) the effective charge on the ion,
- iii) the spatial distribution of the ligands,
- iv) the effective charges on the ligands.

In this thesis DRS spectra have been used to differentiate between  $\text{Co}^{2+}$  ions (which are  $d^7$ ) and  $\text{Co}^{3+}$  ions (which are  $d^6$ ) and to determine whether the  $\text{Co}^{2+}$  ions are in an octahedral or tetrahedral environment.

It should also be noted that charge transfer (CT) i.e. transitions from metal to ligand or vice versa, usually occur in the high energy region and so do not overlap with the d-d transitions. However, examples do exist of CT absorption in the visible region. One such example is cobalt oxide,  $\text{Co}_3\text{O}_4$ . Its black colour is a result of electron transfer between  $\text{Co}^{2+}$  and  $\text{Co}^{3+}$  oxidation states resulting in absorption across the whole of the visible region.

## 2.3 X-RAY PHOTOELECTRON SPECTROSCOPY (XPS)

### 2.3.1 Theory of X-ray Photoelectron Spectroscopy

Each atom present in the surface of a solid (except hydrogen) possesses core electrons. These core electrons are not directly involved in bonding. If these electrons are subjected to X-ray radiation of high enough energy, i.e. greater than the orbital threshold energy, the electron can escape the bounds of the surface and will travel in free space with a residual amount of kinetic energy. The process is known as the photoelectric effect. The resulting photoelectron energy ( $E_K$ ) is related to the X-ray energy ( $h\nu$ ) and the 'binding energy' ( $E_B$ ) of the core electrons by the Einstein relation,<sup>55</sup> and is shown schematically in Fig. 2.7,

$$E_K = h\nu - E_B - \phi \quad \text{Eqn. 2.15}$$

The work function,  $\phi$  is a 'catch all' term which includes various parameters dependant upon sample and spectrometer. The binding energy of each core electron is characteristic of the individual atom to which it is bound and hence can be used to identify the atoms present on the surface.

This equation assumes that the photoionisation process is elastic i.e. each characteristic photon will give rise to a series of photoelectron peaks which reflect the discrete binding energy of each electron present in the surface.<sup>56</sup> The process is inelastic and characteristic energy loss processes occur.

Although the X-rays can penetrate the solid up to a few micrometres, the origin of the photoelectron detected is a much shorter depth. This is because the energy of the electrons is easily dissipated by the solid, by inelastic

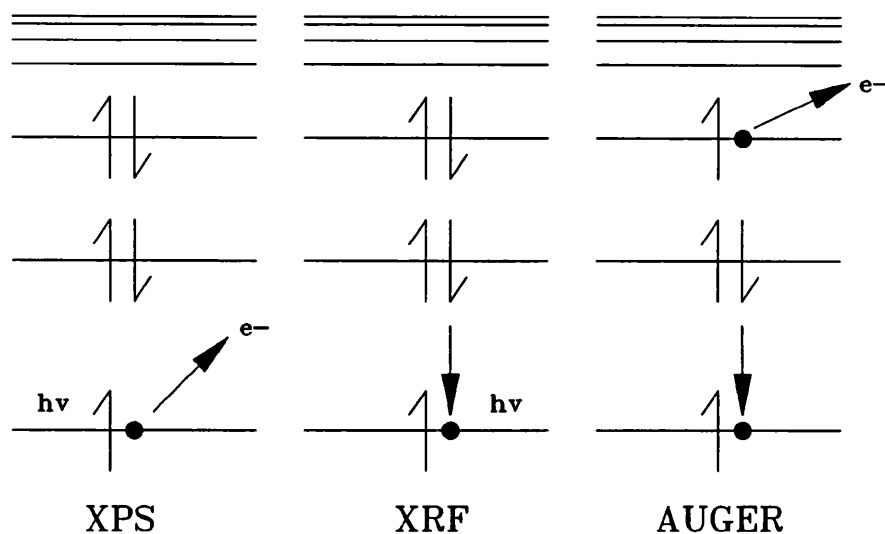


**Fig. 2.7** Diagram of XPS, XRF and Auger processes.

collisions, through which they have to travel. Therefore the depth of analysis depends upon the incident photon energy and the density of the matrix through which the photoelectron has to travel. It has been suggested that the 'surface' be defined as the outermost 1 nm only.<sup>56</sup>

### 2.3.2 Experimental Instrumentation

The data represented in this thesis was collected using an M-probe Surface Spectrometer equipped with a Hewlett Packard Vectra RS/20C computer for data acquisition.

The M-Probe Surface Spectrometer incorporates, like all XPS spectrometers, four specific design requirements.

- a) X-ray source
- b) Ultra - high vacuum (UHV)
- c) Photoelectron detection analyzer
- d) Preparation/analysis chambers

### ***2.3.2a X-Ray Source***

X-rays can be formed when energetic electrons strike a metal target causing the ejection of a core electron from the metal which is replaced by an electron from a higher energy level. This ionisation is accompanied by the emission of an X-ray photon of characteristic energy. The spectrum is, however, not monochromatic as other transitions are accessed as well as a continuous background (known as Bremsstrahlung radiation)

The source used in the M-Probe spectrometer differs considerably from the normal design. A monochromatic stream of electrons is focused onto an anode (spot size *ca.* 0.2 nm) producing Al K<sub>α</sub> X-rays. A focusing quartz is used to produce a monochromated, small spot (100 - 600 μm) X-ray beam at the sample.

### ***2.3.2b Ultra-high Vacuum (UHV)***

There are two main reasons why the spectrometer must operate under vacuum. Firstly, the electrons emitted from the sample should encounter as few gas molecules as possible before reaching the photoelectron detection unit. This is to ensure that they are not scattered and hence lost from the analysis. The second reason is because, as already stated, XPS is such a surface sensitive technique. It is so sensitive that if UHV conditions are not used surface contamination from the surrounding atmosphere (e.g. pump oils) can drastically alter the results of an experiment.

It is therefore necessary when using high surface area powder samples to achieve a vacuum of better than  $10^{-8}$  torr. This can be achieved using a very low pressure oil-diffusion pump.

### ***2.3.2c Photoelectron Detection Analyzer***

The analyzer, which operates on basic electrostatic principles, consists of two concentric hemispherical surfaces (see Fig. 2.8).

A deflecting potential,  $V$ , is applied between the surfaces of the hemispheres such that the outer sphere is negatively charged with respect to the inner sphere. As a consequence of this there exists a median equipotential between these hemispheres which in the ideal situation has a radius  $r_o$ , described by Eqn. 2.16,

$$r_o = \frac{(r_1 + r_2)}{2} \quad \text{Eqn. 2.16}$$

where  $r_1$  is the radius of the outer sphere and  $r_2$  is the radius of the inner sphere, along which electrons with energy equal to  $E_a$  must pass in order to successfully travel through the analyzer,

$$V = E_a (r_2/r_1 - r_1/r_2) \quad \text{Eqn. 2.17}$$

Once they have passed through the exit slit the electrons strike a photomultiplier which in turn sends information to the online computer.

By varying the deflecting potential the electrons of differing energy can be focused upon the photomultiplier. The resolving power ( $\rho$ ) of an analyzer, as described above, is defined by Eqn. 2.18,

$$\rho = 2r_o/w$$

Eqn. 2.18

where  $w$  is the width of the entrance slit. This equation indicates that the larger the analyzer the better the resolving power. However, large analyzers are difficult to machine and take a long time to evacuate. However, if the electrons are retarded before entering the electrostatic field the resolving power is increased.

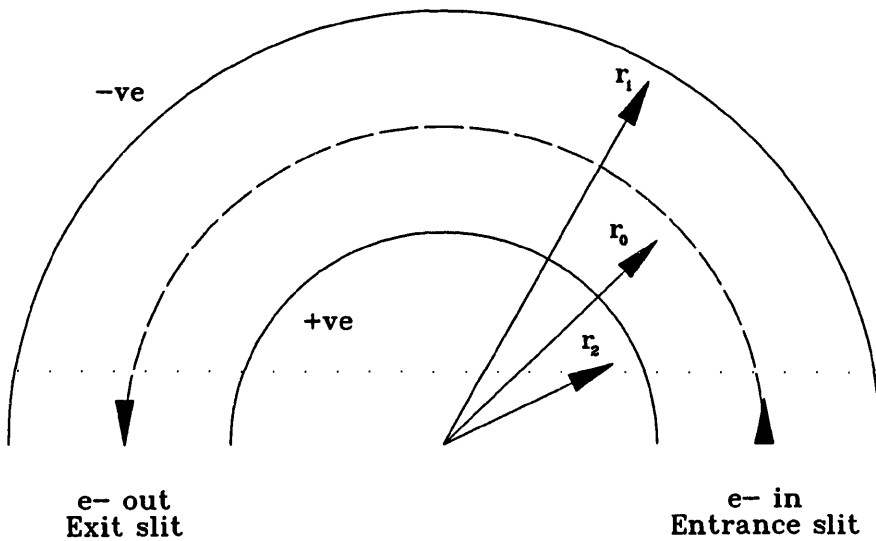


Fig. 2.8 Diagram of photoelectron detection analyzer.

### 2.3.2d Preparation and Analysis Chambers

In Fig. 2.9 and 2.10 a cut away diagram of the preparation and analysis chambers can be seen.

The samples to be analyzed are mounted on a grease-free stainless steel stub using double-sided sticky tape. This stub is then placed in the parking chamber, with up to five other stubs, for outgassing or until required for

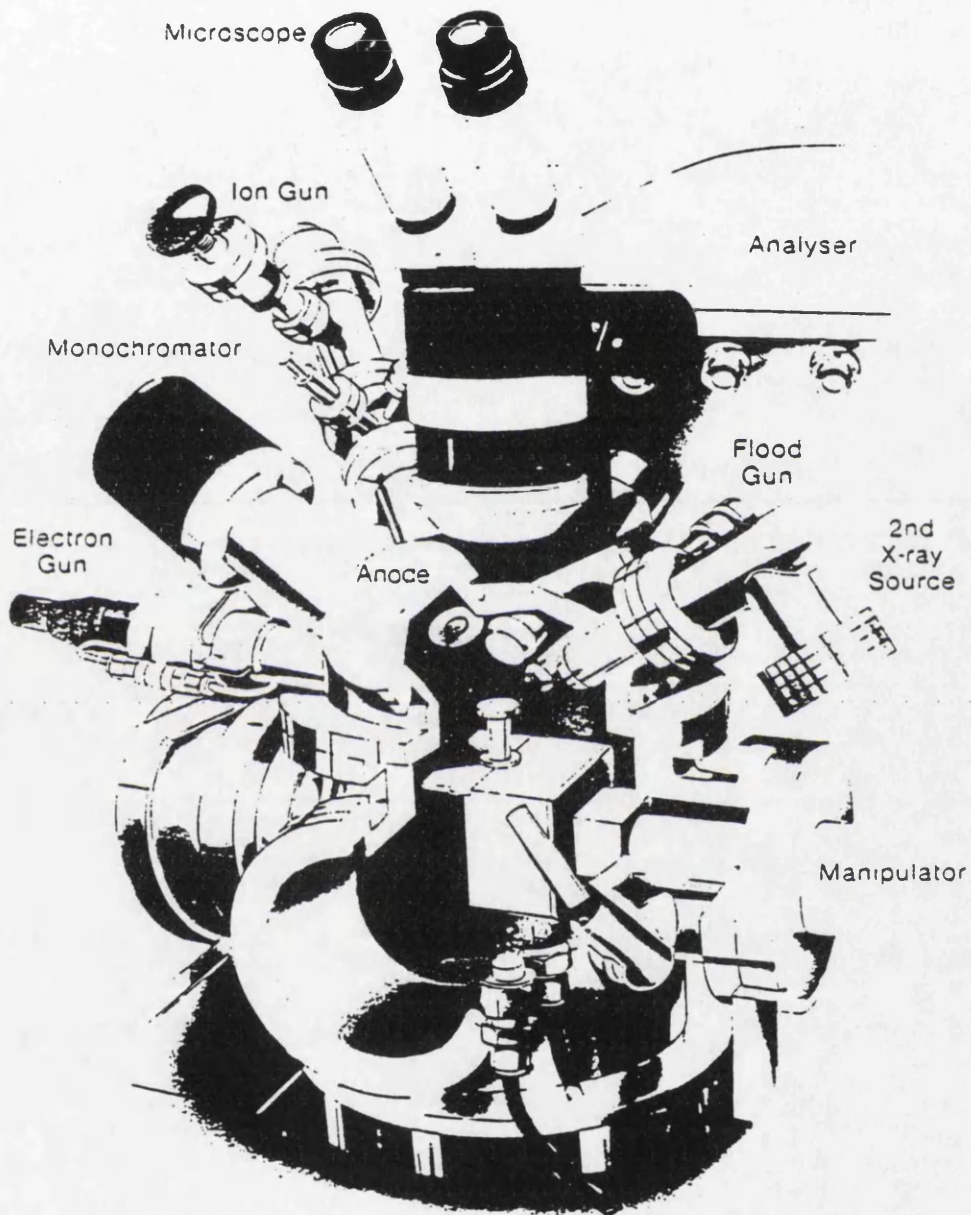


Fig. 2.9 Cut-away diagram of M-Probe Analysis configuration.

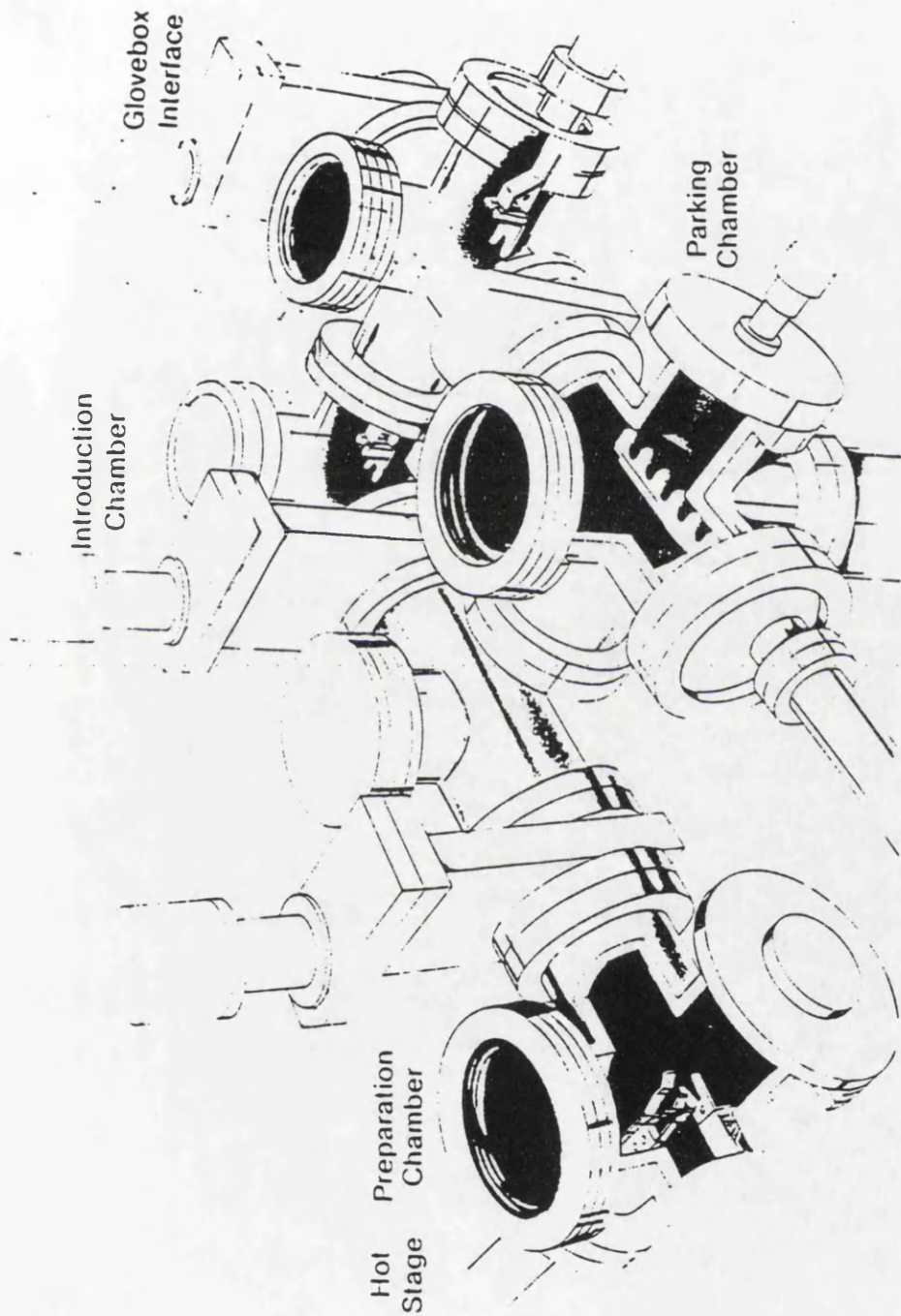


Fig. 2.10 Cut-away diagram of M-Probe preparation system.

analysis. The whole assembly is made from stainless steel and the pressure seal for the introduction chamber is made by means of a knife-edge copper gasket junction.

Once the stub has been transferred to the analysis chamber the optimum height of the X-ray gun must be found. This is achieved by initially using a focused and aligned optical microscope and then by monitoring the signal (photoelectron flux rate) of the analyzer as a function of gun height. In this analyzer the X-ray gun height is fixed and it is the stub which is moved. This is achieved using three computmotors which can move the stub in the xyz orthogonal directions.

Charging of the sample is minimized by the use of a low energy electron flood gun. All samples were mounted under earthed 90% transparent nickel mesh. This ensured that there was a field free region around the sample being investigated.

### **2.3.3 Primary Structure**

A wide scan of pure cobalt oxide ( $\text{Co}_3\text{O}_4$ ), in which monochromatic radiation was used, is shown in Fig. 2.11. It shows a series of peaks observed in a background which increased towards high binding energy (low kinetic energy). The step-like increase after each prominent peak is due to photoemission of secondary electrons which arise from inelastic collisions and these dominated the high binding energy end of the spectrum.

The peaks can be grouped into two basic types, those that arise due to photoemission from core levels or valence levels and those peaks that arise due to X-ray excited Auger emission (Auger series).

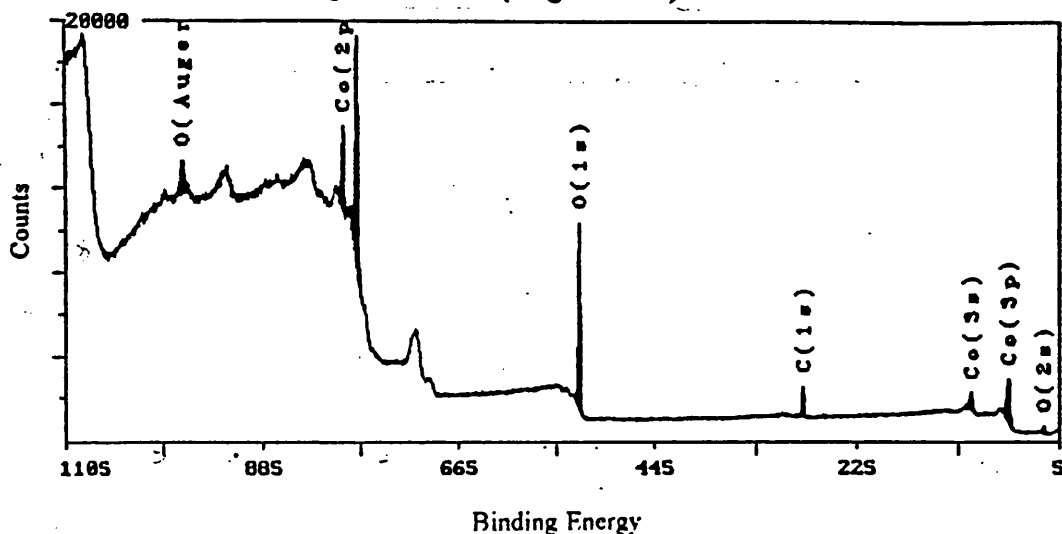


Fig. 2.11 A wide scan of pure cobalt oxide,  $\text{Co}_3\text{O}_4$ .

### 2.3.3a Core Levels

The core-level structure is a direct reflection of the atomic structure. As the binding energy increases for a particular atom the emission observed comes from a lower azimuthal quantum number,  $l$ , and the lower principal quantum number,  $n$ .

It can also be seen that the intensities of the peaks vary and that levels other than  $s$  levels exist as doublets. This is a result of  $j-j$  coupling. The separation is equal to the spin-orbit coupling constant and is expected to increase as a function of atomic number for a given subshell and to decrease as  $l$  increases for a given value of  $n$ .

The nomenclature for the split peaks is therefore derived from the spin-orbit ( $l-s$ ) splitting. L-S coupling gives rise to final states with a configuration

described by  $J=L+S$  or  $J=L+1/2$ . Therefore creation of a singly-charged species results in the possible formation of two final states which can be observed as two separate peaks in the photoelectron spectrum, i.e. the Co2p level gives rise to two peaks, Co2p<sub>3/2</sub> and Co2p<sub>1/2</sub>. They are separated by ca. 15 eV which is equal to their spin-orbit coupling constant. The relative intensities of the doublets is given by  $(2j+1)$  and is shown in Table 2.1.

### 2.3.3b Relative Peak Intensities

The relative peak intensities are governed by the atomic photoionisation cross-section,  $\alpha$ . This describes the probability of ionisation of a specific core level in an atom when the sample is irradiated with a photon of energy,  $h\nu$ . The value of  $\alpha$  is therefore a function of both the core level in which the hole is created and the energy of the impinging photon.<sup>57</sup>

**Table 2.1** The relative intensities of doublets.

Subshells	j-values	Area
s	1/2	-
p	1/2, 3/2	1:2
d	3/2, 5/2	2:3
f	5/2, 7/2	3:4

The peak area of a photoelectron feature is then proportional to the number of atoms present. However, as is usually the case, if more than one atom is present in the analysing chamber there is a finite probability that the photoelectron will collide with another atom. Thus, in general, for a

homogeneous solid of thickness  $t$ , and mean escape depth  $d$ , the photoelectron intensity  $I$ , will be given by Eqn. 2.19,

$$I = F\alpha Dkd(1 - \exp^{-x/d}) \quad \text{Eqn. 2.19}$$

where  $D$  is the density of the atom in the material,  $k$  is a factor of the instrument (such as detector efficiency) and  $F$  is the incident photon intensity.

### **2.3.3c Peak Widths**

Peak width, defined as Full-Width at Half-Maximum (FWHM), is influenced by two main factors

- i) Initial Broadening
- ii) Instrument Broadening

It is of prime importance that the minimum peak width is obtained in order to identify any surface interactions.

Narrower peaks arise from core levels which have long lifetimes. Intrinsic linewidths increase inversely with the azimuthal quantum number ( $l$ ). This is because at lower values of  $l$ , more transitions leading to core-hole neutralisation can occur and this reduces core-hole lifetime and hence increases peak broadening. This is known as initial broadening.

Instrumental broadening provides the largest contribution to the line width in XPS. It arises from the X-ray source and the electron energy analyzer. The most commonly used sources are Al and Mg  $K_{\alpha}$ . They are used because they both have relatively high energies yet have small widths. The resolution of the analyzer may also be reduced but this invariably results in a reduction in sensitivity.

### 2.3.3d Chemical Shifts

Shifts in core level binding energies take place as the chemical environment (or localised electron density) of the emitting atoms change. Information on the oxidation state of the atom can be derived from the binding energy.

Shifts are also observed for changes in the molecular environment due to the change in the localised electron density that results from this. For example Fig. 2.12 shows that the C1s level differs depending on the electronegativity of the atoms directly attached to it.<sup>58</sup>

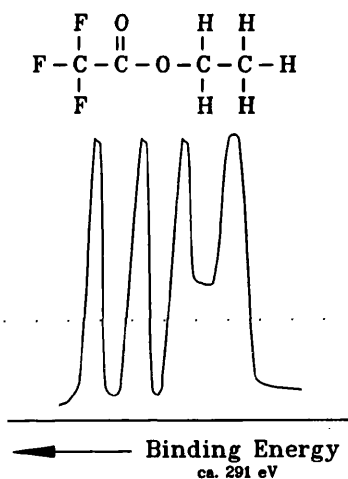


**Fig. 2.12** Chemical shift of C1s peak due to the different neighbouring atoms.<sup>59</sup>

### 2.3.3e Auger Emission

After creation of the core-hole an excited ion remains. From this point there are two possible modes of decay, X-ray fluorescence (XRF) or Auger Emission. Both are competing but Auger is favoured for relatively shallow core levels i.e. with binding energy of *ca.* 2 keV.

Auger emission is a three electron process. An electron can be captured from a valence level. This causes a change in the electronic configuration of

the ion which in turn causes energy to be released (this is XRF, see Fig. 2.7). This photon can cause another electron to be emitted into free space to leave a doubly charged ion. This is Auger Emission. The kinetic energy of Auger electrons marks the difference in energy between it and the singly charged species.

### **2.3.4 Secondary Structure**

Superimposed on the primary features of a photoelectron spectrum are features which are derived from various processes which are termed secondary structures.

#### ***2.3.4a Relaxation***

This is the dominant decay mechanism for core-hole states. It is a radiationless transition in which the atom relaxes or reorganises using valence electrons. This results in an effective increase in overall nuclear charge. This then leads to there being an excess of energy within the system. This excess energy is donated to the emitted electron. The photoelectron therefore has increased kinetic energy and is observed at a correspondingly lower binding energy.

#### ***2.3.4b Multiplet Splitting***

If the transition metal has unpaired electrons in its d-orbitals in the ground state and is then left with an unpaired electron in one of its valence levels after photoionisation the valence electron can then interact with the d electrons in two possible ways. It can adopt a 'parallel' or 'anti-parallel' configuration and

the separation of the two peaks is a result of analyzer momentum vectors which arise from this.

#### ***2.3.4c Shake-up Satellites***

This follows the same initial steps as relaxation except that the energy gained from the reorganisation may involve the excitation of a valence electron to a higher unfilled level (shake-up, see Fig. 2.13). The energy that is required for this process is lost from the energy of the primary photoelectron and consequently is observed as a structure situated at higher binding energy than the main photoelectron peak.

Strong satellites of this type are then observed for transition metal oxides (up to 10% as strong as the main peak). The energy separation of the two peaks is approximately equal to the band gap and, as in the case of multiplet splitting, can have a diagnostic value. For example  $\text{Co}^{2+}$  gives more intense satellites when in the high spin ( $^4\text{F}$ ) state than when in the low spin ( $^2\text{D}$ ) state, while  $\text{Co}^{3+}$  is diamagnetic and has no satellites.<sup>60,61</sup>

#### ***2.3.4d Plasmon Effects***

When an electron is emitted from a surface it can, in addition to the effects mentioned above, also excite the band electrons present in the solid. These excitations are characteristic of the material of the solid and therefore need characteristic energies for the process to occur. An electron that has given up an amount of energy equal to one of these characteristic energies, in the course of excitation, is said to have suffered a plasmon loss. The peaks due to

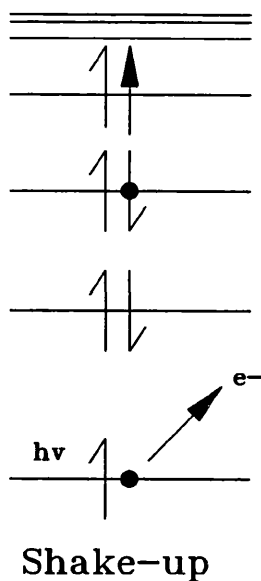


**Fig. 2.13** Diagram of shake-up.

plasmon-loss occur at lower kinetic energy than those peaks due to the electrons which have not undergone the characteristic energy loss.

### 2.3.5 Charging and Referencing

After photoionisation the surface of the non-conductors is left with a positive charge due to the atoms losing electrons. This positive charge produces a retarding field in front of the specimen such that the photoelectrons have a kinetic energy lower than that predicted by Eqn. 2.15. This static build up is not a problem with conductors since they are easily earthed and the rate of replacement of electrons from the bulk is sufficiently fast to replace lost electrons at the surface. This is not the case for insulators. For insulators, such as oxides, this can be a problem as the size of the shift is unknown and therefore leads to difficulties in interpreting chemical shifts.

For surfaces with a static potential  $C$  the apparent binding energy of the photoelectrons  $E_B'$  is related to the true binding energy  $E_B$  by Eqn. 2.20,

$$E_B = E'_B - C \quad \text{Eqn. 2.20}$$

There are several methods for determining the value of C. The most commonly used method is to reference via adventitious carbon-based contaminants. The C 1s binding energy  $285.0 \pm 0.2$  eV is often used, with the difference between its measured position on the energy spectrum and the above value giving the charging value C. However many authors suggest caution in its use.<sup>62,63</sup>

The most reliable method of spectral referencing lies in the use of an internal standard. This makes use of a chemical group within the structure which has a binding energy that is little affected by its environment. The reference is now 'locked' into the unknown material and must reflect the static charge of the system if it is uniform over the surface. The carbonate C1s binding energy  $E_B = 289.1$  eV is often used in this respect.

### **2.3.6 Data Analysis**

Data analysis was performed on a Hewlett Packard Vectra QS/165 computer using associated M-Probe Software (version 1.31).<sup>64</sup>

#### ***2.3.6a Background Removal***

The removal of the background contribution to a spectrum must be undertaken with great care as it is possible to distort the data if incorrectly carried out. There are two possible methods by which background intensity can be removed, namely linear and non-linear. The linear method is the simplest (and most inaccurate) and involves drawing a straight line between points at the start and end of the data set.

The non-linear or Shirley subtraction takes into account removal of inelastic electron ejection processes but leaves any broad elastic features. It assumes that the background intensity at any point in a photoelectron spectrum arises exclusively from the inelastic scattering of electrons of higher kinetic energy and is therefore in proportion to the photoelectron intensity at a higher kinetic energy. Thus the computer integrates the area beneath the spectrum to give a sigmoid shaped line for background noise, with the point of inflexion of this curve lying beneath the point of greatest intensity.<sup>65</sup>

### ***2.3.6b Spectral Smoothing***

Smoothing is a process that attempts to increase the correlation between points while suppressing uncorrelated noise. Again care must be taken not to distort the data. Two methods are generally used to achieve smoothing, namely the least-squares approach and the Fourier Transform process.<sup>66</sup>

### ***2.3.6c Peak Fitting***

Often two discrete peaks may overlap to form a broader non-Gaussian type envelope (see Fig. 2.14). It is possible to fit Gaussian peaks manually and then allow the computer to undergo an iterative routine such that the summation of the fitted peaks results in a good fit with the experimental data. Care must be taken as the best fit may not be a reflection of the true make-up of the envelope. Peak fitting should be carried out with as much reference to known information as possible so that the positions ascribed to peaks by the method are correct and the FWHM values are reasonable.

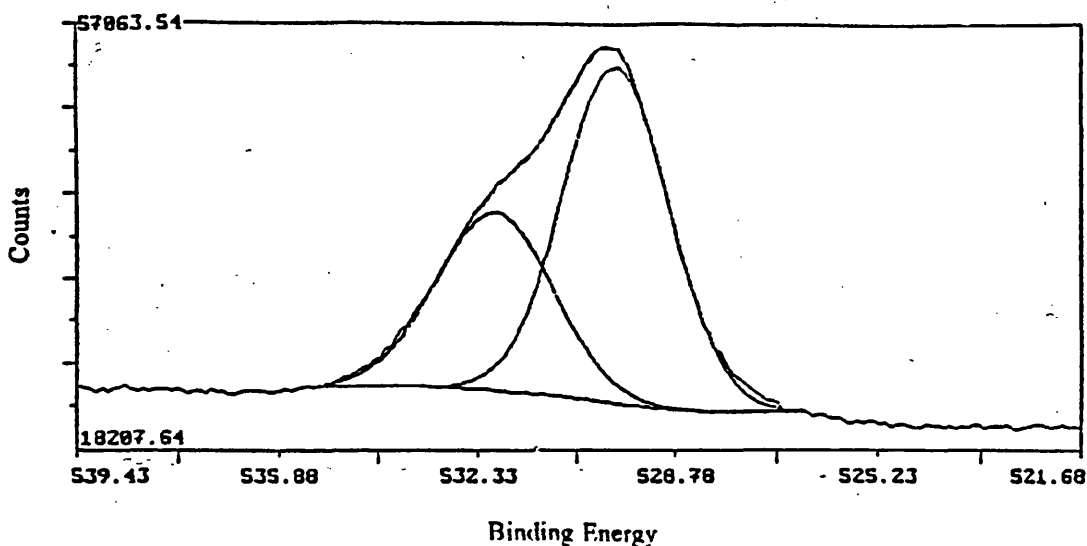


Fig. 2.14 Example of peak fitting for the O1s peak.

### 2.3.6d Integration

After background removal, the area between two points can be integrated. This area can then be used for quantitative analysis such as relative surface concentrations.

### 2.3.6e Quantitative Analysis

If two elements x and y are present at the surface of a powder sample their relative atomic ratio ( $n_x/n_y$ ) can be calculated using the formula

$$\frac{n_x}{n_y} = \frac{I_x}{I_y} \times \frac{\alpha_y}{\alpha_x} \times \frac{\lambda_y}{\lambda_x} \quad \text{Eqn. 2.21}$$

where  $I_x$  and  $I_y$  are the intensities and  $\alpha_x$  and  $\alpha_y$  the photoionisation cross-sections of the respective elements.

The  $\lambda_x$  and  $\lambda_y$  refer to the escape depths. As they refer to the same material it has been shown that this last term can be approximated to

$(KE_y/KE_x)^{3/4}$  where  $KE_{x\&y}$  are the kinetic energies of photoelectrons from the respective atoms x and y.<sup>67</sup>

Depending on which peak ratios are measured it is possible to determine surface ratios ( $Co2p_{3/2}/Zn2p_{3/2}$ ) or bulk ratios ( $Co3s/Zn3s$ ) or  $Co3p/Zn3p$ ).

**CHAPTER 3**  
**OBJECTIVES**

---

---

## OBJECTIVES

The primary aim of this thesis was to investigate the effect of doping zinc oxide with cobalt in order to develop absorbents for low temperature gas desulphurisation.

A range of oxides with nominal Co/Zn ratios of 0/100, 10/90, 20/80, 30/70, 40/60, 50/50, 70/30, 90/10 and 100/0 were prepared via hydroxycarbonate precursors by the coprecipitation route using mixed Co/Zn nitrates and ammonium carbonate. The bulk structures of these precursors and oxides were fully characterised using atomic absorption, powder X-ray diffraction, transmission electron microscopy, UV-VIS-NIR diffuse reflectance spectroscopy, FTIR, thermogravimetric analysis and surface area analysis. The surface of the precursors and the oxides were characterized using X-ray photoelectron spectroscopy.

The oxides were then tested on a continuous flow 'breakthrough' microreactor for their ability to remove hydrogen sulphide. One objective of this thesis was to try and relate the physical characteristics of the precursors and the oxides to the sulphur capacity of the oxides.

It was also the aim of this thesis to select a representative Co/Zn loading, namely the 30/70 loading, and study the effects of modifying conditions during the synthesis of the precursor. The variables altered were the aging time of the precipitate in the mother liquor, pH used, the precipitating agent and the method of precipitation used. All these factors were thought to affect the morphology formed and/or the component interdispersion of the precursor and hence the oxide formed on calcination.

Optimisation of the calcination parameters was another objective. A range of Co/Zn precursors, nominal atomic Co/Zn ratio of 0/100, 20/80, 30/70, 40/60 and 100/0, were synthesized and then calcined at various temperatures to obtain the oxide. This was to see how this affected the number of phases produced and the surface area obtained and then its ability to uptake H<sub>2</sub>S.

The aim of the XPS analysis was to see if either the zinc or the cobalt was enriched on the surface or whether a homogeneous dispersion between the bulk and the surface existed for the precursors. It was also hoped that a study of the oxides would show whether any bulk/surface discontinuities were retained after calcination. Furthermore, the surface analysis would provide evidence as to why one oxide absorbent was more efficient at H<sub>2</sub>S removal than another in addition to indicating which metal species was present on the surface.

It was hoped that this work would establish the optimum conditions for the synthesis and calcination of Co/Zn precursors to give oxides which efficiently removed sulphur from feedstocks. Such studies should enable a mechanism for the absorption of H<sub>2</sub>S by the oxide to be postulated and indicate the rate determining step in the reaction and hence establish what causes 'breakthrough' to occur.

**CHAPTER 4**  
**EXPERIMENTAL**

---

---

#### 4.1 ABSORBENT PREPARATION AND ANALYSIS

Precursors with different nominal atomic ratios of Co/Zn were prepared by the low supersaturation coprecipitation method at a constant pH of 7. A  $1 \text{ mol dm}^{-3}$  solution of cobalt and zinc nitrate was pumped simultaneously into a beaker with a  $2 \text{ mol dm}^{-3}$  ammonium carbonate solution at a temperature of  $70\text{-}75^\circ\text{C}$ . After addition of the solutions was completed (approx. 20 minutes), the precipitate was aged in the mother liquor, for 30 minutes whilst being vigorously stirred (see Fig 4.1). The solutions were then filtered and the solid washed with distilled water. Finally the precursors were dried in an oven at  $110^\circ\text{C}$  for 16 hours. This will be referred to as the standard method.

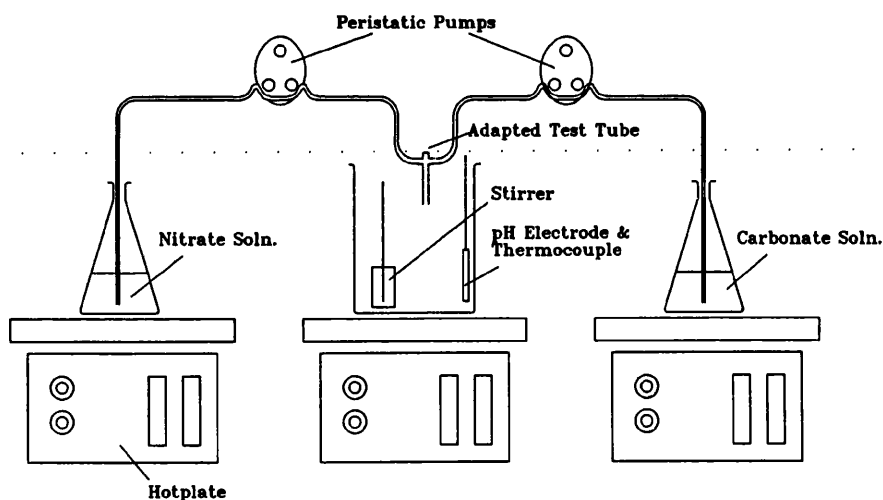


**Fig. 4.1** Schematic diagram of the apparatus used for the coprecipitation experiments.

The reagents used were zinc nitrate hexahydrate,  $\text{Zn}(\text{NO}_3)_2 \cdot 6\text{H}_2\text{O}$  (Fluka); cobalt nitrate hexahydrate,  $\text{Co}(\text{NO}_3)_2 \cdot 6\text{H}_2\text{O}$  (Fluka); ammonium carbonate - equimolar proportions of ammonium hydrogen carbonate and ammonium carbamate,  $\text{NH}_4\text{HCO}_3 \cdot \text{NH}_2\text{COONH}_2$  (BDH).

The cobalt and zinc content of all the precursors and oxides were determined by atomic absorption using a Perkin-Elmer 370A spectrometer. The metals were extracted by digestion in nitric acid. Diluted solutions of the extracted nitrates were then analyzed quantitatively by comparison with standard solutions (BDH-Spectrosol).

## **4.2 ABSORBENT CHARACTERISATION**

### **4.2.1 X-ray Powder Diffraction (XRD)**

The powder diffraction patterns were obtained using a Perkin-Elmer D60 diffractometer and Ni-filtered Co-K $\alpha$  radiation ( $\lambda = 1.7902\text{\AA}$ ). Scans were recorded between  $2\theta = 12$  and  $74^\circ$  for the precursors, and  $2\theta = 20$  and  $100^\circ$  for the oxides. In both cases the scan rate used was  $2^\circ \text{ min}^{-1}$ . The intensities of the peak reflections were estimated from the relative peak heights. The data obtained were compared to the X-ray powder diffraction files from the literature.<sup>49</sup>

### **4.2.2 Transmission Electron Microscopy (TEM)**

The material to be investigated was placed in distilled water and agitated (usually by placing in a sonic bath for a few seconds) to give a fine particulate suspension. A very small drop of this suspension was then placed on a copper grid, covered with a fine layer of graphite. After the grid had been allowed to dry in an oven at  $110^\circ\text{C}$ , for about 45 minutes, it was placed in the electron microscope (either a JEOL 1200X or a JEOL-100C) for investigation. Suitable

photographs and electron diffraction patterns were recorded after visual inspection of the *image*.

#### **4.2.3 UV-VIS-NIR Diffuse Reflectance Spectroscopy (DRS)**

Reflectance spectra were recorded, in the wavelength range 190-2500 nm, using a Perkin-Elmer Lambda 9 UV/VIS/NIR spectrometer equipped with a diffuse reflectance attachment. Barium sulphate, BaSO<sub>4</sub>, was used as a standard. An Amstrad PC-16 computer was used for data acquisition, analysis and Kubelka-Munk conversion of the spectra. The wavelength range 190-2500 nm covers the UV, visible and near-infrared regions.

#### **4.2.4 Infrared Spectroscopy (FTIR)**

Infrared spectra were recorded using the KBr disc method. Approximately 5 mg of sample was ground with *ca.* 40mg KBr and pressed into a 13 mm disc at 10 tons pressure. Spectra were obtained in transmission mode, between 4000 and 400 cm<sup>-1</sup>, using a Phillips PU980 FTIR spectrometer.

#### **4.2.5 Thermal Analysis**

Thermogravimetric Analysis (TGA) was carried out on the precursors, by Mr. G. McCulloch at the University of Glasgow, using an Stanton Redcroft 1500. Decomposition of the precursors was followed using approximately 15 mg of sample and an air flow rate of 1 l hr<sup>-1</sup>. The temperature was raised from room temperature to 1000°C by a linear programme at a heating rate of 20°C min<sup>-1</sup>, except for the precursors from *Section 4.9* where a heating rate of 10°C min<sup>-1</sup>

was used. The calculated weight loss was determined to within  $\pm 2\%$  and the temperatures of decomposition  $\pm 5\%$ .

#### **4.2.6 Surface Area Determination**

BET surface areas ( $N_2$ , 77 K) were calculated from five-point adsorption isotherms. The surface areas were obtained either by Ms. R. Millar, University of Glasgow, using a Digisorb 2500 or by a Flowsorb 2300 Micromeritics instrument at ICI Katalco, Billingham. In both cases the samples were outgassed at 140°C for 8 hours.

#### **4.2.7 Microanalysis**

Analysis of the precursors for the presence of nitrogen was carried out by Ms. K. Wilson at the University of Glasgow.

#### **4.2.7 X-ray Photoelectron Spectroscopy (XPS) - Qualitative Analysis**

X-ray photoelectron spectra were obtained using Al  $K_{\alpha}$  ( $h\nu = 1486.6\text{eV}$ ;  $1\text{eV} = 1.602 \times 10^{-19}\text{ J}$ ) monochromatized radiation with a Surface Science Instruments M-Probe Spectrometer connected to a Hewlett Packard Vectra RS/20C computer for data acquisition and analysis.

The analysis chamber was evacuated to better than  $1 \times 10^{-8}$  Torr before running the spectra. The spectra were recorded at room temperature and at low X-ray fluxes (anode operating at 10 kV and 22 mA).

The data analysis procedure generally involved background subtraction by a Shirley-type integral profile and a curve fitting procedure by a least-squares method (using associated M-Probe software<sup>64</sup>).

The spectra were analyzed in terms of the relative peak area intensities, the full-width at half-maximum height, (FWHM), of the peaks, and the chemical shifts of the  $2p_{3/2}$  transitions of zinc and cobalt, and the oxygen 1s transition. Spectra were collected with a pass energy of 50 eV. The experimental errors were estimated to be  $\pm 0.2$  eV for the photoelectron peak binding energy positions.

The samples were loaded using double-sided Scotch tape. A low energy electron-flood gun was used and residual charging effects were corrected for all the hydroxycarbonate precursors using the C 1s peak specific to the carbonate group which was fixed at  $E_B=289.1$  eV. For the 10/90 and 50/50 series of calcined samples the C 1s peak due to adventitious carbon with  $E_B$  fixed at 285.0 eV was used. For the oxides, calcined 350°C, and sulphided oxides charging effects were corrected using the O 1s peak at  $E_B=530.0$  eV.

### 4.3 ABSORBENT TESTING

The absorbents were tested using the continuous flow microreactor shown in Fig. 4.2. In a typical experiment a 5 cm<sup>3</sup> bed of absorbent particles (sieved to between 500-1000  $\mu\text{m}$ ) was placed into the glass reactor tube. Taps A and B were positioned to allow gas to flow through the by-pass tube and the N<sub>2</sub> and H<sub>2</sub>S flow rates were set such that a 2% H<sub>2</sub>S in nitrogen feed and a space

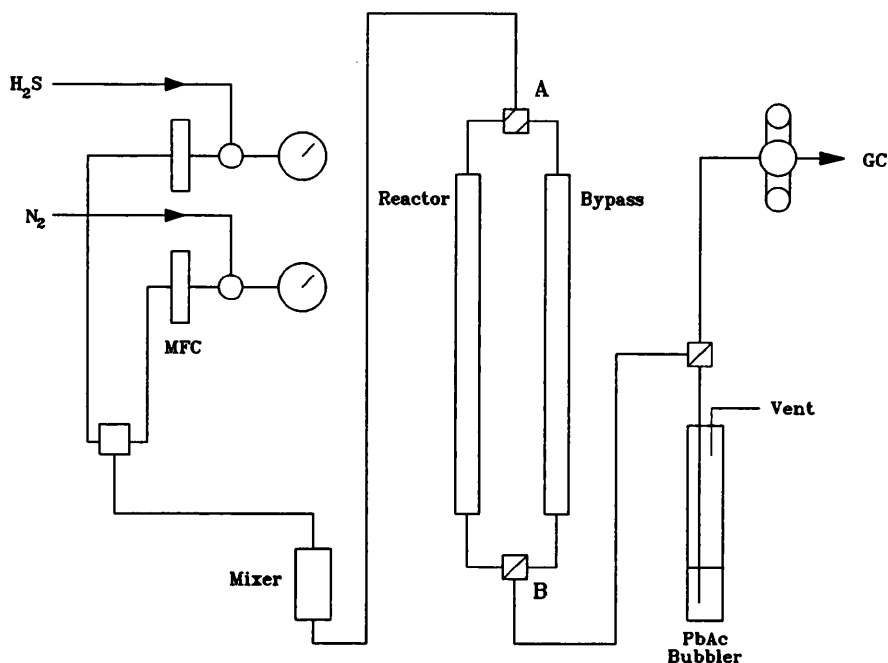


**Fig 4.2** Schematic diagram of continuous flow 'breakthrough' microreactor.

velocity of  $700 \text{ h}^{-1}$  was obtained. This was achieved by setting the  $\text{H}_2\text{S}$  flow rate, to *ca.*  $1.16 \text{ cm}^3 \text{ min}^{-1}$  using a mass-flow controller and measuring the flow rate with a bubble flow meter. The overall flow rate was increased to *ca.*  $58 \text{ cm}^3 \text{ min}^{-1}$  by the addition of  $\text{N}_2$ . The gas stream was then allowed to flow over the absorbent bed and a stop watch was started. The reactor exit stream was bubbled through a solution of 5% (w/v) lead acetate and 10% (w/v) sodium hydroxide prior to passing through a "clean-up" vessel containing  $\text{ZnO}$  granules to remove any  $\text{H}_2\text{S}$  in the exit gas. Breakthrough of the  $\text{H}_2\text{S}$ , i.e. *ca.* 2-3 ppm, was detected by the precipitation of lead sulphide in the alkaline lead acetate. The concentration of  $\text{H}_2\text{S}$  in the feed was determined using a G.C. fitted with a TCD detector.

#### 4.4 COBALT-ZINC 1st SERIES

The coprecipitation method described in *Section 4.1* was used to synthesise a series of hydroxycarbonate precursors with nominal atomic loadings of Co/Zn 0/100, 10/90, 20/80, 30/70, 40/60, 50/50, 70/30, 90/10 and 100/0. These precursors were dried for 16 hours at 110°C and then calcined as a finely ground powder. The calcination was carried out in air under static conditions in a muffle oven at 350°C for 16 hours.

Pellets of the calcined precursors were required for testing. The particles had to be in the range of 500 - 1000 µm so as to prevent problems of pressure drop across the absorbent bed in the flow rig. Initially the pellets were obtained using a 13 mm Specac die. The finely powdered oxides were pressed into discs<sup>†</sup>, crushed and then sieved.

Each set of precursors and oxides were fully characterised by AA, XRD, TEM, DRS, FTIR, TGA/DTA and BET. The oxide particles were tested on the continuous flow microreactor for their ability to remove H<sub>2</sub>S from a H<sub>2</sub>S/N<sub>2</sub> feed.

#### 4.5 XPS STUDY OF COBALT-ZINC 1st SERIES

The surface of the precursors, oxides and sulphided oxides from *Section 4.4* were characterised by XPS. Finely ground precursors with nominal loadings of Co/Zn 10/90 and 50/50 were calcined in the muffle oven at various temperatures between 100 and 700°C for 8 hours. This was to help confirm the

---

<sup>†</sup>Conditions for pressing the discs were found by trial and error. It was found that the pressure resulting from three pulls on the press, held for 15 seconds gave the best discs i.e. discs that just held together with hopefully no significant destruction of the pore structure. Surface areas of the pellets showed little or no change from the original powders.

surface segregation data obtained by the XPS characterisation and also to investigate the effect of calcination temperature on surface area, since the surface areas of oxides have been found to be dependant on calcination temperature.<sup>68,69</sup>

#### 4.6 OPTIMISATION OF CALCINATION PARAMETERS

The method of preparing the particles used in *Section 4.4* was found to be very slow with a small percentage return of particles compared to the powder used. A better method was found to be to first make the finely ground precursors into pellets and then calcine them. The pelletizing of each precursor was achieved by mixing some of the precursor with just enough water to enable the fine particulates of the powder to stick together. The remainder of the dry powdered precursor was then sprinkled onto the damp mass whilst stirring with a spatula. As this was done the powder began to conglomerate into semi-spherical particles of various sizes. These particles were left to dry and then sieved, crushed and sieved again (sieved to 500-1000  $\mu\text{m}$ ).

It was also thought that calcining the precursors in flowing air might improve the surface area of the oxides. To investigate this a precursor sample of nominal atomic loading 30/70 was pelletized by the method described above and calcined in the muffle oven at 300°C for 8 hours. A second sample was calcined in flowing air using a temperature programmed controller (see Fig. 4.3). The temperature was raised linearly from 25 to 300°C at 5°C min<sup>-1</sup> and held at 300°C for 8 hours. Further calcinations were then carried out using the 100% cobalt and 100% zinc precursors. They were calcined at temperatures

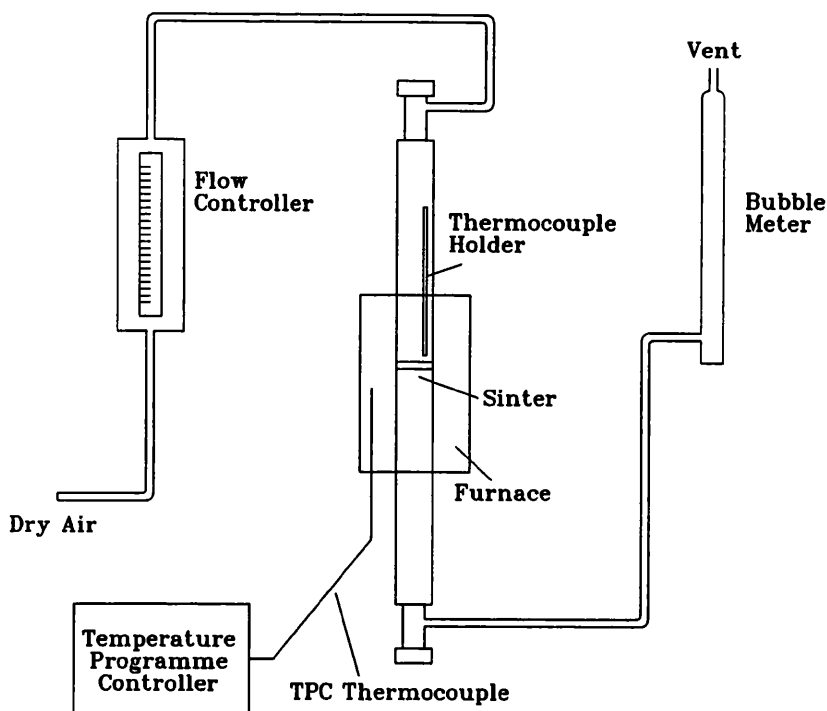


**Fig. 4.3** Schematic diagram of the apparatus used for calcination of precursors in flowing air using a temperature programmed controller.

ranging from 150 to 450°C in flowing air. In each case the temperature was increased at a linear heating rate of 5°C min<sup>-1</sup> from room temperature to the required temperature and held at the maximum temperature for 3 hours.

#### 4.7 COBALT-ZINC 2nd SERIES

A series of hydroxycarbonate precursors of nominal atomic ratios of Co/Zn 0/100, 20/80, 30/70, 40/60 and 100/0 were prepared using the method described in *Absorbent Preparation and Analysis (Section 4.1)*. The precursors were made into pellets by the method described in *Section 4.6* and calcined in flowing air using a temperature programmed controller. The samples were heated linearly (5°C min<sup>-1</sup>) from room temperature to 150, 250, 350 and 450°C, and held for 8 hours.

The dried and calcined precursors were fully characterised using AA, XRD, TGA, FTIR, DRS and BET surface area analyses and tested for their uptake of H<sub>2</sub>S.

#### **4.8 AGING STUDY OF Co/Zn 30/70**

A series of five precursors were made in which the nominal atomic ratio of the Co/Zn nitrate solution was 30/70. This ratio was chosen as a good representative loading for doped ZnO. The preparation method used was the same as described in *Section 4.1* except that the precipitated precursor was aged in the mother liquor for: 0, 15, 30, 60 or 180 minutes rather than the 30 minutes used in the standard method. For the precursor with aging time 0 minutes the coprecipitation reaction was carried out in a Buchner funnel so that the precipitate was filtered immediately.

The precursors were made into pellets by the method outlined in *Section 4.6* and calcined in flowing air at 350°C for 4 hours. The precursors and oxides were fully characterised using the techniques described previously. The oxides were tested for their sulphur absorption capacity.

#### **4.9 DIFFERENT METHODS OF PRECURSOR PREPARATION**

Precursors with a nominal Co/Zn ratio 30/70, were prepared at pH values of 7 and 8 using different carbonate sources.

##### **4.9.1 Precipitation at Low Supersaturation pH 8**

The precursor was prepared by coprecipitation of mixed metal nitrates and

ammonium carbonate by the standard method described in *Section 4.1* but a pH of 8 rather than 7 was used. However, after aging the precipitate in the mother liquor for 10 minutes the pH had risen to pH 8.33 and all the precipitate that had initially formed had been dissolved to leave a very dark purple solution. It is likely that  $\text{NH}_3$  had exchanged with  $\text{H}_2\text{O}$  in the coordination sphere of cobalt to form a  $[\text{Co}(\text{NH}_3)_x(\text{H}_2\text{O})_{6-x}]^{2+}$  species.

The experiment was repeated using sodium hydrogen carbonate,  $\text{NaHCO}_3$  (Rectapur), using the standard low supersaturation method described in *Section 4.1* at a constant pH of either 7 or 8. The pH was readily maintained at 7 and a good yield of precipitate was obtained. When pH 8 was used there was some difficulty in maintaining the high pH and a very poor yield was obtained. The experiment was repeated using  $\text{NaHCO}_3$  and  $\text{NaOH}$  in equal proportions at pH 8.

#### ***4.9.2 Precipitation at High Supersaturation***

This experiment was carried out, using either  $2 \text{ mol dm}^{-3}$  ammonium carbonate or sodium hydrogen carbonate. The carbonate and nitrate solutions were heated to *ca.*  $70^\circ\text{C}$  in each case. The carbonate solution was then added rapidly (*ca.*  $500 \text{ cm}^3 \text{ min}^{-1}$ ) with vigorous stirring to the  $1 \text{ mol dm}^{-3}$  nitrate solution until the pH was 7.5. The precipitate which formed was aged for 30 and 15 minutes for the ammonium and sodium carbonate solutions respectively, at which point the pH had risen to pH 7.8 and 8 respectively.

### 4.9.3 Titration Method

Sodium hydrogen carbonate was added dropwise, (*ca.* 50 ml min<sup>-1</sup>), via a burette to the mixed nitrate solution at 60°C. The pH rose initially from 2.44 to 4.81 then levelled off as more carbonate solution was added. It then rose rapidly to 8.5 at which point the addition of the carbonate solution was stopped and the precipitate was aged for 30 minutes. The pH fell to 8.08 during aging.

All the precursors and oxides prepared in this section were analyzed for sodium using a Corning Flame Photometer 410. The samples were prepared using an identical procedure to that used for atomic absorption analysis for zinc (see *Section 4.1*).

**CHAPTER 5**  
**TREATMENT OF RESULTS**

---

---

## 5.1 'BREAKTHROUGH' RIG DATA

The ability of each absorbent to remove H<sub>2</sub>S from the nitrogen feed is expressed as %Conversion or as %Reaction. The %Conversion (see Eqn. 5.1) was calculated from the grammes of H<sub>2</sub>S absorbed by the absorbent up to the point of 'breakthrough', divided by the weight of absorbent used. This value allowed absorbents run on the same testing rig to be compared.

$$\%Conversion = \frac{\text{wt. of } H_2S \text{ absorbed}}{\text{wt. of absorbent}} \times 100 \quad \text{Eqn. 5.1}$$

The %Reaction (see Eqn. 5.2) was calculated by dividing the number of moles of H<sub>2</sub>S absorbed by the total number of moles of cobalt and zinc present in the absorbent. The number of moles of metal present was calculated from atomic absorption data.

$$\%Reaction = \frac{\text{mols. of } H_2S \text{ absorbed}}{\text{mols. of Co + Zn present}} \times 100 \quad \text{Eqn. 5.2}$$

The number of moles of H<sub>2</sub>S absorbed was calculated by multiplying the measured flow rate, FR/cm<sup>3</sup> min<sup>-1</sup>, of the H<sub>2</sub>S by the 'breakthrough' time, t/mins. and then dividing this by a factor A (see Eqn. 5.3). This factor A is obtained by adjusting standard temperature and pressure to the temperature T/K, in the fume cupboard (Eqn. 5.4). It is applied since the experiment was conducted at 30°C rather than the standard temperature of 0°C.

$$\text{mols. of } H_2S = \frac{FR * t}{A} \quad \text{Eqn. 5.3}$$

$$A = \frac{22400T}{273} \quad \text{Eqn. 5.4}$$

## 5.2 XRD D-SPACINGS

The d-spacings of each sample were calculated from the  $2\theta$  values obtained from the diffractograms using Bragg's Law (see Eqn 2.1, *Section 2.1.2*). A short computer programme was written using SuperCalc® 4.1,<sup>70</sup> to calculate the d-spacings (see Appendix C).

## 5.3 MICROGRAPHS - PARTICLE SIZE

The average particle size was determined from the transmission electron micrographs by measuring a number of particles. A magnification of 100,000 (usually expressed as 100K) means 1 cm measured on the photograph is equivalent to 100 nm. Using Eqn. 5.5, the equivalent distance, d/nm, to 1cm measured, from the photograph, can be calculated for other magnifications.

$$d = \frac{0.01}{mag \times 1 \times 10^{-6}} \quad \text{Eqn. 5.5}$$

## 5.4 ATOMIC ABSORPTION

Metal loadings were determined for cobalt and zinc in the precursors and oxides as described in *Section 4.1*. Calibration curves were constructed using standards for each metal. This gave a linear response in the range of standards used i.e. Co 1-5 ppm and Zn 0.2-1 ppm.

A sample was then tested and the absorbance reading converted to the amount of metal present (expressed as  $\mu\text{g cm}^{-3}$ ), by comparison with the calibration curve. This value was converted to a percentage of metal present

in the sample by taking into account the dilution factors involved. The error was estimated to be  $\pm 2\%$ . This weight for weight percentage was then converted to number of moles present and an atomic ratio obtained by the Eqn. 5.6,

$$x = \frac{Co}{Co + Zn} \quad \text{Eqn. 5.6}$$

where  $x$  is the ratio of cobalt to zinc,  $Co_xZn_{1-x}$ . This allowed Co/Zn experimental ratios to be compared to the Co/Zn calculated ratios.

## 5.5 XPS ANALYSIS

Absolute binding energies are difficult to determine because of the problems of charge referencing (see *Section 2.3.5*). The determination of quantitative surface analysis is also very difficult, the problems being outlined by Briggs & Seah<sup>56</sup> Therefore, the aim of this work was not to obtain absolute values but rather identify any trends that were present.

### 5.5.1 Qualitative Analysis

Charge referencing can be a major problem in XPS studies of insulators. Charge referencing was carried out on the data collected before analysis by one of the several techniques discussed in *Section 2.3.5*.

The precursors were charge referenced by the internal standard method to the carbonate C 1s,  $E_b = 289.1$  eV. The O 1s peak associated with the carbonate group varies only from 531.0 - 531.2 eV which is within experimental error. It is this lack of variation that allows the carbonate to be

confidently used as it suggests that it is not affected to any great extent by the surrounding environment.

Adventitious carbon was not used to charge reference the oxides (cal 350°C, in *Section 6.2.2*) because the C 1s peak appeared outwith the parameters of the narrow energy scan selected for several of the samples due to large charge shifts. Charging was referenced to the O 1s peak at  $E_B = 530.0$  eV. It is appreciated by the author that the chemical environment within the series of oxides will vary and hence affect the true position of the O 1s peak. The O 1s peak was chosen for the sulphides to allow comparison between the two series.

As no problems with detection of adventitious C 1s peak were encountered for the oxides (cal. var. temp., *Section 6.2.3*) they were charge referenced to the adventitious C 1s,  $E_B = 285.0$  eV peak. The O 1s peak was not chosen due to the unknown variable nature of the oxygen species being detected.

### 5.5.2 Quantitative Analysis

The surface Co/Zn ratios were calculated using Eqn. 2.21 in *Section 2.3.6e*. The ratio of the photoionization cross-sections,  $\alpha_{Zn}/\alpha_{Co}$ , were taken from Schofield<sup>57</sup> and was found to be 1.499. The kinetic<sup>energy</sup> values for each element were calculated using Eqn. 2.15, *Section 2.3.1*, with the binding energy values of the atom obtained from Briggs & Seah.<sup>56</sup> The ratio was found to 0.729. The quantitative equation then simplifies to Eqn. 5.7.

$$\frac{n_{Co}}{n_{Zn}} = \frac{I_{Co}}{I_{Zn}} \times 1.499 \times 0.729 \quad \text{Eqn. 5.7}$$

A series of physically mixed ZnO/Co<sub>3</sub>O<sub>4</sub> samples were examined quantitatively. It was found that the cobalt ratio was underestimated in each case. It should be noted that using Al K<sub>α</sub> radiation produces interference in the Co2p<sub>3/2</sub> spectral region (at the lowest binding energies) by an Auger transition, which causes an absolute Co2p<sub>3/2</sub> integrated intensity to be overestimated by 15%.<sup>71</sup>

## **CHAPTER 6**

### **RESULTS**

---

---

## 6.1 COBALT-ZINC 1st SERIES

The precursors in this section were synthesized using the standard method outlined in *Section 4.1*. All the precursors, oxides or sulphided oxides were characterised using the range of techniques listed in *Section 4.2*. The phases present at each nominal loading were determined from analysis by XRD, TEM, thermal analysis, FTIR and UV-VIS-NIR diffuse reflectance spectroscopy. The results of these studies are detailed below for the precursors, oxides and sulphided oxides. Each sample is designated by its nominal atomic Co/Zn ratio unless stated otherwise.

### 6.1.1 Characterisation of the Hydroxycarbonate Precursors

The results from the atomic absorption analyses of the precursors and oxides are shown in Table 6.1. The Co/Zn atomic ratios were close to the nominal loadings used and there was good agreement, within experimental error, between the values obtained for the precursors and the oxides. The C,H,N analyses revealed that no nitrogen was present in the precursors.

The observed d-spacings obtained from XRD studies of the precursors are tabulated in Table 6.2 and a typical example of a diffractogram is shown in Fig. 6.1. The X-ray diffraction pattern for the Co/Zn 0/100 precursor showed exclusively the interplanar spacings characteristic of the mineral hydrozincite,  $\text{Zn}_5(\text{CO}_3)_2(\text{OH})_6$ .<sup>72</sup> The nominal Co/Zn loading of 10/90 also gave a similar XRD pattern to hydrozincite. No additional lines were observed in this pattern, indicating that a monophasic solid solution of cobalt-containing hydrozincite with a chemical formula of  $\text{Co}_x\text{Zn}_{5-x}(\text{CO}_3)_2(\text{OH})_6$  was present. The

**Table 6.1** Atomic absorption data for the precursors and oxides - 1st Series.

Code Nominal atomic loading	Precursor			Oxide		
	%Co (wt/wt)	%Zn (wt/wt)	Calc. Co/Zn atomic ratio	%Co (wt/wt)	%Zn (wt/wt)	Calc. Co/Zn atomic ratio
0/100		54.40			79.97	
10/90	5.55	51.78	10/90	6.79	63.36	11/89
20/80	10.41	39.13	23/77	18.66	59.26	26/74
30/70	13.83	35.93	30/70	21.69	53.39	31/69
40/60	19.06	28.89	42/58	29.13	40.36	44/56
50/50	17.11	25.08	43/57	31.69	40.67	46/54
70/30	33.73	12.05	75/25	43.80	16.42	75/25
90/10	39.24	5.89	88/12	64.74	7.16	91/9
100/0	58.93			69.46		

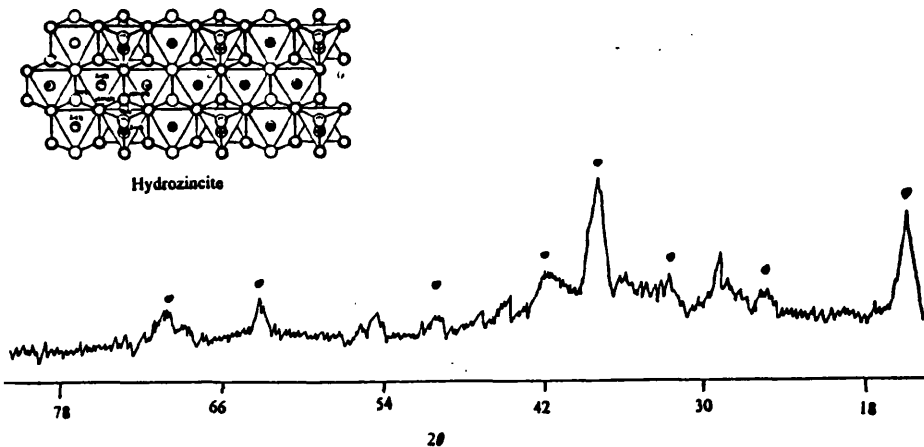


**Fig. 6.1** Typical example of the XRD pattern obtained for an hydroxycarbonate precursor. The example shown is the Co/Zn 40/60 loading. The dots (•) highlight the peaks present for hydrozincite.

**Table 6.2 D-spacings obtained by XRD for precursors - 1st Series. The intensities are shown in parentheses.**

Hz	Sph	Porta	0/100	10/90	20/80	30/70	40/60	50/50	70/30	90/10	100/0
6.77(100)			6.77(100)	6.77(100)	6.81(60)	6.77(100)	6.86(100)				
3.99(20)		5.06(70)	4.01(17)	4.02(20)	3.98(21)	4.04(28)	4.01(26)	3.96(20)		4.80(16)	5.08(84)
3.66(40)		4.44(5)	3.70(15)	3.70(17)	3.67(12)	3.67(12)				4.45(16)	4.49(40)
	3.55(40)				3.56(39)	3.53(19)	3.58(51)	3.56(45)	3.55(43)		3.42(44)
3.14(50)		3.33(40)	3.16(40)	3.17(43)	3.15(30)	3.17(38)	3.17(65)	3.09(32)		3.10(14)	
2.92(20)		2.94(30)	2.94(10)	2.96(12)							2.91(42)
2.85(30)			2.87(22)	2.87(31)	2.87(16)	2.87(22)					2.64(100)
	2.74(100)				2.73(100)		2.75(100)	2.76(100)	2.74(100)		
2.72(60)			2.72(61)	2.72(74)		2.72(75)					
2.69(20)			2.67(7)	2.68(31)							
2.58(10)		2.65(100)	2.57(12)	2.58(20)	2.56(18)						
2.48(70)		2.53(70)	2.49(40)	2.49(41)		2.50(42)	2.50(42)				2.53(65)
2.30(20)			2.31(9)	2.32(20)	2.33(22)	2.32(23)	2.35(26)	2.33(20)	2.33(23)	2.33(18)	
2.21(10)	2.33(20)	2.30(70)	2.21(8)	2.20(12)						2.29(25)	2.28(81)
2.09(5)			2.09(12)		2.10(27)	2.10(15)	2.12(16)	2.13(20)	2.12(29)	2.12(20)	
	1.95(20)				1.94(24)		1.95(26)	1.95(19)	1.93(17)	1.95(29)	
1.92(30)		1.92(40)	1.91(15)	1.92(17)							1.91(42)
	1.78(10)						1.77(11)	1.78(10)			
	1.70(30)					1.70(23)	1.71(40)	1.71(40)	1.71(40)	1.71(40)	1.70(33)
1.69(40)		1.69(10)	1.69(12)								

Hz - Hydrozincite  $Zn_5(CO_3)_2(OH)_6^{72}$ ; Sph - Spherochalcite  $CoCO_3^{73}$ ; Porta -  $Co(CO_{3.0.5}(OH)_{0.0.1}H_2O^{45}$

precursors with Co/Zn ratios 20/80, 30/70, 40/60 and 50/50 each gave XRD patterns which exhibited lines which corresponded to a hydrozincite-like phase in addition to lines which corresponded to the JCPDS pattern of spherocobaltite,  $\text{CoCO}_3$ .<sup>73</sup> At cobalt loadings greater than 50% the XRD patterns indicated that the precursors were monophasic. The patterns for 70/30 and 90/10 matched that of spherocobaltite, indicating that all the zinc was either present in an amorphous phase or, more likely, in solid solution with the cobalt in the spherocobaltite-like phase, having the general formula  $\text{Co}_{1-x}\text{Zn}_x\text{CO}_3$ . The 100/0 precursor matched the diffraction pattern detailed by Porta *et al.*<sup>45</sup> for the cobalt compound they synthesized by a similar method. The chemical formula determined by Porta *et al.* was  $\text{Co}(\text{CO}_3)_{0.5}(\text{OH})_{1.0}\cdot 0.1\text{H}_2\text{O}$ . The 90/10 sample also had peaks present which suggested that a small amount of a Porta-like hydroxycarbonate phase was present. The phases detected are summarised in Table 6.3.

**Table 6.3** Summary of phases detected by XRD for precursors and oxides.

Co/Zn	Precursor
0/100	Hydrozincite
10/90	Hydrozincite
20/80	Hydrozincite(major)+Spherocobaltite(minor)
30/70	Hydrozincite(major)+Spherocobaltite(minor)
40/60	Hydrozincite+Spherocobaltite
50/50	Hydrozincite(minor)+Spherocobaltite(major)
70/30	Spherocobaltite
90/10	Spherocobaltite(major)+Porta(trace)
100/0	Porta

The TGA data obtained for all the precursors is tabulated in Table 6.4. For the Co/Zn 0/100 and 10/90 samples a single-step decomposition with a weight loss of *ca.* 26% was obtained. This corresponded well with the theoretical loss of water and carbon dioxide for the decomposition of hydrozincite to zinc oxide (26.0%). This was evidence for the presence of a single hydrozincite-like phase. The presence of the cobalt caused the temperature of decomposition, calculated from the maximum in the differential of the decomposition curve, to increase from 272°C for hydrozincite to 295°C for the 10/90 sample. A two-stage decomposition pattern was observed for the 30/70, whilst a three-stage decomposition was observed for the 20/80 and 40/60 systems. The first two stages corresponded to the decomposition of mixed Co/Zn hydroxycarbonate compounds to the oxides ZnO and Co<sub>3</sub>O<sub>4</sub>. The third decomposition centred around *ca.* 930°C is believed to be due to the decomposition of Co<sub>3</sub>O<sub>4</sub> to CoO.<sup>74</sup> A very large exothermic transition was

**Table 6.4** Thermogravimetric Analysis for precursors - 1st Series.

Co/Zn	Temperature (°C)				%loss			
	Surface H <sub>2</sub> O	Loss of structural H <sub>2</sub> O and CO <sub>2</sub>		Co <sub>3</sub> O <sub>4</sub> →CoO	150°C	↑H <sub>2</sub> O+ ↑CO <sub>2</sub>	Residue	Co <sub>3</sub> O <sub>4</sub> →CoO
0/100		272			2.0	23.5	2.5	
10/90		295				23.7	1.2	
20/80		302	327(sh)	927	2.5	23.5	2.5	2.0
30/70	70	302		927	8.0	20.5	3.0	2.0
40/60	65	272	310(sh)	940	5.5	24.0	3.0	3.5
50/50		250	285(sh)	960	5.0	33.5	2.2	2.7
70/30		262		925	3.0	23.5	1.7	5.2
90/10	70	255		945	14.0	24.0	2.0	4.5
100/0		255		955		25.5	3.2	5.0

observed on decomposition of the 50/50 hydroxycarbonate precursor. Indeed, it was so large that it disturbed the temperature control in the furnace. The exotherm was centred around 250°C with a shoulder at 285°C. The weight loss of 33.5% observed for the 50/50 sample corresponded well to the theoretical weight loss for the decomposition of  $\text{CoCO}_3$  to  $\text{Co}_3\text{O}_4$  (32.5%). The 70/30, 90/10 and 100/0 precursors all underwent a two-stage weight loss at *ca.* 255°C and at *ca.* 940°C. This was again the initial loss of water and carbon dioxide followed by the decomposition of  $\text{Co}_3\text{O}_4$ . The overall weight loss of *ca.* 25% for Co/Zn 100/0 is in agreement with the expected value for the thermal decomposition of the Porta *et al.* compound to  $\text{Co}_3\text{O}_4$  (25.6%). With the exception of the 50/50 sample, the temperature at which the initial weight loss occurred increased with increasing cobalt content up to the 30/70 loading and then slowly decreased with further increase in the cobalt loading. This suggests that the thermal stability was increased by the synergic effect of the cobalt and zinc together.

A typical UV-VIS-NIR diffuse reflectance spectra of the precursors is shown in Fig 6.2 with the data tabulated in Table 6.5. With the exception of the 0/100 precursor, the spectra showed the presence of a band centred at 520 nm and a second broad band with its centre at *ca.* 1300 nm which had a shoulder at 1382 nm. These bands were typical of a  $\text{Co}^{2+}$  ion ( $3d^7$  electronic configuration) in octahedral symmetry.<sup>45,80</sup> The band at 520 nm was assigned to the transition  ${}^4T_{1g}(\text{F}) \rightarrow {}^4T_{1g}(\text{P})$ , whilst the band at *ca.* 1300 nm was assigned to the  ${}^4T_{1g} \rightarrow {}^4T_{2g}$  transition. The position of the centre of this broad band

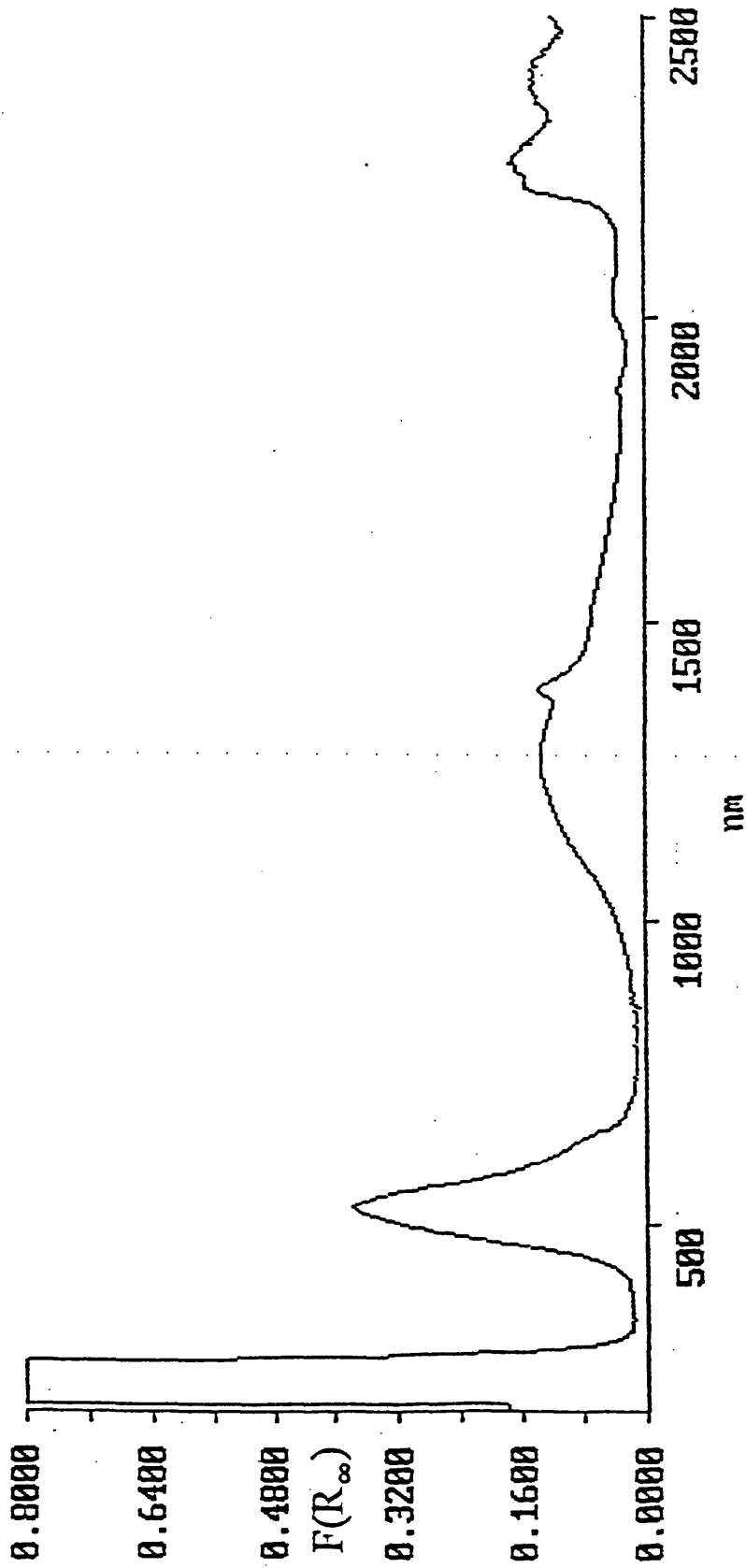


Fig. 6.2 Typical example of a UV-VIS-NIR Diffuse Reflectance spectra of  $\text{Co}^{2+}$  in an octahedral environment. The example shown is for the Co/Zn 30/70 precursor.

**Table 6.5** Summary of the DRS data obtained for the  $\text{Co}^{2+}_{\text{oct}}$  transitions for the precursors - 1st Series.

	${}^4T_{1g}(F) \rightarrow {}^4T_{1g}(P)$	${}^4T_{1g} \rightarrow {}^4T_{2g}$		Other Bands		
0/100				2022	2290	2407
10/10	508	1219	1376		2290	2401
20/80	520,613(sh)	1265	1382			
30/70	520,613(sh)	1242	1382	1929		2302
40/60	514,613(sh)	1265	1382	1923	2017	2267
50/50	520	1312	1382		2022	2209
70/30	520	1315	1382		2022	2220
90/10	520	1317	1382	1923		2220
100/0	520,578(sh)	1300	1382		2226	2395

increased as the cobalt percentage increased. The band at *ca.* 2000 nm was associated with a water overtone.

The FTIR spectra for all of the precursors (Fig. 6.3) exhibited the characteristic vibrational modes of the carbonate group at 1509, 1385, 1045 and 835  $\text{cm}^{-1}$ .<sup>42</sup> The stretching and bending modes of  $\text{H}_2\text{O}$  were observed at 3400 and 1630  $\text{cm}^{-1}$ . Bands specific to hydrozincite and spherocobaltite were observed for Co/Zn 100/0 and 0/100 in the ‘fingerprint’ region (400-1100 $\text{cm}^{-1}$ ), respectively.<sup>75</sup> For the intermediate loadings a strong sharp band appeared at 840  $\text{cm}^{-1}$  and became more intense with further increase in cobalt loading. This band was also present in  $\text{CoCO}_3$  but was broad and of low intensity.

The transmission electron micrographs of selected precursors are shown in Fig. 6.4. The electron diffraction patterns (e.d.p.) were in accordance with the powder diffraction data. The micrograph of the Co/Zn 0/100 sample indicated the presence of fused ‘needle-like’ crystals of monoclinic hydrozincite. The micrograph for the Co/Zn 100/0 sample revealed the

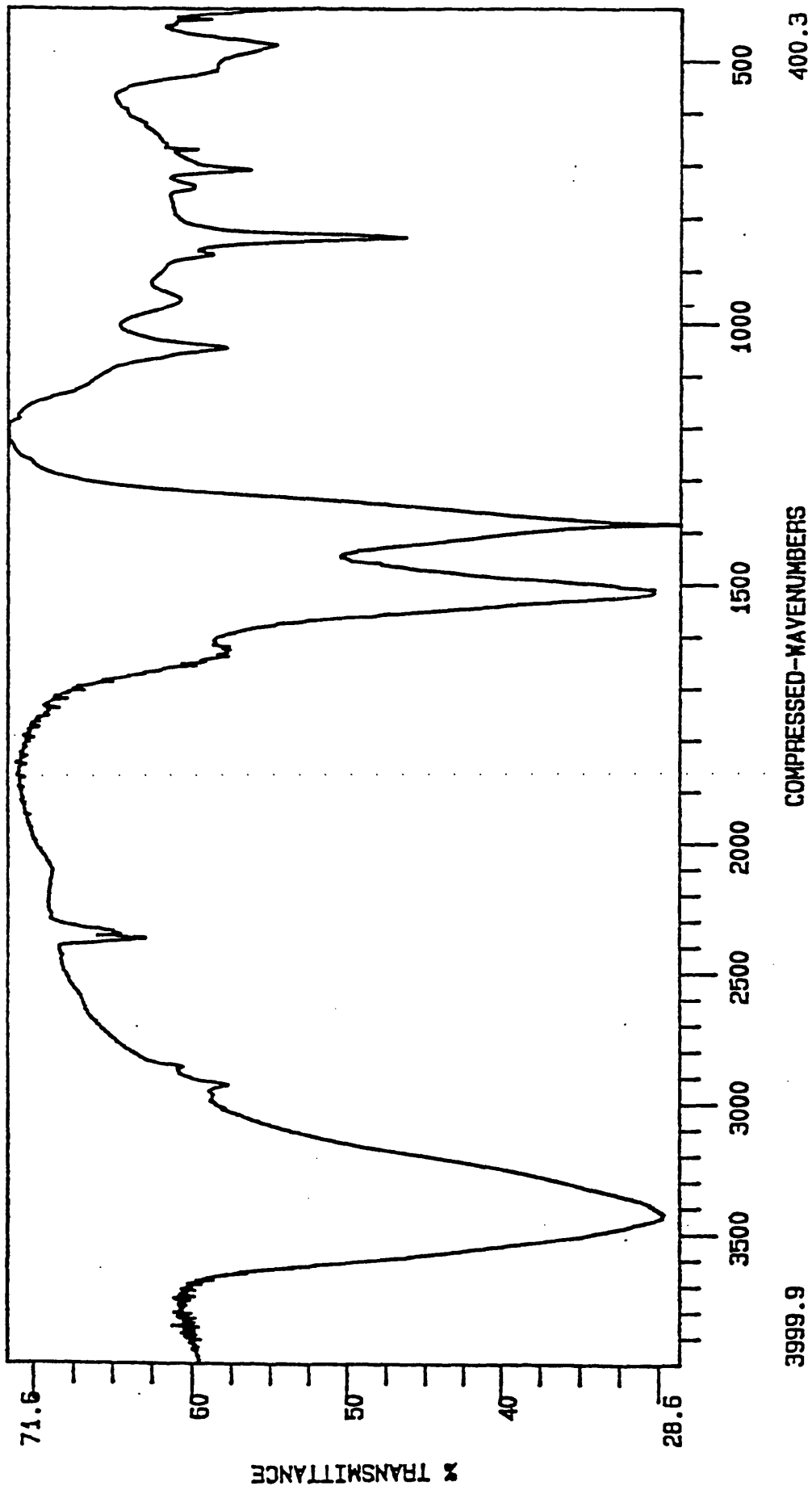
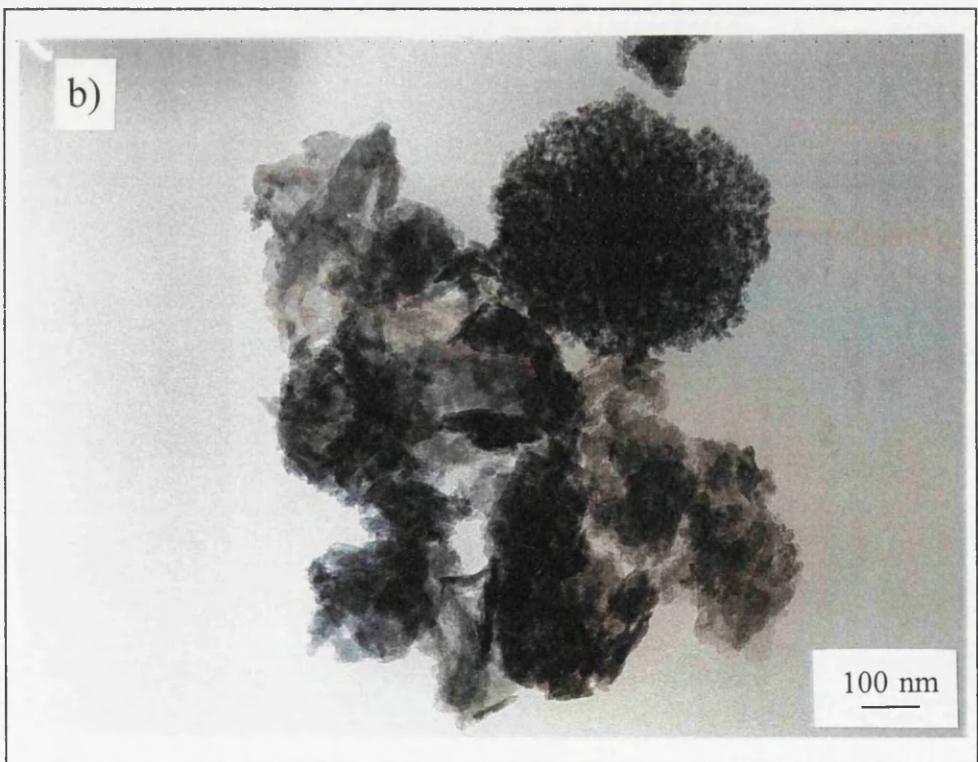
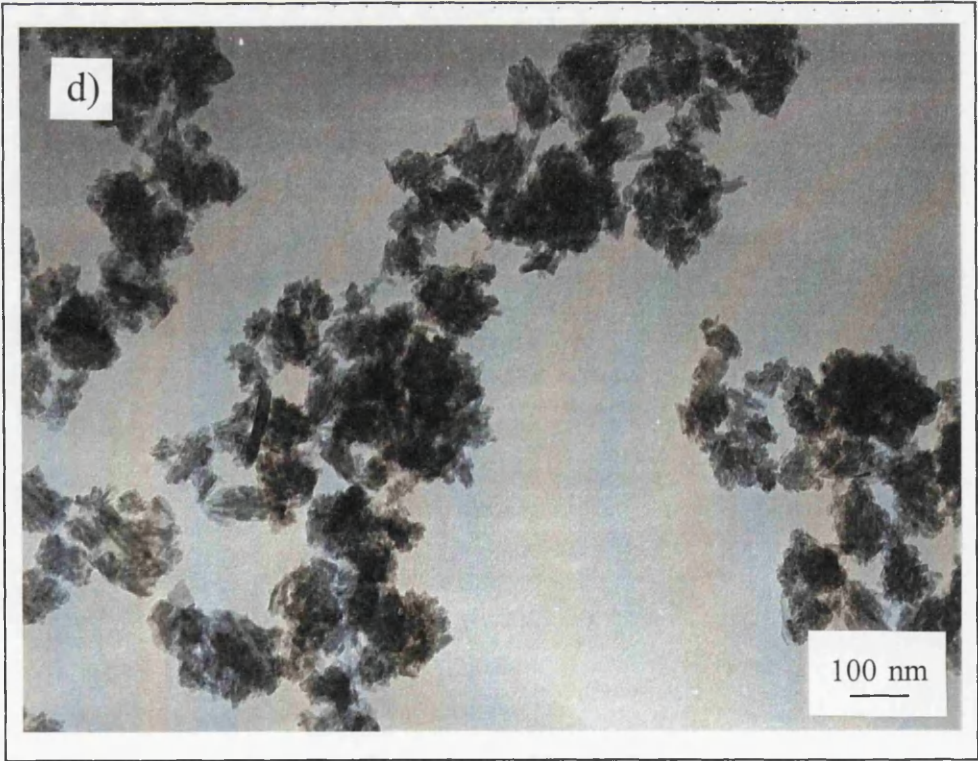
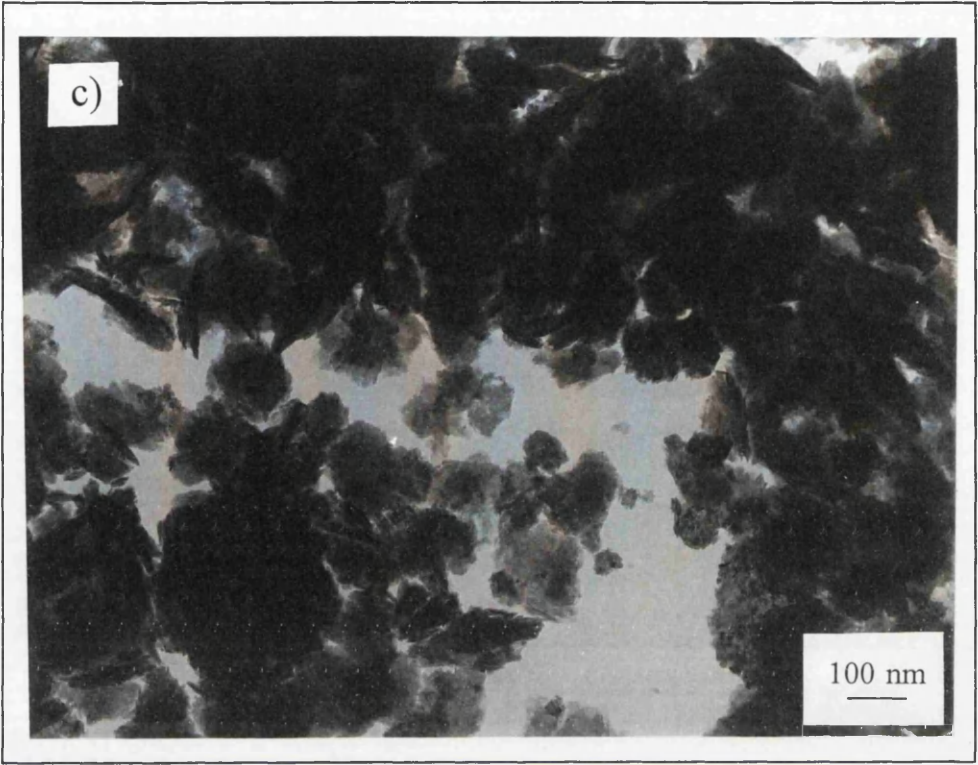


Fig. 6.3 Typical example of FTIR spectra of a precursor. The example shown is that of the nominal Co/Zn ratio 30/70.



**Fig. 6.4** Transmission electron micrographs of the hydroxycarbonate precursor phases of Co/Zn a) 0/100, b) 20/80, c) 40/60, d) 100/0.



presence of smaller clusters which were comprised of smaller ‘finger-like’ crystals. The electron diffraction pattern for the 100/0 sample corresponded to the structure outlined by Porta *et al.*<sup>45</sup> The micrographs for the mixed Co/Zn precursors in which two types of phase were identified by e.d.p. also indicated that two types of phase were present. The two types of crystals seen for the 40/60 sample were very disordered, whilst the micrograph for the 20/80 sample revealed the presence of a cluster of hydrozincite-like crystals with a separate ‘sponge-like’ crystal beside it. The 20/80 micrograph contained crystals resembling those found for both the 100/0 and 50/50 loadings. The 50/50 sample had very large well-defined pseudo-hexagonal crystals of spherocobaltite.

### 6.1.2 Characterisation of the Oxides

The hydroxycarbonate precursors were decomposed by thermal treatment at 350°C for 16 hours in air. The d-spacings obtained by powder X-ray diffraction are tabulated in Table 6.6. The XRD patterns for all the samples showed the presence of broad, well defined peaks (see Fig. 6.5). This suggested that crystalline oxides of small average particle size were formed.

The XRD patterns for Co/Zn 0/100 and 100/0 were similar to the JCPDS patterns for ZnO<sup>76</sup> and Co<sub>3</sub>O<sub>4</sub><sup>77</sup> respectively. The 10/90 loading gave a pattern which corresponded to that of ZnO. It is likely that a monophasic cobalt-containing solid-solution of zinc oxide was formed since no extra peaks were found, although the presence of some amorphous material cannot be entirely discounted. The 70/30 and 90/10 oxides gave a monophasic pattern

**Table 6.6** D-spacing obtained by XRD for the oxides -1st Series. The intensities are shown in parentheses.

Zn <sup>76</sup>	Co <sub>3</sub> O <sub>4</sub> <sup>77</sup>	ZnCo <sub>2</sub> O <sub>4</sub> <sup>78</sup>	0/100	10/90	20/80	30/70	40/60	50/50	70/30	90/10	100/0
	4.67(20)	4.68(10)			4.69(9)	4.73(7)	4.69(11)	4.69(11)	4.65(15)	4.69(22)	4.65(32)
	2.86(40)	2.86(35)					2.88(32)	2.88(31)	2.86(39)	2.86(39)	2.86(43)
2.81(57)			2.81(85)	2.81(65)	2.81(58)	2.82(51)	2.81(36)				
2.60(44)			2.60(78)	2.60(49)	2.60(37)	2.60(34)	2.59(17)	2.60(9)			
2.48(100)			2.47(100)	2.47(100)	2.47(100)	2.47(100)	2.47(100)	2.46(100)			
	2.44(100)	2.44(100)							2.44(100)	2.44(100)	2.43(100)
	2.33(12)	2.34(9)					2.35(12)	2.35(10)	2.34(10)	2.32(12)	2.33(11)
	2.02(25)	2.02(18)			2.03(9)	2.04(11)	2.04(14)	2.03(15)	2.02(18)	2.02(22)	2.02(29)
1.91(23)			1.91(18)	1.91(19)	1.91(12)	1.91(13)	1.91(10)				
	1.65(12)	1.65(12)					1.66(7)	1.66(8)	1.65(12)	1.65(7)	1.65(9)
1.62(32)			1.62(39)	1.62(29)	1.62(22)	1.62(21)	1.62(11)	1.62(6)			
	1.56(35)	1.56(35)			1.56(10)	1.56(14)	1.57(16)	1.57(50)	1.56(29)	1.56(28)	1.55(33)
1.48(29)			1.48(29)	1.48(20)	1.47(14)	1.48(13)		1.48(4)			
	1.43(45)	1.43(35)				1.43(14)	1.43(35)	1.44(25)	1.43(16)	1.43(31)	

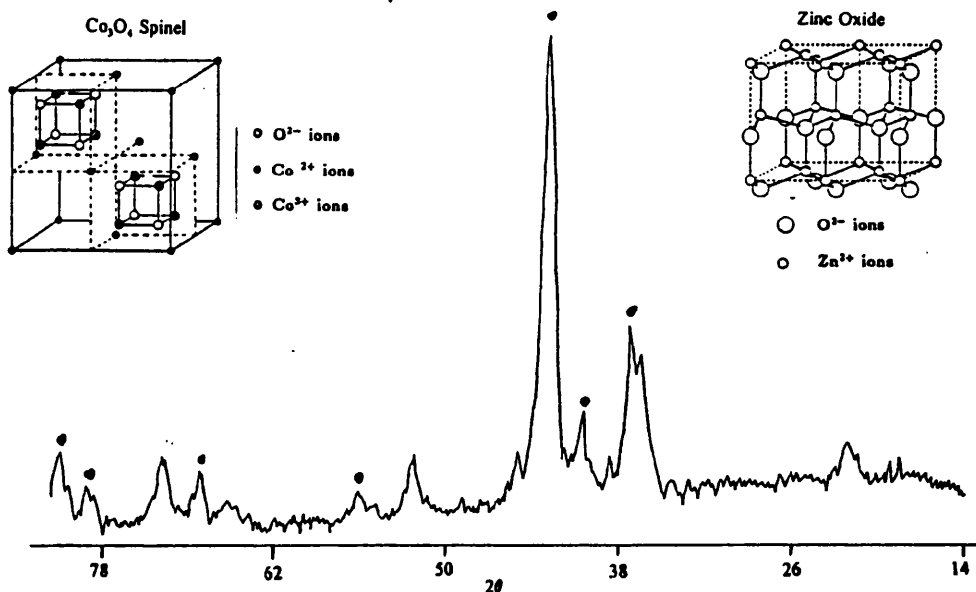


**Fig. 6.5** Typical example of XRD of the oxides. The sample shown is the Co/Zn 40/60 loading. The dots (•) highlight the lines of ZnO whilst the remaining peaks can be assigned to a 'cobalt oxide type' phase.

corresponding to a cobalt oxide phase, indicating that all the zinc was probably in the form of a solid-solution in the cobalt oxide. Biphasic oxides are obtained for nominal loadings 20/80, 30/70, 40/60 and 50/50. All the samples contain zinc oxide and a further phase. The diffraction pattern of the second phase indicated the presence of a 'cobalt oxide type' phase such as cobalt oxide  $\text{Co}_3\text{O}_4$ , or the zinc cobalt oxide spinel,  $\text{ZnCo}_2\text{O}_4$ <sup>78</sup>. However, the diffraction pattern showed consistent differences in position from the literature values preventing a positive identification of the phase. For this reason  $\text{Co}_3\text{O}_4$  will be given as the literature comparison here and in subsequent sections. The position of a number of peaks of the 'cobalt oxide type' phase were measured and compared to the literature values of  $\text{Co}_3\text{O}_4$  (see Table 6.7). Only peaks which had no interference from ZnO were selected. The peaks for the 'cobalt oxide type' phase occurred at lower values of  $2\theta$  than the reference phase in each sample. The shifts in position of the d-spacings suggested that the lattice of the 'cobalt oxide type' phase had expanded. This expansion suggests that  $\text{Zn}^{2+}$  ions

**Table 6.7** Variations of d-spacings of cobalt oxide type phase.

Nominal Co/Zn	<sup>†</sup> Position of nominal $2\theta=52.578^\circ$	d-spacing ( $\text{\AA}$ ) $d=2.021\text{\AA}$	Position of nominal $2\theta=70.240^\circ$	d-spacing ( $\text{\AA}$ ) $d=1.556\text{\AA}$
20/80	52.40	2.027	70.00	1.561
30/70	52.10	2.038	69.80	1.564
40/60	52.10	2.038	69.60	1.578
50/50	52.20	2.035	69.80	1.564

<sup>†</sup>The reference phase used to give the nominal peak positions was  $\text{Co}_3\text{O}_4$ .<sup>77</sup> The peaks at  $2\theta=52.578^\circ$  and at  $70.240^\circ$  are the (400) and (511) reflections respectively. These peaks were selected as there is no interference from zinc oxide.

were dissolved in the ‘cobalt oxide type’ phase. The zinc oxide phase matched the reference pattern very well and was used as an internal standard, confirming that the shift in position of the ‘cobalt oxide type’ phase was a real effect and not a function of the sample preparation. It seems most likely that the phase present was  $\text{Zn}_x\text{Co}_{3-x}\text{O}_4$  ( $x \leq 1$ ). The phases detected are summarised in Table 6.8.

A qualitative measure of the relative proportions of the phases in each sample was obtained from the peak intensities, given in parentheses in Table 6.6. The intensities of the  $\text{Co}_3\text{O}_4$  peaks at  $d=2.02\text{\AA}$  and  $d=1.56\text{\AA}$  were selected as they do not overlap with the ZnO peaks. The intensities were found to increase as the percentage cobalt increased. This suggested that the relative amounts of the ‘cobalt oxide type’ phase increased with increase in cobalt loading. The results are summarised in Table 6.8. The amount of ‘cobalt oxide type’ phase for the biphasic loadings is indicated on a scale of 1 to 4 with 1 indicating that is a minor phase and 4 indicating that it is a major phase.

With the exception of the 10/90 sample, the electron diffraction patterns obtained by TEM again confirmed the presence of the phases detected by XRD. Electron diffraction is more sensitive than X-ray diffraction and it is for that reason that the 10/90 sample showed that although ZnO was the

**Table 6.8** Summary of phase determined by XRD and average particle size from TEM data - 1st Series.

Nominal Co/Zn	Phases Present	Particle Sizes (nm)
0/100	ZnO	40-80
10/90	ZnO	20-50
20/80	ZnO(major)+Co <sub>3</sub> O <sub>4</sub> (minor,1)	10-20
30/70	ZnO(major)+Co <sub>3</sub> O <sub>4</sub> (minor,2)	---
40/60	ZnO(minor)+Co <sub>3</sub> O <sub>4</sub> (major,3)	10-20
50/50	ZnO(minor)+Co <sub>3</sub> O <sub>4</sub> (major,4)	5-15
70/30	Co <sub>3</sub> O <sub>4</sub>	---
90/10	Co <sub>3</sub> O <sub>4</sub>	---
100/0	Co <sub>3</sub> O <sub>4</sub>	10-20

predominant phase there were also some very weak rings corresponding to a 'cobalt oxide type' phase present. The average particle size was measured as described in *Section 5.3*. The results are shown in Table 6.8. Micrographs of selected oxides are shown in Fig. 6.6. The 0/100 sample consisted of quite large, 40-80 nm, fused pseudo-hexagonal crystals. The crystal size decreased to 10-20 nm and the crystals became less fused on increasing cobalt concentration to 20/80. The micrographs for the Co/Zn 40/60 and 50/50 samples showed large conglomerates, 40-80 nm, of very small crystals, 5-10

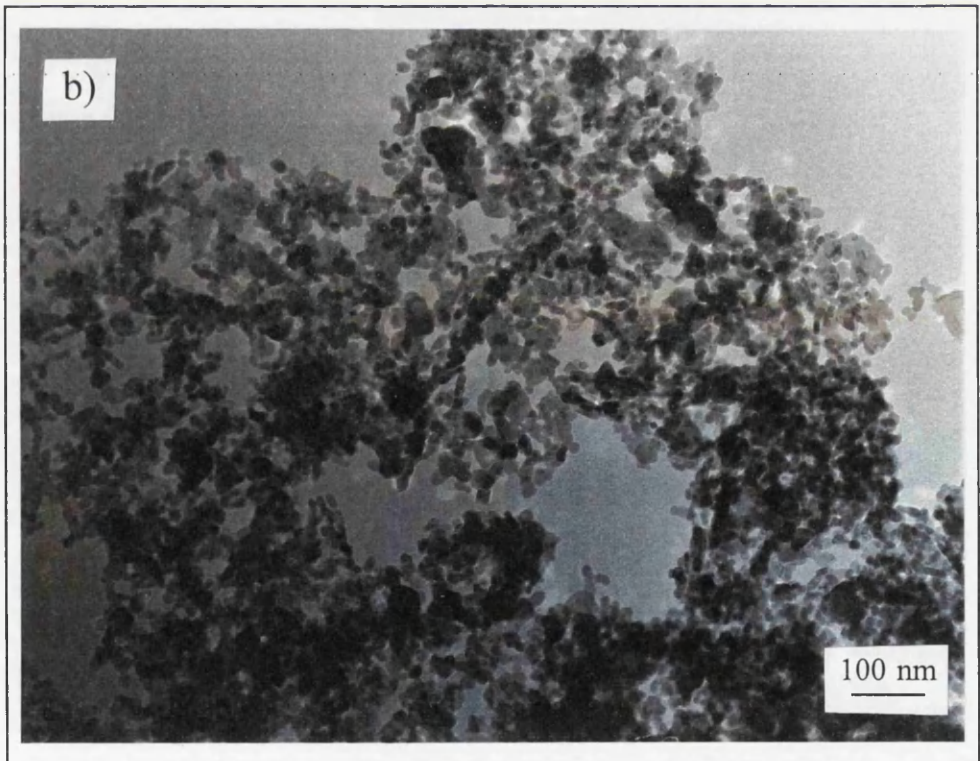
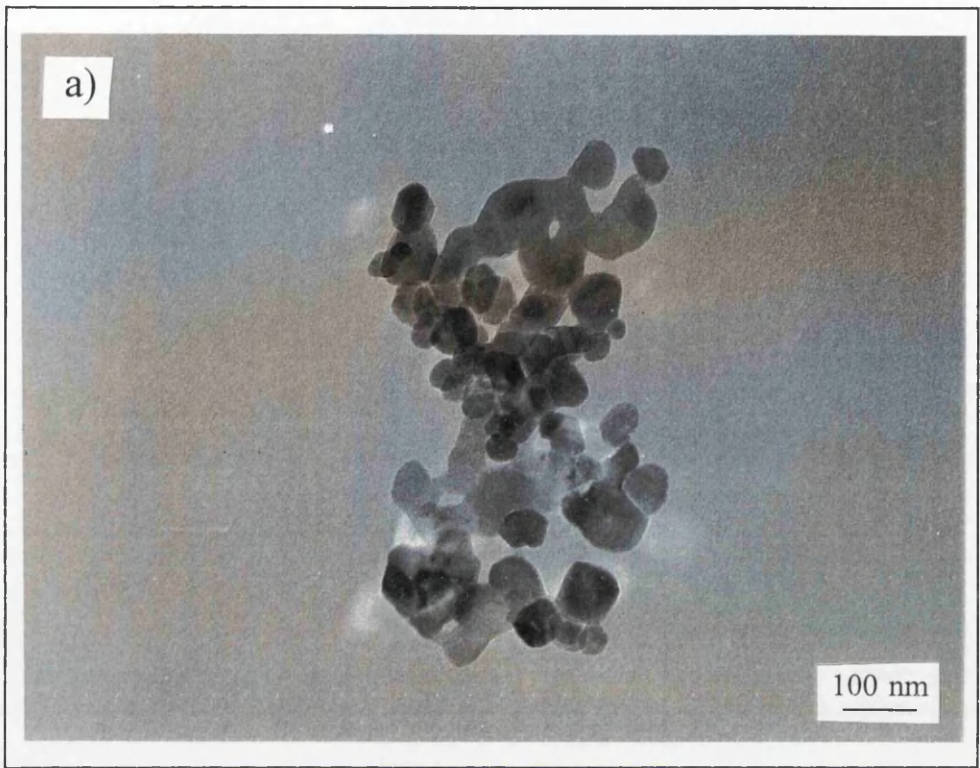
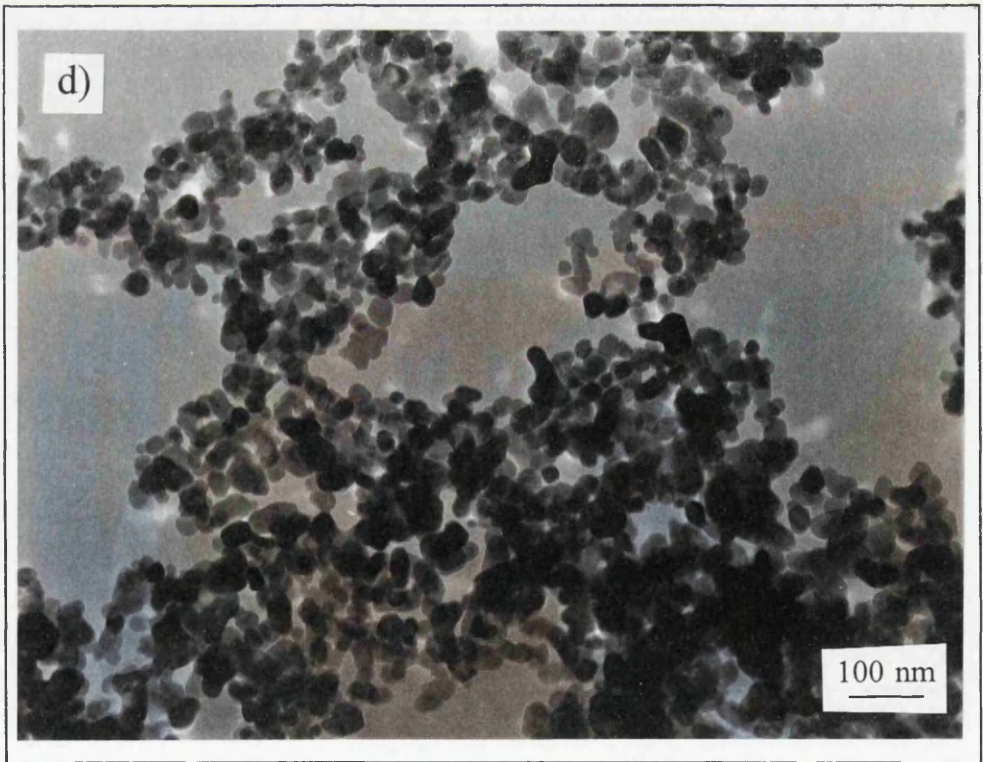
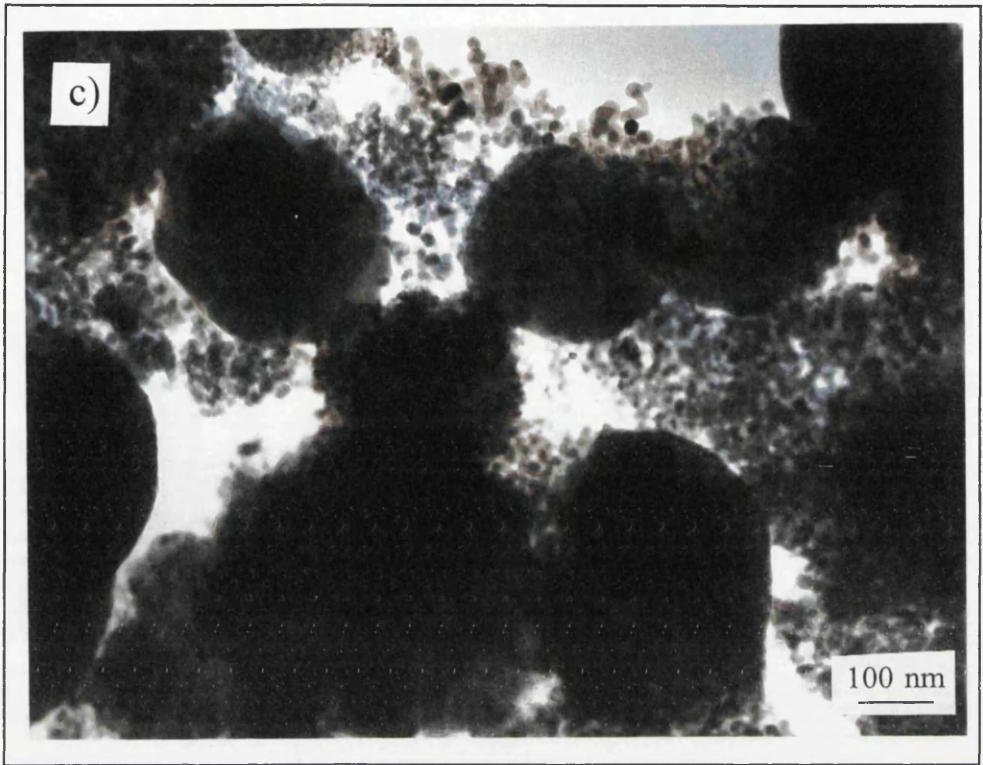


**Fig. 6.6** Transmission electron micrographs of the oxide phases of Co/Zn a) 0/100, b) 20/80, c) 50/50, d) 100/0.



nm. The 100/0 sample was also comprised of very small crystals, 10-20 nm, but showed the largest separation of the particles.

The oxides were investigated using UV-VIS-NIR diffuse reflectance spectroscopy. The peak positions are given in Table 6.9. Spectra of selected oxides are shown in Fig. 6.7. The 0/100 sample showed only the ZnO absorption edge at *ca.* 400 nm<sup>42</sup> and bands at 1387, 1888 and 2220 nm which were assigned to water overtones. Above a cobalt loading of 10% all the oxides were black. This was due to charge transfer between the Co<sup>2+</sup> and Co<sup>3+</sup> ions resulting in absorption extending across the whole of the visible spectrum. The 100/0 loading gave two peaks at 356 and 729 nm and a broad peak centred at *ca.* 1300 nm which consisted of three components at 1329, 1382 and 1521 nm. The first two peaks were assigned to the transitions <sup>1</sup>A<sub>1g</sub>→<sup>1</sup>T<sub>2g</sub> and <sup>1</sup>A<sub>1g</sub>→<sup>1</sup>T<sub>1g</sub> respectively of a Co<sup>3+</sup> ion in octahedral symmetry.<sup>79</sup> The broad peak centred at *ca.* 1300 nm, was assigned to the transition <sup>4</sup>A<sub>2</sub>(F)→<sup>4</sup>T<sub>1g</sub>(F) of Co<sup>2+</sup> ion in tetrahedral symmetry.<sup>42</sup> These transitions would be expected for the

**Table 6.9** Summary of the DRS data obtained for the oxides.

	ZnO Absorption Edge	Co <sup>3+</sup> <sub>oct</sub> (nm)	Co <sup>2+</sup> <sub>tet</sub> (nm)		Other Bands (nm)		
0/100	415		1387		1888	2220	
10/90	333, 368(sh)	647	1323	1382	2232		
20/80	333, 440(sh)		1382		1882	2220	
30/70	333, 440(sh)		1382		1882	2220	
40/60	333, 440(sh)		1312	1382	1882	2220	
50/50		444 753	1335	1382	2220		
70/30							
90/10		444 718	1335	1382	1521	1894	2220
100/0		356 729	1329	1382	1521	1900	2220

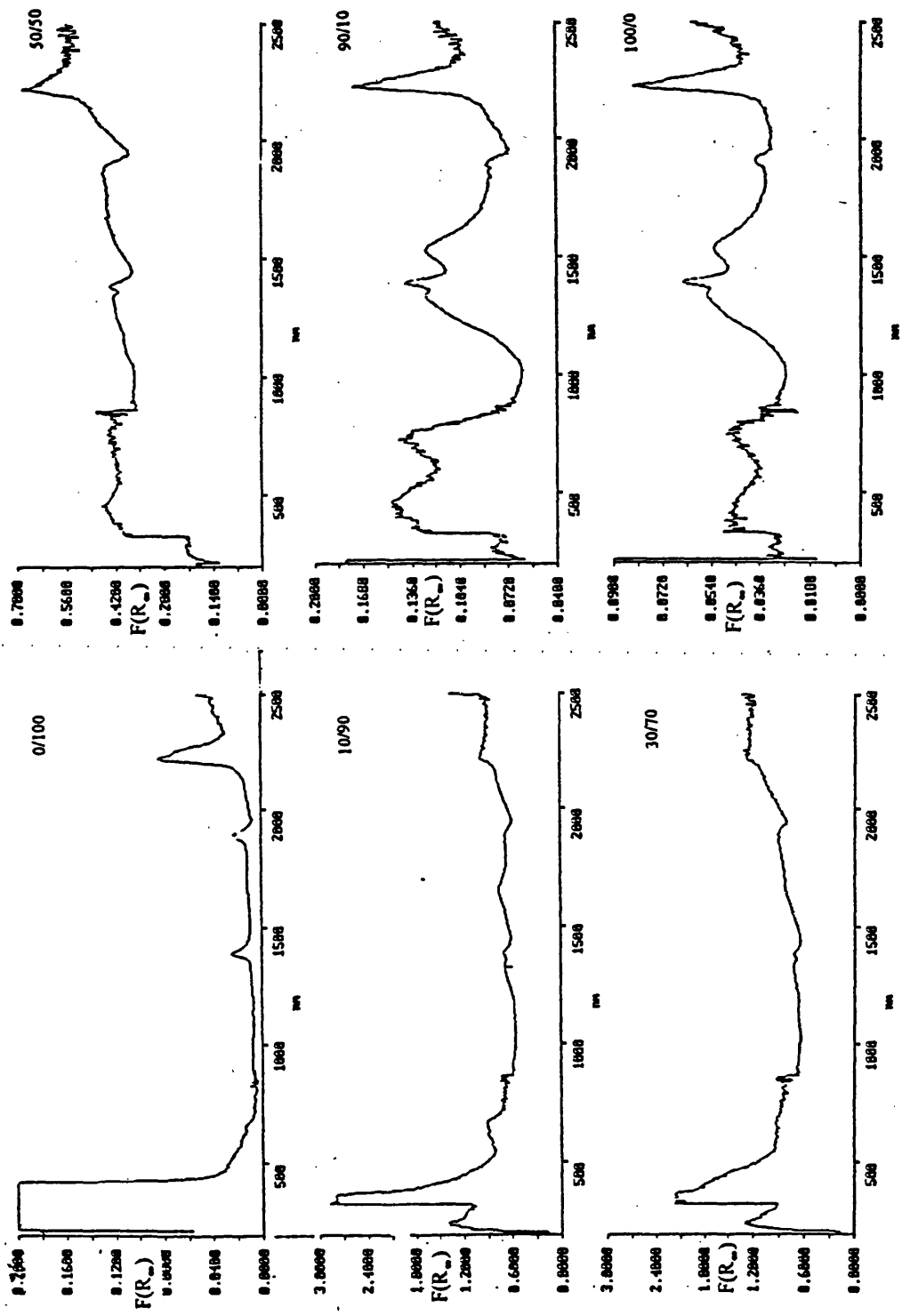


Fig. 6.7 Selected UV-VIS-NIR DRS spectra of the oxides.

normal spinel  $\text{Co}_3\text{O}_4$ , which has  $\text{Co}^{2+}$  tetrahedrally coordinated and  $\text{Co}^{3+}$  octahedrally coordinated. The intensities of the  $\text{Co}^{3+}_{\text{oct}}$  transitions might be expected to be twice as large as those of the  $\text{Co}^{2+}_{\text{tet}}$  transition as there are twice as many. However this is not the case as the d-d transition is only possible for an ion in octahedral symmetry due to vibronic vibrations removing the centre of symmetry. As the cobalt loading was decreased the  $\text{Co}^{3+}_{\text{oct}}$  bands disappeared leaving only a small contribution from  $\text{Co}^{2+}_{\text{tet}}$  transitions.

The FTIR showed that water was present at *ca.*  $3400\text{ cm}^{-1}$  and *ca.*  $1625\text{ cm}^{-1}$  for all the oxides. Also the band at *ca.*  $1510\text{ cm}^{-1}$  suggested that some residual carbonate was present. The Co/Zn 0/100 sample had an intense, broad peak at  $550\text{ cm}^{-1}$ . As the cobalt loading increased this band decreased and two sharp bands at *ca.*  $588$  and  $575\text{ cm}^{-1}$  appeared. These bands are indicative of  $\text{Co}_3\text{O}_4$ .<sup>75</sup>

Surface areas determined by the  $\text{N}_2$  B.E.T. method are listed in Table 6.10. The monophasic oxide with a Co/Zn ratio of 10/90 had an area of *ca.*  $45\text{ m}^2\text{g}^{-1}$ . As the cobalt content was increased the surface area increased to *ca.*  $67\text{ m}^2\text{g}^{-1}$  for the biphasic solids with a Co/Zn ratio of 20/80, 30/70 and 40/60. However, as the cobalt loading was increased further the surface area dropped to *ca.*  $57\text{ m}^2\text{g}^{-1}$  for the 50/50 and 70/30 samples whilst it increased again to *ca.*  $85\text{ m}^2\text{g}^{-1}$  for the 90/10 and 100/0 loadings.

**Table 6.10** Summary of BET Surface Area Data for Oxides.

Co/Zn	0/100	10/90	20/80	30/70	40/60	50/50	70/30	90/10	100/0
S.A. $\text{m}^2\text{g}^{-1}$	38.8	45.1	64.9	68.2	66.4	59.7	56.5	82.9	87.1

### 6.1.3 Sulphided Oxides

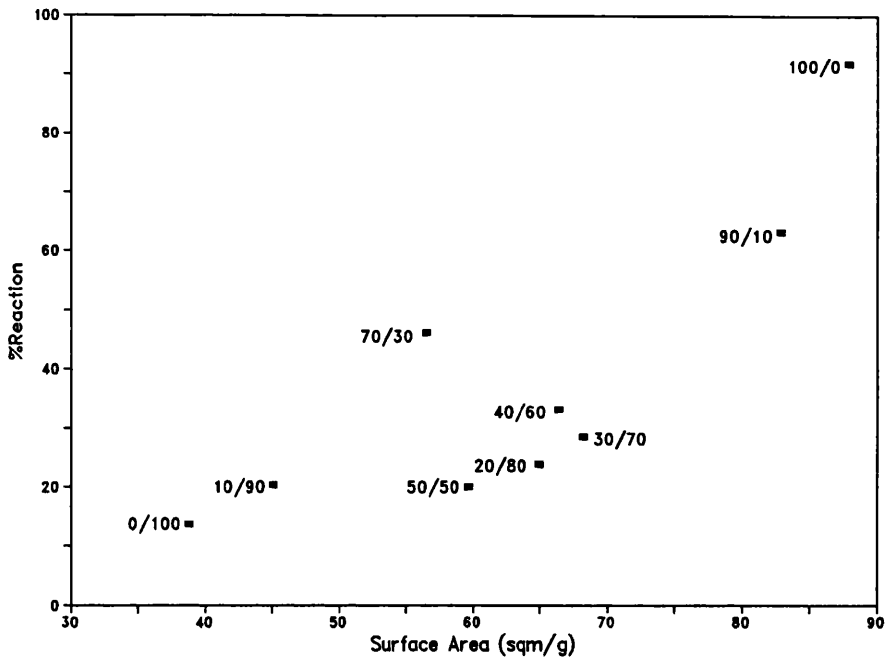
The oxides were sulphided as described in *Section 4.3*. The data obtained from the H<sub>2</sub>S 'breakthrough' tests is summarised in Table 6.11. With the exception of the 50/50 sample, the table shows that the absorbent 'breakthrough' time increased with increasing cobalt loading. There was a corresponding increase in the %Conversion and %Reaction as the cobalt loading was increased. The %Reaction has been plotted against the surface area of the oxides in Fig. 6.8. The %Reaction, with the exception of the 70/30 sample, was found to increase exponentially with surface area. The %Reaction has been plotted against %Co(wt/wt) in Fig. 6.9. An almost linear relationship can be seen between the 0/100 and 90/10 loadings, with the exceptions of the 50/50 sample and the 100/0 samples which deviate below and above the line respectively.

Transmission electron micrographs of selected sulphided oxides are shown in Fig. 6.10. It can be noted that, apart from the Co/Zn 0/100 sample, all the samples showed an increase in particle fusion with respect to their oxides after sulphiding. The average particle size increased and the particles became semi-fused making an exact measurement of their size difficult. It should also be noted that all the samples, again excepting the 0/100 ratio, had very thin sheets of material around the sides of the semi-fused particles. Energy dispersive X-ray spectroscopy, EDX, studies of these sheets showed the presence of Co, Zn and S. Unfortunately this technique was not very sensitive for oxygen.

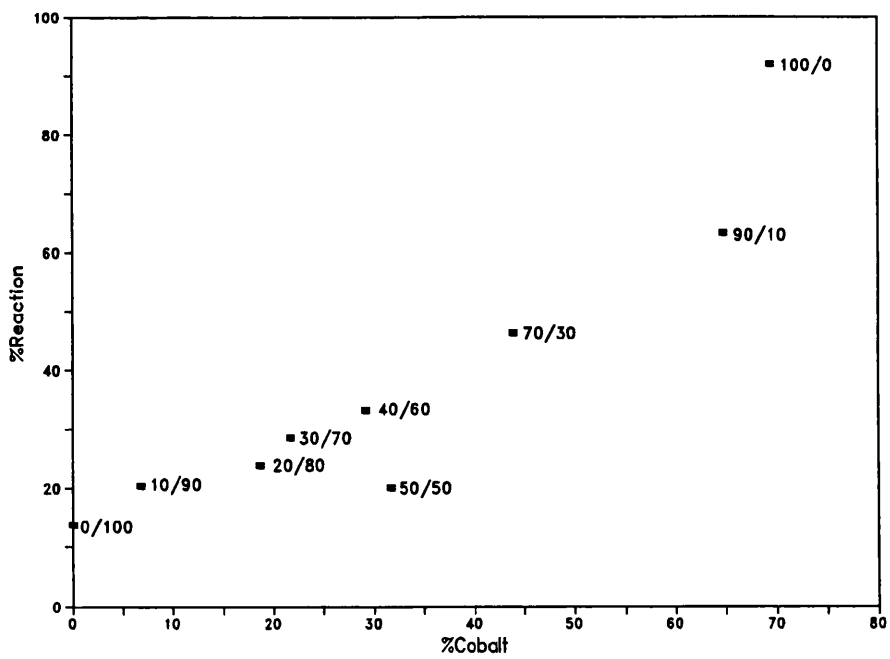
A 'breakthrough' test was carried out on the 30/70 sample, split into 5 separated beds, in order to investigate whether these sheets were present

**Table 6.11** Summary of data from H<sub>2</sub>S absorption 'breakthrough' test rig - 1st Series.

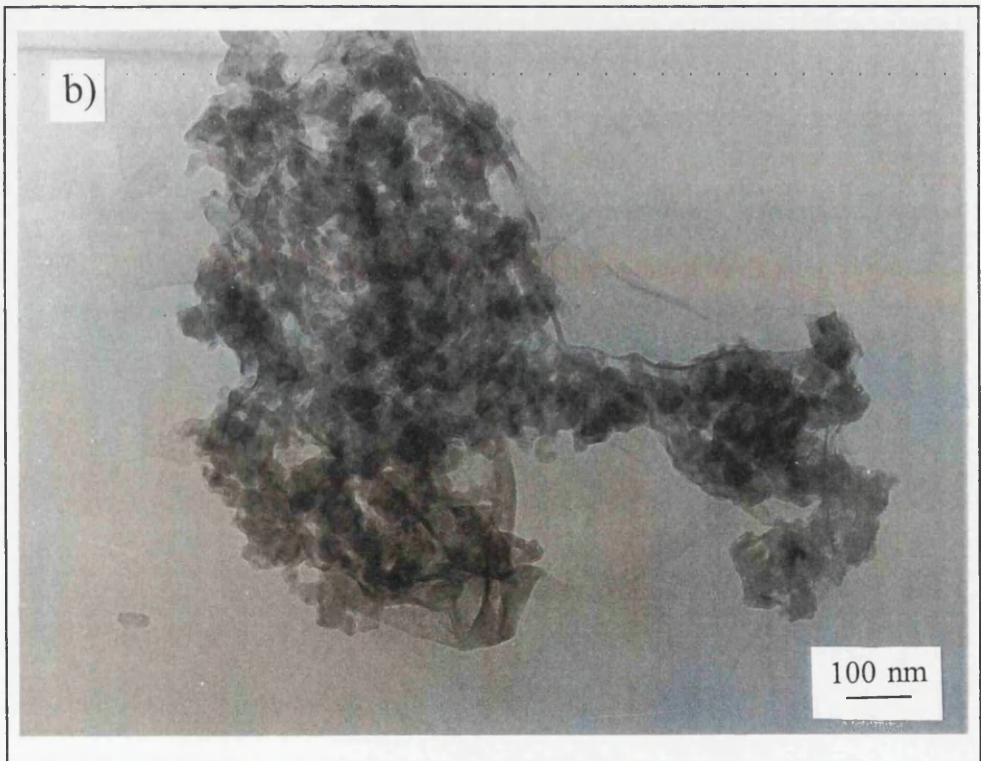
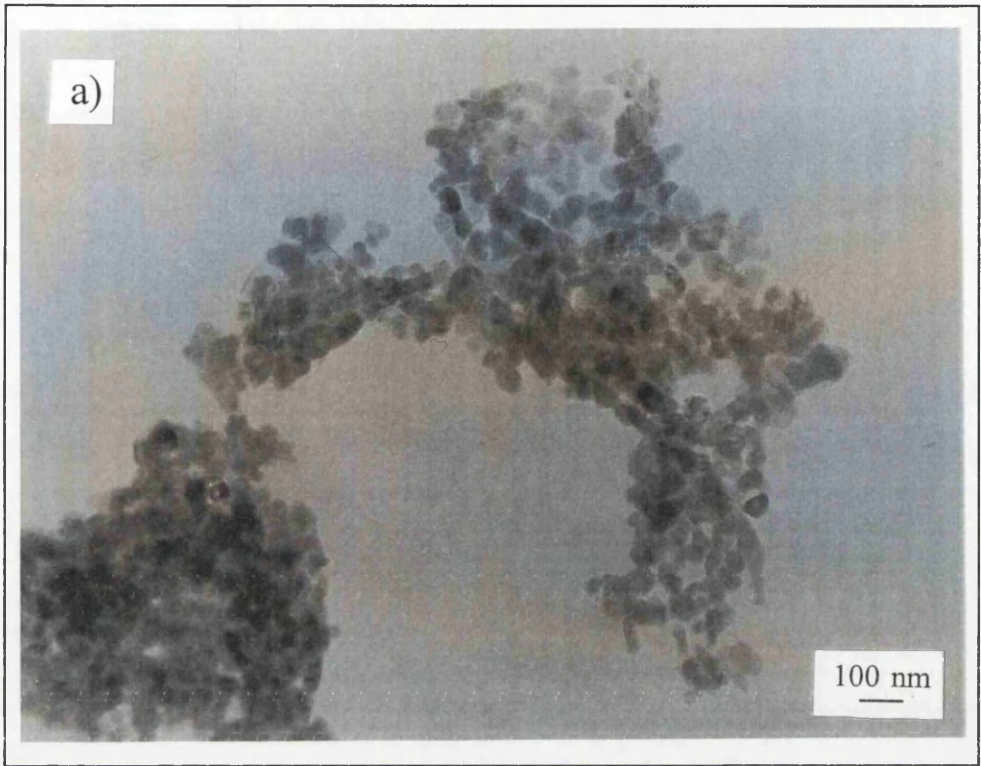
Co/Zn	%Conversion	%Reaction	wt. of absorbent (g)	'Breakthrough' time (mins)	Flow Rate H <sub>2</sub> S (cm <sup>3</sup> min <sup>-1</sup> )	Temp. (K)
0/100	5.75	13.73	3.4998	119	1.19	292
10/90	7.58	20.46	3.9100	172	1.21	291
20/80	9.97	23.86	3.6300	209	1.22	291
30/70	11.56	28.58	2.9038	206	1.14	290
40/60	12.58	33.18	3.1259	230	1.20	291
50/50	7.94	20.07	3.8007	181	1.17	289
70/30	15.56	46.22	3.3493	305	1.21	292
90/10	25.93	63.11	3.4489	530	1.18	290
100/0	36.78	91.82	3.4161	753	1.18	292



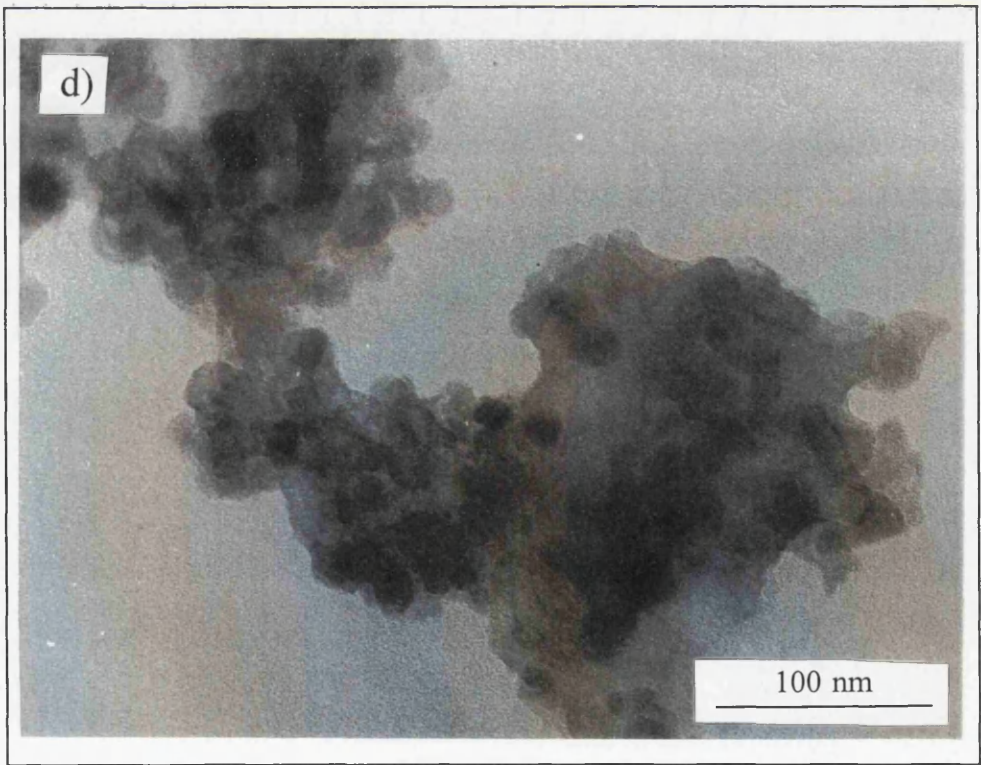
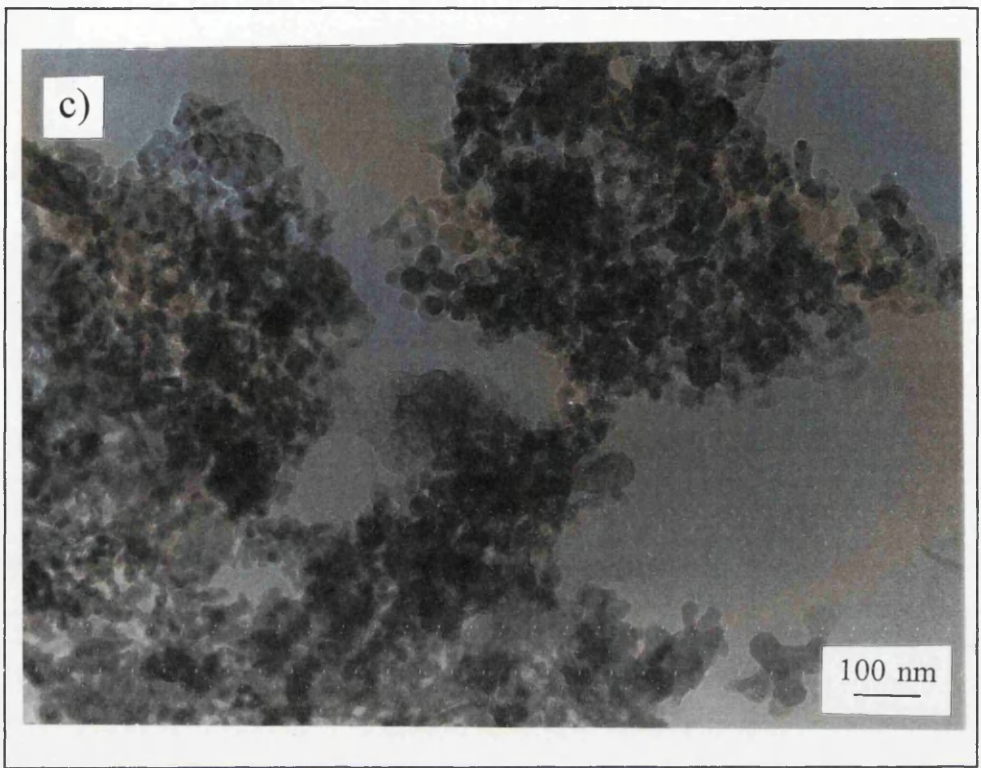
**Fig 6.8** Plot of %Reaction vs. Surface Area for sulphided oxides in 1st Series.



**Fig. 6.9** Plot of %Reaction vs. %Cobalt for sulphided oxides 1st Series.



**Fig. 6.10** Transmission electron micrographs of the sulphided oxide phases of Co/Zn a) 0/100, b) 30/70, c) 40/60, d) 100/0.



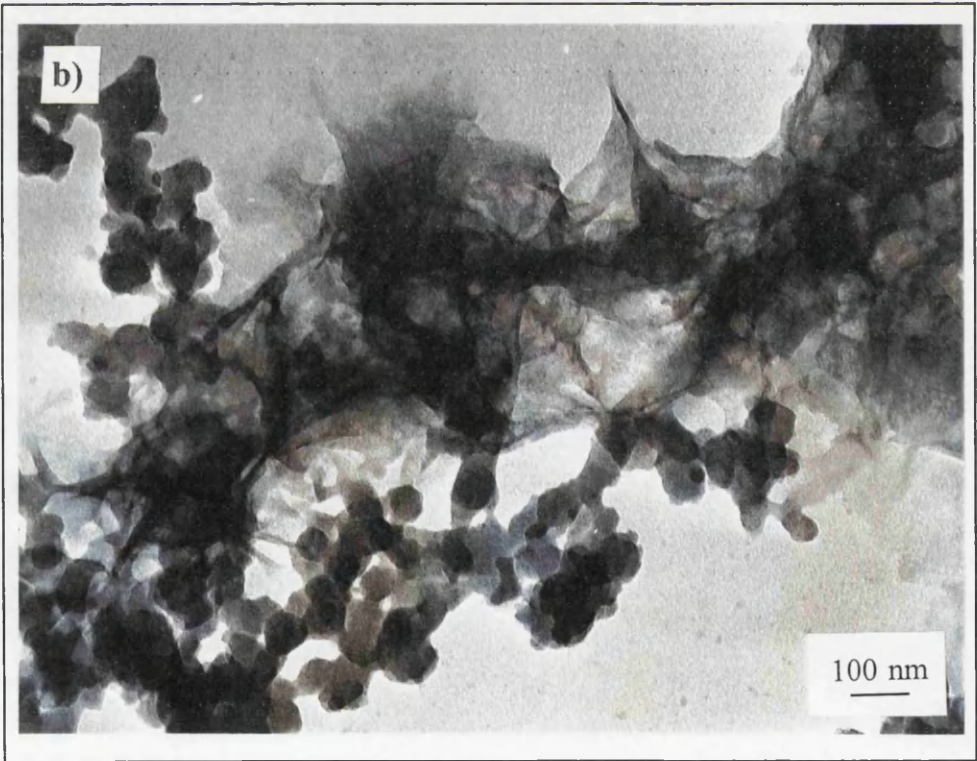
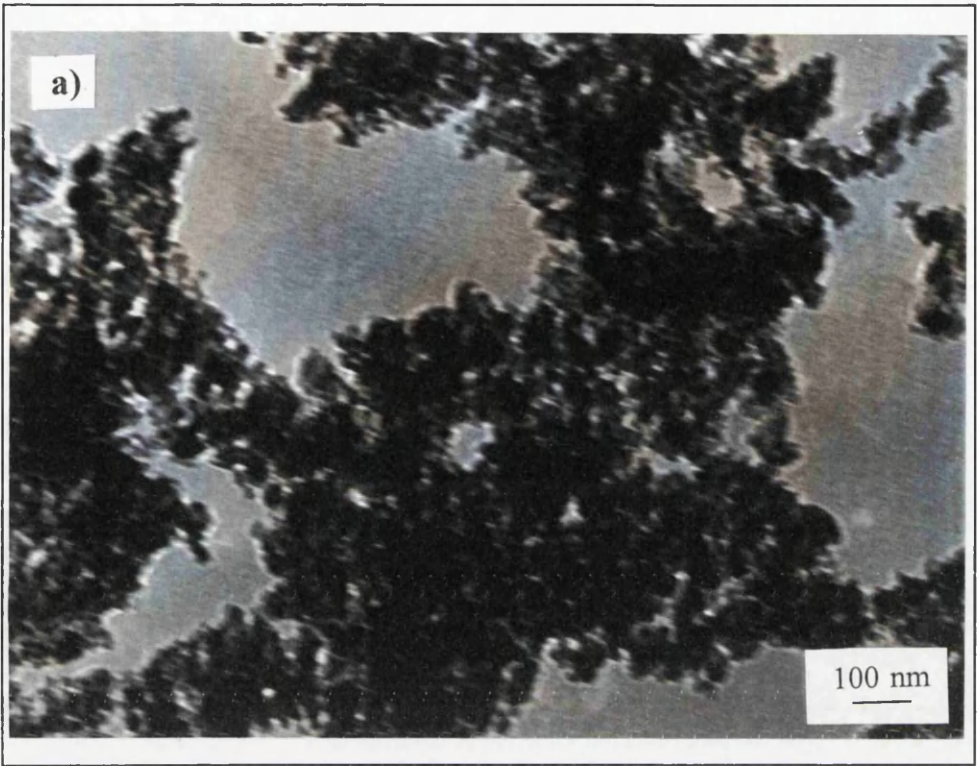
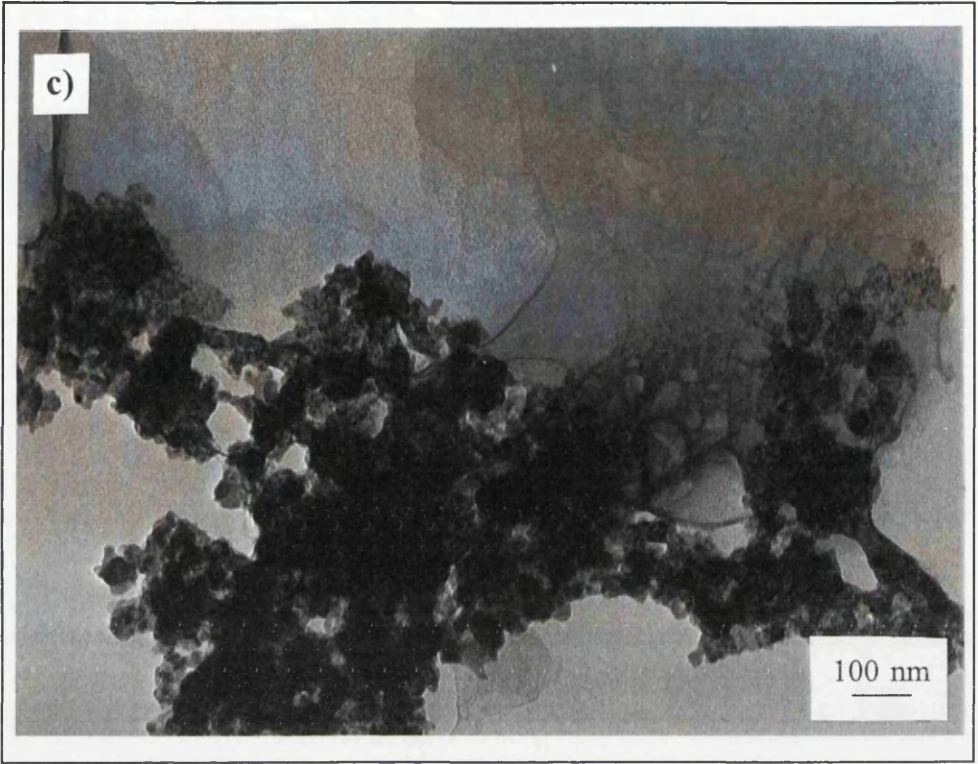


**Fig. 6.11** Transmission electron micrographs of the split beds of the 30/70 sample before and after sulphidation, a) Unsulphided oxide, b) Bed 1, c) Bed 3, d) Bed 5.



uniformly across the absorption bed. The micrographs of Beds 1, 3 and 5 are shown in Fig. 6.11. The pictures clearly showed that the sheet effect was most pronounced in Bed 1, the top bed, whilst it was least evident in Bed 5, the bottom bed. The micrograph of Bed 1 showed the presence of well defined semi-fused crystals surrounded by a thick sheet-like material. The micrographs of Beds 3 and 5 indicated that sulphidation had resulted in an initial breakdown of the crystal definition. The crystals later regained their former sharpness as the sheet-like material developed and grew.

An initial study of Bed 3 by electron energy loss spectroscopy, EELS, was undertaken by Dr. M. Huxam.<sup>81</sup> The results showed that the ratio of Co/Zn in the bulk was 42/58. It remained constant across the sample (see Fig. 6.12), though with an excess of cobalt compared to the nominal loading. On the other hand, the Co/Zn ratio for the sheet-like material varied across the sample but in all cases showed that zinc was present in a large excess. However, this

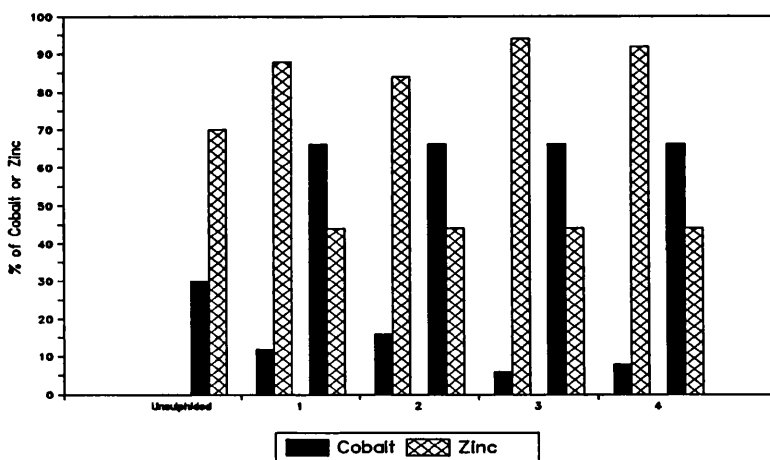


**Fig. 6.12** Graph showing the percentage Co/Zn obtained after the examination of the sheet-like material (first two bars in each group) and the main body (second two bars in each group) in 4 separate areas by EELS.

variation could have been due to experimental error due to the difficulty of selecting only the sheet-like material during analysis.

The FTIR for the Co/Zn 0/100 sulphided oxide sample was virtually identical to the FTIR of the oxide. This was probably because only very small amounts of H<sub>2</sub>S were absorbed, i.e. the average %Conversion was only *ca.* 15%. However the sample 10/90 had a low intensity peak at 1129 cm<sup>-1</sup>, and a shoulder at 1180 cm<sup>-1</sup>, which can be attributed to β-ZnS.<sup>75</sup> The intensities of the peaks at 669 and 590 cm<sup>-1</sup> in the oxide (Co<sub>3</sub>O<sub>4</sub>) were reduced relative to the unsulphided oxides. This pattern was followed in the 20/80, 30/70 and 40/60 samples. For the 50/50 loadings and above the peak and shoulder at *ca.* 1120 cm<sup>-1</sup> were of much lower intensity compared to the more zinc rich oxides.

## 6.2 XPS STUDY OF COBALT-ZINC 1st SERIES

### 6.2.1 Precursors

Selected narrow energy scans of the Zn2p<sub>3/2</sub> and Co2p<sub>3/2</sub> photoelectron peaks of the precursors are shown in Figs. 6.13 and 6.14 respectively. The photoemission energies for zinc, cobalt and oxygen are reported in Table 6.12.

It can be seen that the 2p<sub>3/2</sub> transition for zinc for each precursor consisted of only a single peak, at *ca.* E<sub>B</sub> = 1022.0 eV. The presence of the low binding energy feature at *ca.* E<sub>B</sub> = 1019.6 eV is caused by the highly focused M-Probe electron source reducing the ion to its metallic state. The Co2p<sub>3/2</sub> peak, positioned at *ca.* E<sub>B</sub> = 781.0 eV, consisted of a main peak with a satellite peak at a higher binding energy, *ca.* E<sub>B</sub> = 785.8 eV. The values of the binding energies and the presence of the satellite peak for the Co2p<sub>3/2</sub> transition were typical of zinc and cobalt in the 2+ oxidation state.<sup>56,61</sup> This satellite was due to shake-up transitions between filled O 2p levels and vacancies in the metal d orbitals and is typical of the first row transition metal series. This accounts for its occurrence for Co<sup>2+</sup> and not Zn<sup>2+</sup> ions (see *Section 2.3.4c*). The O 1s transition at E<sub>B</sub> = 531.0 eV was similar to that expected for oxygen in -CO<sub>3</sub><sup>2-</sup>.<sup>82</sup>

It has been reported that for Co<sup>2+</sup> containing compounds the satellite-main peak energy separation increases and the satellite/main peak intensity ratio decreases with increasing covalent character of the metal-ligand bond.<sup>44</sup> Applying this to the Co-Zn precursor data (see Table 6.12), it was seen that the satellite main peak energy separation decreased as the cobalt loading increased for compounds with a Co/Zn ratio of 20/80 and above. This was accompanied by an increase in the satellite/main peak intensity ratio. This

**Table 6.12** Binding Energies for the precursors and finely ground precursors. Charging effects have been referenced to the C1s peak of the carbonate group at  $E_B = 289.1$  eV. The FWHM are given in parentheses.

	Zn2p <sub>3/2</sub> eV	Co2p <sup>3/2</sup> eV	Sat-Main E Sep eV	Ratio sat/main	O1s eV	C1s eV
0/100	1021.9(2.9) 1019.6(3.8)				531.2(2.9) 528.2(2.6)	289.1(2.5) 284.2(2.9)
10/90	1022.4(2.9) 1019.9(3.7)	781.5(4.9) 786.4(5.3)	4.95	0.40	531.1(2.9) 528.5(2.6)	289.1(2.4) 284.3(3.1)
20/80	1022.0(3.1) 1019.4(3.1)	781.0(4.4) 785.8(5.2)	4.87	0.46	531.2(2.8) 530.0(2.9)	289.1(2.8) 284.2(3.4)
30/70	1021.5(3.1) 1018.8(2.8)	780.9(4.3) 785.6(4.9)	4.77	0.45	531.0(3.0) 528.6(3.4)	289.1(2.7) 284.3(3.2)
40/60	1022.6(2.9) 1020.4(3.0)	780.9(4.0) 785.4(5.4)	4.60	0.53	531.2(2.9) 529.0(3.1)	289.1(2.4) 283.4(4.6)
50/50	1021.7(2.9) 1019.5(3.3)	780.9(4.2) 785.4(5.4)	4.55	0.58	531.1(2.8) 528.6(2.7)	289.1(2.6) 284.1(3.2)
100/0		781.0(5.4) 786.3(4.2)	5.31	0.22	531.2(3.1) 528.7(3.7)	289.1(2.6) 284.3(4.1)
10/90G	1021.4(2.8) 1019.0(3.5)	781.1(4.1) 785.7(3.7)			531.1(2.9) 528.9(3.0)	289.1(2.6) 284.3(3.3)
30/70G	1021.9(3.4) 1019.3(4.8)	781.4(4.9) 786.4(4.6)			531.1(3.2) 528.7(3.8)	289.1(2.4) 283.9(5.0)
50/50G	1022.0(3.0) 1019.5(4.1)	781.2(3.8) 785.6(5.6)			531.7(3.1) 528.7(2.8)	289.1(2.9) 284.3(3.3)

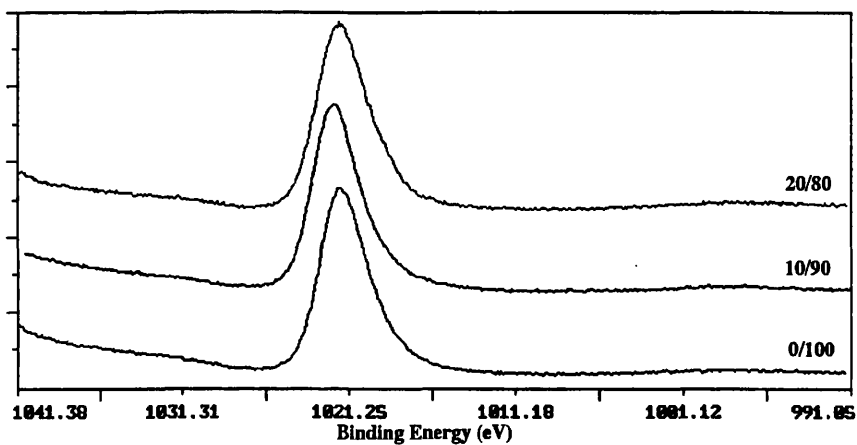


**Fig. 6.13** Typical examples of the zinc 2p<sub>3/2</sub> transition for the hydroxycarbonate precursors. The intensities have been normalised.

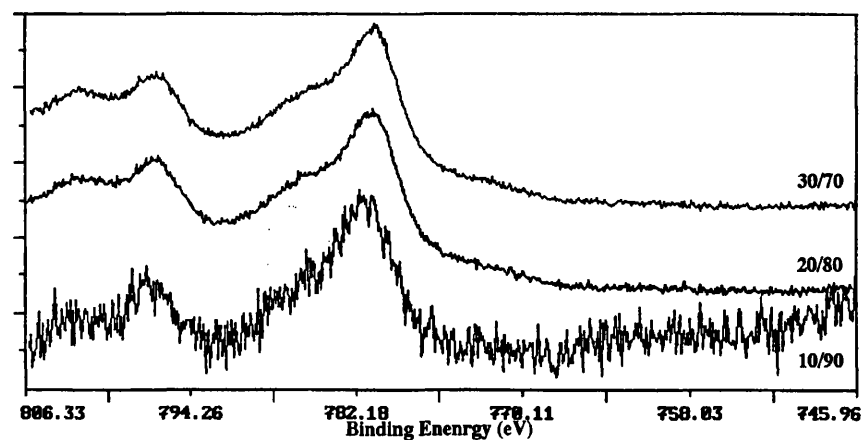
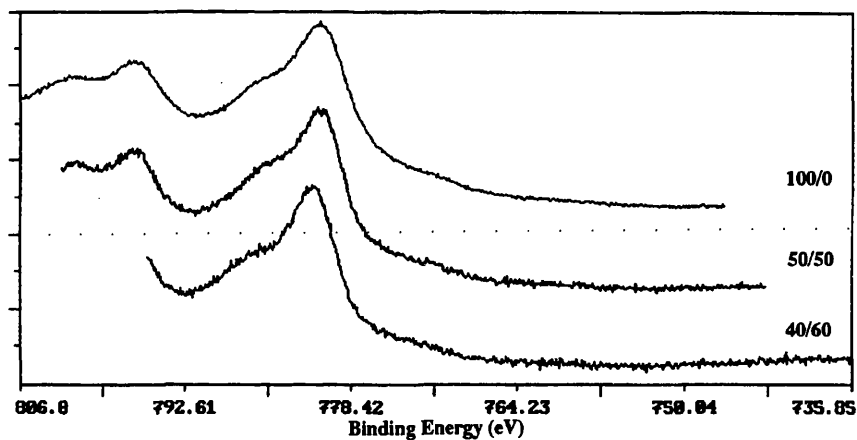


**Fig. 6.14** Cobalt 2p<sub>3/2</sub> transition for the hydroxycarbonate precursors. The intensities have been normalised.

suggested an increase in the ionic character of the chemical bonding around the  $\text{Co}^{2+}$  ions for the mixed Co/Zn precursors with increasing cobalt concentration.

The peak shapes of the zinc and cobalt transitions were very similar for all the precursors. The main binding energy positions of  $\text{Zn}2p_{3/2}$  and  $\text{Co}2p_{3/2}$  varied from 1021.5 to 1022.6 eV and from 780.9 to 781.5 eV respectively. The reason for this inconsistency probably resulted from the variable nature of the  $\text{CO}_3/\text{OH}$  ratio fixed during the precipitation process.

The surface Co/Zn atomic ratios were derived from the peak intensity ratios of the  $2p_{3/2}$  and are shown in Table 6.13. The relationship between atomic ratios at the surface (XPS,  $2p_{3/2}$ ) and the bulk (AA) are shown in Fig. 6.15. The straight line (slope = 1) represents a homogenous distribution of the Co/Zn ratio between the surface and the bulk. The data clearly showed that there was a trend towards cobalt enrichment at the surface of these precursors.

In order to further investigate the surface Co/Zn ratio, the 10/90, 30/70 and 50/50 precursors were finely ground and the spectra collected under identical conditions. The quantitative data (see Tables 6.13 and Fig. 6.15) showed that for the 30/70 and 50/50 ground samples there was a lowering of the Co/Zn ratio on the surface compared with their unground counterparts, whereas there was a small increase in the ratio for the ground 10/90 precursor. This suggested that the particles had zinc rich cores and that a more homogeneous distribution of the cobalt and zinc between the bulk and the surface resulted due to the particles continually shearing/reforming during the grinding process.

**Table 6.13** Quantitative analysis of precursors and finely ground precursors (G).

	Co <sub>2</sub> p <sub>3/2</sub> /Zn <sub>2</sub> p <sub>3/2</sub> Peak intensity ratio	Co <sub>x</sub> Zn <sub>1-x</sub> X
10/90	0.079	0.086
20/80	0.346	0.378
30/70	0.450	0.491
40/60	0.679	0.742
50/50	0.813	0.888
10/90G	0.083	0.095
30/70G	0.339	0.301
50/50G	0.737	0.483

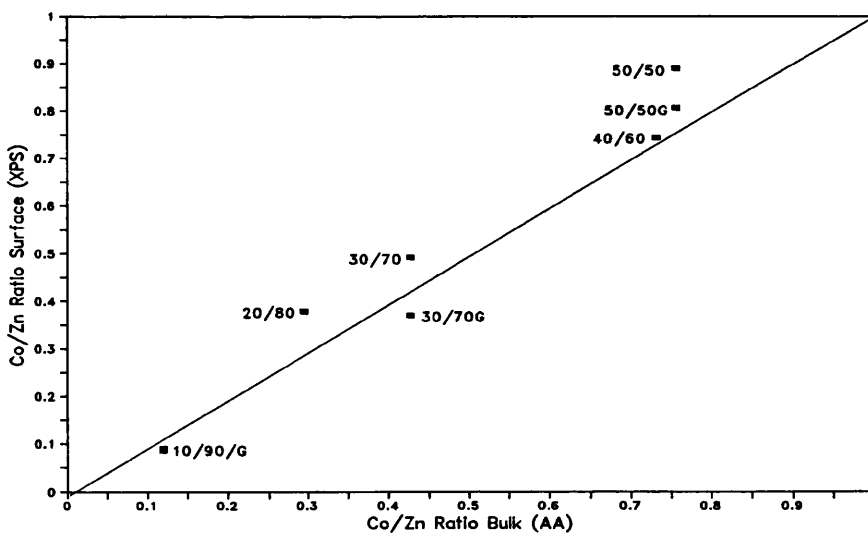


**Fig. 6.15** Co/Zn composition at the surface (XPS, 2p<sub>3/2</sub>) and in the bulk (AA) for the precursors.

### 6.2.2 Oxides (Cal. 350°C, 16 hrs.)

The Zn2p<sub>3/2</sub> XP spectra of the Co/Zn 0/100 sample is shown in Fig. 6.16. All the oxides showed similar spectra. Its shape and binding energy, *ca.* E<sub>B</sub> = 1021.6 eV (see Table 6.14), was typical of Zn in a 2+ oxidation state.

The Co2p<sub>3/2</sub> XP spectra for all the oxides are shown in Fig. 6.16. For Co/Zn 100/0 the Co2p<sub>3/2</sub> main peak was at E<sub>B</sub> = 780.3 eV with the Co2p<sub>3/2</sub>-2p<sub>1/2</sub> spin-orbit splitting equal to 15.1 eV. Peak fitting using Gaussian curves gave binding energies of 780.1 and 782.1 eV for the Co<sup>3+</sup> and Co<sup>2+</sup> ions respectively. This was in agreement with Chuang *et al.* for their assignments of a high purity Co<sub>3</sub>O<sub>4</sub> powder.<sup>83</sup> As the cobalt loading decreased the photoelectron peak indicating the presence of the Co<sup>2+</sup> ion decreased in intensity. Only the Co<sup>3+</sup> ion was present for Co/Zn 30/70 and lower loadings (see Fig. 6.16). This indicated that at low cobalt loadings the normal spinel ZnCo<sub>2</sub>O<sub>4</sub> may be formed at the surface. Fig. 6.16 also indicates that the background step decreased as the cobalt loading decreased. This was deduced from the step-size of the baseline between the low and high binding energies of the peak, (see Table 6.14). The background step was caused by inelastic collisions of the emitted photoelectron which created an increasing signal level between the high and low binding energies of the photoelectron peak. This is illustrated in Fig. 6.17. It shows that for a small increase in the background step all the signal originated from the outermost surface. As this step after photoemission gets bigger it shows that some of the electrons detected are also coming from further inside the 'bulk'. Therefore the lower the step the greater is the contribution of the surface ions to the signal. Therefore, it can be

**Table 6.14** Binding Energies and Quantitative Analysis for the oxides. Charging effects have been referenced to the O1s peak at  $E_B=530.0$  eV. The FWHM are given in parenthesis.

Co/Zn	Zn2p <sub>3/2</sub> eV	Co2p <sub>3/2</sub> eV	O1s eV	Diff. in e <sup>-</sup> count between High & Low B.E. for the Co2p <sub>3/2</sub> peak.	Quantitative Analysis Co2p <sub>3/2</sub> /Zn2p <sub>3/2</sub>	Co <sub>x</sub> Zn <sub>1-x</sub>
0/100	1021.46(2.36)		530.0(2.1) 531.9(2.1)			
10/90	1021.2(3.2)	779.4(3.4)	530.0(3.2)	1594	0.044	0.053
20/80	1021.4(3.8) 1018.3(4.1)	778.9(3.2) 777.6(4.2)	530.0(3.6) 532.4(3.0)	4213	0.337	0.299
30/70	1021.7(3.7) 1018.7(3.2)	780.1(3.9) 778.1(3.9)	530.0(4.1)	5209	0.469	0.373
40/60	1021.7(3.2) 1018.9(2.6)	782.4(2.5) 780.4(2.6) 777.6(1.5)	530.0(2.3) 532.2(2.4)	5995	0.452	0.364
50/50	1022.0(3.0) 1019.4(1.7)	782.4(2.6) 780.3(2.9) 777.6(1.5)	530.0(2.5) 532.4(2.0)	10593	0.818	0.521
0/100		782.1(2.6) 780.1(2.9) 777.3(1.0)	530.0(2.3) 532.2(2.7)	17799		

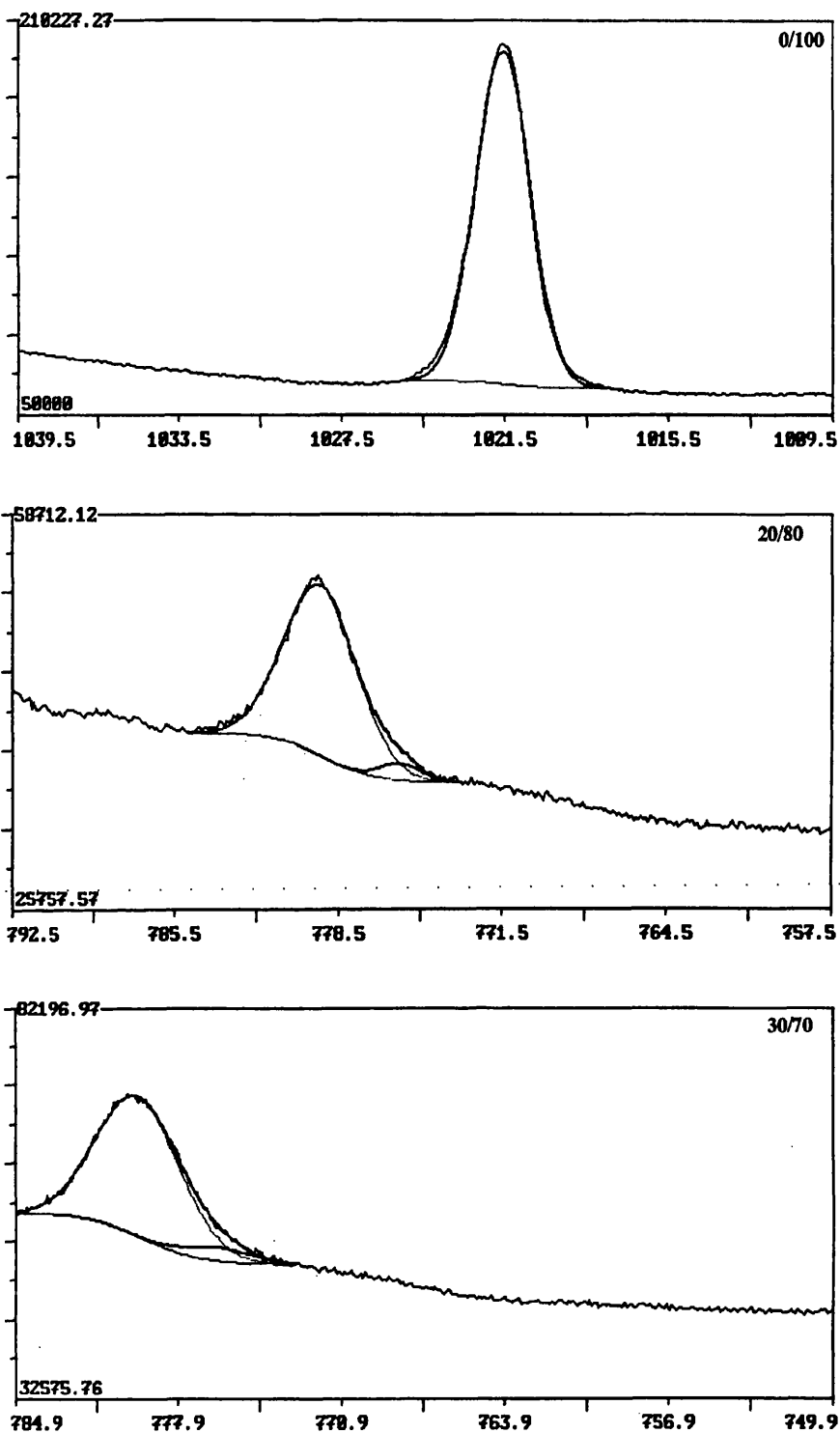
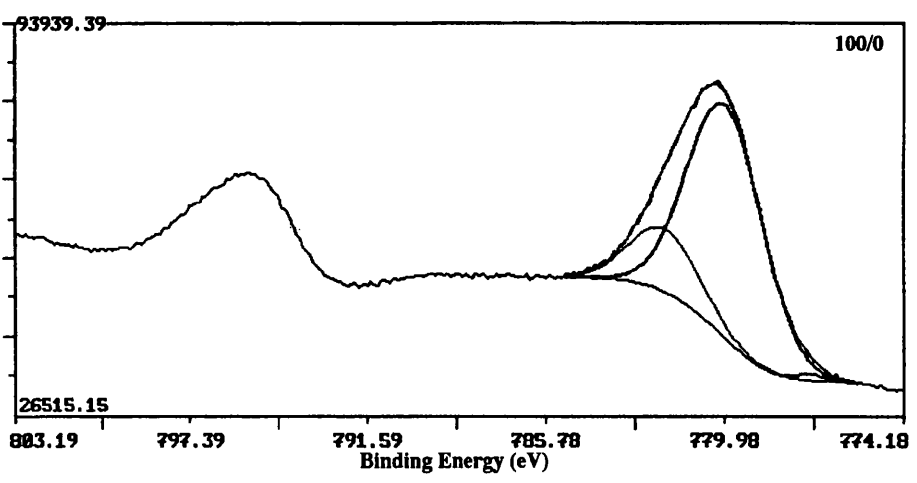
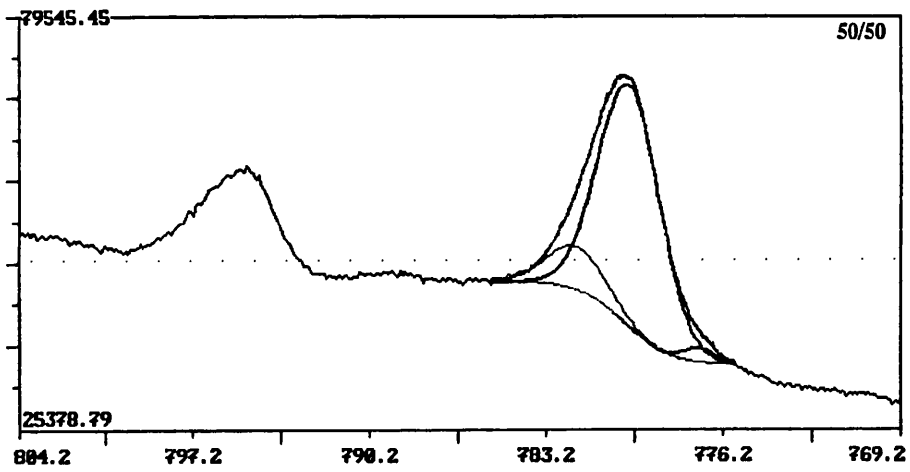
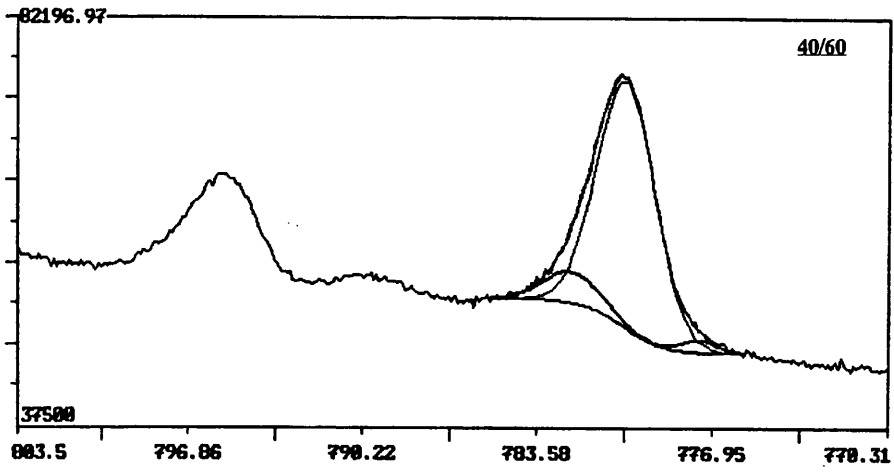


**Fig. 6.16** The  $2p_{3/2}$  transition for the oxides (cal. 350°C, 16 hrs.). Only the Zn  $2p_{3/2}$  transition of the Co/Zn 100/0 is shown as it is typical in shape and position of the other loadings. The Co  $2p_{3/2}$  transition is shown for nominal Co/Zn loadings 20/80, 30/70, 40/60, 50/50 and 100/0. Peak fitting showed the presence of  $\text{Co}^{2+}$  ions *ca.*  $E_B = 779$  eV,  $\text{Co}^{3+}$  *ca.*  $E_B = 781$  eV and reduced Co *ca.*  $E_B = 777$  eV.



concluded that for low loadings much of the cobalt was at the surface and as the overall cobalt concentration in the sample increased, the cobalt rich surface layer increased.

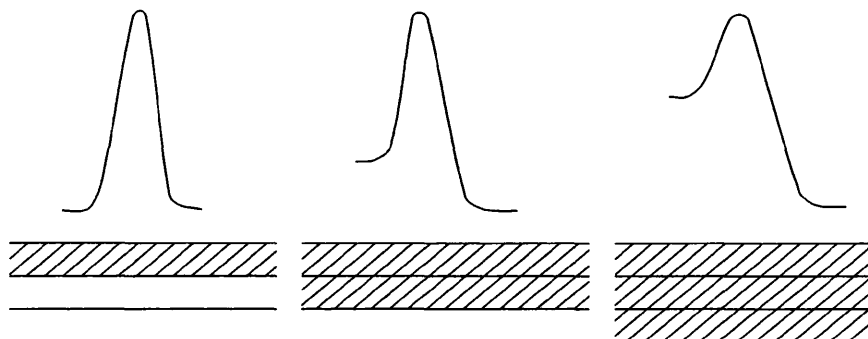


**Fig. 6.17** Diagram of the effect of increasing penetration of cobalt into the bulk on the step-size increase of the  $\text{Co}2p_{3/2}$  transition.

The atomic ratios derived from the peak intensity ratios of the  $2p_{3/2}$  peaks are reported in Table 6.14. Segregation at the surface was clearly seen from the  $2p_{3/2}$  derived ratios and this is highlighted in Fig. 6.18. If the  $2p_{3/2}$  atomic ratios are compared with the figures for the precursors it can be seen that they are in good agreement. This leads to the conclusion that the cobalt segregation at the surface was achieved at the stage when the precursors were synthesized and that calcining the precursors at  $350^\circ\text{C}$  for 16 hours had little effect on the eventual segregation of the cobalt in the oxide.

With the exception of the Co/Zn 10/90 sample the zinc and cobalt ions in the mixed Co/Zn systems gave a second and third distinct region at lower binding energies, separated by *ca.* 3 eV. They were most apparent for the 20/80, 30/70 and 40/60 loadings. This low binding feature, which was seen at *ca.*  $E_B = 1018.8$  eV for zinc ions and at *ca.*  $E_B = 777.7$  eV for cobalt ions, was the result of the metal ions at the surface of a solid being reduced by the

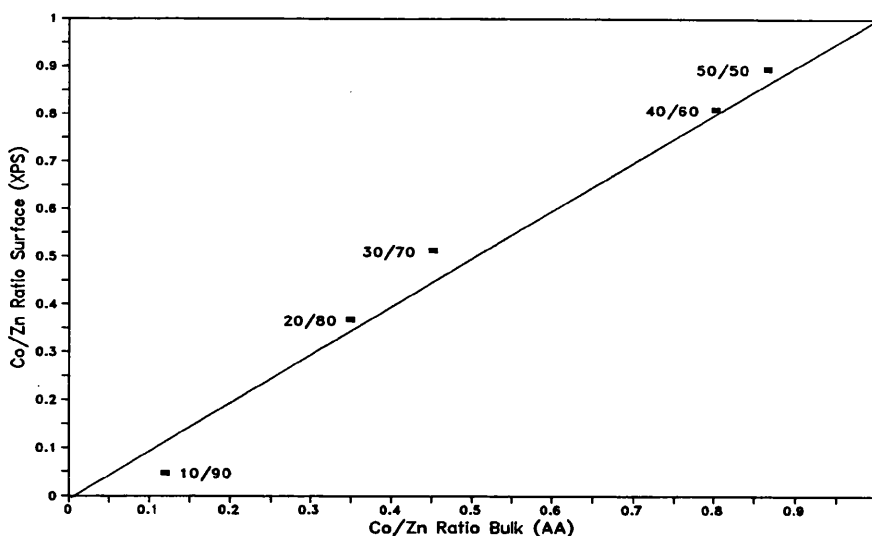


**Fig. 6.18** Co/Zn composition at the surface (XPS,  $2p_{3/2}$ ) and in the bulk (AA) for the oxides. The straight line (slope=1) represents a homogeneous distribution between surface and bulk.

highly focused M-Probe XPS source to their respective metallic forms. The O 1s spectra of the oxides were all very similar in shape. The spectra were curve fitted into two Gaussians curves and the main peak binding energy was fixed at  $E_B = 530.0$  eV. The second feature at higher binding energy,  $E_B = 532.2$  eV, was most likely to be due to the presence of an hydroxyl species at the surface.

### 6.2.3 Oxides (Cal. Var. Temp., 8 hrs.)

To further investigate the effect of the calcination process on surface enrichment of cobalt the precursors with nominal Co/Zn concentrations of 10/90 and 50/50 were calcined at various temperatures between 100 and 700°C for 8 hours. These ratios were chosen as they are at the extremes of the cobalt loadings in the mixed samples under investigation.

The binding energies are tabulated in Tables 6.15a and 6.15b for the 10/90 and 50/50 series respectively. The  $Zn2p_{3/2}$  binding energies varied slightly for both loadings within each series but are in accordance with literature values for zinc in the  $2+$  oxidation state. The XP spectra of the  $Co2p_{3/2}$  transition for the 10/90 series are shown in Fig. 6.19. At temperatures below  $350^{\circ}C$  the  $Co2p_{3/2}$  transition consisted of a main peak, positioned at *ca.*  $E_B = 781.7$  eV, with a satellite peak at higher binding energy, *ca.*  $E_B = 787.7$  eV (see Table 6.15a). This is typical of a  $Co^{2+}$  ion. The signal to noise ratio of the spectra increased noticeably as the calcination temperature was increased. At  $350^{\circ}C$  and above, peak fitting of the  $Co2p_{3/2}$  peak revealed the presence of the  $Co^{3+}$  ion,  $E_B = 779.9$  eV, with only a very small contribution from the  $Co^{2+}$  ion,  $E_B = 782.6$  eV, and its corresponding shake-up satellite. If these samples had been calcined for a further 8 hours it is believed that the  $Co^{2+}$  contribution would have completely disappeared with the formation of the 'surface spinel'  $ZnCo_2O_4$  (*cf Section 6.2.2*).

The  $Co2p_{3/2}$  spectra for the 50/50 series are shown in Fig. 6.20. Calcination at less than  $200^{\circ}C$  gave a  $Co2p_{3/2}$  peak at *ca.*  $E_B = 781.1$  eV (see Table 6.15b). The peak shape and binding energy of the  $Co2p_{3/2}$  photoelectron peak was characteristic of the presence of  $Co^{2+}$  ions. The photoelectron peak obtained after calcination at temperatures between 200 and  $400^{\circ}C$  was peak fitted and this indicated the presence of a  $Co^{3+}$  component,  $E_B = 780.0$  eV and a very small contribution from a  $Co^{2+}$  component,  $E_B = 782.0$  eV. However at  $480^{\circ}C$  and above, only the  $Co^{3+}$  ion was present. Again it was thought that

**Table 6.15** Binding Energies of the Co/Zn a) 10/90 and b) 50/50 series, calcined at various temperatures. Charging effects have been referenced to the C1s peak of adventitious carbon at  $E_B = 285.0$  eV The FWHM are given in parentheses.

**Table 6.15a**

Temperature (°C)	Zn2p <sub>3/2</sub> eV	Co2p <sub>3/2</sub> eV	O1s eV	C1s eV
100	1021.8(5.4) 1026.3(3.8)	784.3(8.0)	530.8(4.5) 533.6(4.1)	285.0(4.6) 289.6(3.6)
170	1020.7(3.1) 1023.5(3.0)	781.9(5.5)	530.9(4.7) 534.7(3.3)	285.0(4.4) 288.5(2.0)
200	1022.6(4.1) 1027.2(3.4)	781.1(6.4) 787.4(5.4)	530.7(3.2) 534.4(4.4)	285.0(2.8) 288.7(3.5)
250	1022.3(3.2) 1025.6(3.4)	782.1(7.0)	531.3(4.0) 535.1(4.5)	285.0(2.8) 288.2(5.2)
310	1023.7(6.7)	781.9(6.2)	530.6(4.4) 533.6(3.6)	285.0(4.7) 288.4(2.5)
355	1022.1(2.6) 1019.9(2.0)	779.9(3.0) 782.6(2.4) 786.9(7.2)	530.5(2.5) 532.8(1.4)	285.0(1.9) 288.5(2.8)
400	1022.1(2.5) 1019.9(1.9)	779.8(2.7) 782.1(2.8) 787.3(5.9)	530.4(2.5) 532.7(1.3)	285.0(1.9) 288.6(3.0)
480	1022.1(2.5) 1020.0(1.8)	779.9(2.8) 782.4(2.8) 787.9(6.6)	530.4(2.8) 533.0(1.3)	285.0(2.0) 288.2(2.6)
575	1021.9(2.3) 1019.7(1.6)	779.8(2.5) 782.1(3.6) 788.8(5.4)	530.5(2.5) 532.8(1.6)	285.0(1.8) 287.0(3.4)
700	1021.8(2.6) 1019.5(1.6)	779.8(2.7) 781.9(3.6) 787.9(7.6)	530.5(2.6) 533.0(1.4)	285.0(2.0) 288.5(2.3)

**Table 6.15b**

Temperature (°C)	Zn2p <sub>3/2</sub> eV	Co2p <sub>3/2</sub> eV	O1s eV	C1s eV
100	1021.7(2.9) 1019.5(3.3)	780.9(4.2) 785.4(5.4)	531.1(2.8) 528.6(2.7)	285.0(3.2) 289.1(3.2)
170	1023.4(4.5)	782.0(3.8)	532.2(4.6)	285.0(2.7) 287.2(2.2)
200	1021.0(2.7)	779.9(2.1) 781.4(2.3)	529.3(1.8) 531.6(2.7)	285.0(1.7) 286.9(3.3)
250	1022.9(4.3)	780.6(2.9) 783.3(3.0)	531.1(3.9)	285.0(2.7) 287.6(2.9)
310	1021.3(2.7)	780.2(2.3) 782.1(2.2)	529.6(1.9) 532.0(2.7)	285.0(1.9)
355	1021.0(2.9)	780.0(2.5) 782.0(2.7)	529.4(2.0) 531.5(2.8)	285.0(2.1) 286.9(4.0)
400	1020.8(2.6)	779.8(2.1) 781.4(2.5)	529.3(1.8) 531.5(2.4)	285.0(1.8) 288.1(3.0)
480	1021.1(3.4)	779.8(3.4)	529.7(4.1)	285.0(2.6)
575	1021.7(3.4)	780.2(3.2)	529.6(3.7)	285.0(2.6)
700	1021.6(3.4) 1018.2(3.8)	780.1(3.2)	529.6(3.8)	285.0(2.4)

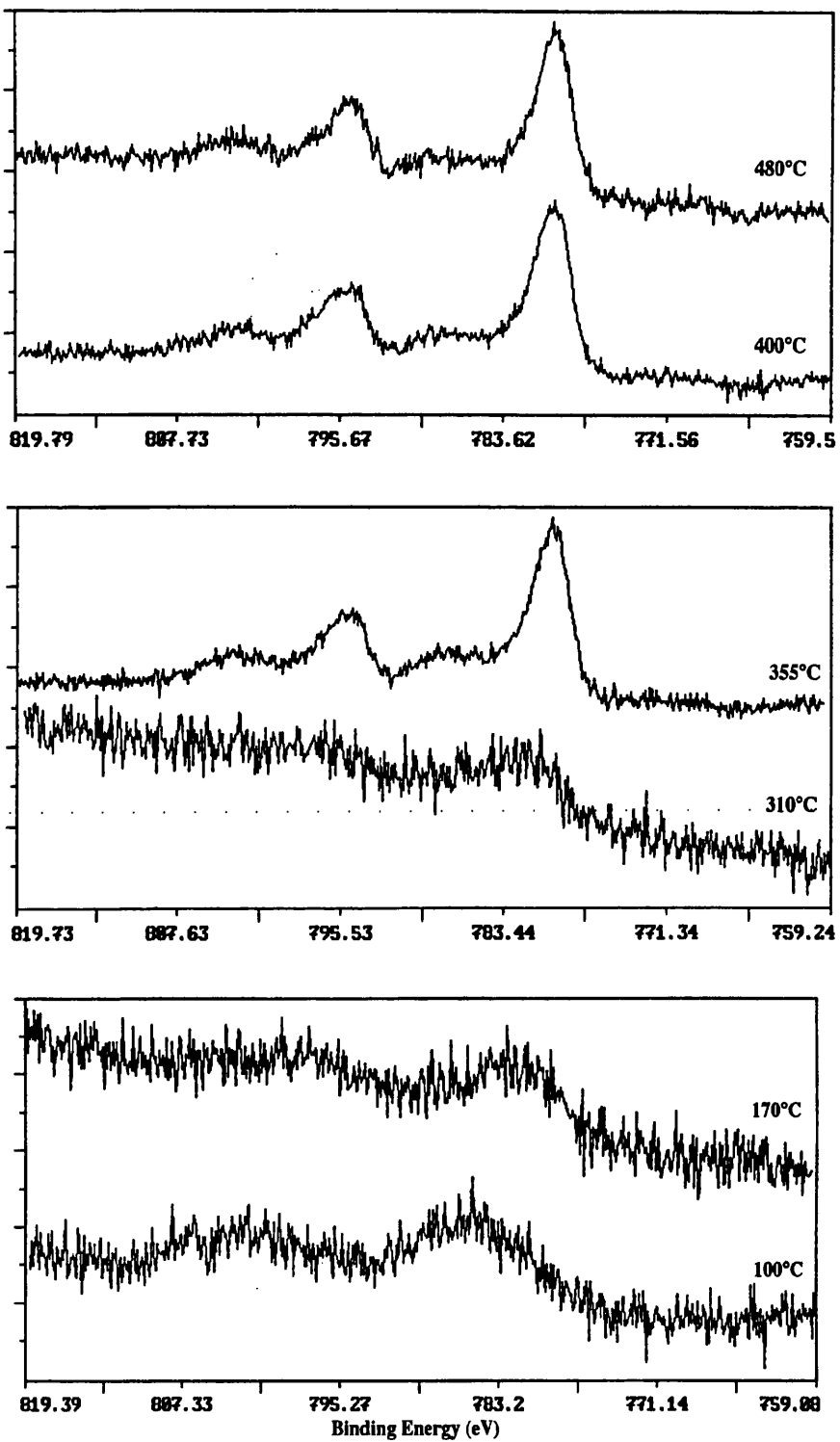


**Fig. 6.19** Cobalt 2p<sub>3/2</sub> transition for Co/Zn 10/90 Series (cal. var. temp.). The intensities have been normalised.

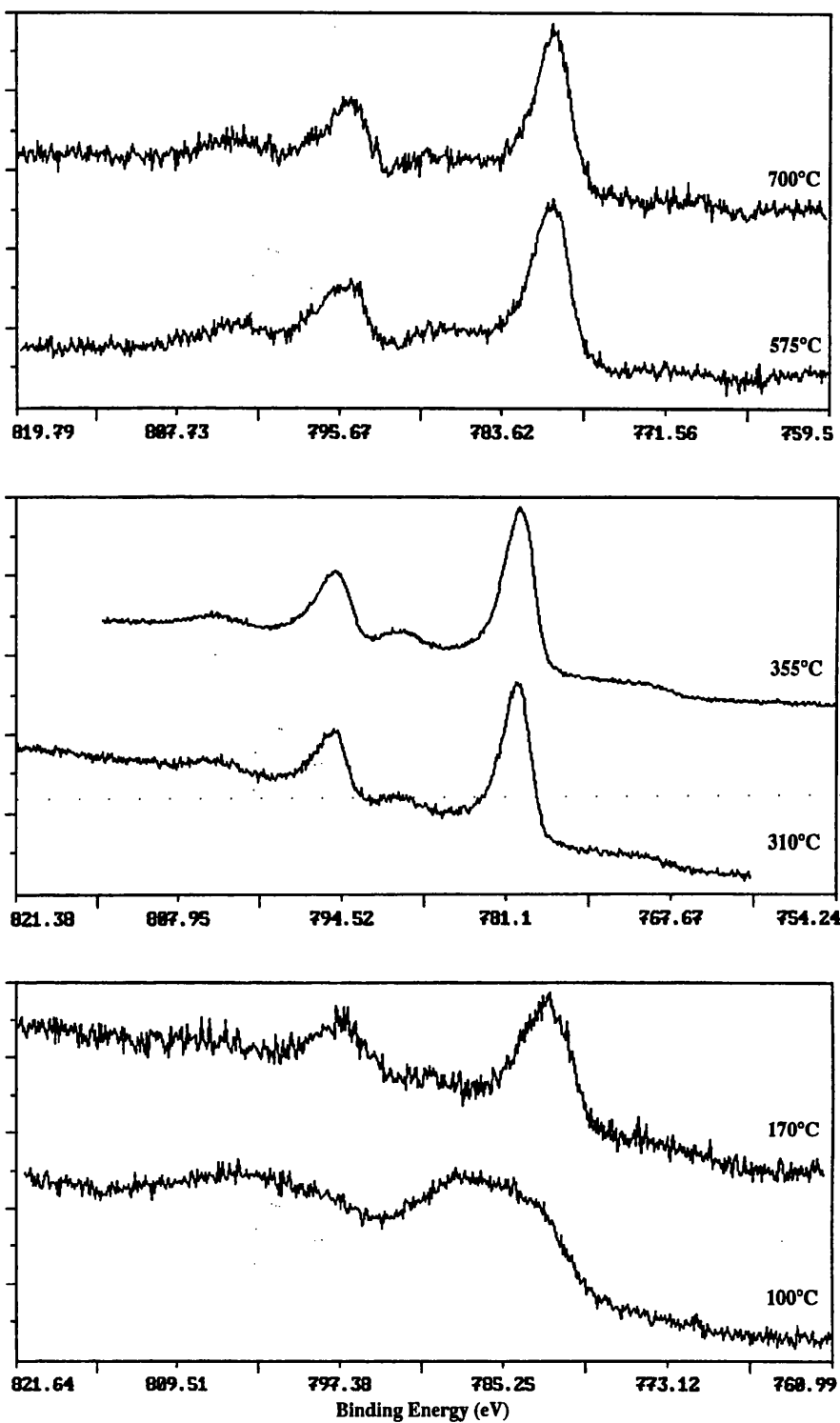


**Fig. 6.20** Cobalt  $2p_{3/2}$  transition for Co/Zn 50/50 Series (cal. var. temp.). The intensities have been normalised.

increasing the time of calcination for the oxides (calcined between 200 and 400°C) would have reduced the amount of the  $\text{Co}^{2+}$  component.

Quantitative analyses for the 10/90 and 50/50 series are shown in Table 6.16. For both series there was a slight variation in the surface Co/Zn ratios for the samples calcined at temperature below 350°C. However, above 350°C the surface Co/Zn ratio were closer to the expected values, i.e. 0.1 and 0.5 for the 10/90 and 50/50 series respectively. This suggested that little segregation of cobalt to the surface occurred as the calcination temperature was increased above 350°C.

**Table 6.16** Quantitative analyses for 10/90 and 50/50 Cal. Var. Temps. Series.

	10/90		50/50	
	$\text{Co}2p_{3/2}/\text{Zn}2p_{3/2}$	$\text{Co}_x\text{Zn}_{1-x}$	$\text{Co}2p_{3/2}/\text{Zn}2p_{3/2}$	$\text{Co}_x\text{Zn}_{1-x}$
100	0.063	0.074	0.430	0.353
170	0.023	0.028	0.276	0.258
200	0.035	0.042	0.567	0.419
250	0.024	0.029	0.038	0.066
310	0.034	0.041	0.700	0.470
355	0.094	0.106	0.732	0.482
400	0.094	0.106	0.728	0.480
480	0.116	0.128	0.838	0.515
575	0.156	0.165	0.761	0.491
700	0.112	0.124	0.621	0.441

For both series of loadings the variation in the binding energies and the Co/Zn atomic ratios at the surface for the samples calcined at  $<350^\circ\text{C}$ , is most likely to be due to variations in the concentrations of carbonate and hydroxyl groups at the surface of the sample as decomposition of the precursors took

place. At temperatures above 350 - 400°C, where the decomposition process was thought to be nearing completion, there was only a small variation in the surface Co/Zn ratios and the binding energies for the Zn2p<sub>3/2</sub> and Co2p<sub>3/2</sub> peaks became more consistent.

#### 6.2.4 Sulphided Oxides

The binding energies and the quantitative analyses obtained for the sulphided oxides are shown in Tables 6.17 and 6.18 respectively. The shape of the Zn2p<sub>3/2</sub> peaks for each sample were all very similar. Peak fitting using Gaussian curves revealed the presence of two components at *ca.* E<sub>B</sub> = 1021.6 and 1019.5 eV. The higher binding energy component was consistent with Zn<sup>2+</sup> ions in an oxide environment. The lower binding energy was thought to relate to Zn<sup>2+</sup> ions which were bonded to sulphide since the percentage contribution of this Zn(sulphide) peak decreased as the Co/Zn ratio increased.

The shape and position of the Co2p<sub>3/2</sub> peak for the 10/90 sample suggested that the cobalt was present in the 2+ oxidation state unlike the oxide where the cobalt had an oxidation state of 3+. Curve fitting of the 20/80 sample indicated that the main contribution to the Co2p<sub>3/2</sub> peak was from Co<sup>3+</sup> ions with a small percentage from the Co<sup>2+</sup> ions (*ca.* 7%). As the cobalt loading was increased to 30/70 the Co<sup>2+</sup> contribution to the photoelectron peak increased also. Again, only the Co<sup>3+</sup> ion had been previously observed in the oxides (see *Section 6.2.2*). The binding energy indicated that the Co<sup>2+</sup> and Co<sup>3+</sup> ions were present in an oxide environment. The binding energies of the 40/60 and 100/0 samples indicated the presence of Co<sup>2+</sup> ions in a sulphide

**Table 6.17** Binding Energies of the Sulphided Oxide series .Charging effects have been referenced to the O1s peak at  $E_B = 530.0$  eV The FWHM are given in parentheses.

Co/Zn	Zn2p <sub>3/2</sub>		Co2p <sub>3/2</sub>		S2p		O1s B.E.(eV)
	B.E.(eV)	%	B.E.(eV)	%	B.E.(eV)	%	
0/100	1021.4(2.6) 1019.7(2.9)	72.52 27.48			161.5(3.0)	100.00	530.0
10/90	1021.6(3.5) 1025.0(3.0)	77.97 22.03	780.2(5.0) 785.3(5.5)	71.63 28.37	161.0(4.6)	100.00	530.0
20/80	1021.5(2.9) 1019.3(2.2)	86.28 13.72	779.0(3.1) 781.6(2.2)	93.44 6.56	161.6(3.1) 167.4(4.1)	83.53 16.47	530.0
30/70	1021.2(2.7) 1019.5(1.9)	94.55 5.45	779.9(3.0) 782.6(2.2)	91.90 8.10	160.9(3.1) 167.0(3.7)	81.43 18.47	530.0
40/60	1021.6(2.4) 1019.5(1.4)	94.04 5.96	778.9(2.3) 780.9(2.6)	69.34 30.66	161.7(2.9) 166.7(4.7)	70.07 29.93	530.0
100/0			778.1(2.1) 780.4(2.8)	74.15 25.85	160.2(2.5)	100.00	530.0

**Table 6.18** Quantitative analysis for Sulphided Oxides.

	S2p <sub>Tot</sub> /Zn2p <sub>3/2</sub>	S2p <sub>Tot</sub> /Co2p <sub>3/2</sub>	S2p <sub>Tot</sub> /Zn+Co2p <sub>3/2</sub>
0/100	0.097	---	0.097
10/90	0.184	1.372	0.162
20/80	0.160	0.561	0.125
30/70	0.219	0.733	0.169
40/60	0.467	0.485	0.238
100/0	---	0.448	0.448

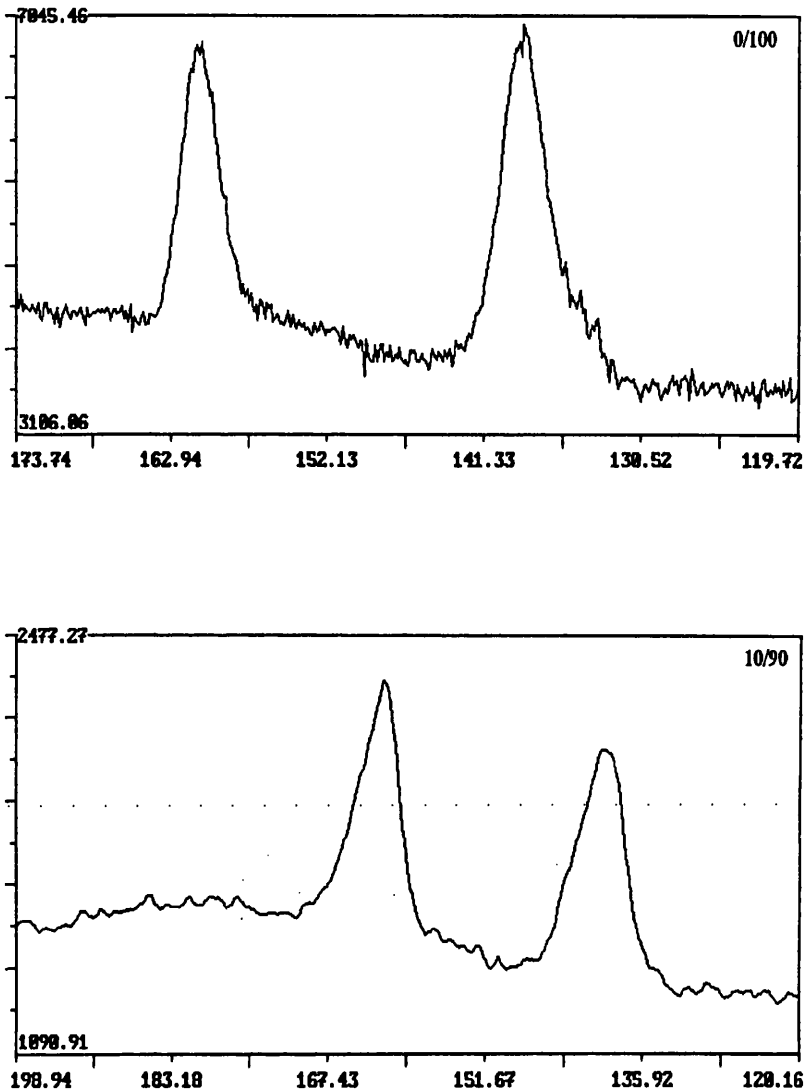
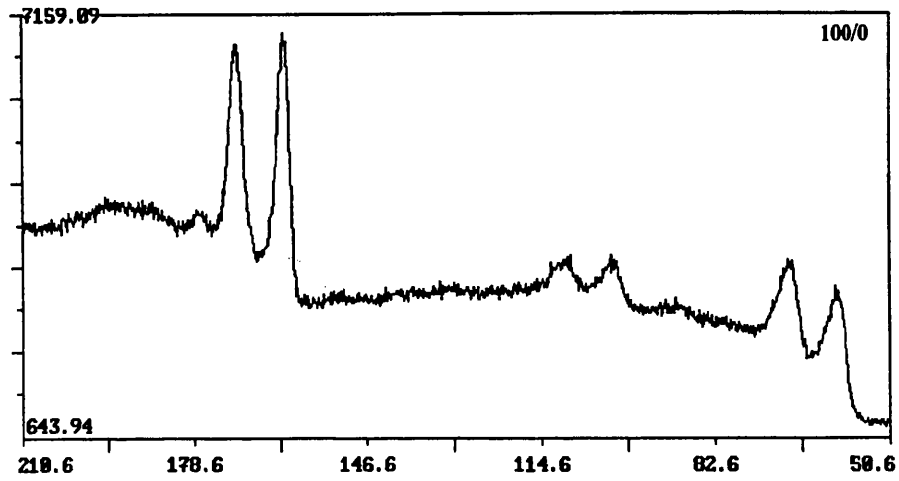
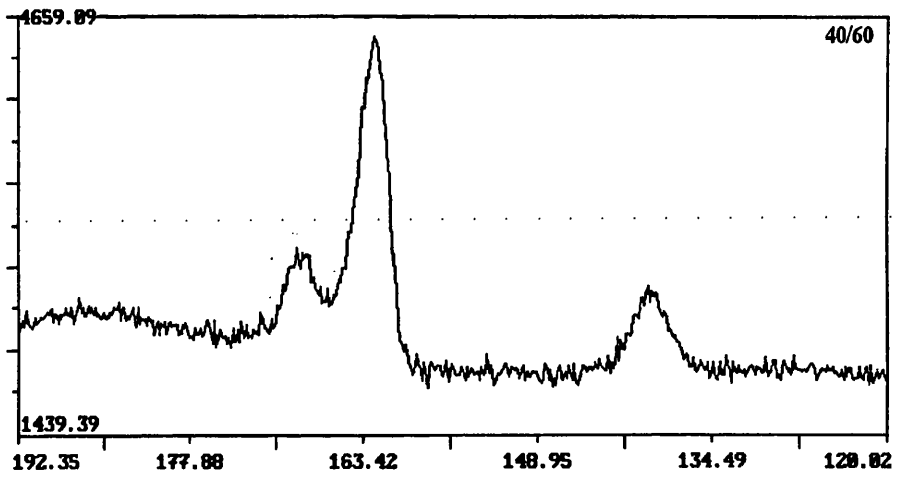
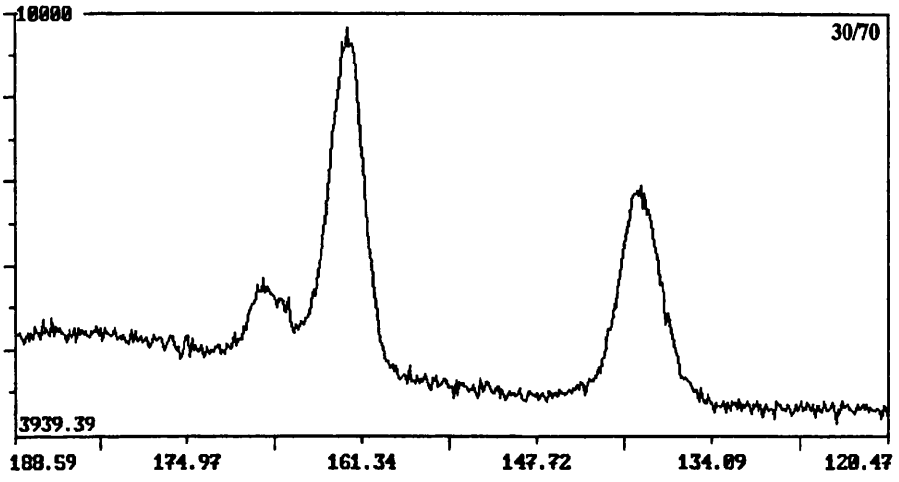


**Fig. 6.21** Sulphur 2p transitions for the sulphided oxides. In the Co/Zn 0/100 and 10/90 samples only one S 2p photoelectron peak, *ca.*  $E_B = 161$  eV, was observed. As the cobalt loading was increased a second S 2p was seen at *ca.*  $E_B = 168$  eV. The Co/Zn 100/0 sample showed two spectra superimposed due to effects of differential charging. Note the other peak present was Zn 3s, *ca.*  $E_B = 139$ eV.



environment, *ca.*  $E_B = 778.5$  eV. A small amount of  $\text{Co}^{3+}$  in an oxide environment was also indicated by the presence of the higher binding energy feature.

All the samples had an  $\text{S}^{2-}$  peak at *ca.*  $E_B = 161.0$  eV. For the mixed systems a peak at *ca.*  $E_B = 167$  eV was also observed and its intensity increased as the cobalt concentration increased, see Fig. 6.21. This was believed to be due to sulphur present as sulphate,  $\text{SO}_4^{2-}$ .<sup>84</sup> For the Co/Zn 100/0 sample it was difficult to unambiguously assign the presence of a small higher binding energy feature for the  $\text{S}^{2-}$  peak due to differential charging. Curve fitting did suggest there might be a  $\text{S}(\text{SO}_4^{2-})$  2p peak present.

The quantitative analysis, Table 6.18, showed that at the surface the sulphur content,  $S_{\text{Tot}}/\text{Total Metal}$  ratio, increased with increasing  $\text{H}_2\text{S}$  uptake, calculated on the basis of the %Reaction for each absorbent (see Section 6.1.3). The high  $\text{S}2p_{\text{Tot}}/\text{Zn}+\text{Co}2p_{3/2}$  ratio for the Co/Zn 10/90 sample compared with the 0/100 and 20/80 samples suggests that the sulphur tended to remain on the surface of the 10/90 sample. Sulphided Co/Zn 100/0 contained the most sulphur at the surface.

For the mixed systems there was an increase in the  $S_{\text{Tot}}/\text{Zn}2p_{3/2}$  ratio whilst the  $S_{\text{Tot}}/\text{Co}2p_{3/2}$  ratio passed through a maximum at the 30/70 loading. This could be indicating that most of the sulphur was associated with either the zinc component or a Co/Zn solid-solution phase. The decrease in the low binding energy feature of zinc with increase in sulphur content and the narrowing of the  $\text{Co}2p_{3/2}$  peak with increasing cobalt loading indicated that the sulphur was associated with the mixed phase rather than a zinc phase alone.

The maximum seen for the  $S_{\text{Tot}}/Co2p_{3/2}$  ratio at 30/70 suggested that this ratio could be the best for the synergic interaction of Co/Zn with respect to sulphur absorption.

After completing these XPS studies of the sulphided oxides, they were ground to a fine powder and the spectra were collected again under identical conditions to those described previously. This second study was carried out in order to investigate whether the observed effects were due to inhomogeneities in the particle sizes of the sulphided oxides. The  $Zn2p_{3/2}$  peak again showed the presence of a low binding energy feature at  $E_B = 1019.1$  eV. It was, however, considerably larger than before. Curve fitting the  $Co2p_{3/2}$  peak indicated that only the  $Co^{3+}$  ion, bonded to sulphur, was present at the surface of the samples with a Co/Zn ratio between 10/90 and 40/60.

The quantitative analyses showed no changes in the trends seen previously.

### 6.3 OPTIMISATION OF CALCINATION PROCEDURES

The precursor of nominal atomic loading 30/70, was calcined either in flowing air, 30/70-AIR or in a muffle oven, 30/70-OVEN, as described in *Section 4.6*.

The X-ray diffraction patterns of both oxides showed that each consisted of predominantly a zinc oxide phase with evidence of a 'cobalt oxide type' phase present as a minor phase. A comparison of the number and intensity of the d-spacings indicated that more 'cobalt oxide type' phase was present in the 30/70-AIR than in the 30/70-OVEN sample. The surface areas of the oxides and the %Reaction obtained after testing them for H<sub>2</sub>S removal are listed in Table 6.19. It shows that calcining in air increased both the surface area of the oxide and the H<sub>2</sub>S absorption capacity of the Co/Zn 30/70 oxide.

**Table 6.19** Summary of data obtained for oxides calcined in flowing air and in a muffle oven. The numbers in parentheses indicate the amount of Co<sub>3</sub>O<sub>4</sub> phase present. The number 1 indicates most, 2 least.

30/70	%Co (wt/wt)	%Zn (wt/wt)	Co/Zn molar	XRD	S.A. m <sup>2</sup> g <sup>-1</sup>	%Reaction	%Conversion
AIR	16.63	56.77	24/76	ZnO(major)+ Co <sub>3</sub> O <sub>4</sub> (1)	105.7	49.13	19.31
OVEN	12.22	43.57	24/76	ZnO(major)+ Co <sub>3</sub> O <sub>4</sub> (2)	94.9	47.71	14.24

The surface areas obtained for the precursors of Co/Zn 0/100 and 100/0 calcined at various temperatures, in flowing air (see *Section 4.6*), are shown in Table 6.20 and plotted in Fig. 6.22. The data showed that the surface area obtained for cobalt oxide is higher than that for zinc oxide, and for both sets of data the surface area passed through a maximum at *ca.* 150°C.

**Table 6.20** Summary of surface areas obtained for Co/Zn 0/100 and 100/0 loadings calcined at various temperatures.

Co/Zn	Temperature (°C)								
	0	100	150	200	250	300	350	400	450
0/100	51.6	53.3	157.2	131.9	73.1	40.9	29.23	16.0	9.9
100/0	150.8	161.1	220.0	195.4	118.4	82.7	83.9	60.6	51.4

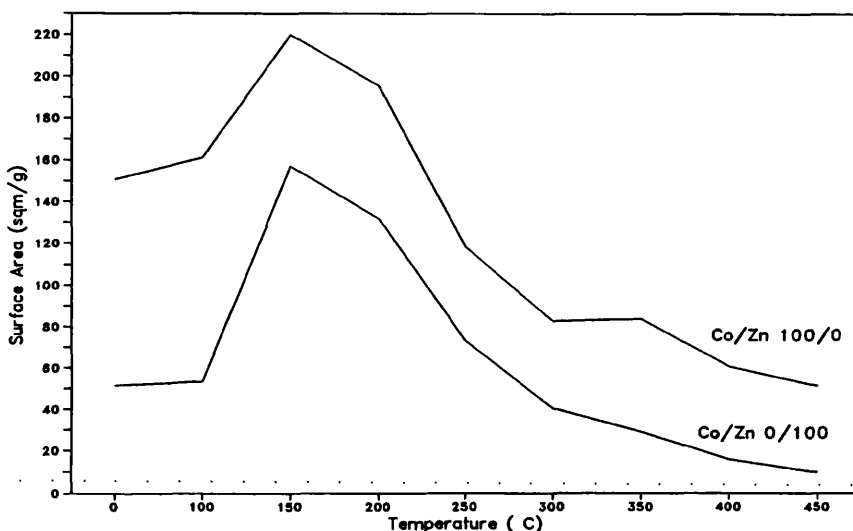


**Fig. 6.22** Plot of the Surface Area of the Co/Zn 0/100 and 100/0 samples vs. the Temperature of Calcination.

The surface areas of the 10/90 and 50/50 samples, calcined at various temperatures in the *Section 6.2.3*, were measured and are shown in Table 6.21 and Fig. 6.23. The surface area was found to pass through a maximum as the temperature of calcination of the precursor was increased. The surface area increased rapidly to a maximum of *ca.* 100 m<sup>2</sup>g<sup>-1</sup> at around 200°C. The total surface area decreased slowly at the higher calcination temperatures.

**Table 6.21** Surface Areas of 10/90 and 50/50 Cal. Var. Temps.

	Temp (°C)	100	170	200	250	310	355	400	480	575	700
Surface Areas (m <sup>2</sup> g <sup>-1</sup> )	10/90	20.1	73.2	100.1	67.4	62.0	44.1	31.7	16.2	7.1	2.3
	50/50	5.7	101.2	101.6	79.3	58.0	40.5	33.2	19.6	10.4	6.7

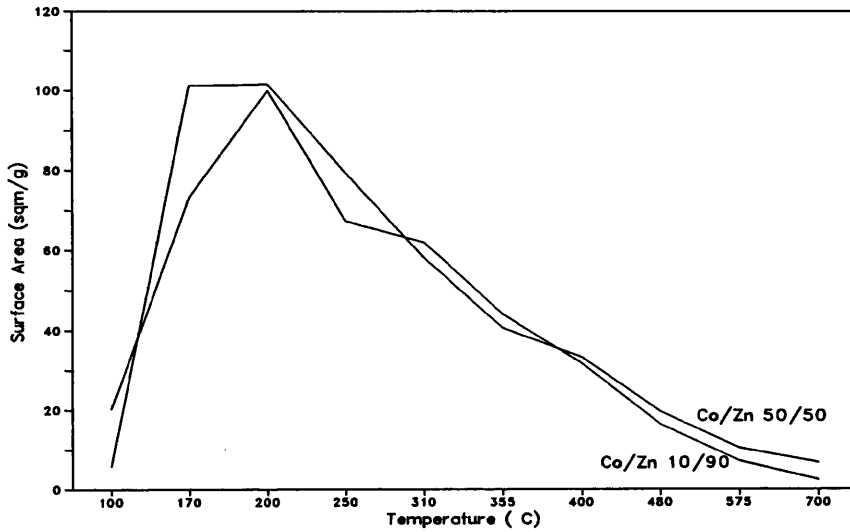


**Fig. 6.23** Plot of the Surface Area of the Co/Zn 10/90 and 50/50 samples (Section 6.2.3) vs. the Temperature of Calcination.

## 6.4 COBALT-ZINC 2nd SERIES

A new set of precursors and oxides with nominal loadings Co/Zn 0/100, 20/80, 30/70, 40/60 and 100/0 were synthesized as described in *Section 4.7*. This was to examine the sulphur absorption capacity of the pure and mixed oxides after calcination of the respective precursors at various temperatures.

### 6.4.1 Characterisation of the Precursors

The atomic absorption data, Table 6.22, showed that the Co/Zn ratios in the mixed samples were lower than expected owing to the cobalt concentration being 3-6% lower than the nominal value. Red cobalt nitrate was observed in the filtrate during the washing stage.

**Table 6.22** Summary of Atomic Absorption Data for the Precursors - 2nd Series.

Nominal Co/Zn	%Co (wt/wt)	%Zn (wt/wt)	Co/Zn molar
0/100	---	57.20	---
20/80	13.50	72.73	17.1/82.9
30/70	14.27	51.29	23.6/76.4
40/60	21.63	45.83	34.4/65.6
100/0	36.99	---	---

The d-spacings obtained for the precursors are tabulated in Table 6.23. The precursor of Co/Zn 0/100 had an X-ray diffraction pattern similar to that of hydrozincite,  $Zn_5(CO_3)_2(OH)_6$ .<sup>72</sup> The diffractogram of the Co/Zn 100/0 sample indicated that spherocobaltite was the major phase present with the structure assigned by Porta *et al.*<sup>45</sup>,  $Co(CO_3)_{0.5}(OH)_{1.0} \cdot 0.1H_2O$ , present as a

**Table 6.23** D-spacings, (Å), obtained by XRD for the precursors - 2nd Series.

Hz	Sph	Porta	0/100	20/80	30/70	40/60	100/0
6.77(100)			6.77(100)	6.77(100)	6.81(93)		
		5.06(70)					5.13(22)
3.99(20)			4.02(25)	4.04(28)			
3.66(40)			3.64(19)				
	3.55(40)				3.58(37)	3.55(39)	3.58(34)
		3.33(40)					
3.14(50)			3.17(34)	3.15(48)			
		2.94(30)					2.93(12)
2.85(30)			2.88(28)	2.86(31)	2.88(25)		
	2.74(100)				2.73(100)	2.76(100)	2.75(100)
2.72(60)			2.72(64)	2.72(99)			
2.69(20)			2.66(15)		2.69(33)		
		2.65(100)					2.67(29)
2.58(10)			2.57(33)	2.56(28)			2.57(25)
		2.53(70)					
2.48(70)			2.50(40)	2.50(50)	2.50(33)		
	2.33(20)				2.33(25)	2.34(19)	2.34(20)
2.30(20)		2.30(70)	2.31(19)	2.31(21)			2.29(18)
2.21(10)			2.21(16)	2.22(13)	2.21(12)		
	2.11(20)		2.11(15)		2.12(22)	2.12(17)	2.13(20)
2.09(5)				2.09(19)			
2.01(5)			1.99(12)				
	1.95(20)					1.96(17)	1.96(19)
1.92(30)		1.92(40)	1.92(14)	1.92(19)	1.93(20)		
	1.78(10)					1.78(10)	
	1.70(30)				1.70(33)	1.71(33)	1.71(39)

Hz - Hydrozincite  $Zn_5(CO_3)_2(OH)_6^{72}$ ; Sph - Sphero-cobaltite  $CoCO_3^{73}$   
 Porta -  $Co(CO_3)_{0.5}(OH)_{1.0} \cdot 0.1H_2O^{45}$

second minor phase. This is different from the structure obtained for the 100% cobalt loading in the Cobalt-Zinc 1st Series (*Section 6.1.1*).

The XRD patterns for the second series Co/Zn 20/80 corresponded to a hydrozincite structure. This was in accordance with the results for the *1st Series* since the actual Co/Zn ratio for the nominal 20/80 2nd series was 17/83 and a spherocobaltite phase was not detected in the first series until the actual Co/Zn ratio was 23/77. The nominal Co/Zn 20/80 2nd series precursor therefore formed a monophasic solid-solution of cobalt-containing hydrozincite.

Extra lines corresponding to spherocobaltite<sup>73</sup>,  $\text{CoCO}_3$ , were detected when the cobalt loading was increased from 20/80 to 30/70. This was accompanied by a reduction in the number and intensity of the lines which corresponded to the hydrozincite phase. The two sets of d-spacings in the 30/70 precursor were compared to the patterns of pure hydrozincite and pure spherocobaltite. Deviations in the d-spacings from the pure materials were clearly seen. This suggested that the lattice had expanded and that some cobalt was in solid solution in the hydrozincite and some zinc in solid solution in the spherocobaltite.

The diffraction pattern for the 40/60 sample corresponded to the presence of a spherocobaltite phase. As no other lines were detected it was concluded that a solid solution of zinc-containing spherocobaltite phase was present.

The data obtained from thermogravimetric analysis is shown in Table 6.24. The 0/100 sample showed a single step decomposition with a weight loss

**Table 6.24** Thermogravimetric Analysis - 2nd Series.

Co/Zn	Temperature (°C)			%loss				
	Surface H <sub>2</sub> O	Loss of structural H <sub>2</sub> O and CO <sub>2</sub>	Co <sub>3</sub> O <sub>4</sub> → CoO	150°C	↑H <sub>2</sub> O+ ↑CO <sub>2</sub>	Residue	Co <sub>3</sub> O <sub>4</sub> → CoO	
0/100	87.5	280			25.0	1.7		
20/80		290		937	21.5	18.5	1.7	1.2
30/70		305		932	3.7	21.75	2.0	2.2
40/60		310	347	942	5.0	28.75	1.2	3.7
100/0		250	275	945	6.5	23.5	2.5	4.7

of 25% at 280°C. This corresponded well to the theoretical value for the loss of H<sub>2</sub>O and CO<sub>2</sub> in the decomposition of hydrozincite to zinc oxide (26%).

The 20/80 precursor showed a large initial loss of surface water centred at 87.5°C which was completed by 150°C. This was followed by a two-stage decomposition. The first weight loss at 290°C corresponded to the loss of structural water and carbon dioxide. The second weight loss, at *ca.* 940°C, was thought to be due to the conversion of Co<sub>3</sub>O<sub>4</sub> to CoO.<sup>74</sup> The 30/70 sample again underwent an initial loss of surface water followed by the loss of structural H<sub>2</sub>O and CO<sub>2</sub> centred at 305°C and the decomposition of Co<sub>3</sub>O<sub>4</sub> at 932°C. The 40/60 sample underwent a three-stage decomposition (indicated by the shoulder on the differential curve) after the initial loss of surface water. The first loss of 18.5% weight was centred at 310°C followed by a second loss at 347°C of 10.2%, i.e. overall 28.75% (CoCO<sub>3</sub>→Co<sub>3</sub>O<sub>4</sub> 32.5%). Once again the further weight loss at 942°C was attributed to the decomposition of Co<sub>3</sub>O<sub>4</sub> to CoO.

The Co/Zn 100/0 sample underwent a three-stage decomposition. Water and carbon dioxide were lost in two stages, 20.0% at 250°C and 3.5% at

275°C. The third weight loss was at 945°C and was again attributed to the decomposition of  $\text{Co}_3\text{O}_4$  to  $\text{CoO}$ .

The initial two stage loss of the 40/60 sample, which the XRD studies had indicated to be predominantly comprised of  $\text{CoCO}_3$ , indicated that this sample possessed some structurally bound water and carbonate that was held more strongly than in the lower cobalt loading samples. They showed a single-step decomposition which indicated that  $\text{H}_2\text{O}$  and  $\text{CO}_2$  were lost simultaneously.<sup>68</sup> This idea that the hydroxide and carbonate molecules could be bound in thermally distinct regions may also be the explanation for the decomposition of Co/Zn 100/0 which lost  $\text{H}_2\text{O}$  and  $\text{CO}_2$  in two stages. The distinct regions may have resulted from the presence of the two phases indicated by the XRD patterns. Therefore the two-stage decomposition may be due to the isolated decomposition of each XRD distinct region. However it is not possible to discount the hypothesis that the two-stage weight loss of  $\text{Co}_{1-x}\text{Zn}_x\text{CO}_3 \rightarrow \text{Co}_{3-x}\text{Zn}_x\text{O}_4$  might also be due to rearrangement of the lattice during decomposition to give zinc oxide and cobalt oxide.

The temperature at which  $\text{H}_2\text{O}$  and  $\text{CO}_2$  was lost increased as the cobalt loading increased in the mixed samples compared to the 100% loadings. This suggested a synergic effect between the cobalt and zinc atoms which increased the thermal stability of the precursors.

The UV-VIS-NIR diffuse reflectance spectra showed two broad bands at ca. 520 and 1300 nm. These were attributed to the  ${}^4\text{T}_{1g}(\text{F}) \rightarrow {}^4\text{T}_{1g}(\text{P})$  and  ${}^4\text{T}_{1g} \rightarrow {}^4\text{T}_{2g}$  transitions, respectively, of a  $\text{Co}^{2+}$  ion in an octahedral environment.

The FTIR spectra for the Co/Zn 0/100, 20/80 and 30/70 loadings were all very similar to that of pure hydrozincite.<sup>75</sup> The 40/60 loading had a very strong broad stretch centred at *ca.* 1450 cm<sup>-1</sup> and two medium sharp bands at 860 and 750 cm<sup>-1</sup>. These bands corresponded to those expected for spherocobaltite<sup>75</sup>, and were also observed in the 100/0 sample. The 100/0 sample also had an additional band at 820 cm<sup>-1</sup>. All the precursors exhibited the bending and stretching modes of -OH.

#### **6.4.2 Characterisation of the Oxides**

Each precursor loading was treated at various temperatures; 150, 250, 350 and 450°C. A number in parentheses will be used to indicate the temperature at which the precursor was heat treated. Thus, for example, 20/80(350) is the precursor with Co/Zn ratio of 20 to 80, heat treated at 350°C.

The atomic absorption data obtained for the oxides is tabulated in Table 6.25. The calculated Co/Zn ratios were in good agreement with those calculated for the precursors.

The d-spacings of each 150°C heat treated sample are listed in Table 6.26. Samples calcined at 250, 350 and 450°C are listed in Table 6.27. The results show that the precursor was the only phase detected after heat treatment at 150°C and with the exception of the 30/70 sample, there was very little difference between the initial precursor and the 150°C heat treated sample. The XRD of the 30/70(150) sample indicated that the spherocobaltite contribution seen in the precursor had disappeared.

**Table 6.25** Atomic absorption data for the oxides obtained by calcination at various temperatures - 2nd Series.

		%Co (wt/wt)	%Zn (wt/wt)	Calc. Co/Zn
100/0	Pre		57.2	
	150		71.53	
	250		57.74	
	350		78.91	
	450		84.34	
20/80	Pre	13.50	72.73	17/83
	150	10.30	52.34	18/82
	250	12.00	62.76	17/83
	350	12.90	65.19	18/82
	450	12.58	63.86	18/82
30/70	Pre	14.27	51.29	24/76
	150	12.92	47.12	23/77
	250	16.86	59.16	24/76
	350	16.88	63.87	22/77
	450	17.72	57.71	25/75
40/60	Pre	21.63	45.83	34/66
	150	18.14	36.28	36/64
	250	22.49	48.00	34/66
	350	22.22	48.83	34/66
100/0	Pre	36.99		
	150	44.05		
	250	56.07		
	350	52.92		
	450	59.04		

**Table 6.26** D-spacings, (Å), obtained by XRD for 150°C heat treated samples - 2nd Series.

Hz	Sph	Porta	0/100(150)	20/80(150)	30/70(150)	40/60(150)	100/0(150)
6.77(100)			6.76(100)	6.76(100)	6.77(100)		
		5.06(70)					5.05(18)
3.99(20)			3.99(19)	4.01(19)	3.99(26)		
3.66(40)			3.67(20)	3.67(18)	3.65(22)		
	3.55(40)					3.55(44)	
		3.33(40)					
3.14(50)			3.15(36)	3.16(41)	3.15(43)		
		2.94(30)					
2.85(30)			2.86(34)	2.87(28)	2.87(37)		
	2.74(100)					2.74(100)	2.74(100)
2.72(60)			2.72(82)	2.72(84)	2.72(91)		
2.69(20)							
		2.65(100)					
2.58(10)			2.56(32)	2.56(24)			2.57(29)
		2.53(70)					
2.48(70)			2.50(40)	2.48(53)	2.49(44)		
	2.33(20)					2.33(23)	2.33(27)
2.30(20)		2.30(70)	2.31(12)	2.31(18)	2.31(18)		
2.21(10)			2.21(19)				
	2.11(20)						2.12(27)
2.09(5)			2.09(18)			2.11(17)	
2.01(5)							
	1.95(20)					1.95(18)	
1.92(30)		1.92(40)	1.91(18)	1.92(16)			
	1.78(10)		1.78(10)			1.77(11)	
	1.70(30)					1.70(38)	
		1.69(10)	1.69(19)		1.69(23)		

Hz - Hydrozincite  $Zn_5(CO_3)_2(OH)_6^{72}$ ; Sph - Sphero-cobaltite  $CoCO_3^{73}$ ; Porta -  $Co(CO_3)_{0.5}(OH)_{1.0} \cdot 0.1H_2O^{45}$

**Table 6.27** D-spacings obtained by XRD for 250,350 and 450°C heat treated samples - 2nd Series. The intensities are in parentheses.

ZnO <sup>76</sup>	Co <sub>3</sub> O <sub>4</sub> <sup>77</sup>	Sph <sup>45</sup>	0/100		20/80		30/70		40/60		100/0		
			250°C	350°C	450°C	250°C	350°C	450°C	250°C	350°C	450°C	250°C	350°C
	4.67(20)									4.69(9)		4.67(25)	4.63(31)
	3.55(40)									3.55(30)			
	2.86(40)									2.86(28)		2.85(34)	2.85(58)
2.81(37)		2.81(63)	2.81(64)	2.81(65)	2.81(69)	2.81(62)	2.81(69)	2.81(56)	2.81(54)	2.81(37)			
	2.60(44)	2.60(54)	2.60(51)	2.59(49)	2.61(40)	2.60(44)	2.60(71)	2.60(37)	2.60(43)	2.60(23)			
2.48(100)		2.48(100)	2.48(100)	2.48(100)	2.48(100)	2.48(100)	2.45(100)	2.47(100)	2.46(100)	2.47(100)		2.43(100)	2.43(100)
	2.44(100)												
	2.33(12)											2.33(13)	2.32(15)
	2.02(25)						2.02(8)	2.03(6)	2.02(11)	2.04(17)	2.03(12)	2.02(23)	2.01(37)
1.91(23)		1.91(17)	1.91(19)	1.91(17)	1.91(15)	1.91(10)	1.91(27)	1.91(11)	1.91(12)	1.91(12)	1.92(8)		
	1.95(20)									1.95(20)			
	1.78(10)									1.78(12)			
	1.70(30)									1.70(26)			
	1.65(12)											1.65(8)	1.65(15)
1.62(32)		1.62(33)	1.62(26)	1.62(29)	1.62(28)	1.62(26)	1.62(49)	1.62(21)	1.62(26)	1.62(14)			
	1.56(35)					1.56(6)	1.56(14)	1.56(11)	1.56(15)	1.56(19)			
1.48(29)		1.48(23)	1.48(22)	1.48(21)	1.47(16)	1.48(14)	1.48(32)	1.46(14)	1.48(17)	1.48(8)			
	1.43(45)						1.43(13)	1.44(9)	1.43(15)	1.44(19)			
1.38(23)		1.38(19)	1.38(16)	1.38(4)	1.38(17)	1.38(22)	1.38(28)	1.38(17)	1.38(18)	1.38(15)			

At temperatures above 150°C the precursors of the 0/100 and 100/0 loadings yielded ZnO and Co<sub>3</sub>O<sub>4</sub> respectively. As the temperature was increased the full-width half-maximum decreased whilst the overall intensity (indicated by the counts per second) increased. This suggested that the crystallinity and average particle size had increased with increasing calcination temperature.

The 20/80(250) and 30/70(250) samples showed only lines which corresponded to the pattern of ZnO. As the temperature was increased to 350°C and above, both samples were still predominantly ZnO but had additional lines which corresponded to a 'cobalt oxide type' phase. Again this 'cobalt oxide type' phase was believed to be Zn<sub>x</sub>Co<sub>3-x</sub>O<sub>4</sub> (x≤1) so the literature values for Co<sub>3</sub>O<sub>4</sub> were used for comparison. The increased temperature of calcination resulted in the the width of the peaks becoming narrower and the number and intensity of the lines which correspond to the Co<sub>3</sub>O<sub>4</sub> component increasing.

The 40/60 loading gave reflections which corresponded to sphero-cobaltite in both the 150°C and the 250°C samples. Partial decomposition had been achieved at 250°C since the 40/60(250) sample also gave reflections with d-spacings of 2.62 and 2.47 Å. These corresponded to the (002) and (101) lines in ZnO respectively. The higher temperature required for decomposition for 40/60 compared to the 30/70 loading was in accordance with the TGA data (see *Section 6.4.1*). The 40/60(350) sample gave reflections which corresponded to the patterns for ZnO and a 'cobalt oxide type' phase. The phase data of the precursors and heat treated precursors are summarised in Table 6.28.

**Table 6.28** Summary of XRD phase data.

Co/Zn	Pre.	150°C	250°C	350°C	450°C
0/100	Hz	Hz	ZnO	ZnO	ZnO
20/80	Hz	Hz	ZnO	ZnO+Co <sub>3</sub> O <sub>4</sub>	ZnO+Co <sub>3</sub> O <sub>4</sub>
30/70	Hz+Sph	Hz	ZnO	ZnO+Co <sub>3</sub> O <sub>4</sub>	ZnO+Co <sub>3</sub> O <sub>4</sub>
40/60	Sph	Sph	Sph+ZnO	ZnO+Co <sub>3</sub> O <sub>4</sub>	—
100/0	Sph+Porta+Hz-like	Sph+Porta	Co <sub>3</sub> O <sub>4</sub>	Co <sub>3</sub> O <sub>4</sub>	Co <sub>3</sub> O <sub>4</sub>

Hz - hydrozincite<sup>72</sup>; Sph - spherocobaltite<sup>73</sup>; Porta - Co(CO<sub>3</sub>)<sub>0.5</sub>(OH)<sub>1.0</sub>·0.1H<sub>2</sub>O<sup>45</sup>

The emergence of a separate ‘cobalt-oxide type’ phase is also suggested by the FTIR data. All the loadings exhibited a residual carbonate stretch at *ca.* 1385 cm<sup>-1</sup>. The intensity of this peak decreased significantly for the samples calcined at 450°C. All the samples had surface and structural water present as indicated by the bands at *ca.* 3434 cm<sup>-1</sup> and 1630 cm<sup>-1</sup>. Peaks in the fingerprint region corresponding to Co<sub>3</sub>O<sub>4</sub> at *ca.* 670, 655 and 460 cm<sup>-1</sup> were detected for the mixed samples and they became stronger as the temperature was increased (see Fig. 6.24).

The BET surface area data for all the 2nd Series samples are shown in Table 6.29. The data for each sample has been plotted against its corresponding calcination temperature in Fig. 6.25. As the temperature of heat treatment was increased there was an increase in the surface area from 15.2 and 51.6 m<sup>2</sup>g<sup>-1</sup> to a maximum of 43.1 and 126.5 m<sup>2</sup>g<sup>-1</sup> for the 0/100 and 100/0 loadings respectively at 250°C. A further increase in the temperature from 250 to 450°C resulted in the surface area decreasing to 10.4 and 29.6 m<sup>2</sup>g<sup>-1</sup> for the Co/Zn 0/100 and 100/0 samples respectively. This was probably due to sintering and an increase in particle size as suggested by the XRD data. For the mixed

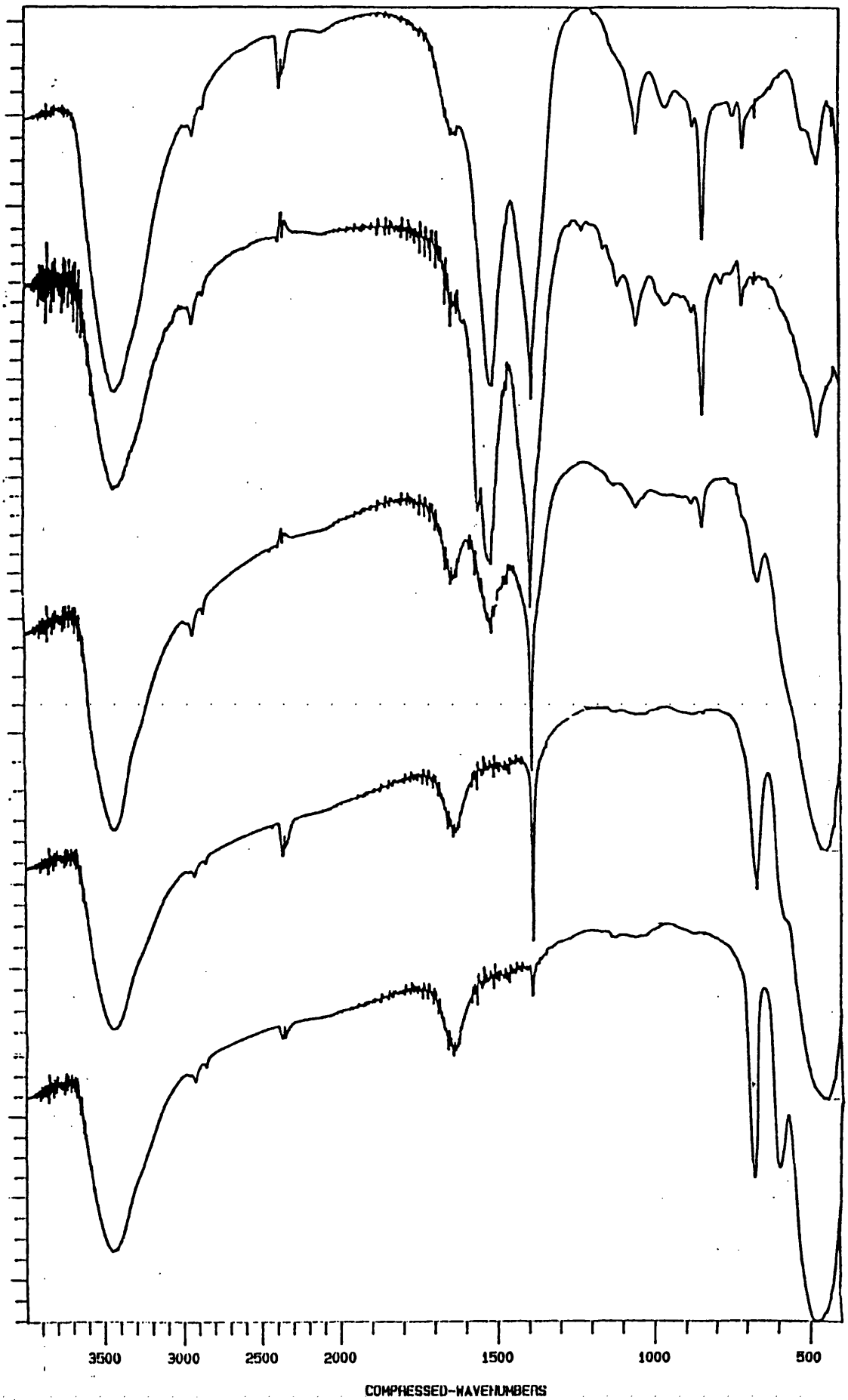


**Fig. 6.24** FTIR spectra of the nominal Co/Zn 30/70 sample (2nd Series) calcined at various temperatures.

**Table 6.29** BET Surface Area of all samples - 2nd Series.

	Temp. (°C)	S.A. m <sup>2</sup> g <sup>-1</sup>		Temp. (°C)	S.A. m <sup>2</sup> g <sup>-1</sup>
0 / 1 0 0	Pre.	15.2	4 0 / 6 0	Pre.	59.4
	150	24.5		150	52.3
	250	43.1		250	113.7
	350	26.1		350	82.5
	450	10.4		Pre.	51.6
2 0 / 8 0	Pre.	58.6	1 0 0 / 0	150	100.2
	150	53.5		250	126.5
	250	99.3		350	51.5
	350	55.3		450	29.6
	450	29.0			
3 0 / 7 0	Pre.	83.7			
	150	68.1			
	250	117.8			
	350	68.2			
	450	40.0			

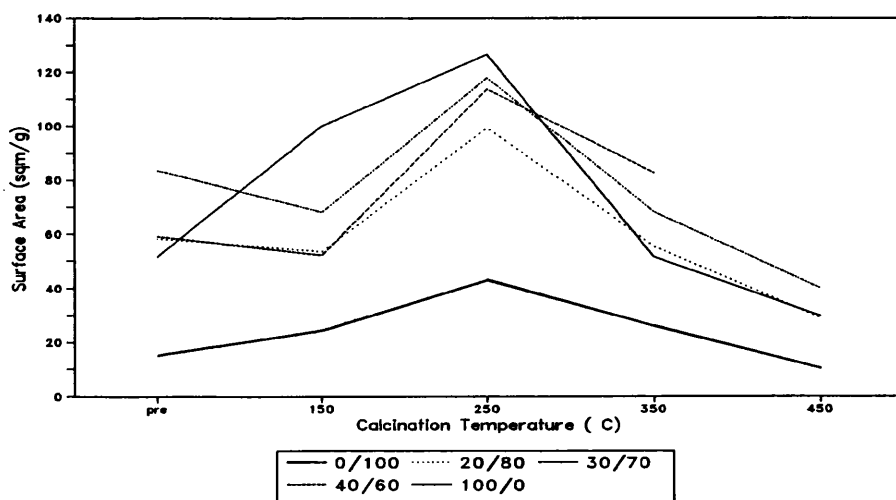


**Fig. 6.25** Plot of the Surface Area vs. the Temperature of Calcination.

Co/Zn samples there was a decrease in the surface area after the precursors had been heated to 150°C. However as the temperature was increased further, the surface area passed through a maximum at 250°C and then decreased as the temperature was increased up to 450°C. Doping ZnO with cobalt increased its surface area, with the 30/70(250) sample having the highest surface area for the mixed ratios, the surface area being 117.8 m<sup>2</sup>g<sup>-1</sup>.

### 6.4.3 Absorbent Testing

The precursors and each heat treated precursor were tested for their ability to remove 2% H<sub>2</sub>S from a nitrogen stream by the method described in *Section 4.3*. The results from these experiments are tabulated in Table 6.30.

The 'breakthrough' times for the Co/Zn 0/100 and 20/80 loadings decreased as the temperature of calcination was increased. The 30/70 and 100/0 loadings passed through a maximum at 150 and 250°C respectively. The 'breakthrough' time for the 40/60 sample decreased initially at 150°C then passed through a maximum at 250°C.

The line diagram of the %Reaction versus the temperature of calcination is shown in Fig. 6.26. The %Reaction at all temperatures was highest for the Co/Zn 100/0 loading and lowest for the 0/100. For the mixed samples the %Reactions were very similar at 250°C (*ca.* 36%). All the samples calcined at >250°C showed a decrease in the %Reaction as the temperature of calcination of the precursor was increased. For the oxides calcined at 350 or 450°C it can clearly be seen that the %Reaction increased with increase in the

**Table 6.30** Data from H<sub>2</sub>S 'breakthrough' rig - 2nd Series.

		%Conversion	%Reaction	wt. of absorbent (g)	'Breakthrough' time (mins.)	F.R.H <sub>2</sub> S (cm <sup>3</sup> min <sup>-1</sup> )	Temp. (K)
0/100	Pre	6.47	21.62	2.7500	105	1.19	291
	150	5.64	15.07	2.1751	75	1.16	294
	250	6.88	22.77	1.8070	76	1.16	294
	350	4.00	9.68	1.8796	45	1.18	293
	450	1.65	3.75	1.5143	15	1.18	293
20/80	Pre	18.42	40.18	3.3846	374	1.17	291
	150	12.80	38.39	2.1530	165	1.18	293
	250	14.44	36.32	2.0580	165	1.26	290
	350	7.58	18.25	2.1952	99	1.18	291
	450	2.36	5.79	2.1257	30	1.18	293
30/70	Pre	12.26	34.95	3.2231	235	1.18	291
	150	22.71	70.72	2.2211	300	1.18	291
	250	14.86	36.54	1.8914	165	1.20	292
	350	9.52	22.06	1.9686	110	1.20	292
	450	4.72	11.68	2.2149	62	1.20	295
40/60	Pre	14.72	40.37	3.7409	332	1.16	290
	150	6.67	22.63	2.5740	100	1.20	290
	250	13.15	34.52	2.1094	162	1.21	293
	350	11.23	29.27	2.0010	130	1.23	295
100/0	Pre	24.43	114.53	3.0200	430	1.2	290
	150	28.98	114.09	2.4950	433	1.18	293
	250	48.55	152.32	2.1817	620	1.18	291
	350	22.14	65.03	2.8791	383	1.16	289

nominal cobalt loading. For all the loadings, with the exception of the 30/70 loading, there was an initial decrease in the %Reaction, with respect to the untreated precursor, when the precursor was heated at 150°C. The 30/70 loading showed a significant increase. For all the precursors and 150°C samples

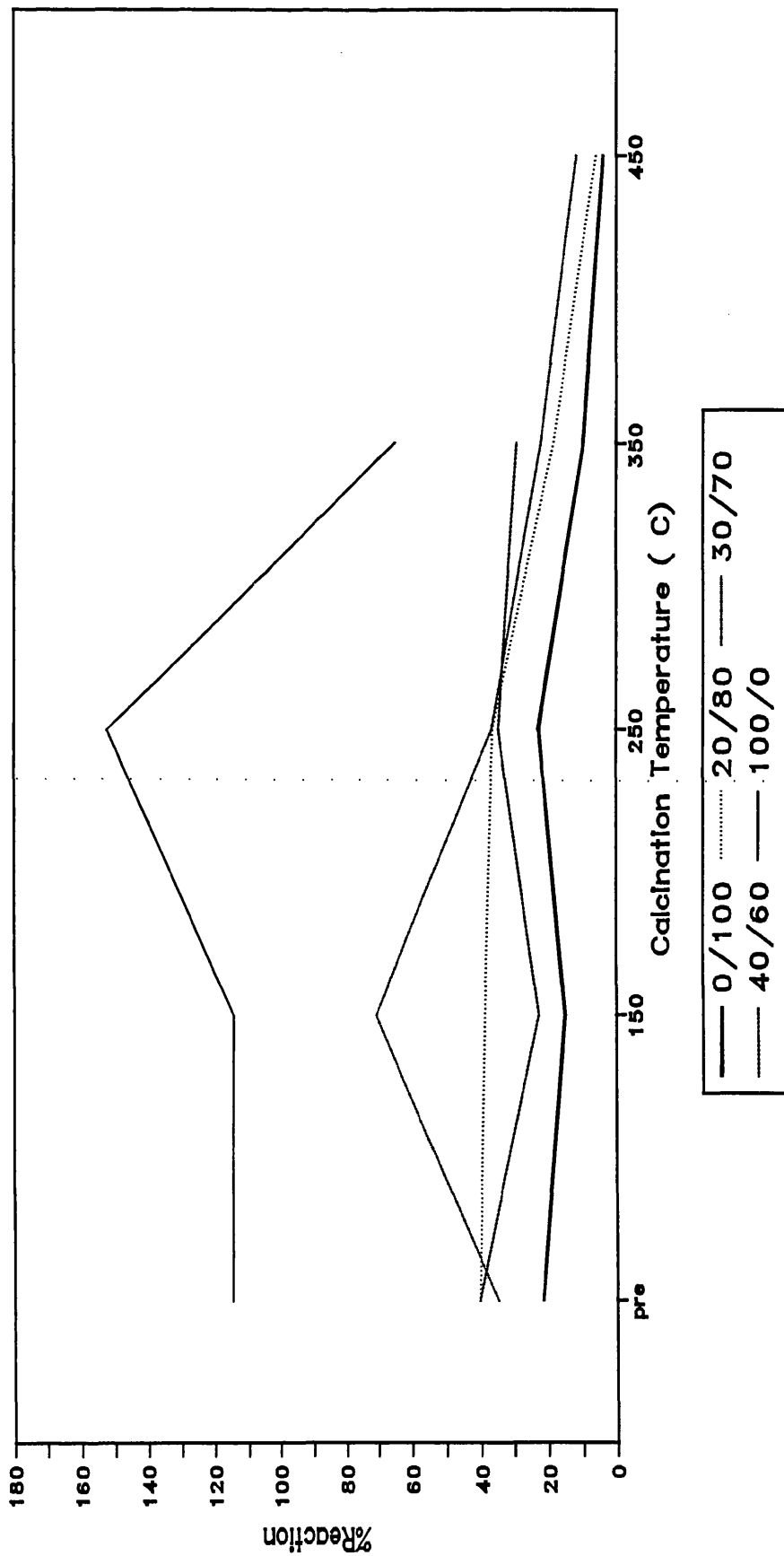
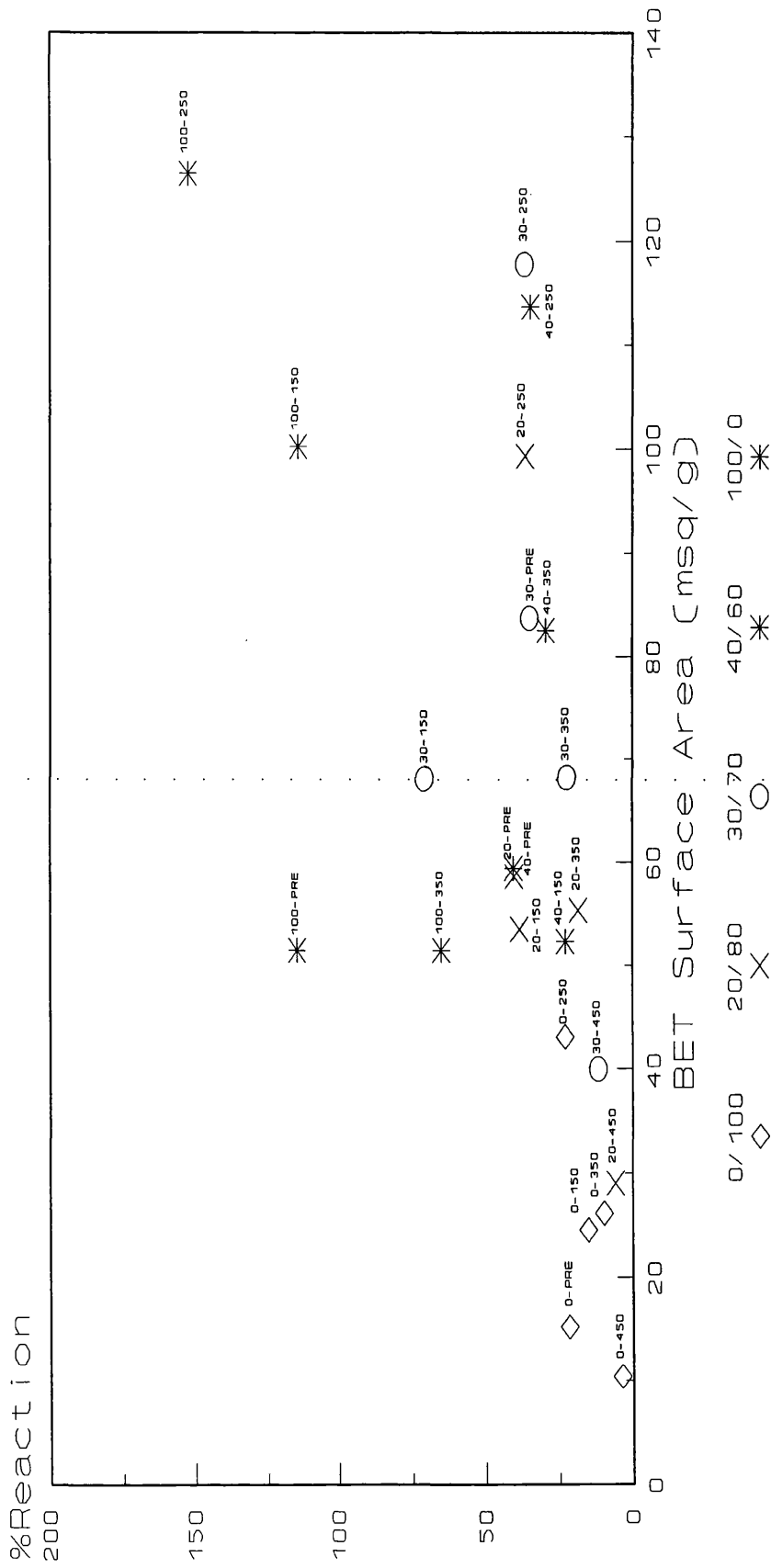


Fig. 6.26 Plot of the %Reaction vs. the Temperature of Calcination.

carbon dioxide was observed in the exit gas by G.C. analysis when it was examined before 'breakthrough' had occurred.

The %Reaction versus BET surface area has been plotted in Fig. 6.27 and then shown in an expanded form for the oxides calcined at 250°C and above (see Fig. 6.27a) and for the precursors and heat treated 150°C samples (see Fig. 6.27b). For the loadings treated at 250°C and above (see Fig. 6.27a) it can be seen that there was a linear relationship between the %Reaction and the surface area for the 0/100 to 40/60 loading. The plot for the precursors and 150°C treated samples (see Fig. 6.27b) showed no relationship between the %Reaction and the surface area.

In Fig. 6.28 the %Reaction has been plotted against the %Cobalt. The low percentage cobalt region has been expanded in Fig. 6.28a. For mixed samples treated at 350°C the %Reaction was directly proportional to the percentage cobalt in each absorbent. This was also true for the samples heat treated at 450°C except that the %Reaction was always lower with respect to the 350°C samples. With the exception of the 40/60(250), absorbents heat treated at 250°C also showed a linear relationship between the %Reaction and %Cobalt. The precursors and samples heat treated at 150°C showed no relationship between the %Reaction and %Cobalt. The 100/0(250) showed the highest %Reaction and surface area obtained for any of the samples.



**Fig. 6.27** Plot of %Reaction vs. Surface Area for the sulphided oxides in the 2nd Series.

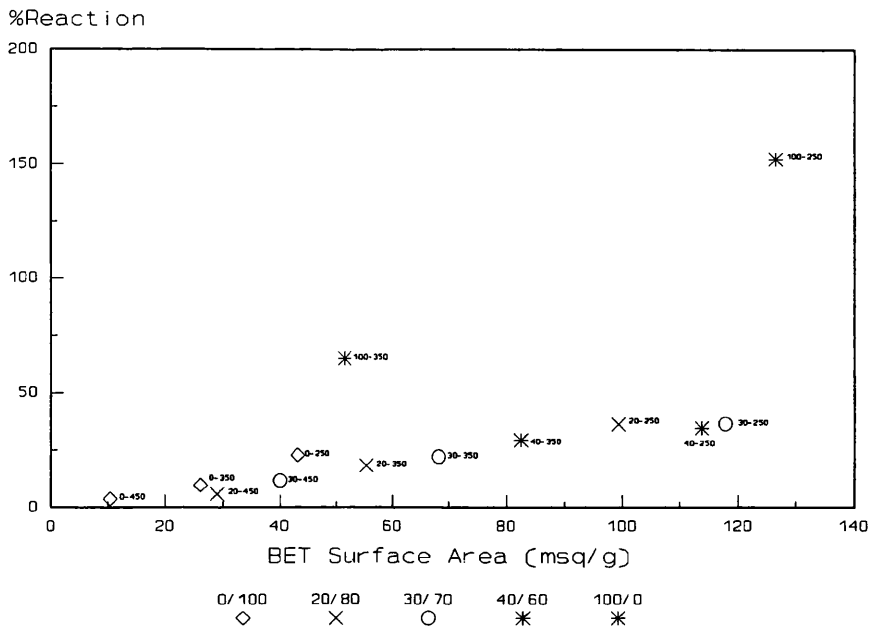


**Fig 6.27a** Expanded plot of %Reaction vs. Surface Area for sulphidated oxides in 2nd Series showing samples calcined at 250°C and above.

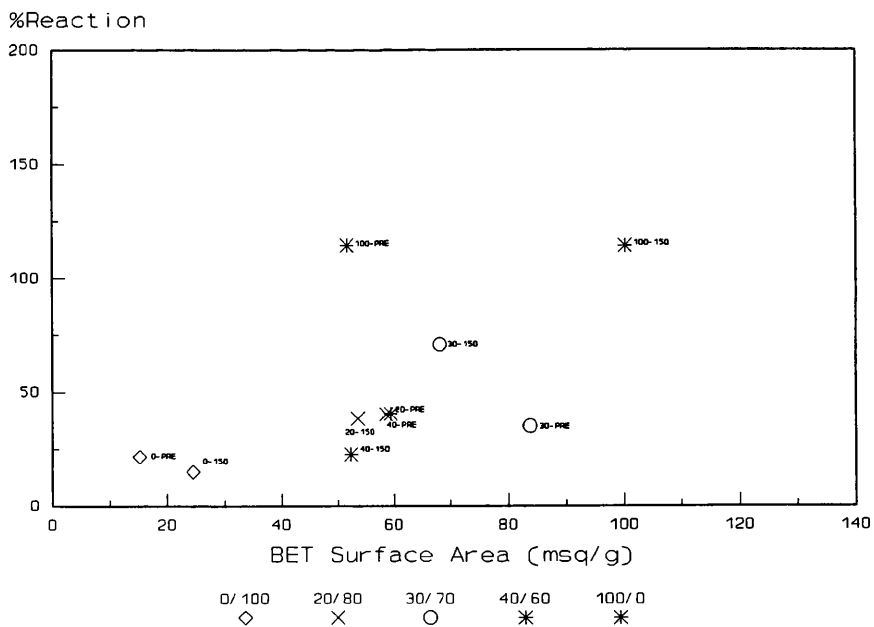


**Fig. 6.27b** Expanded plot of %Reaction vs. Surface Area for sulphidated oxides 2nd Series showing the precursors and samples heat treated at 150°C.

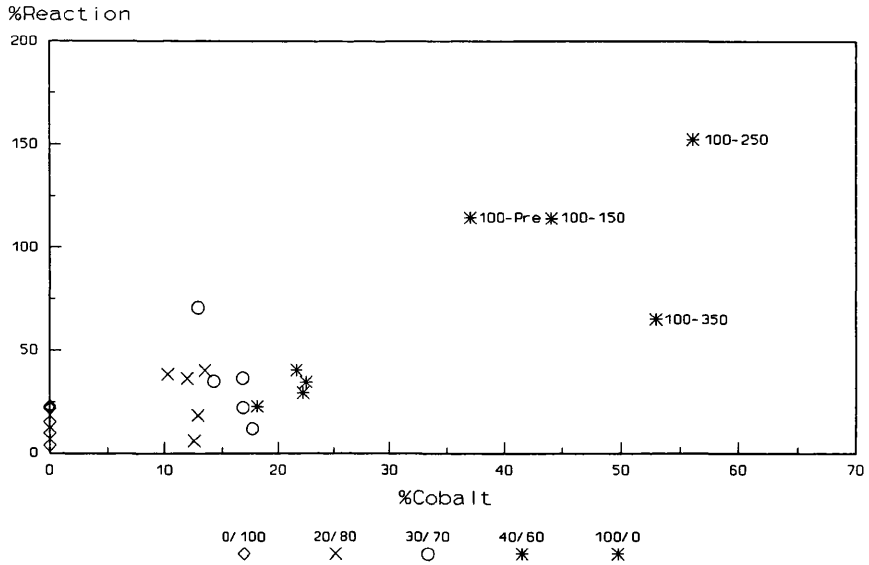


**Fig 6.28** Plot of %Reaction vs. %Cobalt for sulphided oxides in 2nd Series.

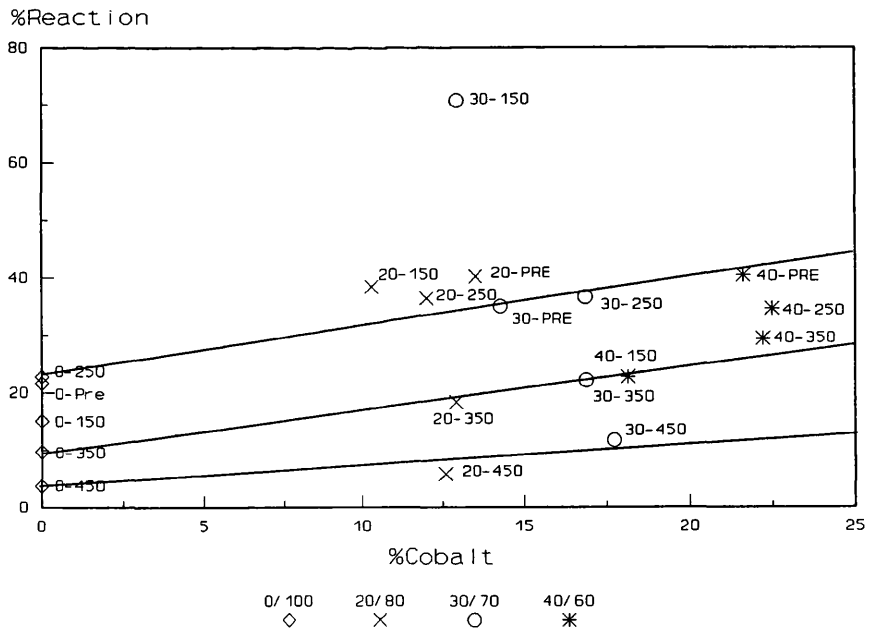


**Fig. 6.28a** Expanded plot of %Reaction vs. %Cobalt for sulphided oxides 2nd Series showing the samples with low cobalt loading.

## 6.5 AGING STUDY OF Co/Zn 30/70

The effects of aging the precipitate in the mother liquor were investigated using an initial atomic Co/Zn loading of 30/70 (see *Section 4.8*).<sup>87</sup> The samples are identified by their aging time and a prefix indicating whether they are precursors (Pre), oxides (Cal), or sulphided oxides (Sul). For example, Pre-30 refers to the sample in the precursor form which was aged for 30 minutes.

### 6.5.1 Characterisation of the Precursors

The atomic absorption results for both the precursors and the oxides are shown in Table 6.31. The results show that the cobalt concentration passed through a maximum after the precursors were aged for 30 minutes. The calculated molar ratios were lower than the expected nominal loading in every case and

**Table 6.31** Atomic Absorption and Nitrogen Analysis Data for Aged Precursors and Oxides.

Aging Time(mins)	Precursors				Oxides		
	%Co (wt/wt)	%Zn (wt/wt)	Co/Zn molar	%N (wt/wt)	%Co (wt/wt)	%Zn (wt/wt)	Co/Zn molar
Pre-0	12.6	47.6	21/79	0.15	10.0	40.7	21/79
15	14.0	40.8	26/74	—	12.5	45.2	23/77
30	14.2	40.2	26/74	—	19.1	57.2	27/73
60	13.0	46.0	22/78	0.43	16.6	57.9	24/76
180	13.8	49.2	22/78	0.15	16.8	56.3	24/76

cobalt nitrate was observed in the filtrate during the washing stage. The percentage of nitrogen found by microanalysis is also shown in Table 6.31. It showed that at short and long aging times nitrogen, probably in the form of nitrate, was incorporated into the structure. However the samples Pre-15 and

Pre-30 showed no evidence of nitrogen being present. Unfortunately the Co/Zn ratios obtained for the oxides differ significantly from the precursors. This is thought to be due to experimental error. However, the maximum Co/Zn ratio was observed after aging for 30 minutes as seen for the precursors.

The d-spacings obtained for the precursors are tabulated in Table 6.32. The diffractogram of sample Pre-0 indicated that three major phases were present. These phases were hydrozincite, spherocobaltite and the basic cobalt carbonate previously reported by Porta *et al.*<sup>45</sup> When the aging time was increased to 15 mins., i.e. Pre-15, hydrozincite and spherocobaltite were present. The number and intensity of the peaks from the spherocobaltite contribution had decreased considerably. The XRD of the Pre-30 sample indicated that again hydrozincite was the major phase present. The number and the intensity of the spherocobaltite peaks suggested that it was present only as a minor phase. When the aging time was increased to 60 minutes the predominant phase present was that of hydrozincite. The peaks in the diffraction pattern were broad suggesting low crystallinity. As the aging time was increased further to 180 minutes the crystallinity increased and a second minor phase of spherocobaltite was observed alongside the major hydrozincite phase. In the Pre-30 and Pre-60 samples peaks were also observed which corresponded to the diffraction patterns of  $Zn_4CO_3(OH)_6H_2O$ .<sup>85</sup> The indication that this phase is present could be the result of the variable nature of the hydroxycarbonate species which was fixed during precipitation.

The TGA results are summarised in Table 6.33. With the exception of the Pre-0 sample, all the differently aged samples underwent a two-stage

Table 6.32 D-spacings, (Å), of Aged Precursors. The Intensities are in parentheses.

Hz	Sph	Porta	Pre-0	Pre-15	Pre-30 <sup>†</sup>	Pre-60 <sup>†</sup>	Pre-180
6.77(100)			6.77(98)	6.77(100)	6.81(100)	6.81(90)	6.81(100)
		5.06(70)	5.08(42)				
	3.99(20)		4.02(32)		4.06(27)		
		3.69(5)	3.69(77)				
	3.55(40)		3.53(14)	3.55(23)			3.55(9)
3.14(50)			3.16(35)	3.16(35)	3.17(33)	3.16(42)	3.17(25)
3.00(10)			3.04(17)		3.03(10)		
2.85(30)			2.85(53)	2.87(61)	2.87(25)		2.87(17)
	2.74(100)						
2.72(60)			2.71(91)	2.70(39)	2.71(70)	2.72(100)	2.72(58)
		2.66(100)	2.62(100)				
2.58(10)			2.51(58)	2.52(15)	2.57(31)	2.57(50)	
2.48(70)		2.52(70)					2.51(23)
2.30(20)				2.30(12)			2.32(18)
	1.70(10)		1.71(18)		1.70(13)		1.71(8)
1.69(40)				1.68(15)			1.68(15)
1.55(10)		1.55(20)	1.55(42)	1.55(29)	1.56(19)	1.55(37)	1.55(15)

Hz - Hydrozincite,  $Zn_3(CO_3)_2(OH)_6^{72}$ ; Sph - Spheroobalbite,  $CoCO_3$ ; Porta -  $Co(CO_3)_{0.5}(OH)_{1.0} \cdot 0.1H_2O^{45}$ ; † Evidence of peak at  $d=3.72\text{\AA}$  which could be assigned to  $Zn_4CO_3(OH)_6 \cdot H_2O^{45}$ .

decomposition. Firstly, there was an initial weight loss of ca. 26%. This corresponded well to the loss of structural H<sub>2</sub>O and CO<sub>2</sub> to give the oxide. This was then followed by the decomposition of Co<sub>3</sub>O<sub>4</sub> to CoO at ca. 900°C.<sup>74</sup> The differential of the decomposition curve of the Pre-0 sample indicated that it passed through an initial two-stage loss, the first centred at 272°C and the second at 310°C. The overall percentage weight loss agreed well with the expected theoretical weight loss of structural H<sub>2</sub>O and CO<sub>2</sub>. This initial two-stage loss could have been due to the decomposition of the hydrozincite, at 272°C (*cf.* pure hydrozincite, *Section 6.1.1*) and a cobalt/zinc hydroxycarbonate species at the higher temperature. The diffractogram of the Pre-15 sample indicated that the proportion of the separate cobalt/zinc phase had decreased and the TGA of this sample showed that the decomposition was single-stage, centred at 272°C. The decomposition temperature corresponding to the loss of H<sub>2</sub>O and CO<sub>2</sub> increased from 272°C in Pre-15 to 267°C and 268°C in Pre-30 and Pre-60 respectively. However the Pre-60 had an initial decomposition temperature of only 217°C. This could be a result of the noncrystalline nature of the sample.

**Table 6.33** Thermogravimetric Analysis - Aged Precursors.

Co/Zn 30/70	Temperature (°C)		%Loss		
	Loss of structural H <sub>2</sub> O and CO <sub>2</sub>	Co <sub>3</sub> O <sub>4</sub> →CoO	↑H <sub>2</sub> O+ ↑CO <sub>2</sub>	Residue	Co <sub>3</sub> O <sub>4</sub> →CoO
Pre-0	272, 310	880	25.0	1.2	1.2
Pre-15	272	905	23.7	1.5	2.2
Pre-30	267	885	23.7	1.2	2.0
Pre-60	217	900	26.0	0.7	2.0
Pre-180	268	882	24.2	1.2	1.7

The FTIR of all the precursors exhibited the bending and stretching modes of both the carbonate and water groups. The fingerprint region had peaks which were assigned to the mineral hydrozincite.<sup>75</sup>

### 6.5.2 Characterisation of the Oxides

A summary of the d-spacings derived from the diffractograms for the oxides is given in Table 6.34. Two phases were found to be present for each aging time. The predominant phase in each sample was ZnO. The minor phase was a ‘cobalt oxide type’ phase, again taken to be  $\text{Co}_3\text{O}_4$ . By examining the (511) line of cobalt oxide, chosen because it has no interference from any ZnO lines, at  $d=1.55\text{\AA}$  it can be seen that the intensity of this line increased as the aging time was increased to 30 minutes. This suggested that the relative quantity of  $\text{Co}_3\text{O}_4$  present was increasing. As the aging time was increased further the relative ratio of the cobalt oxide phase decreased. The opposite effect was seen for the intensities of the ZnO peaks. The number and intensity of the peaks with respect to this ‘cobalt oxide type’ phase suggested that it was present in very small amounts compared to the ZnO phase.

The BET surface areas obtained for each sample are shown in Table 6.35. The surface areas obtained passed through a maximum for the Cal-30 sample at  $82.0\text{ m}^2\text{g}^{-1}$ .

**Table 6.35** BET Surface Areas of Oxides Derived from Aged Precursors.

	Cal-0	Cal-15	Cal-30	Cal-60	Cal-180
Surface Area ( $\text{m}^2\text{g}^{-1}$ )	64.4	76.4	82.0	76.6	43.3

**Table 6.34** D-spacing, (Å), of Oxides (Aged Precursors). The Intensities are in parentheses.

ZnO <sup>76</sup>	Co <sub>3</sub> O <sub>4</sub> <sup>77</sup>	Cal-0	Cal-15	Cal-30	Cal-60	Cal-180
2.81(57)		2.81(63)	2.81(55)	2.81(55)	2.82(52)	2.81(61)
2.60(44)		2.60(54)	2.60(50)	2.60(41)	2.60(39)	2.60(42)
2.48(100)		2.48(100)	2.48(100)	2.48(100)	2.48(100)	2.48(100)
	2.44(100)	2.44(48)				
1.91(23)		1.91(19)	1.91(14)	1.91(17)	1.91(13)	1.91(13)
	1.65(12)			1.65(16)		
1.62(32)		1.63(28)	1.63(25)	1.62(23)	1.63(25)	1.63(25)
	1.56(35)	1.56(9)	1.56(13)	1.56(17)	1.56(9)	1.56(10)
1.48(29)		1.48(20)	1.48(15)	1.48(17)	1.48(12)	1.48(16)
	1.43(45)		1.43(15)			1.44(10)
1.38(23)		1.38(24)	1.38(11)	1.38(17)		1.38(20)
1.36(11)		1.36(15)				1.36(10)

### 6.5.3 Sulphided Oxides

The oxides were sulphided as outlined in *Section 4.3*. The data obtained from these 'breakthrough' tests are tabulated in Table 6.36. The table shows that the %Conversion passed through a maximum for the sample aged at 30 minutes. The plot of %Conversion versus surface area is shown in Fig. 6.29. It clearly shows that the %Conversion obtained was directly proportional to the surface area of the oxide.

**Table 6.36** Data from H<sub>2</sub>S 'breakthrough' rig - Aged Precursors.

	%Conversion	wt. of absorbent (g)	'Breakthrough' time (mins.)	F.R.H <sub>2</sub> S (cm <sup>3</sup> min <sup>-1</sup> )	Temp. (K)
Cal-0	8.70	2.9516	154	1.17	291
Cal-15	11.24	1.2163	82	1.17	291
Cal-30	11.58	1.9434	135	1.17	291
Cal-60	11.09	1.2225	82	1.16	291
Cal-180	5.20	1.7957	56	1.17	291

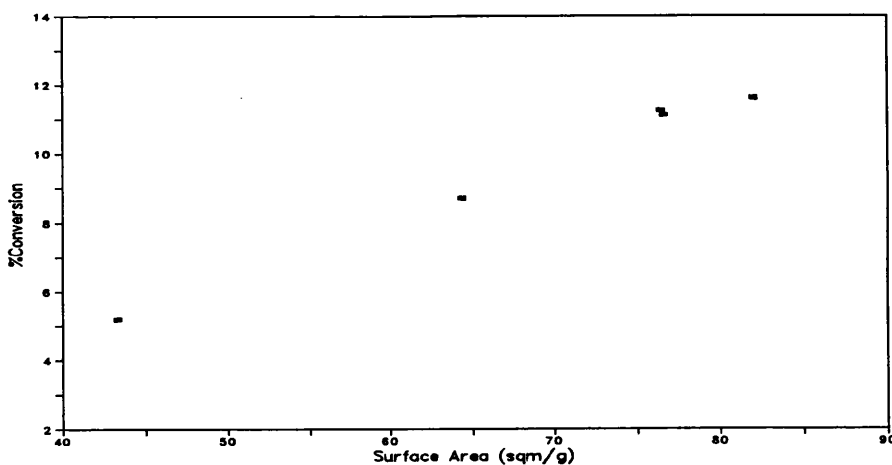


**Fig. 6.29** Plot of %Conversion vs. Surface Area (sqm/g)

## 6.6 DIFFERENT METHODS OF PRECURSOR PREPARATION

All the samples in this section were synthesized with an initial Co/Zn ratio of 30/70. The samples have been coded by the following system;

Method:pH:Co-agent-Pre,Cal,Sul<sup>‡</sup>

For example LSS8Na-Pre refers to the precursor made in *Section 4.9.1* using the low supersaturation method, at a constant pH of 8 using NaHCO<sub>3</sub> as the coprecipitating agent.

### 6.6.1 Characterisation of the Precursors

The atomic absorption data for the precursors and the oxides is shown in Table 6.37. With the exception of the HSS7Am sample, the calculated Co/Zn ratios were in good agreement with the expected nominal loading of 30/70. The HSS7Am sample had a Co/Zn ratio of 40/60. The agreement in calculated Co/Zn ratio for all the samples between the precursors and oxide series was

**Table 6.37** Atomic absorption data - precursors.

Code	Precursors					Oxides		
	%Co (wt/wt)	%Zn (wt/wt)	Molar Co/Zn	%N (wt/wt)	%Na (wt/wt)	%Co (wt/wt)	%Zn (wt/wt)	Molar Co/Zn
LSS8Am	15.78	40.97	30/70		0.01	21.82	56.18	30/70
LSS7Na	13.55	34.45	30/70		1.34	19.60	51.85	29/71
LSS8Na	9.24	25.00	29/71		8.57	14.27	38.16	29/71
LSS8NaOH	14.39	37.11	30/70		0.35	19.58	53.31	29/71
HSS7Am	19.26	32.39	40/60	0.56	0.02	24.16	38.47	41/59
HSS8Na	9.87	28.92	27/73		6.71	14.34	42.01	27/73
TM8Na	12.85	33.50	30/70	0.28	5.55	14.11	36.69	30/70

<sup>‡</sup>LSS - Low Supersaturation Method; HSS - High Supersaturation Method; TM - Titration Method. Am - ammonium carbonate; Na - sodium hydrogen carbonate; NaOH - sodium hydrogen carbonate/hydroxide.

very good. The incorporation of nitrate, determined by microanalysis, into the precursors was negligible. The sodium content of the precursors was also determined (see *Section 4.9*) since sodium containing precipitating agents were used. Table 6.37 shows that when  $\text{NaHCO}_3$  was used sodium was incorporated into the precursors. Traces of sodium were present even when ammonium carbonate was used. However, the sodium content of the ammonium carbonate precursors was negligible compared with that found when sodium based precipitating agents were used. It was hence thought to be due to impurities in the chemicals used. A higher incorporation of sodium into the precursors was encountered when the precipitation was done at a pH of 8 rather than 7. However, when NaOH was used in conjunction with  $\text{NaHCO}_3$  at pH 8, the incorporation of sodium was greatly reduced.

The d-spacings obtained by XRD for the precursors are tabulated in Table 6.38 and summarised in Table 6.39. The predominant phase present for the precursor LSS8Am was hydrozincite. There were also peaks present which indicated the presence of a second, minor spherocobaltite phase. The d-spacings for the hydrozincite phase showed deviations from the literature values, suggesting that some cobalt was in solid-solution. However, it was not possible to determine how much cobalt was in solid-solution and whether an X-ray amorphous cobalt phase was present.

When the coprecipitation agent was changed from ammonium carbonate to sodium carbonate different phases were obtained for the precursors. The LSS7Na-Pre sample gave a diffraction pattern which indicated that two phases were present. The predominant phase was that of spherocobaltite,  $\text{CoCO}_3$ ,<sup>73</sup> (*cf.*

**Table 6.38** D-spacings obtained by powder XRD for precursors *Section 6.6.1.*

Hz	Sph	SZC	LSS8Am	†LSS7Na	†LSS8Na	LSS8NaOH	HSS7Am	†HSS8Na	TM8Na
6.77(100)			6.68(94)		6.86(50) 4.84(47)	6.77(87)	6.77(100)	6.81(33) 4.82(30)	6.81(81) 4.82(42)
3.99(20)		4.83(10)					4.09(26)		
3.66(40)		3.95(100)			3.95(100) 3.66(5)		3.64(17)	3.93(100)	3.95(90) 3.70(42)
3.14(50)	3.55(40)					3.15(58)		3.54(11)	
3.00(10)			3.23(32)				3.17(30) 3.02(18)		3.16(58)
2.85(30)			2.87(24)		2.88(6) 2.81(47)	2.88(56)	2.88(30)		2.87(42) 2.79(48)
	2.74(100)	2.78(20)		2.74(100)				2.74(25)	
2.72(60)			2.72(100)				2.73(90)		2.72(100)
2.69(20)						2.70(100)	2.68(50)		
2.58(10)							2.57(30)		2.59(49)
2.48(70)			2.49(62)			2.49(67)	2.49(43)	2.50(5) 2.42(39)	2.42(61)
		2.42(25)			2.43(42) 2.32(18) 2.29(24)			2.31(19) 2.28(21)	2.31(38)
2.33(10)	2.33(20)		2.34(23)	2.34(23)					
2.30(20)							2.12(20)		
	2.11(20)		2.09(26)	2.11(23)				2.17(7)	
		2.06(13)						2.07(13)	
1.92(30)	1.95(20)	1.98(13)			2.07(17) 1.98(16)			1.98(18)	
				1.95(23)					
	1.70(30)		1.70(30)		1.71(6) 1.67(4) 1.58(13)		1.94(26)	1.70(11)	
		1.66(4)							
		1.57(12)				1.55(58)	1.55(31)		
1.56(20)			1.54(47)					1.53(16)	1.56(38) 1.53(37)
		1.53(11)			1.54(10)				

†These samples exhibited peaks which could possibly be assigned to a zinc carbonate hydrate phase.<sup>85</sup> Hz - Hydrozincite<sup>72</sup>; Sph - Spherochalrite<sup>73</sup>; SZC - Sodium Zinc Carbonate<sup>86</sup>.

*Section 6.1.1* where hydrozincite was the predominant phase for this loading when ammonium carbonate was used as the coprecipitating agent). The second, much weaker phase, was suggested by the presence of the peaks at  $d=6.86(19)$ ,  $3.17(10)$  and  $2.52(12)\text{\AA}$ . These peaks could be assigned to a zinc carbonate hydrate,  $\text{Zn}_4\text{CO}_3(\text{OH})_6 \cdot \text{H}_2\text{O}^{85}$  phase. It was thought that some of the zinc would be present in solid-solution with the spherocobaltite phase,  $\text{Zn}_x\text{Co}_{1-x}\text{CO}_3$  since the peaks attributed to the zinc carbonate hydrate phase were much weaker and could not account for the 70% zinc in the sample. The remainder of the zinc may be present as an amorphous phase.

When the pH was increased to 8 the d-spacings of the precursor LSS8Na obtained indicated that sodium zinc carbonate,  $\text{Na}_2\text{Zn}_3(\text{CO}_3)_4 \cdot 13\text{H}_2\text{O}^{86}$  was present as the major phase. This would account for the high percentages of sodium found in the precursors (see Table 6.37). The number and intensities of the remaining peaks indicated that hydrozincite and spherocobaltite were also present as minor phases. Zinc carbonate hydrate was also present as a fourth very minor phase. However, when a mixture of  $\text{NaHCO}_3$  and  $\text{NaOH}$  was used at a pH of 8 the diffraction pattern of the LSS8NaOH-Pre sample obtained indicated the presence of only hydrozincite. The cobalt could either be present in solid-solution in the hydrozincite structure or as an amorphous material.

The precursor prepared by the high supersaturation method, *Section 4.6.3*, HSS7Am, had two phases present. The predominant structure was that of hydrozincite whilst the minor phase was spherocobaltite. When the coprecipitating agent was changed to  $\text{NaHCO}_3$ , the precursor HSS8Na was

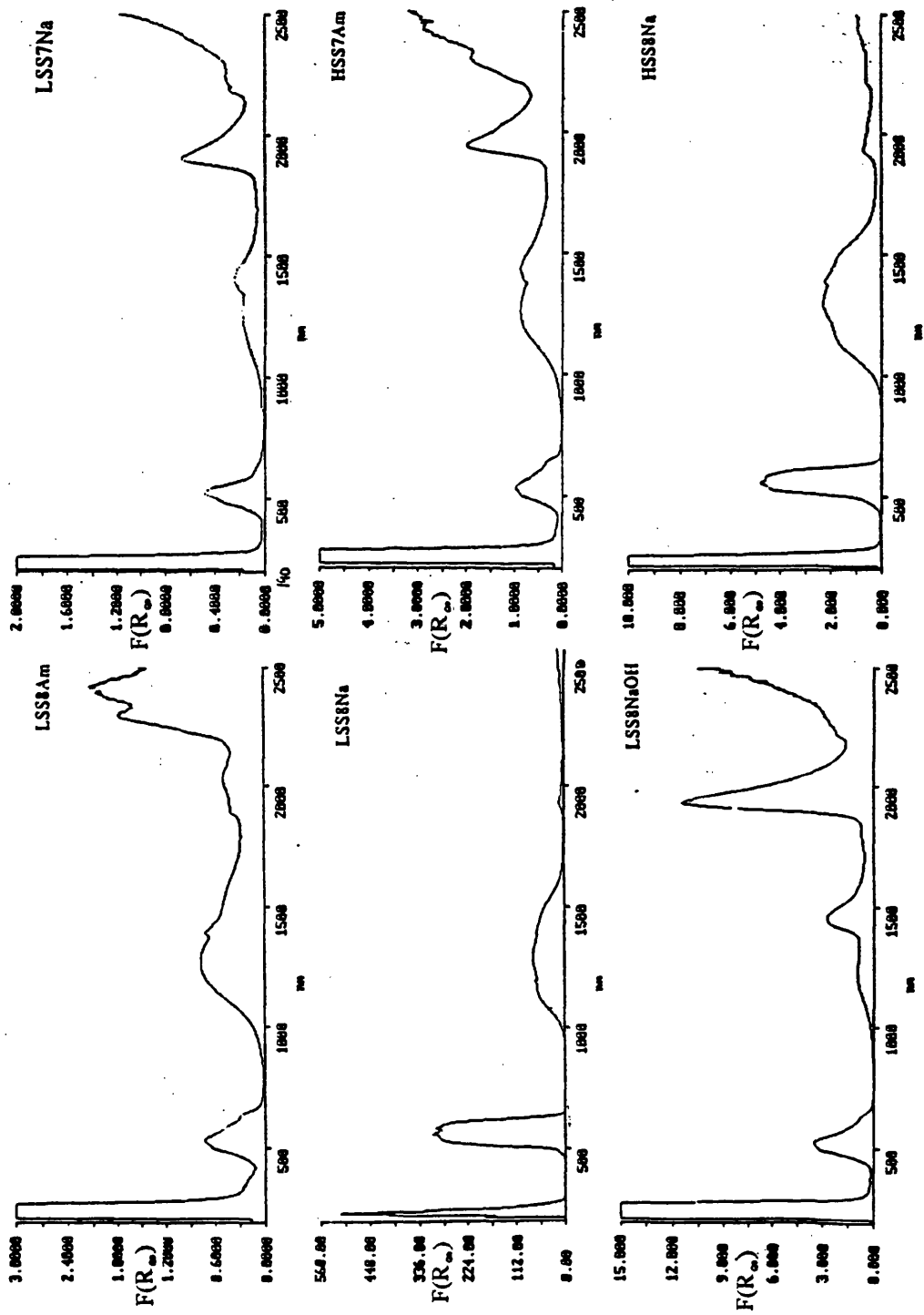


Fig. 6.30 UV-VIS-NIR diffuse reflectance spectra of the precursors obtained in Section 6.6.1.

obtained. The major phase present was sodium zinc carbonate. The remaining peaks suggested the presence of very small amounts of hydrozincite, spherocobaltite and zinc carbonate hydrate. The hydrozincite phase showed deviations from the literature d-spacings, suggesting cobalt dissolution. The assignment of the zinc carbonate hydrate phase was not clear due to very large deviations from the literature values. However both the variable nature of the (CO<sub>3</sub>)/OH species plus the dissolution of cobalt could cause deviation from the standard literature values and hence make it difficult to assign a definite structure.

The sample TM8Na-Pre, prepared according to the procedure listed in *Section 4.9.3*, was predominantly hydrozincite plus a small contribution from a sodium zinc carbonate phase.

**Table 6.39** Summary of XRD data for the precursors.

Code	Precursor
LSS8Am	Hz(major)+Sph(vw)
LSS7Na	Sph(major)+ZCH(vw)
LSS8Na	SZC+HZ(vw)+ZCH(vw)
LSS8NaOH	Hz
HSS7Am	Hz(major)+Sph(vw)
HSS8Na	SZC+HZ+Sph+ZCH
TM8Na	Hz(major)+SZC(vw)

Hz - hydrozincite; Sph - Spherocobaltite; ZCH - Zinc Carbonate hydrate; SZC - Sodium Zinc Carbonate; (vw) - very weak

The TGA data is shown in Table 6.40. All the samples, with the exception of LSS8Na, HSS8Na and TM8Na, went through a two-stage

decomposition after the initial loss of surface water. The samples LSS8Am, LSS8NaOH and HSS7Am all underwent an initial weight loss of ca. 25% at 275, 285 and 270°C respectively. This was in reasonable agreement with the theoretical weight loss of CO<sub>2</sub> and H<sub>2</sub>O for the decomposition of a hydrozincite structure to zinc oxide (26.0%). The second decomposition which occurred at ca. 890°C was thought to be due to the decomposition of Co<sub>3</sub>O<sub>4</sub> to CoO.<sup>74</sup> The sample LSS7Na underwent an initial decomposition of 27.7% at 295°C. The higher temperature for the initial decomposition suggests a synergic effect between the cobalt and zinc atoms which increased the thermal stability of the precursors.<sup>‡</sup>

**Table 6.40** Thermogravimetric data for precursors *Section 6.6.1*.

	Temperature (°C)				%Weight Loss				
	Loss of Structural H <sub>2</sub> O + CO <sub>2</sub>			Co <sub>3</sub> O <sub>4</sub> →CoO	Loss of Structural H <sub>2</sub> O + CO <sub>2</sub>		Residue		Co <sub>3</sub> O <sub>4</sub> →Co O
LSS8Am	275			910	23.0		1.8		1.5
LSS7Na	295			875	27.8		1.8		3.8
LSS8Na		325	810	975	31.0		2.5	4.0	4.3
LSS8NaOH	285			880	23.5		1.5		3.5
HSS7Am	270			867	23.0		1.5		3.8
HSS8Na	285	370	735	985	20.5	5.5	1.0	3.0	6.3
TM8Na	278	362	730	993	18.3	5.3	1.5	3.5	2.8

The remaining samples, LSS8Na, HSS8Na and TM8Na, underwent a three-stage decomposition after the initial loss of surface water. The sample LSS8Na showed the largest initial weight loss of 31.0%. This was centred at

<sup>‡</sup> Note that the temperature of decomposition is also a function of experimental conditions.<sup>68</sup> These samples were run at a lower heating rate which resulted in the initial decomposition occurring at a lower temperature. However comparison with the spherocobaltite structure in *Section 6.2* or *6.4* shows that the temperature of decomposition is still higher for the sample LSS7Na-Pre.

325°C. There were two subsequent small weight losses of 4.0 and 4.5% at 810 and 975°C respectively. The large initial loss was thought to be due to the sodium zinc carbonate decomposing to zinc oxide containing sodium. The decomposition at 810°C was thought to be the result of the presence of the sodium. The loss at 975°C would be due to  $\text{Co}_3\text{O}_4 \rightarrow \text{CoO}$ .<sup>74</sup> This two-stage decomposition in the region 730 to 1000°C was also found in samples HSS8Na and TM8Na, and was thought to be a consequence of the presence of sodium zinc carbonate in the samples. However, unlike LSS8Na, both these samples underwent an initial two-stage weight loss at *ca.* 280 and *ca.* 365°C. The lower temperature loss could be due to the loss of water and carbonate from the hydrozincite and/or sphaerocobaltite phases followed by the initial decomposition of sodium zinc carbonate at the higher temperature.

The UV-VIS-NIR DRS data are tabulated in Table 6.41 and selected spectra are shown in Fig. 6.30. The samples LSS8Am, LSS8NaOH and HSS7Am all had two major peaks at 520 nm and *ca.* 1350 nm. The peak at *ca.* 1350 nm was broad and had a second feature at *ca.* 1422 nm. The spectra were very similar to those observed for the precursors in *Section 6.1.1*. The two sets of peaks were assigned to the transitions  ${}^4\text{T}_{1g}(\text{F}) \rightarrow {}^4\text{T}_{1g}(\text{P})$  and  ${}^4\text{T}_{1g} \rightarrow {}^4\text{T}_{2g}$  for a  $\text{Co}^{2+}$  ion in octahedral symmetry.

The DRS spectra for the LSS7Na and TM8Na precursors were very similar. Again it was thought that the two spectra could be assigned to the transitions of a  $\text{Co}^{2+}$  ion in an octahedral environment. However the  ${}^4\text{T}_{1g}(\text{F}) \rightarrow {}^4\text{T}_{1g}(\text{P})$  transition occurs at *ca.* 514 nm and the  ${}^4\text{T}_{1g} \rightarrow {}^4\text{T}_{2g}$  transition at *ca.* 1300 nm. This was lower than seen previously for the samples above

**Table 6.41** Summary of DRS data obtained for the  $\text{Co}^{2+}$  transitions for the precursors.

$\text{Co}^{2+}_{\text{oct}}$	${}^4\text{T}_{1g}(\text{F}) \rightarrow {}^4\text{T}_{1g}(\text{P})$	${}^4\text{T}_{1g} \rightarrow {}^4\text{T}_{2g}$		Other Bands		
LSS8Am	520,613(sh)	1253	1387		2302	2418
LSS8NaOH	520,613(sh)	1300	1452	1941		
HSS7Am	520,613(sh)	1253	1428	1941	2302	
LSS7Na	518,613(sh)	1270	1391	1891		
TM8Na	512,613(sh)	1190	1385	1880		
$\text{Co}^{2+}_{\text{tet}}$	${}^4\text{A}_2(\text{F}) \rightarrow {}^4\text{T}_1(\text{P})$	${}^4\text{A}_2 \rightarrow {}^4\text{T}_{1g}(\text{F})$		Other Bands		
LSS8Na	554	1288		1929		
HSS8Na	543	1288	1382	1929		

which possibly indicates that the ligand field surrounding the cobalt was stronger.

The spectra for LSS8Na and HSS8Na were very similar. They showed the presence of two bands at *ca.* 549 nm and 1288 nm. The positions and shape of these bands suggested that the cobalt was again present in the 2+ oxidation state but in a tetrahedral rather than an octahedral environment. This would account for these samples having a darker, purple colour compared to the pale pink colour of the other samples. The two bands can be assigned to the  ${}^4\text{A}_2(\text{F}) \rightarrow {}^4\text{T}_1(\text{P})$  and  ${}^4\text{A}_2 \rightarrow {}^4\text{T}_{1g}(\text{F})$  transitions respectively.<sup>79</sup>

### 6.6.2 Characterisation of the Oxides

The d-spacings for the oxides have been tabulated in Table 6.42. For all the samples ZnO was the predominant phase present with a ‘cobalt oxide type’ phase, similar to  $\text{Co}_3\text{O}_4$ , being present as a second minor phase. The XRD traces for samples TM8Na, LSS8Na and HSS8Na also contained additional

**Table 6.42** D-spacings, (Å), for Oxides *Section 6.6.2*

ZnO <sup>76</sup>	Co <sub>3</sub> O <sub>4</sub> <sup>77</sup>	LSS8Am	LSS7Na	LSS8Na	LSS8NaOH	HSS7Am	HSS8Na	TM8Na
	4.67(20)			4.61(9)		4.69(14)		
2.81(57)		2.81(49)	2.81(44)	2.81(40)	2.81(60)	2.81(39)	2.79(54)	2.81(71)
2.60(44)		2.60(41)	2.60(34)	2.63(47)	2.59(46)	2.58(30)	2.59(59)	2.60(41)
2.48(100)		2.47(100)	2.48(100)	2.46(100)	2.47(100)	2.46(100)		2.47(100)
	2.44(100)						2.45(100)	
	2.02(25)	2.07(14)	2.05(6)	2.04(15)	2.02(6)	2.02(12)	2.02(18)	2.03(15)
1.91(23)		1.91(11)	1.89(13)	1.90(12)	1.91(10)		1.89(13)	1.91(16)
	1.65(12)					1.66(12)		
1.62(32)		1.62(19)	1.62(20)	1.62(19)	1.62(24)	1.62(17)	1.62(24)	1.63(29)
	1.56(35)	1.56(14)	1.56(8)	1.56(14)	1.56(17)		1.55(20)	1.56(16)
1.48(29)		1.44(14)	1.48(13)	1.48(13)	1.48(12)			1.48(16)
	1.43(45)			1.43(11)		1.44(24)		

peaks which were assigned to an unidentified phase. This third phase was present only when the precursor was synthesized at pH 8 using NaHCO<sub>3</sub> and when sodium zinc carbonate was formed as the major phase. The unidentified phase in the calcined precursors was thought to have originated from the decomposition of the sodium zinc carbonate. It is likely that it was due to a sodium zinc oxide species. There is some disagreement in the value of these extra lines between the LSS8Na and HSS8Na samples. This could be due to the higher crystallinity of the LSS8Na sample as indicated by the sharp diffractogram. The phases identified are summarised in Table 6.43.

**Table 6.43** Summary of XRD data for the oxides.

Code	Oxide
LSS8Am	ZnO(major)+Co <sub>3</sub> O <sub>4</sub>
LSS7Na	ZnO(major)+Co <sub>3</sub> O <sub>4</sub>
LSS8Na	ZnO(major)+Co <sub>3</sub> O <sub>4</sub> (vw)+??(vw)
LSS8NaOH	ZnO(major)+Co <sub>3</sub> O <sub>4</sub>
HSS7Am	ZnO(major)+Co <sub>3</sub> O <sub>4</sub>
HSS8Na	ZnO+Co <sub>3</sub> O <sub>4</sub> (vw)+?? \
TM8Na	ZnO(major)+Co <sub>3</sub> O <sub>4</sub> +??(vw)

Hz - hydrozincite; Sph - Spherochalcite; ZCH - Zinc Carbonate hydrate; SZC - Sodium Zinc Carbonate; ?? - unidentified phase, Na<sub>x</sub>Zn<sub>1-x</sub>O; (vw) - very weak

The surface areas obtained for the oxides are shown in Table 6.44. The highest surface areas obtained at 300°C were from the precursors synthesized using ammonium carbonate. It appeared that sodium retained in the precursors synthesized using sodium containing bases resulted in a lowering of the surface area. This can be seen in Fig. 6.31 where the percentage sodium found in precursors has been plotted against the surface area of the oxides. It can clearly

be seen that the higher the sodium content of the precursor the lower the surface area obtained for the oxide.

**Table 6.44** BET surface areas of oxides,  $\text{m}^2\text{g}^{-1}$ .

LSS8Am	LSS7Na	LSS8Na	LSS8NaOH	HSS7Am	HSS8Na	TM8Na
118.5	68.4	28.8	97.7	124.1	34.2	30.9

### 6.6.3 Sulphided Oxides

The oxides were sulphided as described in *Section 4.3*. The data obtained from the sulphur absorption tests has been tabulated in Table 6.45.

The %Conversion has been plotted against surface area in Fig. 6.32. This plot shows that the %Conversion increased as the surface area increased and that the highest conversions were achieved when ammonium carbonate was used as the precipitating agent. The only exception to the almost linear relationship observed between the surface area and the %Conversion was the LSS7Na-Cal sample.

**Table 6.45** Data obtained from absorption 'breakthrough' rig.

	%Conversion	wt. of absorbent (g)	'Breakthrough' time (mins)	F.R.H <sub>2</sub> S ( $\text{cm}^3 \text{min}^{-1}$ )	Temp. (K)
LSS8Am	16.89	1.7973	167	1.28	292
LSS8Na	8.24	2.3491	113	1.21	293
LSS8NaOH	14.68	2.0232	171	1.24	296
LSS7Na	15.32	1.8383	155	1.28	292
HSS7Am	17.65	1.7077	179	1.19	293
HSS8Na	9.55	2.2002	124	1.21	296
TM8Na	6.92	2.5305	104	1.19	293

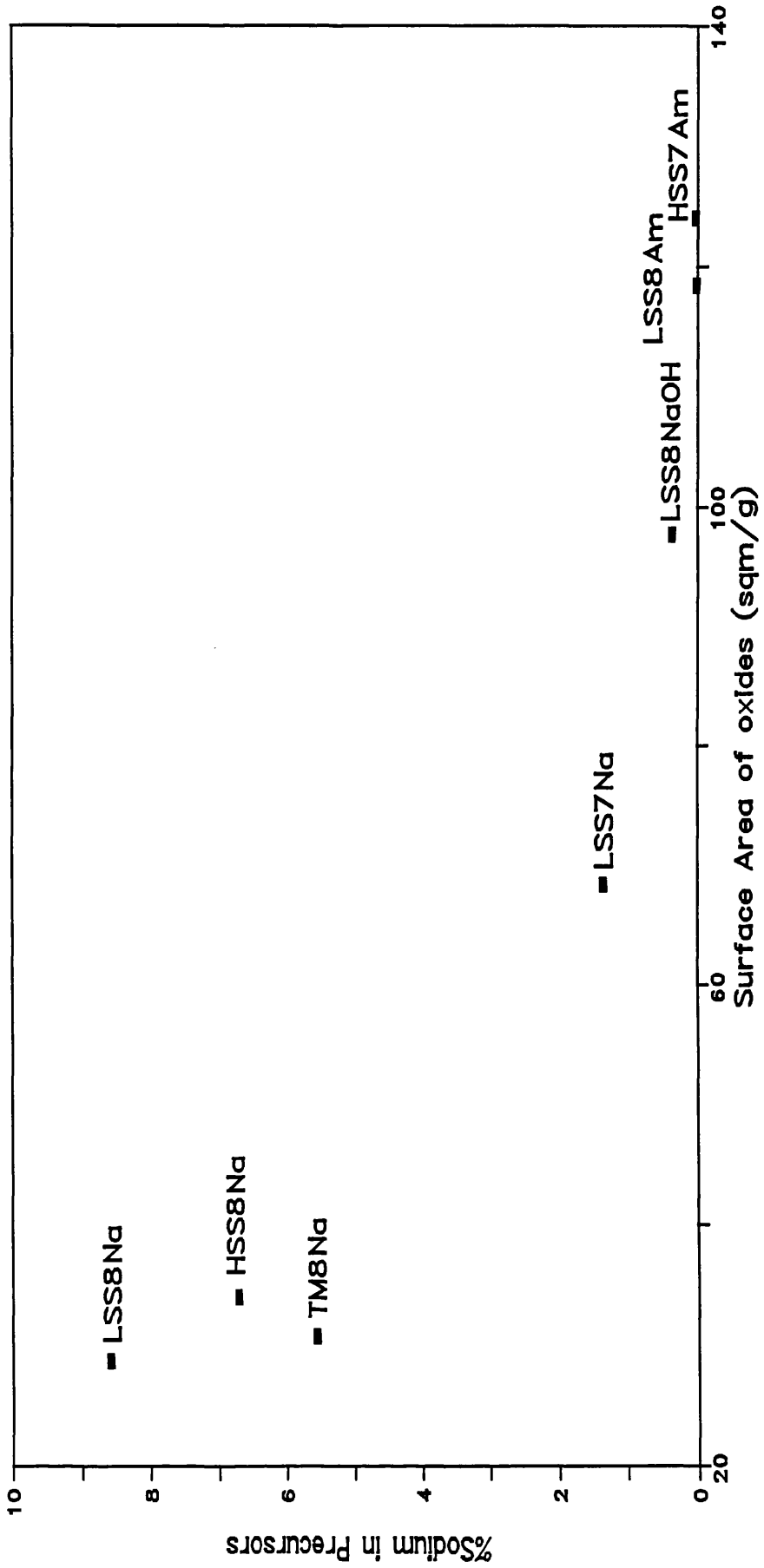
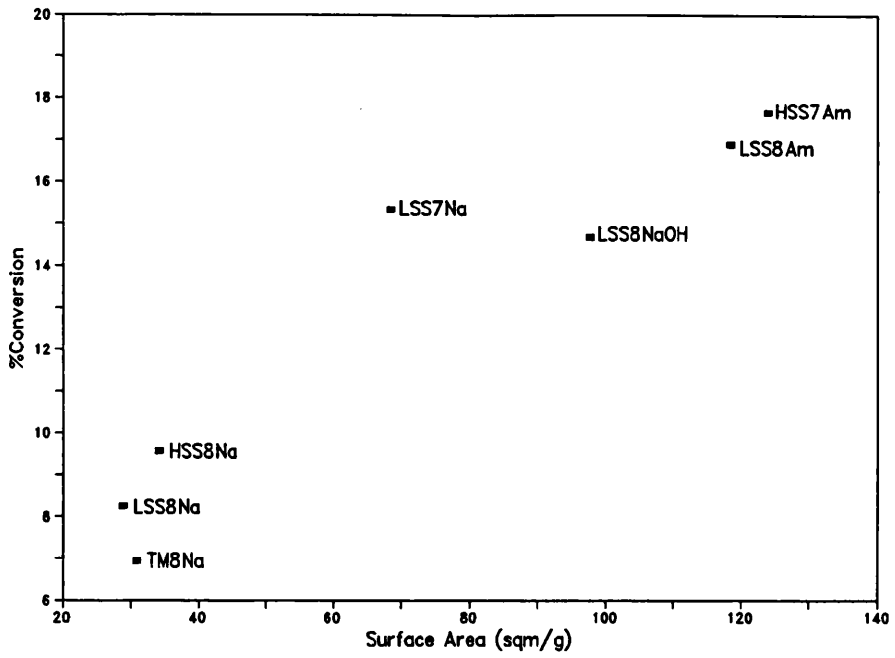
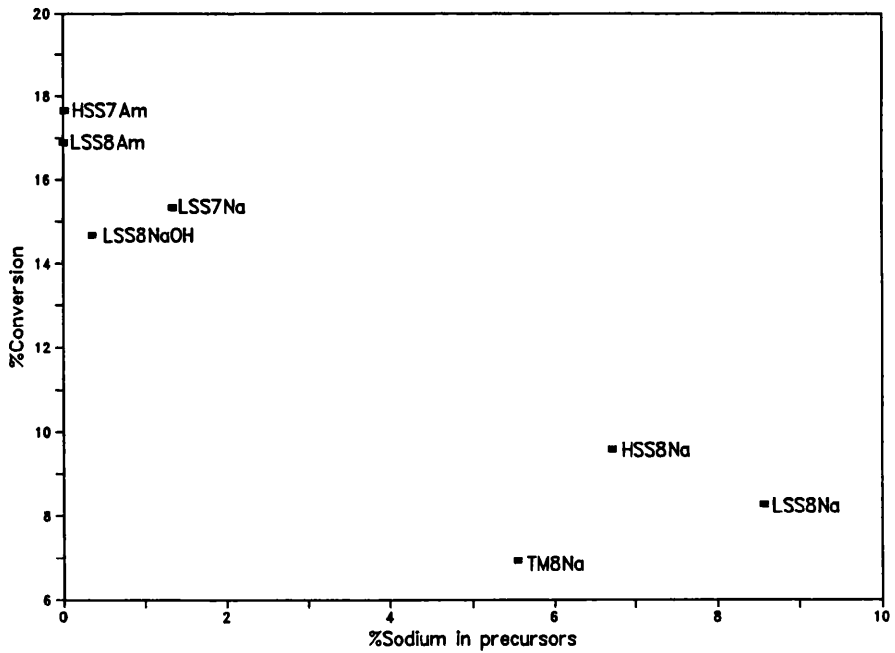


Fig. 6.31 Plot of %Sodium in the precursors vs. Surface Area of the oxides formed by thermal decomposition.

The %Conversion versus %Na has been plotted in Fig. 6.33. It shows that as the sodium content of the precursors decreased the %Conversion increased. This was as expected from the corresponding relationships exhibited for the %Na and surface area (Fig. 6.31). Once again the LSS7Na sample did not correlate with the observed trend, showing a higher %Conversion than its %Na should indicate. The %Conversion was lower than expected for TM8Na.



**Fig 6.32** Plot of %Conversion vs. Surface Area of oxides.



**Fig. 6.33** Plot of %Conversion vs. %Sodium in the precursors.

**CHAPTER 7**  
**DISCUSSION**

## 7.1 INTRODUCTION

The effect of the chemical composition and morphology of the precursors and their oxides on their sulphur absorption capacity is discussed in this chapter. The events likely to be occurring during the precipitation stage are considered and a mechanism for the formation of the precursor is formulated. Finally, some possible ways of improving the precursor preparation procedure will be discussed. With regards to the reaction between hydrogen sulphide and cobalt/zinc oxides a possible mechanism will be discussed.

## 7.2 PRECURSORS

The precipitation step outlined in *Section 1.6* consists of three stages: supersaturation, nucleation and crystal growth. Coprecipitation takes place when the solution is supersaturated and this is achieved by careful control of the pH. Nucleation is usually very fast in coprecipitation and is generally initiated on solid impurities, such as dust, which are unavoidably present in the reaction vessel. The rate of nucleation will be greatest at  $t=0$  and will decrease very rapidly until supersaturation reaches the metastable limit. Beyond this point nucleation will be negligible and the continued decline in the concentration is solely the result of growth of the crystals.<sup>35</sup> The growth process proceeds at a rate that is a function of the concentration, temperature, pH and the identity of the counterion.<sup>88</sup> A general guide to crystal growth is that those surfaces that are most prominent in a crystal are those that grew most slowly.<sup>48</sup>

### 7.2.1 Ammonium Carbonate Precursors - Standard Method

Coprecipitation of Co/Zn nitrates and ammonium carbonate generally led to the formation of hydrozincite and/or spherocobaltite (see *Section 6.1.1* and *6.3.1*).

Supersaturation was achieved for the precipitation of  $\text{Zn}(\text{OH})_2$  under the conditions used. However as only a pH of 7 was being used, precipitation with respect to the cobalt took place in the metastable region.

#### 7.2.1a Nucleation

Nucleation leading to the formation of  $\text{Zn}(\text{OH})_2$  would be almost instantaneous. The precipitation of  $\text{Zn}(\text{OH})_2$  is more favourable than that of  $\text{Co}(\text{OH})_2$  since it has a lower Solubility Constant,  $K_{\text{sp}}$ , value (see Appendix B). The rate of nucleation of  $\text{Zn}(\text{OH})_2$  is therefore expected to be higher than that of cobalt in the very early stages of the precipitation reaction. However, the precipitation of cobalt becomes increasingly more favourable as the zinc concentration in the solution falls. Theoretically the zinc concentration should fall to *ca.* 1% of its original level before  $\text{Co}(\text{OH})_2$  precipitation will occur (see Appendix B for calculations). This would lead to the formation of a relatively pure hydrozincite structure. This would account for the fact that the Pre-0 aged precursor (*Section 6.5.1*) gave a single decomposition at 272°C which is identical to that obtained for hydrozincite (*Section 6.1.1*). In reality however, the coprecipitation of  $\text{Co}(\text{OH})_2$  or a coballean  $\text{Zn}(\text{OH})_2$  will occur to some extent shortly after the  $\text{Zn}(\text{OH})_2$  precipitation. This is because the solutions required for precipitation to occur are altered by the presence of other ions. Furthermore, there may also be entrainment of solution by the  $\text{Zn}(\text{OH})_2$

precipitate and  $\text{Co(OH)}_2$  may fall out of solution under these conditions. However, as the  $\text{Co(OH)}_2$  precipitation is on the edge of the metastable region the nucleation process will be more limited than for zinc.

The hydroxycarbonates will then be formed through anion exchange, see Eqn. 7.1.



A study of the structure of hydrozincite (see *Section 1.7*) indicates that the anion exchange stage leads to the formation of layers of  $\text{Zn}_{\text{tet}}/\text{Zn}_{\text{oct}}(\text{OH})$  chemically joined by the carbonate groups. This process would probably pass through a metastable basic zinc carbonate intermediary stage but must be extremely fast as the XRD patterns gave only evidence of hydrozincite, basic cobalt carbonate and spherocobaltite for the Pre-0 sample (0 mins. aged) reported in *Aging Study of Co/Zn 30/70 Loading, Section 6.5*. The anion exchange step is given credence by the disappearance of the basic cobalt carbonate contribution in the XRD patterns as the aging time was increased to 15 minutes. However, the XRD patterns would not have shown evidence of any amorphous material which may be present in the precursor and therefore cannot be discounted.

The XRD of the Co/Zn 100/0 sample showed only the presence of the metastable basic cobalt carbonate,  $\text{Co(CO}_3)_{0.5}(\text{OH})_{1.0} \cdot 0.1\text{H}_2\text{O}$ , as determined by Porta et al.<sup>45</sup> They synthesized their 100% cobalt precursor at pH 8 and this resulted in the  $K_{\text{sp}}$  curve shifting to the right (see Fig. 1.11). Therefore nucleation would have been more extensive before the  $\text{Co}^{2+}$  concentration reached the metastable region. This resulted in more time for anion exchange

to occur and this led to the formation of spherocobaltite as the predominant phase with the metastable phase present only in very small amounts. The precipitations described in this thesis for Co/Zn 100/0 were carried out at a pH of 7. Under these conditions the rate of nucleation of  $\text{Co}(\text{OH})_2$  would be lower than in the Porta preparation since the precipitation would occur under metastable supersaturation conditions. The precursor yield for the Co/Zn 100/0 was therefore low compared to the other yields obtained for the other loadings. However, in the mixed samples the precipitation of zinc hydroxide provided nucleation points for the precipitation of cobalt hydroxide. This is evidenced from the presence of spherocobaltite rather than a metastable product when mixed Co/Zn ratios are used which have a high cobalt content. The presence of the zinc provides the nucleation points in sufficient time for anion exchange to take place. Furthermore, the phase observed by Porta et al.<sup>45</sup> was again observed when the cobalt concentration was increased from Co/Zn 70/30 to 90/10 indicating that the nucleation step was slower in this case.

### ***7.2.1b Crystal Growth***

The zinc concentration would eventually fall into the metastable region and crystal growth would begin on the predominantly zinc rich Zn/Co hydroxide nuclei. At low Co/Zn ratios where only the hydrozincite structure was formed, the  $\text{Zn}^{2+}$  concentration in solution would decrease as the hydrozincite crystals grew. Eventually the precipitation of  $\text{Co}^{2+}$  would be favoured over that of  $\text{Zn}^{2+}$  and this would result in an increase in concentration of the cobalt at the surface relative to that in the bulk. Evidence for this mechanism is provided by the

observed surface segregation of cobalt detected by XPS (*Section 6.2*). Fig. 7.1 is a diagram of the eventual Co/Zn distribution in a precursor crystal. An alternative explanation for the segregation of cobalt at the surface could be the result of strain in the structure. However, the ionic radii for  $\text{Co}^{2+}$  and  $\text{Zn}^{2+}$  are of similar size (0.078 nm and 0.074 nm respectively<sup>14</sup>) with the octahedral positions in the hydrozincite structure suffering no significant distortion.<sup>46</sup> It is therefore unlikely that strain was the driving force for segregation.

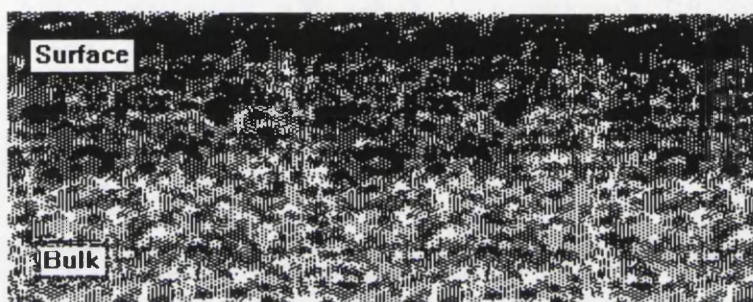


**Fig. 7.1** Diagram of the Co/Zn distribution in a precursor pellet. The cobalt is shown in black.

At Co/Zn ratios where hydrozincite and spherocobaltite phases were present together, incorporation of cobalt into the hydrozincite structure would occur from the aqueous phase which in turn would be replenished by redissolution of the spherocobaltite, i.e. the structure which has the lowest lattice stability. This depletion of the spherocobaltite phase is evident from the decrease in its contribution to the XRD patterns as the aging time was increased from 0 to 30 minutes, see *Section 6.5*. Only the hydrozincite structure was seen at 60 minutes. However, the Co/Zn ratio decreased as the

aging time increased and a spherocobaltite phase reappeared. It is possible that the  $\text{CO}_3^{2-}$  concentration could have dropped to below its  $K_{sp}$  as the aging time increased to greater than 30 minutes. This would cause the Co/Zn carbonate equilibrium to shift to the right, resulting in redissolution of cobalt and zinc. As their concentration increases in the aqueous phase the precipitation of hydroxides would again become favourable and the process would cycle again. This would again result in the precipitation of  $\text{Zn(OH)}_2$  being slightly more favourable and cause to the Co/Zn ratio in the precursor to drop.

### *7.2.1c Thermogravimetric Analysis*

The TGA of the Pre-0 sample gave a peak at 272°C with a shoulder at 310°C. The peak at 272°C corresponded well to the loss of structural water and  $\text{CO}_2$  by pure hydrozincite. The loss of the  $\text{H}_2\text{O}$  and  $\text{CO}_2$  occurred simultaneously, hence giving the single step decomposition.<sup>68</sup> The TGA data for the 1st and 2nd Co/Zn series (Tables 6.4 and 6.24 respectively) showed that the initial decomposition occurred in a single step even when two phases were present. The presence of a tail in the differential of the decomposition curve indicated that decomposition commenced at a lower decomposition temperature in the mixed carbonates. This was presumably due to the decomposition of the thermally less stable cobalt carbonate phase. The loss of  $\text{H}_2\text{O}$  and  $\text{CO}_2$  from an amorphous phase would also be expected at similar temperatures. However, it can be seen that the centre of this decomposition passed through a maximum with increasing cobalt concentration. This could possibly be due to the synergic effect of cobalt and zinc being in intimate contact in either the hydrozincite or

sphero-cobaltite phase. However, as the cobalt concentration was increased further some of the cobalt was not associated with the zinc and this resulted in the Co-Zn interaction becoming diluted and hence a reduction in the precursor thermal stability. Therefore the presence of the shoulder on the TGA curve at 310°C could be accounted for by the hypothesis that two distinct Co/Zn ratios were present. These distinct Co/Zn ratios may have resulted from the initial preferential nucleation of Zn(OH)<sub>2</sub> nuclei which is superseded by Co/Zn(OH)<sub>2</sub> precipitation. For example, although sphero-cobaltite was the only phase detected by XRD for the Co/Zn 40/60 2nd Series, TGA analysis showed that there was a two-stage weight loss with peaks at 310 and 3470°C. This was believed to be evidence of two distinct mixed Co/Zn regions. It is this separate Co/Zn phase which probably accounts for the shoulder observed in the TGA at higher temperatures.

Under these conditions of coprecipitation the highest single phase cobal-tean hydrozincite structure was obtained for Co/Zn ratios  $\leq 17/83$ . However it can be seen from the TGA data (Table 6.4) that the temperature of decomposition increased further as the percentage of cobalt increased. This suggests that more cobalt was incorporated into the hydrozincite structure which led to a further increase in the thermal stability. At cobalt loadings 20 - 40%, cobalt was distributed in both hydrozincite and the zincian sphero-cobaltite structures.

It can be seen in the *1st Series* that the TGA studies indicated the presence of two distinct mixed Co/Zn regions for the 20/80 and 40/60 loadings

but not the 30/70. This is thought to be an effect of the aging time, i.e. human error for the 30/70 ratio.

The initial two-stage loss seen for the Co/Zn 100/0 2nd series could be due to the loss of H<sub>2</sub>O and CO<sub>2</sub> first from basic cobalt carbonate and spherocobaltite and then a similar loss from the thermally more stable hydrozincite-like structure that is indicated by the XRD pattern.

#### ***7.2.1d Structure of Cobalt Doped Hydrozincite***

The cobalt was found to occupy exclusively the octahedral sites in the hydrozincite structure. This is in accordance with results obtained for Cu/Zn hydroxycarbonates where copper atoms were found to be present only in the octahedral positions in aurichalcite, (Cu,Zn)<sub>5</sub>(CO<sub>3</sub>)<sub>2</sub>(OH)<sub>6</sub>.<sup>32</sup> This is the result of the copper and cobalt adopting their preferred coordination of 6 and the zinc atoms their preferred coordination of 4.

The tetrahedral Zn-O bond (1.95Å) in hydrozincite is significantly shorter than the octahedral bond (2.10Å) suggesting that tetrahedral bonds are more covalent.<sup>46</sup> Substitution of cobalt into the octahedral positions would account for the increase in ionicity, observed from the satellite/main peak ratio and the satellite-main peak separation of the Co2p<sub>3/2</sub> peak in the XPS analysis (see *Section 6.2.1*), as the cobalt loading was increased. The carbonate group binds the complex sheets together in a three dimensional network by sharing a corner of the Zn(3) tetrahedron occurring away from the sheet and a corner of the Zn(1) octahedron occurring in the next sheet above; the third corner is hydrogen bonded to one OH(1) and two OH(2), i.e. octahedral zinc atoms. It

is therefore likely that the cobalt would substitute into these octahedral positions and the effect of the substitution on the hydrogen bonding and the increase in ionicity would have led to the increase in thermal stability.

### **7.2.2 Ammonium Carbonate Precursors - Variations**

Preparing the precursor at a pH of 8, sample LSS8Am (see *Section 6.6*), led to a greater inclusion of cobalt into the hydrozincite structure, <30%. This is suggested by the XRD studies which showed hydrozincite to be the predominant phase (though it is not possible to rule out an amorphous cobalt phase). This greater inclusion was probably a direct result of the precipitation of the cobalt occurring deeper in the supersaturation region than before (see *Section 7.2.1a*). Fast addition of the reactants, sample HSS7Am, favoured cobalt rather than zinc inclusion in the precursor. The rapid mixing of the two solutions led to a very highly mixed system which resulted in a very high rate of nucleation compared to that for the low supersaturation samples. This probably resulted in more cobalt being included in the cores of the many abundant crystal nuclei where it was unaffected by the later effects of aging redissolution.

### **7.2.2 Sodium Carbonate Precursors**

Due to the problems encountered with redissolution of the ammonium carbonate derived precipitates at high pH, i.e.  $\geq 8$ , precursors of nominal Co/Zn ratio 30/70 were synthesized using  $\text{NaHCO}_3$ .

As the coprecipitation was carried out at a pH of 8 the supersaturation conditions required for  $\text{Co}(\text{OH})_2$  precipitation were readily satisfied. This would result in intimately mixed  $\text{Co}/\text{Zn}(\text{OH})_2$  solid solutions. The hydroxides would then undergo anion exchange as before to give a metastable basic cobalt/zinc carbonate phase.

In the reaction of zinc nitrate and sodium carbonate to form hydrozincite, sodium zinc carbonate is thought to be produced as an intermediate (see Fig. 7.2).<sup>89</sup> The cobalt solid solutions could be further enhanced by the aging of metastable basic cobalt/zinc carbonate and sodium zinc carbonate to give cobalt doped hydrozincite (*cf.* aging amorphous  $\text{Cu}_2(\text{CO}_3)_x(\text{OH})_{4-2x}$  and sodium zinc carbonate led to the formation of aurichalcite<sup>89</sup>). The very distorted zinc carbonate hydrate structure seen by the XRD patterns could be an intermediate of this sodium zinc carbonate to hydrozincite transition. The presence of the sodium zinc carbonate in the precursors, LSS8Na, HSS8Na and TM8Na could be accounted for by the short aging time of 30 minutes employed (*cf.* 90 minutes for the Cu/Zn system<sup>89</sup>). However, when a mixture of  $\text{NaHCO}_3/\text{NaOH}$  was used as the coprecipitating agent only a hydrozincite-like phase was observed by XRD. This could possibly be the result of a suppression of the sodium zinc carbonate route in favour of the route outlined in the *Section 7.2.1*.

Dissolution of cobalt in the sodium zinc carbonate, hydrozincite, zinc carbonate hydrate phase plus zinc solid solution in spherocobaltite phases seems probable unless the cobalt is present only as an X-ray amorphous phase.

Coprecipitation at pH 7 greatly affected the final precursor structure. The XRD of the precursor LSS7Na showed that the cobalt/zinc carbonate (spherocobaltite-like) structure was the predominant phase present. It appears that the presence of the Na<sup>+</sup> ions can force the adoption of a hydrozincite-like

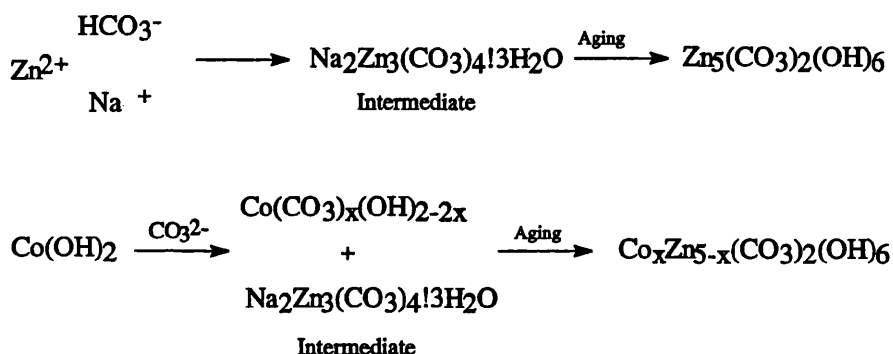


**Fig. 7.2** Diagram of the steps involved in the precipitation of NaHCO<sub>3</sub> derived precursors.

structure irrespective of the Co/Zn loading at pH ≥ 8 and a spherocobaltite-like structure at a pH < 8. Klissurski & Uzunova<sup>42</sup> synthesized a hydrozincite structure at pH 9 using Na<sub>2</sub>CO<sub>3</sub>, which had a Co/Zn ratio of 67/33. It should be noted that both increases in the ionic strength of the aqueous solution and complex formation tend to increase the solubility of the precipitate over the value calculated from the solubility product alone. Thus, for example, the CO<sub>3</sub><sup>2-</sup> concentration decreases as the pH increases.

### 7.3 OXIDES

Atoms on the surface of a solid have a chemical environment that is markedly different from that of atoms within the bulk of the solid. The atoms at the surface have fewer neighbours than those in the bulk and hence have a lower

coordination number. All solids have a surface Gibbs energy, or surface tension. The surface of a solid will undergo reconstruction in order to minimize the surface Gibbs energy per unit surface area. The driving force behind this surface reconstruction is to attain a thermodynamically more stable system. However, metastable surface structures can exist if the energy barrier for reconstruction is too high.<sup>90</sup>

### 7.3.1 Decomposition of Precursors

The calcination in air of the hydrozincite and/or spherocobaltite-like precursors gave oxides in which ZnO and/or Co<sub>3</sub>O<sub>4</sub> phases were present. It can be seen from Fig 6.22 and Fig 6.25 that as the temperature of calcination was increased the surface area for the Co/Zn 0/100 and 100/0 samples passed through a maximum at *ca.* 200°C. This initial increase in the surface area was thought to be an effect of the dehydration of the precursor surface. As the temperature was increased further micropores collapsed and this led to a further increase in the surface area.<sup>68</sup> This is the result of diffusion of material across bridges between micropores, where surface tension forces are highest, and leads to a greater available surface area. As the temperature was further increased the surface area steadily reduced because of sintering. Sintering is believed to occur due to further diffusion of material across bridges between the small pores (see Fig. 7.3) reducing the surface tension of the oxide overall. This is true also for the mixed Co/Zn samples except that the surface area dipped initially for the samples heat treated at 150°C.

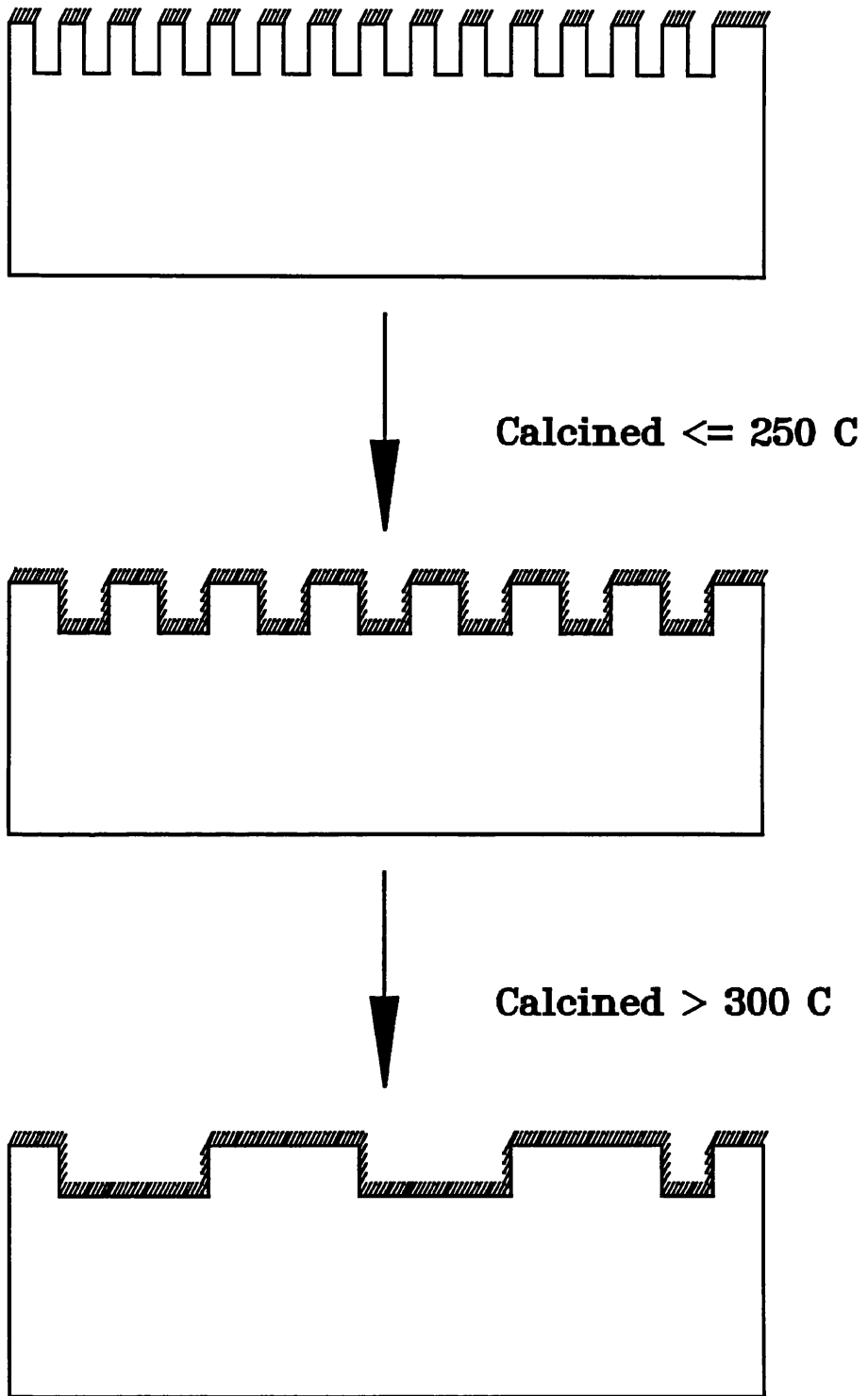


**Fig. 7.3** Diagram of the effect of the calcination temperature on the pore structure of the oxide. The measurable surface area is shown by the hatched line.

In *Section 6.3* it was observed that calcining in flowing air, as opposed to calcining in a muffle oven, increased the surface area of the mixed oxide of nominal Co/Zn loading 30/70. In flowing air the products of the decomposition ( $\text{CO}_2 + \text{H}_2\text{O}$ ) are being removed and this drives the reaction towards completion. Therefore, the decomposition can take place at a lower temperature. Also, the removal of the water may prevent it from assisting in sintering processes during decomposition.

As the temperature of decomposition of the precursors of the 2nd Series was increased (*Section 6.4*) the lines in the XRD patterns became sharper and increased in intensity. This could indicate an increase in particle size and the formation of more crystalline phases. It was thought that mass bulk migration would not have occurred since the mobility of ions occurs at approximately a temperature of  $\frac{1}{2}$  of the melting point for bulk atoms and  $\frac{1}{3}$  for surface atoms. However, diffusion of atoms at phase boundaries could have been assisted and this could help to explain the increase in the crystallinity and possible segregation of the phases at higher temperatures.

### **7.3.2 Nature of Solid-Solutions**

Examination of the XRD tables for the oxides indicated that doping of cobalt into the zinc oxide structure did not result in any change in the observed d-spacings for ZnO with respect to the literature values. The  $\text{Co}^{2+}$  and  $\text{Zn}^{2+}$  ions are a very similar size (0.074 nm and 0.078 nm respectively) and doping with cobalt presumably results in lattice substitution of  $\text{Co}^{2+}$  for  $\text{Zn}^{2+}$ . As the ions are of similar size the substitution does not affect the lattice parameters to any

observable extent. However, substitution of zinc into the cobalt oxide spinel structure resulted in deviations in the d-spacings from literature values. In Fig 7.4 the values for the d-spacings of the mixed oxides of the *1st Series* (taken from Table 6.7) have been plotted against the calculated Co/Zn ratio. According to Vegard's Law, unit cell parameters should change linearly with composition.<sup>48</sup> In the case of cubic systems an increase in the unit cell parameters leads to a lowering of the  $2\theta$  value of the powder lines and this results in an increase in the d-spacing. It assumes implicitly that the change in unit cell parameters with composition is the direct result of the simple substitution of different sized atoms and that the doped ion is randomly distributed. However, as can be seen in Fig. 7.4 change in the d-spacing with composition is not linear. The positive departure observed may be evidence for the presence of clusters of the cobalt and zinc on the microscopic level within the 'cobalt oxide type' phase.<sup>48</sup> The segregation of 'like with like' in the solid

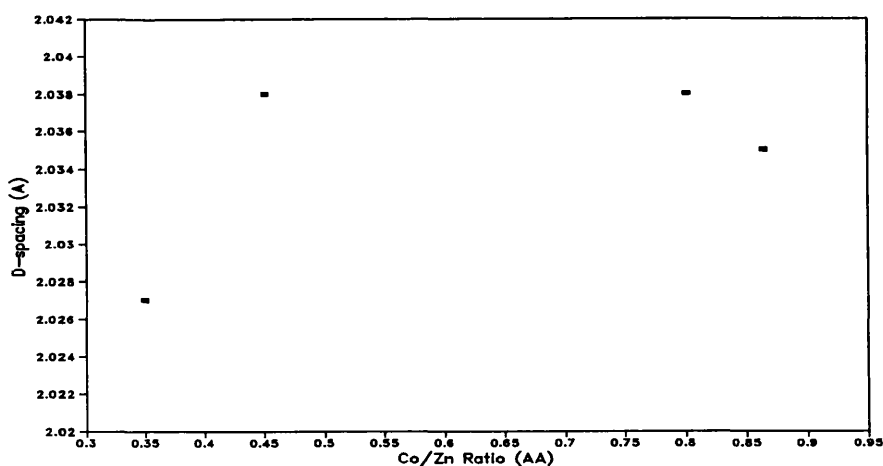


**Fig. 7.4** D-spacing of 'cobalt oxide type' phase vs. Oxide Co/Zn Composition.

solution causes a small increase in the unit cell parameters compared to the values expected by a random arrangement of non-interacting  $\text{Co}^{2+}$  and  $\text{Zn}^{2+}$  ions. This effect would be expected to be determined by the precursor preparation and carried through to the oxides.

### 7.3.3 Surface Effects

The segregation of cobalt was observed at the surface of the oxides of the *1st Series* by XPS (see *Section 6.2*). The surface cation ratio with respect to the bulk depends on a number of factors. These factors include:

1. surface tension of the component oxides.
2. the bulk strain of the solid solution due to mismatch of ionic sizes or the coordination symmetry. The larger ion tends to be segregated to the surface as does the ion whose preferred coordination symmetry differs from that provided by the matrix.

The calcination temperature of  $350^\circ\text{C}$  was not high enough to allow full surface reconstruction to occur, i.e. leading to full segregation of phases. Instead the metastable 'surface spinel',  $\text{ZnCo}_2\text{O}_4$  was formed under the conditions used here. The segregation of cobalt at the surface, which was determined by the precursor conditions and the formation of the 'surface spinel', satisfies each atom's requirements for preferred coordination symmetry, i.e.  $\text{Zn}^{2+}$  is in tetrahedral configuration whilst  $\text{Co}^{3+}$  is in an octahedral configuration.

### 7.3.3a Ionic Charge at Surface

There is little doubt that the true ionic charges in many transition metal oxides are less than those predicted from formal oxidation states. Ionicity affects oxide properties including the surface electric field gradient, the surface electrostatic potential and the mode of surface reconstruction.<sup>35</sup>

Siegbahn *et al.*<sup>91</sup> showed that, using Eqn. 7.2, the chemical shift determined from XPS data of an ion with respect to that atom with zero charge could be used to calculate the true ionic charge of the ion,

$$\text{Shift} = K_B^{q_c} - K_B^0 = q_c \left( \frac{1}{r} - \frac{\phi}{R} \right) \quad \text{Eqn. 7.2}$$

where  $r$  is the ionic radius,  $\phi/R$  is the self-potential and  $K_B^{q_c}$  and  $K_B^0$  are the binding energies of atoms of charge  $q_c$ , the true ionic charge, and zero charge respectively. This theory has been further developed by a number of authors.<sup>92</sup> Problems arise in the calculation of  $q_c$  due to the use of the lattice self-potentials of bulk ions in a calculation which involves surface ions. Because of these limitations the ionic charge obtained is at best qualitative and should only be used for comparison of ionicity among similar solids. In this thesis however the true ionic charges could not be calculated because of a lack of specific data. However the shift in the binding energy between the metal and the ion is directly proportional to  $q_c$  such that the greater the shift in binding energy the greater the value of  $q_c$ . Due to the highly reducing environment created by many X-ray probes reduced metal will be present alongside the ions of interest. Presumably since both the metal ion and metal atom are embedded

in the same solid matrix their extra-atomic relaxation effects<sup>†</sup> should be the same.<sup>93</sup> The data were taken from Table 6.14 and the further analysis is shown in Table 7.1. The true cation charge of both zinc and cobalt ions shows trends across the series. It can be seen that the true cation charge of the Zn<sup>2+</sup> ions slowly decreased as the cobalt loading was increased. In contrast, the true cation charge with respect to the Co<sup>3+</sup> ions increased rapidly to a plateau for nominal Co/Zn ratio of 40/60 and above. Also at Co/Zn 40/60 the presence of the Co<sup>2+</sup> ions became apparent and it was observed that the ionic charge remained constant as the cobalt loading increased. The low cationic charge of the Co<sup>3+</sup> ions observed for the low cobalt loadings, with respect to the high cobalt loading oxides, was due to 'surface spinel', ZnCo<sub>2</sub>O<sub>4</sub>, being in the vicinity of major quantities of ZnO. As the cobalt was located on the surface, the Co<sup>3+</sup> ions were located in positions which lowered the overall electronic charge. As the cobalt loading was increased the surface and near-surface regions became richer in cobalt and hence the surface coverage by the 'surface spinel' increased (see *Section 6.2.2*). The critical point was met when the nominal Co/Zn loading was 40/60. Here the excess of cobalt at the surface allowed not only the formation of the 'surface spinel' ZnCo<sub>2</sub>O<sub>4</sub> but also Co<sub>3</sub>O<sub>4</sub>. At this point the electronic structure of the surface remained constant as the cobalt loading was increased further and hence the true cation charge of the Co<sup>2+</sup> and Co<sup>3+</sup> ions for each loading were very similar.

---

<sup>†</sup>The final state extra-atomic relaxation affects the kinetic energy of the escaping photoelectron due to the relaxation of the electron in the lattice surrounding the ion in response to removal of the photoelectron from the ion (see *Section 2.3.4a*).

**Table 7.1** Trends in the ionicity of the cobalt and zinc ions at the surface of the oxides from the 1st Series.

Co/Zn	$K_B(\text{Zn}^0) - K_B(\text{Zn}^{2+})$	$K_B(\text{Zn}^0) - K_B(\text{Co}^{2+})$	$K_B(\text{Zn}^0) - K_B(\text{Co}^{3+})$
0/100	---	---	---
10/90	---	---	---
20/80	3.1	---	1.3
30/70	3.0	---	2.0
40/60	2.8	4.8	2.8
50/50	2.6	4.8	2.8
100/0	---	4.8	2.8

## 7.4 SULPHIDED OXIDES

If there is a linear relationship between the surface area of the absorbent and the %Reaction lattice diffusion is thought to be the rate limiting step. Therefore 'breakthrough' occurs when the rate of replenishment of the surface is less than the rate of reaction (see *Section 1.3*).

### 7.4.1 Sulphidation of Oxides $\geq 350^\circ\text{C}$

For the ammonium carbonate derived oxides in the *1st Series* (see *Section 6.1*) an almost linear relationship between the %Reaction and the surface area (see Fig. 6.8) was observed for the Co/Zn ratios  $\leq 40/60$ . This suggests that lattice diffusion plays a major role in the rate limiting step. These oxides had a predominantly ZnO structure for the bulk with increasing quantities of the spinel  $\text{ZnCo}_2\text{O}_4$  present at the surface. Lattice diffusion seems also to be the

limiting factor for the low cobalt loading absorbents in the 2nd Series (see Fig. 6.27a) which are also predominantly zinc oxide in structure.

It can be seen in Fig. 6.9 that as the %Cobalt increased in the oxides of the *1st Series* there was, with the exception of the 50/50 and 100/0 samples, a linear increase in the %Reaction. This was again also seen for the *2nd Series* 350 and 450°C oxides of low cobalt loading. This suggests that the surface area was being increased by the increased cobalt loading. This increased surface area resulted in an increased surface coverage of H<sub>2</sub>S and hence the %Reaction increased. Calculations of the number of monolayers present at 'breakthrough' suggests that the oxides react to only *ca.* 3 monolayers.<sup>†</sup> This is again strongly suggesting that lattice diffusion is the rate limiting factor. As suggested by other workers<sup>13,20</sup> an inert sulphide shell is formed which reduces the rate of diffusion of fresh absorbent such that 'breakthrough' occurs when the rate of replenishment of surface < rate of reaction.

Although no pore data is available for any of these absorbents it would seem most likely that lattice diffusion is the most important factor in determining 'breakthrough' for the oxides calcined  $\geq 350^{\circ}\text{C}$ .

For the oxides obtained from different precursors aged for various times (*Section 6.5*) it can be seen that lattice diffusion was the rate limiting step and the precursor morphology obtained after aging for 30 minutes gave the oxide with the highest sulphur absorption capacity.

---

<sup>†</sup>The number of monolayers was calculated by dividing the number of molecules of H<sub>2</sub>S absorbed by the product of the surface area, the weight of absorbent and  $1 \times 10^{19}$ . The figure  $1 \times 10^{19}$  is an estimate of the number of Co/Zn<sup>2+</sup>/O<sup>2-</sup> ions pairs per m<sup>2</sup>.

In Fig. 6.8 and 6.9 it can be seen that for the 50/50 sample in the *1st Series* the %Reaction obtained showed no relationship with its cobalt loading or its surface area with respect to the other loadings. The surface area obtained is lower than expected and the surface area available for H<sub>2</sub>S adsorption has been under utilised. Differential Thermal Analysis (DTA) of this precursor suggested that a massive exothermic transition occurred during the initial decomposition process. This possibly indicates that alongside the endothermic loss of H<sub>2</sub>O and CO<sub>2</sub>, surface reconstruction occurred which has lowered the overall surface tension of the oxide and hence lowered the surface area. This lowering in the surface tension makes the chemisorption of H<sub>2</sub>S less favourable than in the other systems and this results in the lower %Reaction observed. The lower surface area and the fact that the reaction takes place at the surface results in the seemingly under utilisation of the available cobalt. Both the 70/30 and 90/10 loadings have much higher %Reactions than the other mixed oxides. They are both based on the Co<sub>3</sub>O<sub>4</sub> structure which seems to produce better absorbents. In both the *1st* and *2nd Series* the 100/0 loadings, i.e. Co<sub>3</sub>O<sub>4</sub>, have consistently been the absorbents with the highest sulphur capacity. They are of much higher surface area than the mixed oxides. However, in the *2nd Series* it can be seen that lowering the surface area does lower the %Reaction with the exception of the precursor sample. This suggests that the surface area, hence lattice diffusion, is important but the driving force behind surface reconstruction, leading to a rejuvenation of the surface is much stronger for Co<sub>3</sub>O<sub>4</sub> than for ZnO. Monolayer calculations for Co<sub>3</sub>O<sub>4</sub> suggest that *ca.* 7

monolayers are formed by 'breakthrough' indicating that an almost bulk reaction has occurred.

In conclusion, the presence of the cobalt at the surface increased the surface area of the oxides which led to greater reaction. However, from Section 7.3.3.a it was seen that as the cobalt loading was increased there was an increase in the true ionic charge of the cobalt ions at the surface of the oxides. This increased electrostatic gradient assists in surface reconstruction and hence could assist in keeping the rate of replenishment of the surface > the rate of reaction.

#### **7.4.2 Sulphidation of Oxides $\leq 250^{\circ}\text{C}$**

For the absorbents of Co/Zn ratio  $\leq 40/60$  in the *2nd Series* an almost linear relationship in  $\text{H}_2\text{S}$  uptake with respect to surface area was suggested for the  $250^{\circ}\text{C}$  samples, again suggesting lattice diffusion plays a major role as the limiting factor. The precursors and  $150^{\circ}\text{C}$  samples showed no correlation between sulphur uptake and surface area. This suggests that for these samples obtained at  $\leq 250^{\circ}\text{C}$ , factors other than lattice diffusion affect the point at which 'breakthrough' occurs. Such factors may include pore diffusion. At these very low temperatures of heat treatment it is possible that mesopores are present which allows the  $\text{H}_2\text{S}$  to diffuse into the bulk. These pores are created by the collapse of micropores (see *Section 7.3.1*). This mode of  $\text{H}_2\text{S}$  interaction is probably not as important for the absorbents calcined  $\geq 350^{\circ}\text{C}$  because the number of small pores present will be destroyed through the effects of sintering.

### 7.4.3 Effect of Sodium

In Fig. 6.32 it seems that lattice diffusion was the rate limiting step for the oxides derived from the sodium hydrogen carbonate precursors. However, the surface area of the oxides was controlled by the levels of sodium present in the precursors, i.e the lower the percentage sodium in the precursors, the higher the surface areas of their corresponding oxides (see Fig. 6.31). The percentage sodium in the precursors was thought to be an artefact of the shorter aging time used (see *Section 7.2.2*). In Fig. 6.33 it can be seen that the %Conversion decreased with increase in the %Na in the precursors.

Although lattice diffusion is thought to be the major rate determining step it can be seen from Fig. 6.32 that other factors are also thought to be affecting the 'breakthrough' of sample LSS8Na. The higher %Conversion seen for the LSS7Na sample could be the result of increased surface segregation of cobalt at the surface. As a pH of 7 was used, this would lead to the increased preferential precipitation of zinc in the early stages of synthesis leading to the segregation of cobalt at the surface in the final precursor. As observed previously the segregation determined in the precursors is maintained in the oxide. This increased concentration of cobalt at the surface could allow a similar situation to that postulated for the 100% cobalt samples. The very rich cobalt surface increases the driving force for surface reconstruction which increase the rate of replenishment of the surface.

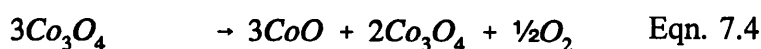
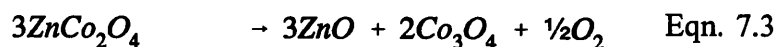
### 7.3.4 Segregation of Phases

After sulphidation it has been observed that segregation of phases has occurred for those oxides which had a 'surface spinel' structure present. The TEM showed the presence of a sheet-like material, which seemed to be present in larger amounts the more the sample had been sulphided. This was observed in the 1st Series with an increase in sulphidation as the cobalt loading was increased and when sections of an absorbent bed were examined. An EELS study of the split bed absorbent revealed that these areas showed that the sheet-like regions were zinc rich. The XPS study of the 1st Series revealed that both  $\text{Co}^{2+}$  and  $\text{Co}^{3+}$  ions were present at the surface after sulphidation where previously the oxides had shown only evidence of  $\text{Co}^{3+}$  ions being present. Holliman *et al.* also observed an increase in the  $\text{Co}^{2+}$  component after sulphidation by UV-VIS-NIR DRS for their study of Co/Zn/Al - oxides.<sup>94</sup>

An explanation of this effect can be based on the assumption that chemisorption lowers the surface energy of the solid. Thus chemisorption tends to induce surface segregation of the component that binds more strongly with the adsorbate.<sup>90</sup> This is a surface phenomena so the segregation occurs only at the surface, hence the growth of very thin sheet-like material at the surface of the absorbent (see Fig. 7.4).

XPS studies of the sulphided oxides also observed that a S2p peak specific to  $\text{SO}_4^{2-}$ , was present in those oxides which had a 'surface spinel' present. It has been suggested that when a mixed oxide system is sulphided, separation of the two oxide components into two distinct phases occurs.<sup>95</sup> As either  $\text{ZnCo}_2\text{O}_4$  or  $\text{Co}_3\text{O}_4$  was present at the surface of each oxide before

sulphiding and H<sub>2</sub>S is a mild reducing agent Eqns. 7.3 or 7.4 could take place. This would result in oxygen being released which could in turn oxidize the S<sup>2-</sup> to SO<sub>4</sub><sup>2-</sup>.



For the mixed Co/Zn oxides the S/SO<sub>4</sub><sup>2-</sup> ratio decreased as the cobalt loading was increased. As the sulphate is assumed to originate from the effect of segregation of the mixed oxides, the decrease in the S/SO<sub>4</sub><sup>2-</sup> ratio could be further evidence of an initial interaction between cobalt and zinc.

## 7.5 CONCLUSIONS

1. A single phase hydrozincite structure was formed for precursors with a Co/Zn ratio  $\leq 17/83$ . However, as the cobalt loading was increased further inclusion of cobalt still occurred alongside the formation of a spherocobaltite phase.
2. The presence of a two-stage initial decomposition curve is indicated by the presence of distinct areas of different Co/Zn ratios.
3. When NaHCO<sub>3</sub> was used as the precipitating agent, altering the pH of precipitation altered the precursor structure. Thus, Na<sup>+</sup> ions can force the adoption of a hydrozincite-like structure irrespective of the Co/Zn loading at pH  $\geq 8$  and a spherocobaltite-like structure at a pH  $< 8$ .
4. Aging time is very important in determining the number and structure of the phases in the final precursor.

5. The variation of the Co/Zn ratios and appearance of secondary phases at the low cobalt loadings is believed to be a function of the pH and the temperature of reaction used.
6. The surface segregation of cobalt in the precursors results from the precipitation conditions. The segregation in the precursors is maintained in the oxides.
7. Bulk segregation at the temperatures of calcination used seems unlikely. However, segregation at phase boundaries may occur at these low temperatures.
8. The formation of the 'surface spinel'  $\text{ZnCo}_2\text{O}_4$  is a metastable structure which lowers the overall surface tension.
9. The segregation of cobalt occurs on the surface and as the cobalt loading increases the cobalt concentration in the near-surface region increases. This caused the true ionic charge of the  $\text{Co}^{3+}$  ion to increase with increasing cobalt loading.
10. The positive deviation in Vegard's Law suggests small 'like for like' interactions are occurring within the oxides.
11. Doping ZnO with cobalt increased the surface area and for low cobalt loading mixed oxides calcined  $\leq 350^\circ\text{C}$  lattice diffusion is the rate determining step.
12. For low cobalt loading mixed oxides heat treated  $\leq 250^\circ\text{C}$ , lattice diffusion plays a major role in the rate determining step. However the rate is possibly controlled in the later stages by pore diffusion.

13. The presence of sodium in the precursors is severely detrimental to the subsequent oxide's sulphur absorption capacity.
14. Cobalt oxide,  $\text{Co}_3\text{O}_4$ , is the best low temperature sulphur absorbent. This is possibly due to a higher driving force towards surface reconstruction.

## APPENDIX A

## ABBREVIATIONS

The abbreviations used are listed for each chapter.

### CHAPTER 1. INTRODUCTION

ccp	cubic close packing
COP	Coprecipitation
DRIFTS	Diffuse Reflectance Infrared Fourier <sup>Transform</sup> Spectroscopy
FPD	Flame Photometric Detector
$h^{-1}$	space velocity
hcp	Hexagonal close packing
HSS	Precipitation at High Supersturation
IMP	Impregnation
$K_{sp}$	Solubility constant
LSS	Precipitation at Low Supersturation
MPa	mega Pascals
ppm	parts per million
pss	pseudo-steady state rate
RSU	Relative Sulphur Uptake
TCD	Thermal Conductivity Detector
TM	Titration Method
XPS	X-ray Photoelectron Spectroscopy
$\Delta G_r^\circ$	Change in Gibbs free energy of reaction

### CHAPTER 2. THEORY OF TECHNIQUES

#### 2.1 Powder X-ray Diffraction

d	d-spacing
I	Intensity
n	Order of diffraction
$\theta$	Bragg angle
$\lambda$	Wavelength

## 2.2 Diffuse Reflectance Spectroscopy

KM	Kubelka-Munk
$d_x$	Infinitesimally thin layer
I	Intensity +ve direction
J	Intensity -ve direction
UV-VIS-NIR	Ultra-violet Visible Near-Infrared
DRS	Diffuse Reflectance Spectroscopy
$d\xi_1$	Mean free path
$\mu$	Intergral (accounting for light rays striking at all angles)
$\kappa$	Fraction of light absorbed per unit path length
$\sigma$	Fraction of light scattered per unit path length
k	$2\kappa$
s	$2\sigma$
R	Reflectance
T	Transmittance
$F(R_\infty)$	Kubelka-Munk function
L	Light source
M	Oscillating mirror
S	Sample
S'	Standard
C	Highly reflecting coating
D	Detector
CT	Charge Transfer

## 2.3 X-ray Photoelectron Spectroscopy

$E_B$	Photoelectron binding energy
$E_K$	Photoelectron kinetic energy
$h\nu$	X-ray energy
$\phi$	'Catch all' term
XRF	X-ray fluorescence
UHV	Ultra high vacuum
V	Deflecting potential

$r_0$	Ideal radius
$r_1$	Radius of outer sphere
$r_2$	Radius of inner sphere
$E_a$	Ideal energy
$\rho$	Resolving power
w	Photoelectron detector entrance slit width
I	Photoelectron intensity
$\alpha$	Photoionisation cross-section
t	Thickness of homogeneous solid
d	Mean escape depth
D	Density of the atom in the material
k	Instrument constant
F	Incident photon intensity
FWHM	Full-Width Half-Maximum
C	Static potential
$\lambda$	Escape depth
KE	Kinetic energy

#### **CHAPTER 4. EXPERIMENTAL**

AA	Atomic Absorption
FTIR	Fourier Transform Infrared Spectroscopy
TGA	Thermogravimetric Analysis
TEM	Transmission Electron Microscopy
XRD	Powder X-ray Diffraction

#### **CHAPTER 5. TREATMENT OF RESULTS**

A	Factor to adjust for standard temperature and pressure
d	Equivalent distance
FR	Flow Rate
mag	Magnification
R	Molar ratio
T	Temperature - Kelvins

## CHAPTER 6. RESULTS

Am	Ammonium carbonate
Cal	Calcined precursor - oxide
EDX	Energy Dispersive X-ray Spectroscopy
EELS	Electron Energy Loss Spectroscopy
Hz	Hydrozincite
Na	Sodium hydrogen carbonate
oct	octahedral
Pre	Precursor
Sph	Sphero-cobaltite
Sul	Sulphided oxide
tet	tetrahedral

## CHAPTER 7. DISSCUSION

$q_c$	True cationic charge
$K_B^{qc}$	Binding energy of atoms of charge $qc$
$K_B^o$	Binding energy of atoms of charge $o$
$r$	ionic radius
$\phi/R$	self-potential

## APPENDIX B

## SOLUBILITY CONSTANT CALCULATIONS

The solubility constant  $K_{sp}$ , is shown below for the precipitation of a metal hydroxide.



$$K_{sp} = [M^+]^x [OH^-]^y = Q \quad \text{Eqn. B.2}$$

Where  $Q$  is the reaction quotient such that if,

- $Q > K_{sp}$       precipitation occurs until  $Q = K_{sp}$
- $Q = K_{sp}$       equilibrium exists (saturated solution)
- $Q < K_{sp}$       solid dissolves until  $Q = K_{sp}$

The values for the solubility constants used are given in the table below. The data was taken from Ref. 14.

Precipitate	$K_{sp}$
$Co(OH)_2$	$1.6 \times 10^{-15}$
$Zn(OH)_2$	$1.2 \times 10^{-17}$
$CoCO_3$	$1.4 \times 10^{-13}$
$ZnCO_3$	$1.4 \times 10^{-11}$

Simple calculations based on the equilibrium concentrations can show the maximum degree of separation which can be achieved under given conditions. In practice, the separation will be poorer than calculated due to coprecipitation. In this phenomenon are included the mechanical enclosure of some solution by the precipitate, adsorption of foreign ions on the surface of the precipitate and solid-solution formation.

**Example 1** A solution, at 25°C, is 1 mol dm<sup>-3</sup> in  $Co(NO_3)_2$  and 1 mol dm<sup>-3</sup> in  $Zn(NO_3)_2$ . What is the concentration of the  $Zn^{2+}$  ions when  $Co(OH)_2$  begins to precipitate?

In solution in equilibrium with both solids, the ratio of  $CoK_{sp}/ZnK_{sp}$  gives the ratio of the concentrations of the cobalt and zinc ions,

$$\frac{[Co^{2+}]}{[Zn^{2+}]} = 133.33 \quad \text{Eqn. B.3}$$

When  $Co(OH)_2$  starts to precipitate, neglecting dilution,

$$[Co^{2+}] = 1 \text{ mol dm}^{-3}$$

Therefore the  $[Zn^{2+}]$  should theoretically be  $7.5 \times 10^{-3} \text{ mol dm}^{-3}$ , i.e. *ca.* 1% of original  $[Zn^{2+}]$ , before  $Co(OH)_2$  precipitation will occur.

## APPENDIX C

## D-SPACING CALCULATIONS

Printout of the SuperCalc<sup>®68</sup> program used for the calculation of the XRD d-spacings from the measured 2θ values.

```

A1           = "Template for d-spacing detemination from 2th valu
A4           P= "Compound Code:
B4           P= "Code:
A5           P= "Compound Name:
B5           P= "Name:
AB           P= "Lamda
B8           2   P= 1.7902
B10          P= "2 th
C10          P= "d/A
D10          P= "I/I
A11         P= '-----
C12          = B8/(2*SIN(.017453292*(.5*B12)))
C13          = B8/(2*SIN(.017453292*(.5*B13)))
C14          = B8/(2*SIN(.017453292*(.5*B14)))
C15          = B8/(2*SIN(.017453292*(.5*B15)))
    
```

RH20B 20/80

Compound Code: RH20B 20/80  
Compound Name:

Lamda 1.7902

	2 th	d/A	I/I
	22.00	4.6911	9
	37.20	2.8063	58
	40.20	2.6046	37
	42.50	2.4697	100
	52.40	2.0274	9
	56.00	1.9066	12
	67.00	1.6217	22
	70.00	1.5606	10
	74.80	1.4737	14

## REFERENCES

## 1.8 REFERENCES

1. R.D. Eden, P.J. Laycock, G. Wilson in *Recent Advances in Oilfield Chemistry*, Ed P.H. Ogden, RSC, 1994.
2. C.H. Bartholemew, P.K. Agranal, J.R. Katzer, *Advances in Catalysis*, 1982, **31**, 136.
3. S. Riddell & B.P. Williams, ICI Katalco - private communication
4. J.M. Parera, J.N. Beltramini, C.A. Querini, E.E. Martinelli, E.J. Churin, P.E. Aloe, N.S. Figoli, *J. Catal.*, 1986, **99**, 39.
5. J.R. Rostrup-Nielsen, *J. Catal.*, 1971, **21**, 171.
6. B. Engler, R. Domesle, E. Koberstein, Eur. Pat. Appl. EP 505,853 (Cl Bo1D53/36) 30 Sept. 1992 DE Appl. 4,110,054 27 Mar 1991 6pp.
7. F.W. Sperr Jr., *Am. Gas Assoc.*, Proc 3:282-364, 1921.
8. D. McManus & A.E. Martell in *Recent Advances in Oilfield Chemistry*, Ed P.H. Ogden, RSC, 1994.
9. A. Kohl & F. Riensenfeld, *Gas Purification*, Gulf Publishing Co., London, 1985.
10. P.J.H. Carnell & P.E. Starkey, *Chem. Eng.*, 1984, **408**, 30.
11. R.H. Griffith, *Gas J.*, 1954, **280**, 254.
12. P.J.H. Carnell, *Feedstock Purification in Catalyst Handbook*, Ed M.V. Twigg, Wolfe Publishing Ltd, London, 1989.
13. P.J.H. Carnell & P.J. Denny, *AIChE Ammonia Safety Symp.*, 1984, 99.
14. *CRC Handbook of Chemistry and Physics*, Ed in Chief D.R. Lide, CRC Press, Boca Raton, 1993-4.
15. C.H. Lawrie, PhD thesis 'Reaction of Hydrogen Sulphide with Zinc Oxide', Dept of Chemical Engineering, University of Edinburgh, 1990.
16. T. Baird, P.J. Denny, R. Hoyle, F. McMonagle, D. Stirling, J. Tweedy, *J. Chem Soc. Faraday Trans.*, 1992, **88(22)**, 3375.
17. J.B. Gibson & D.P. Harrison, *Ind. Eng. Chem. Process Des. Dev.*, 1980, **19**, 231.
18. P.J. Holliman, R. Millar, D. Stirling - unpublished results
19. Yu. V. Furmer, V.I. Kosovotov, O.I. Brui, R.N. Pronina, V.I. Kolmin, *The Soviet Chemical Industry*, 1979, **11.3**, 158.

20. Yu. V. Furmer, V.S. Beskov, O.I. Brui, V.V. Yudina, M.L. Danstig, *The Soviet Chemical Industry*, 1982, **14.12**, 1499.
21. Yu. V. Furmer, O.I. Brui, R.N. Pronina, V.V. Yudina, A.A. Bondareva, *The Soviet Chemical Industry*, 1982, **14.4**, 436.
22. P.K. Gour, S.N. Upadhyay, S. Pande, R. Chatterjee, N.B. Bhattacharyya, S.P. Sen, *Proc. Symp. on Sci. Cat. & Appl. Ind.*, 1979, **48**, 467.
23. J.M. Davidson, P.J. Denny, C.H. Lawrie, *J. Chem. Soc. Chem. Commun.*, 1989, 1695
24. P.J. Denny & B.P. Williams, ICI Katalco - private communication.
25. P.R. Westmoreland & D.P. Harrison, *Environ. Sci. Technol.*, 1976, **10**, 659.
26. P.R. Westmoreland, J.B. Gibson, D.P. Harrison, *Environ. Sci. Technol.*, 1977, **11**, 488.
27. K. Eddington & P.J.H. Carnell, *Oil Gas J.*, 1991, **89**, 69.
28. G.W. Spicer & C. Woodward, *Oil Gas J.*, 1991, **89**, 76.
29. J.M. Cognion, *Chim. Ind. Gen. Chim.*, 1972, **105**, 757.
30. a) T. Grindley, *Desulphurisation of Hot Coal Gas by Zinc Ferrite in Acid and Sour Gas Treating Processes*, Gulf, London, 1984.  
b) S. Lew, K. Jothimurugesan, M. Flytzani-Stephanopoulos, *Ind. Eng. Chem. Res.*, 1989, **28**, 535.
31. P.B. Himelfarb, G.W. Simmons, K. Klier, R.G. Herman, *J. Catal.*, 1985, **93**, 442.
32. D. Waller, D. Stirling, F.S. Stone, M.S. Spencer, *Faraday Discuss. Chem. Soc.*, 1989, **87**, 107.
33. P. Porta, G. Fierro, M. Lo Jacono, G. Moretti, *J. Catal.*, 1988, **109**, 367.
34. S. Angelov, D. Mehandjiev, B. Piperov, V. Zarkov, A. Terlecki-Baricević, D. Joranovic, Z. Jovanović, *Appl. Catal.*, 1985, **16**, 431.
35. H.H. Kung, *Transition Metal Oxides: Surface Chemistry & Catalysis: 45*, Elsevier Publishing, New York, 1989.
36. J.T. Richardson, *Principles of Catalyst Development*, Plenum Press, New York, 1989.
37. F. Cavarni, F. Trifiró, A. Vaccari, *Catal. Today*, 1991, **11(2)**, 173.

38. J.R.H. Ross in *Catalysis, Specialist Periodical Reports*, Ed G.C. Bond & G. Webb, RSC, 1985, vol. 7.
39. *Preparation of Catalysts III*, Ed G. Poncelet, P. Grange, P. Jacobs, Elsevier Publishers, New York, 1983.
40. J.E. Baker, R. Burch, S.E. Golunski, *Appl. Catal.*, 1989, **53**, 279.
41. G. Fornasuri, S. Gusi, F. Trifiró, A. Vacari, *Ind. Eng. Chem. Res.*, 1987, **26**, 1500.
42. D.G. Klissurski & E.L. Uzunova, *J. Mater. Sci. Lett.*, 1990, **9**, 576.
43. P.Porta, R. Dragone, G. Fierro, M. Inversi, M. Lo Jacono, G. Moretti, *J. Mater. Chem.*, 1991, **1**(4), 531.
44. G. Firro, R. Dragone, G. Moretti, P. Porta, *Surface & Interface Anal.*, 1992, **19**, 565.
45. P.Porta, R. Dragone, G. Fierro, M. Inversi, M. Lo Jacono, G. Moretti, *J. Chem. Soc. Faraday Trans.*, 1992, **88**(3), 311.
46. S. Ghose, *Acta Cryst.*, 1964, **17**, 1051.
47. R.W.G. Wyckoff, *Crystal Structures Vol. 2*, Interscience Publishers, Chichester, 1964.
48. A. West, *Solid State Chemistry and it's Applications*, Wiley, Chichester, 1989.
49. JCPDS International Centre for Diffraction Data, *Powder Diffraction File Inorganic Phases*, 1989.
50. A. Schuster, *Astrophys. J.*, 1905, **21**, 1.
51. G. Kortüm, *Reflectance Spectroscopy*, Spinger-Verlag, Berlin, 1969.
52. W.W. Wendlandt & H.G. Hecht, *Reflectance Spectroscopy*, Interscience, New York, 1966.
53. F.S. Stone in *Surface Properties and Catalysis by Non-metals*, Ed J.P. Bonnelle, B. Delmon, E.Derouane, NATO ASI Series D. Reidel Publishing, Dordrecht, 1982.
54. a) M. Gerloch & R.G. Woolley, *Prog. Inorg. Chem.*, 1983, **31**, 371.  
b) F.A. Cotton, G. Wilkinson, P.L. Gaus, *Basic Inorganic Chemistry*, Wiley, Chichester, 1987.
55. A. Einstein, *Annalen der Physik*, 1905, **17**, 132.

56. D. Briggs & M.P. Seah, *Practical Surface Analysis By Auger And XPS*, Wiley, Chichester, 1985.
57. J.H. Scofield, *J. Electron Spectra Relat. Phenom.*, 1976, **8**, 129-137.
58. W.E. Swartz Jr., *Anal. Chem.*, 1973, **45**, 788A.
59. U. Gelius, E. Basilier, S. Svensson, T. Bergmark, K. Siegbahn, *J. Electronic Spectr.*, 1974, **2**, 405.
60. D. Briggs, V.A. Gibson, *Chem. Phys. Lett.*, 1974, **25**, 493.
61. D.C. Frost, A. McDowell, A. Ishitani, *Mol. Phys.*, 1972, **24**, 861.
62. P. Swift, *Surf. Interface Anal.*, 1982, **4**, 47.
63. C.D. Wagner, *Anal. Chem.*, 1975, **47**, 1201.
64. M-Probe 1.34, Surface Science Instruments, Copyright 1989 - 90.
65. D.A. Shirley, *Phys. Rev. B*, 1972, **5**, 4709.
66. P.R. Griffiths, *Transform Techniques in Chemistry*, Plenum Press, New York, 1978.
67. J. Szajman, J. Liesgeng, J.G. Jenluin, R.G.G. Leckey, *J. Electron Spectrosc.*, 1981, **23**, 69.
68. A.M. Khahil & S. Kolboe, *Surface Technology*, 1983, **18**, 249.
69. D. Klissurski, I. Uzunov, K. Kumbilieva, *Thermochimica Acta*, 1985, **93**, 485.
70. SuperCalc4, Version 1.00, Computer Associates International Inc., S/N 4156-046588, IBM DOS (8087 not present), Copyright 1986.
71. N.G. Farr & H.J. Griess, *J. Electron Spectrosc. Relat. Phenom.*, 1989, **49**, 293.
72. JCPDS 19-1458 Hydrozincite,  $Zn_5(CO_3)_2(OH)_6$
73. JCPDS 11-692 Sphero-cobaltite,  $CoCO_3$
74. O Garcia-Martinez, P. Millan, R.M. Rojas, M.J. Torralio, *J. Mater. Sci.*, 1988, **23**, 1334.
75. J.A. Gadsden, *Infrared Spectra of Minerals and Related Inorganic Compounds*, Butterworth, London, 1975.
76. JCPDS 5-664 Zinc Oxide,  $ZnO$
77. JCPDS 9-418 Cobalt Oxide,  $Co_3O_4$
78. JCPDS 23-1390 Zinc Cobalt Oxide,  $ZnCo_2O_4$

79. D.S. McClure, *J. Chem. Phys.*, 1962, **36**(3), 2757.
80. P. Pappalardo, D.C. Wood, R.C. Linavesta Jr., *J. Chem. Phys.*, 1961, **35**(6), 2041.
81. Dr. M. Huxham - unpublished work.
82. J.S. Hammond, S.W. Gaarenstroom, N. Winograd, *Anal. Chem.*, 1975, **47**, 2194.
83. J.J. Chuang, C.R. Brundle, D.W. Rice, *Surf. Sci.*, 1976, **59**, 413.
84. C. D. Wagner in *Handbook of X-Ray and Ultraviolet Photoelectron Spectroscopy*, Ed D. Briggs, Hayden, London, 1978.
85. JCPDS 11-287 Zinc Carbonate Hydrate  $Zn_4CO_3(OH)_6 \cdot H_2O$
86. JCPDS 1-457 Sodium Zinc Carbonate Hydrate,  $Na_2Zn_3(CO_3)_4 \cdot 3H_2O$
87. A. Massinon & R. Hoyle - Unpublished work
88. J. N. Butler, *Solubility and pH Calculations*, Addison-Wesley, Reading, 1964.
89. G.C. Shen, S. Fujita, N. Takezaw, *J. Catal.*, 1992, **138**, 754.
90. G. A. Somorjai, *Introduction to Surface Chemistry and Catalysis*, Wiley-Interscience, Chichester, 1994.
91. K. Seighban, C. Nordling, A. Fahlman, R. Nordberg, K. Harnrin, J. Hedman, G. Johannson, T. Bergmark, S.E. Karlsson, I. Lundgren, B. Lingberg, *ESCA: Atomic, Molecular and Solid State Structure Studied by Means of Electron Spectroscopy*, Nova Acta. Regiae. Sci., Upsalensis Ser. IV, 1967.
92. J.Q. Broughton & P.S. Bagus, *J. Electron Spectro. Related Phenom.*, 1980, **20**, 127.
93. T. Dickenson, A.F. Povey, P.M.A. Sherwood, *J. Chem. Soc. Faraday Trans. I*, 1976, **72**, 686.
94. P.J. Holliman, T. Baird, K.C. Campbell, R. Hoyle, D. Stirling, B.P. Williams - paper submitted
95. R.V. Siriwardane & J.A. Poston, *Appl. Surf. Sci.*, 1990, **45**(2), 841.

